Università degli Studi di Bologna

FACOLTÀ DI SCIENZE MATEMATICHE, FISICHE E NATURALI

Dipartimento di Astronomia

STATISTICAL PROPERTIES OF RADIO HALOS AND THE RE-ACCELERATION MODEL

DOTTORATO DI RICERCA IN ASTRONOMIA

XIX CICLO - FIS/05

Coordinatore Chiar.mo Prof. LAURO MOSCARDINI

Tesi di Dottorato di:

ROSSELLA CASSANO

Relatore: Chiar.mo Prof.

GIANCARLO SETTI

Co-relatore:

Dr. **GIANFRANCO BRUNETTI**

Contents

Abstract

Galaxy clusters occupy a special position in the cosmic hierarchy as they are the largest bound structures in the Universe. There is now general agreement on a hierarchical picture for the formation of cosmic structures, in which galaxy clusters are supposed to form by accretion of matter and merging between smaller units. During merger events, shocks are driven by the gravity of the dark matter in the diffuse barionic component, which is heated up to the observed temperature.

Radio and hard-X ray observations have discovered non-thermal components mixed with the thermal Intra Cluster Medium (ICM) and this is of great importance as it calls for a "revision" of the physics of the ICM. The bulk of present information comes from the radio observations which discovered an increasing number of Mpc-sized emissions from the ICM, Radio Halos (at the cluster center) and Radio Relics (at the cluster periphery). These sources are due to synchrotron emission from ultra relativistic electrons diffusing through μG turbulent magnetic fields. Radio Halos are the most spectacular evidence of non-thermal components in the ICM and understanding the origin and evolution of these sources represents one of the most challenging goal of the theory of the ICM.

Cluster mergers are the most energetic events in the Universe and a fraction of the energy dissipated during these mergers could be channelled into the amplification of the magnetic fields and into the acceleration of high energy particles via shocks and turbulence driven by these mergers. Present observations of Radio Halos (and possibly of hard X-rays) can be best interpreted in terms of the re-acceleration scenario in which MHD turbulence injected during these cluster mergers re-accelerates high energy particles in the ICM. The physics involved in this scenario is very complex and model details are difficult to test, however this model clearly predicts some simple properties of Radio Halos (and resulting IC emission in the hard X-ray band) which are almost independent of the details of the adopted physics. In

particular in the re-acceleration scenario MHD turbulence is injected and dissipated during cluster mergers and thus Radio Halos (and also the resulting hard X-ray IC emission) should be *transient phenomena* (with a typical lifetime $\lesssim$ 1 Gyr) associated with dynamically disturbed clusters. The physics of the re-acceleration scenario should produce an unavoidable cut-off in the spectrum of the re-accelerated electrons, which is due to the balance between turbulent acceleration and radiative losses. The energy at which this cut-off occurs, and thus the maximum frequency at which synchrotron radiation is produced, depends essentially on the efficiency of the acceleration mechanism so that observations at high frequencies are expected to catch only the most efficient phenomena while, in principle, low frequency radio surveys may found these phenomena much common in the Universe.

These basic properties should leave an important imprint in the statistical properties of Radio Halos (and of non-thermal phenomena in general) which, however, have not been addressed yet by present modellings.

The main focus of this PhD thesis is to calculate, for the *first time*, the expected statistics of Radio Halos in the context of the re-acceleration scenario. In particular, we shall address the following main questions:

- Is it possible to model "self-consistently" the evolution of these sources together with that of the parent clusters?

- How the occurrence of Radio Halos is expected to change with cluster mass and to evolve with redshift? How the efficiency to catch Radio Halos in galaxy clusters changes with the observing radio frequency?

- How many Radio Halos are expected to form in the Universe? At which redshift is expected the bulk of these sources?

- Is it possible to reproduce in the re-acceleration scenario the observed occurrence and number of Radio Halos in the Universe and the observed correlations between thermal and non-thermal properties of galaxy clusters?

- Is it possible to constrain the magnetic field intensity and profile in galaxy clusters and the energetic of turbulence in the ICM from the comparison between model expectations and observations?

Several astrophysical ingredients are necessary to model the evolution and statistical properties of Radio Halos in the context of re-acceleration model and to address the points given above. For these reason we deserve some space in this PhD thesis to review the important aspects of the physics of the ICM which are of interest to catch our goals. In Chapt. 1 we discuss the physics of galaxy clusters, and in particular, the clusters formation process; in Chapt. 2 we review the main observational properties of non-thermal components in the ICM; and in Chapt. 3 we focus on the physics of magnetic field and of particle acceleration in galaxy clusters.

As a relevant application, the theory of Alfvénic particle acceleration is applied in Chapt. 4 where we report the most important results from calculations we have done in the framework of the re-acceleration scenario. In this Chapter we show that a fraction of the energy of fluid turbulence driven in the ICM by the cluster mergers can be channelled into the injection of Alfvén waves at small scales and that these waves can efficiently re-accelerate particles and trigger Radio Halos and hard X-ray emission.

The main part of this PhD work, the calculation of the statistical properties of Radio Halos and non-thermal phenomena as expected in the context of the re-acceleration model and their comparison with observations, is presented in Chapts.5, 6, 7 and 8.

In Chapt.5 we present a first approach to semi-analytical calculations of statistical properties of giant Radio Halos. The main goal of this Chapter is to model cluster formation, the injection of turbulence in the ICM and the resulting particle acceleration process. We adopt the semi–analytic extended Press & Schechter (PS) theory to follow the formation of a large synthetic population of galaxy clusters and assume that during a merger a fraction of the PdV work done by the infalling subclusters in passing through the most massive one is injected in the form of magnetosonic waves. Then the processes of stochastic acceleration of the relativistic electrons by these waves and the properties of the ensuing synchrotron (Radio Halos) and inverse Compton (IC, hard X-ray) emission of merging clusters are computed under the assumption of a constant rms average magnetic field strength in emitting volume. The main finding of these calculations is that giant Radio Halos are *naturally* expected only in the more massive clusters, and that the expected fraction of clusters with Radio Halos is consistent with the observed one.

In Chapt. 6 we extend the previous calculations by including a scaling of the magnetic field strength with cluster mass. The inclusion of this scaling allows us to derive the expected correlations between the synchrotron radio power of Radio Halos and the X-ray properties (T, L_X) and mass of the hosting clusters. For the first time, we show that these correlations, calculated in the context of the re-acceleration model, are consistent with the observed ones for typical μG strengths of the average B intensity in massive clusters. The calculations presented in this Chapter allow us to derive the evolution of the probability to form Radio Halos as a function of the cluster mass and redshift. The most relevant finding presented in this Chapter is that the luminosity functions of giant Radio Halos at 1.4 GHz are expected to peak around a radio power $\sim 10^{24}$ W/Hz and to flatten (or cut-off) at lower radio powers because of the decrease of the electron re-acceleration efficiency in smaller galaxy clusters. In Chapt. 6 we also derive the expected number counts of Radio Halos and compare them with available observations: we claim that ~ 100 Radio Halos in the Universe can be observed at 1.4 GHz with deep surveys, while more than 1000 Radio Halos are expected to be discovered in the next future by LOFAR at 150 MHz. This is the first (and so far unique) model expectation for the number counts of Radio Halos at lower frequency and allows to design future radio surveys.

Based on the results of Chapt. 6, in Chapt.7 we present a work in progress on a "revision" of the occurrence of Radio Halos. We combine past results from the NVSS radio survey ($z \sim 0.05 - 0.2$) with our ongoing GMRT Radio Halos Pointed Observations of 50 X-ray luminous galaxy clusters (at $z \sim 0.2 - 0.4$) and discuss the possibility to test our model expectations with the number counts of Radio Halos at $z \sim 0.05 - 0.4$.

The most relevant limitation in the calculations presented in Chapt. 5 and 6 is the assumption of an "averaged" size of Radio Halos independently of their radio luminosity and of the mass of the parent clusters. This assumption cannot be released in the context of the PS formalism used to describe the formation process of clusters, while a more detailed analysis of the physics of cluster mergers and of the injection process of turbulence in the ICM would require an approach based on numerical (possible MHD) simulations of a very large volume of the Universe which is however well beyond the aim of this PhD thesis.

On the other hand, in Chapt.8 we report our discovery of novel correlations between

the size (R_H) of Radio Halos and their radio power and between R_H and the cluster mass within the Radio Halo region, M_H. In particular this last "geometrical" $M_H - R_H$ correlation allows us to "observationally" overcome the limitation of the "average" size of Radio Halos. Thus in this Chapter, by making use of this "geometrical" correlation and of a simplified form of the re-acceleration model based on the results of Chapt. 5 and 6 we are able to discuss expected correlations between the synchrotron power and the thermal cluster quantities relative to the radio emitting region. This is a *new powerful tool* of investigation and we show that all the observed correlations ($P_R - R_H$, $P_R - M_H$, $P_R - T$, $P_R - L_X$, ...) *now* become well understood in the context of the re-acceleration model. In addition, we find that observationally the size of Radio Halos scales non-linearly with the virial radius of the parent cluster, and this immediately means that the fraction of the cluster volume which is radio emitting increases with cluster mass and thus that the non-thermal component in clusters is not self-similar.

Chapter 1

Clusters of Galaxies

In this Chapter we give a brief description of the main properties of galaxy clusters and focus on the theory of *structure formation* which is extensively used during this PhD work.

1.1 Introduction

Galaxy clusters are the largest concentrations of matter in our Universe. They form through the gravitational collapse of rare high peaks of primordial density perturbations in the hierarchical clustering scenario for the formation of cosmic structures (*e.g.,* Peebles 1993; Coles & Lucchin 1995; Peacock 1999). They extend over 1-3 Mpc regions and are characterized by a total mass of $\sim 10^{14} - 10^{15}\ M_{\odot}$. They contain large concentrations of galaxies, so that they were first identified in the optical band (*e.g.,* Abell 1958; Zwicky et al. 1966; Abell 1989). The optical observations showed that galaxy clusters are associated with deep gravitational potential wells in which galaxies are moving with velocities dispersion of the order of $\sigma_v \sim 1000$ km/s. The crossing time for a cluster of size R can be estimated as:

$$t_{cr} = R/\sigma_v \simeq \left(\frac{R}{1\mathrm{Mpc}}\right)\left(\frac{10^3\mathrm{km/s}}{\sigma_v}\right)\mathrm{Gyr} \tag{1.1}$$

Therefore, in a Hubble time, $t_H \simeq 10h^{-1}$ Gyr, such a system, at least in its central ~ 1 Mpc, has enough time to dynamically relax, a condition that cannot be achieved in the surrounding, ~ 10 Mpc, environment. Assuming virial equilibrium, the typical cluster mass results:

$$M \simeq \frac{R\sigma_v^2}{G} \simeq \left(\frac{R}{1\mathrm{Mpc}}\right)\left(\frac{\sigma_v}{10^3\mathrm{km/s}}\right)^2 10^{15}\mathrm{M}_{\odot} \tag{1.2}$$

First optical studies using Eq.1.2 noticed that the mass implied by the motion of galaxies in the clusters was largely exceeding (about a factor of ~ 10) the sum of the mass of all visible galaxies and this was the first evidence of the presence of dark matter (Zwicky 1933, 1937; Smith 1936). Indeed, the total mass of galaxy clusters is contributed by 10% of galaxies, by 15-20% of hot diffuse gas and by 70% of dark matter.

If the hot diffuse gas, permeating the cluster potential well, shares the same dynamics as member galaxies, then it is expected to have a typical temperature:

$$K_B T \simeq \mu m_p \sigma_v^2 \simeq 6 \Big(\frac{\sigma_v}{10^3 \mathrm{km/s}} \Big)^2 \mathrm{keV} \tag{1.3}$$

where m_p is the proton mass and μ is the mean molecular weight ($\mu = 0.6$ for a primordial composition with a 76% fraction contributed by hydrogen). X-ray observation of clusters actually are in agreement with this relation, although with some scatter, indicating that the idealized picture of clusters as relaxed structures in which both gas and galaxies feel the same dynamics is a reasonable description.

1.2 Intracluster Gas

X-ray observation of clusters show that they are bright X-ray sources (in the 0.1-10 keV band), with luminosities of $\sim 10^{43} - 10^{45}$ergs/s. The X-ray continuum emission from a hot ($\sim 10^8$K) and low density ($n_e \sim 10^{-3} - 10^{-4}\,\mathrm{cm}^{-3}$) plasma, such as the ICM, is due primarily to thermal bremsstrahlung. The emissivity for this process at frequency ν scales as:

$$\epsilon_\nu \propto n_e n_i g(\nu, T) T^{1/2} exp(-h\nu/k_B T) \tag{1.4}$$

where n_e and n_i are the number density of electrons and ions, respectively, and $g(\nu, T) \propto \ln(k_B T/h\nu)$ is the Gaunt factor. For systems with $T > 3$ keV the pure bremsstrahlung emissivity is a good approximation, while for lower temperature line emission (bound-bound transitions) become more important. The spectral shape of the emissivity $\epsilon_\nu(r)$ provides a measure of $T(r)$, while its normalization gives a measure of $n_e(r)$.

1.2.1 Cooling flows

The X-rays emitted from clusters of galaxies via thermal bremsstrahlung represent the main energy losses for the ICM. The cooling time scale for this process can be defined as $t_{cool} \equiv (d \ln T/dt)^{-1}$. If the gas cools isobarically, the cooling time is (*e.g.,* Sarazin 1986):

$$t_{cool} \simeq 8.5 \times 10^{10} \Big[\frac{n_p}{10^{-3}\,cm}\Big]^{-1} \Big[\frac{T}{10^8\,\mathrm{K}}\Big]^{1/2} \tag{1.5}$$

which is longer than a Hubble time. However, the thermal bremsstrahlung depends on the square of the gas density (Eq.1.4), which rises towards the cluster centre (see Sec.1.2.2 and Eq.1.16), thus in some clusters of galaxies it can happen that the gas density within the central 100 kpc or so is high enough that the radiative cooling time of the gas becomes less than 10^{10} yr. The cooling time drops further at smaller radii, and in the absence of any balancing heating of the gas much of the gas in the central regions should cooling out of the hot ICM. As the gas begins to cool, it is compressed by the surrounding atmosphere and this increases its X-ray emissivity. In order to maintain the pressure required to support the weight of the overlying gas, a slow, subsonic inflow known as "cooling flow" should develop.

The final result is that the gas within the cooling radius, r_c, radiates the thermal energy plus the PdV work done on it as it enters the cooling region (see Fabian 1994, for a review). Sharply peaked X-ray surface brightness distribution observed in several clusters of galaxies were the primary evidence for cooling flow. Observationally, the fraction of clusters with high central surface brightnesses which imply $t_{cool} < 10^{10} yr$ at the cluster center, is as large as $\sim 70 - 80\%$, which means that cooling flow must be common and long-lived (*e.g.,* Fabian 1994).

X-ray observations made before Chandra and XMM-Newton were roughly consistent with the standard cooling flow picture. The situation of cooling flows has been modified thanks to the high spatial resolution imaging of Chandra and the high spectral resolution of XMM-Newton spectrometer.

As a matter of fact, there is a clear evidence that in the central 100 kpc the gas temperature drops by a factor of 3 or more, down to 2-3 keV but not to lower temperatures (*e.g.,* Peterson et al. 2003), and what really happens is not obvious, since the gas does not appear to be piling up at the lower temperature but it seems that the gas temperature profile is 'frozen' and has been so for some Gyrs

(*e.g.,* Bauer et al. 2005).

The profile of t_{cool} is similar in many clusters with a common central minimum value for t_{cool} of about 200 Myr. This strongly suggests that heating is continuous, at least on timescales of 10^8 yr or more and is spatially distributed. Moreover, no shock waves have been found in these regions so any mechanical energy injection must be subsonic.

Some mechanisms of heating may balance radiative cooling but the source of heating remains unsolved, although several good candidates have been proposed: supernovae (*e.g.,* Silk et al. 1986; Domainko et al. 2004), active galactic nuclei (*e.g.,* Bailey 1982; Tucker & Rosner 1983; Binney & Tabor 1995; Fabian et al. 2002; Bîrzan et al. 2004), thermal conduction (*e.g.,* Rosner & Tucker 1989; Voigt et al. 2002; Cho et al. 2003).

ROSAT HRI and Chandra data clearly showed that the central radio sources of several clusters are strongly interacting with the ICM (*e.g.,* Böhringer et al. 1993; Fabian et al. 2005). In particular holes in the X-ray surface brightness coincident with radio lobes are commonly seen and generally referred to as *radio bubbles*. They are interpreted as bubbles of relativistic gas blown by the AGN into the thermal ICM. Bubbles are expected to detach from the core and rise up buoyantly trough the cluster, *e.g.,* Perseus (Churazov et al. 2000). These evidences have been considered in favour of heating mechanism driven by the dissipation of energy propagating through the ICM from a central radio source. However, difficulties and doubts remain in this regard and future studies are needed in order to better understand the heating/cooling balance. We refer the reader to the recent works by Peterson & Fabian (2006) and Dunn & Fabian (2006).

1.2.2 Hydrostatic equilibrium model

The sound speed in galaxy clusters is given by:

$$c_s = \sqrt{\frac{\partial P}{\partial \rho}} = \sqrt{\frac{5 K_B T}{3 \mu m_p}} \sim 1470 \sqrt{\frac{T}{10^8 K}}\,\mathrm{km/s} \tag{1.6}$$

and the sound crossing time is:

$$t_s \simeq 0.67 \sqrt{\frac{10^8 K}{T}} \cdot \left(\frac{R}{1\mathrm{Mpc}}\right) \mathrm{Gyr} \tag{1.7}$$

Therefore, given that the sound crossing time is $\ll$ than the cluster lifetime ($\sim$ the Hubble time), as a first approximation the gas in galaxy clusters can be treated as a collisional fluid in hydrostatic equilibrium (the last assumption is valid as long as the cluster is stationary, *i.e.,* the gravitational potential does not change on a sound crossing time). Under these circumstances, the gas obeys the hydrostatic equation and from the variations of pressure and density one can determine the total mass. The equation of the hydrostatic equilibrium, which is based on spherical symmetry, static gravitational potential and isotropy velocity field, is:

$$\frac{dP_{gas}}{dr} = -\rho_{gas}\frac{d\Phi(r)}{dr} = -\rho_{gas}\frac{GM(r)}{r^2} \tag{1.8}$$

where $P = \rho_{gas}K_BT_{gas}/\mu m_p$ is the gas pressure, ρ is the gas density, $\Phi(r)$ is the gravitational potential of the cluster, r is the distance from the cluster centre and $M(r)$ is the total cluster mass inside r. From Eq.1.8 one has the total mass $M(r)$ interior to r:

$$M_{tot}(< r) = -\frac{K_BTr}{\mu m_p G}\Big[\frac{\mathrm{dln}\rho_{gas}}{\mathrm{dln}r} + \frac{\mathrm{dln}T}{\mathrm{dln}r}\Big], \tag{1.9}$$

It is important to note that the mass depends only weakly on density, but strongly on the temperature distribution, $T(r)$, which is not easy to derive. One approach is to assume a simple "polytropic" equation of state connecting the temperature and density $T \propto n_e^{\gamma-1}$, where $\gamma = 1$ means that the gas is isothermal. The assumption that the gas is isothermal leads to a particularly simple density distribution for the gas; from Eq.1.8 one has:

$$\frac{d\ln\rho_{gas}}{dr} = -\frac{\mu m_p}{K_BT}\frac{d\Phi(r)}{dr} \tag{1.10}$$

In order to derive the expression for the gas density profiles in galaxy clusters it is necessary to get the gravitational potential Φ of the cluster. By considering the cluster as a self-gravitating system of collisionless particles (essentially galaxies and dark matter) with a density profile $\rho(r)$ and isotropic velocity dispersion σ_r^2, it is:

$$\frac{d\ln\rho}{dr} = -\frac{1}{\sigma_r^2}\frac{d\Phi(r)}{dr} \tag{1.11}$$

which may be integrated and solved for $\rho(r)$ as:

$$\rho(r) = \rho_o \exp\left[\frac{\Phi(r)}{\sigma_r^2}\right] \tag{1.12}$$

Combining this equation with the Poisson equation

$$\nabla^2\Phi(r) = 4\pi G\rho(r) \tag{1.13}$$

one obtains $\rho(r)$ and $\Phi(r)$. Although Eq.1.12 and Eq.1.13 do not give a trivial solution, King (1962) derived an approximate solution for $\rho(r)$ and $\Phi(r)$ in the form:

$$\Phi(r) = -4\pi G\rho_o(r) r_c^2 \frac{\ln[r/r_c + (1+(r/r_c)^2)^{1/2}]}{r/r_c} \tag{1.14}$$

$$\rho(r) = \rho_o\left[1 + \left(\frac{r}{r_c}\right)^2\right]^{-3/2} \tag{1.15}$$

where ρ_o is the central density and r_c is a characteristic radius. These two expressions satisfy the Poisson equation (Eq.1.13) exactly, while they satisfy approximately the equation hydrostatic equilibrium (Eq.1.11). As the hot gas and the collisionless "particles" must obey the same gravitational potential $\Phi(r)$, combining Eq.1.11 and Eq.1.10, one has $\rho_{gas} = \rho^\beta$, with $\beta \equiv \mu m_p \sigma_r^2 / K_B T$, and thus the isothermal gas distribution is given by:

$$\rho_{gas}(r) = \rho_{gas,o}\left[1 + \left(\frac{r}{r_c}\right)^2\right]^{-3\beta/2} \tag{1.16}$$

which is commonly referred to as the β-model (Cavaliere & Fusco-Femiano 1976). This can be regarded as a realistic gas density profile under the conditions that the cluster potential can be approximated with a King model (Eq.1.14 and Eq.1.15) and that the intracluster gas is essentially isothermal. The β parameter indicates the ratio between specific kinetic energy of the "particles" responsable of the cluster potential and the specific thermal energy of the gas particles. When all the constituent components of the cluster have the same energy for unit mass, we expect $\beta = 1$. In many clusters of galaxies the β-model with $\beta \simeq 0.5 - 1$ gives a fairly good approximation of the observed X-ray surface brightness.

This model has the advantage that the resulting gas distribution and all the integral to compare the model to the observations are analytic (for example, the total cluster mass and the X-ray brightness distribution), although the basic assumptions

that both galaxy and gas are in hydrostatic equilibrium and isothermal, and that the mass profile of galaxies is representative of the total mass profile are not in general fully motivated.
By combining Eq.1.16 and Eq.1.9, and assuming the gas to be isothermal yields:

$$M_{tot}(< r) = \frac{3K_B T r^3 \beta}{\mu m_p G} \left(\frac{1}{r^2 + r_c^2} \right), \tag{1.17}$$

The X-ray mass determination method usually gives good results in relaxed clusters, although, the temperature in real clusters decreases with increasing radius and this may cause an overestimation of the cluster mass of about 30% at about six core radii (Markevitch et al. 1998).

Eq.1.17 may fail in the case of dynamically disturbed clusters as merging clusters, because the merger may cause substantial deviation from hydrostic equilibrium and spherical symmetry (*e.g.,* Evrard, Metzler & Navarro 1996; Röttiger, Burns & Loken 1996; Schindler 1996). Several numerical simulation studies have been undertaken in order to determinate whether the above assumptions introduce significant uncertainties in the mass estimates. Generally, these simulations indicate that in the case of merging clusters the hydrostatic equilibrium method can lead to errors up to 40% of the true mass (*e.g.,* Evrard, Metzler & Navarro 1996; Röttiger, Burns & Loken 1996; Schindler 1996; Rasia et al. 2006). In particular, the masses in merging clusters can be either overestimated in the presence of shocks, or underestimated since substructures tend to flatten the average density profile (see Schindler 2002).

1.3 Dark Matter, galaxies and mass determination

In a galaxy cluster with N galaxies the short-range gravitational effects are marginally effective. Indeed the two-body relaxation time for such a system can be estimated as (*e.g.,* Binney & Tremaine 1987):

$$t_{relax} \sim \frac{N}{\ln N} t_{cr} \tag{1.18}$$

Thus, taking $N \sim 10^2$ and $t_{cr} \sim 1$ Gyr, t_{relax} is somewhat larger than the Hubble time and galaxies in clusters are a collisionless system under the influence of the *mean*

potential. Also the dark matter component, which dominates the gravitational field of galaxy clusters, can be described as a collisionless system.

In fact, galaxy clusters are expected to reach the condition of dynamical equilibrium under the effect of a process know as *violent relaxation* (Lynden-Bell 1967), essentially under the action of rapid changes in the gravitational potential during the collapse of the structure. The dynamical equilibrium of a collisionless system is described by the Jeans equation and for a static and spherical system it is (*e.g.,* Binney & Tremaine 1987):

$$M_{tot}(< r) = -\frac{\sigma_r^2(r) r}{G}\Big[\frac{\mathrm{dln}\rho(r)}{\mathrm{dln}r} + \frac{\mathrm{dln}\sigma_r^2(r)}{\mathrm{dln}r} + 2\beta_a(r)\Big], \tag{1.19}$$

where $\rho(r)$, σ_r and β_a refer to any distribution of tracers (*e.g.,* galaxies) in dynamical equilibrium within the global potential. $\beta_a \equiv 1 - \frac{\sigma_t^2}{\sigma_r^2}$ is the anisotropy parameter and σ_r and σ_t are the radial and tangential velocity dispersion respectively. Usually, in measuring the cluster mass from Eq.1.19, it is customary to assume isotropy of the velocity field and derive ρ_{gal} deprojecting the observed 2d density of galaxies. Eq.1.19 with $\beta_a = 0$ is the equivalent of Eq.1.9 where the tracer of the gravitational potential is the gas and it can also be shown that Eq.1.19 in the case of $\beta_a = 0$ and $d\sigma_r^2/dr = 0$ is equivalent to the the virial theorem:$\langle v^2 \rangle = GM_{tot}/r$. The dynamical mass of a cluster obtained from the virial theorem is larger than the sum of the masses of the galaxies and emitting gas, and this was first known as the *missing mass* problem and was the first evidence of the existence of dark matter (DM) in galaxy clusters (Zwicky 1933, from optical observations).

Several candidates for this DM are being discussed. While, for instance, observations of the large scale clustering of galaxies rule out neutrinos (candidates for Hot Dark Matter, HDM) as forming the main component of the dark matter (*e.g.,* White et al. 1983), the recent strong evidence that neutrinos with finite rest mass do exist (*e.g.,* Fukuda et al. 1998) leaves the possibility that at least part of the missing mass is provided by neutrinos. One of the frequently invoked possible Cold Dark Matter (CDM) particles are the axions (*e.g.,* Overduin & Wesson 1993); also the contribution of the heavier neutralino and gravitino is often discussed (*e.g.,* Overduin & Wesson 1997).

The CDM paradigm has been extremely successful in explaining observations of the universe on large scale at various epochs. Tanks to N-body simulations, which

are now able to resolve structures on highly nonlinear scales, the properties of DM halos can be modeled. A central prediction arising from CDM simulations is that the density profiles of DM halos is universal as it does not depend on their mass, on the power spectrum of initial fluctuations, and on the cosmological parameters Ω_o and Λ (*e.g.,* Navarro, Frenk & White 1995, 1997). It appears that mergers and collisions during halo formation act as a "relaxation" mechanism to produce an equilibrium largely independent of initial conditions. This profile is referred to Navarro-Frenk-White (NFW) profile:

$$\rho_{NFW}(r) = \frac{\rho_c \delta_c}{(r/r_s)(1+r/r_s)^2} \tag{1.20}$$

where $r_s = r_{200}/c$ is the "scale" radius where the profile changes shape; $\rho_c = 3H^2/8\pi G$ is the critical density (H is the current value of Hubble's constant); δ_c and c are two dimensionless parameters, they are called respectively the characteristic overdensity of the halo and its concentration. δ_c and c are linked by the requirement that the mean density of the halo within r_{200} should be $200 \times \rho_c$, this leads to:

$$\delta_c = \frac{200}{3} \frac{c^3}{(ln(1+c) - c/(1+c))} \tag{1.21}$$

The asymptotical behavior of the NFW profile is:

$$\rho_{NFW}(r) \propto \begin{cases} r^{-1} & \text{for } r << r_s \\ r^{-3} & \text{for } r >> r_s \end{cases}$$

thus the NFW profile is singular, *i.e.,* it diverges like r^{-1} near the center (although the mass and potential converge near the center). It has been found, both observationally and with numerical simulations (see Dolag et al. 2004; Biviano 2006), that smaller mass halos are more concentrated (have large values of c) than the higher mass halos, this is because lower mass systems have higher formation redshift than the larger mass systems. A consistent view has now emerged in which a real dispersion among the values of the inner slopes for individual cluster halos is expected, where typical values for the inner slopes lie in the range $\sim 1.1 \pm 0.4$ (Moore et al. 1999; Navarro et al. 2004; Diemand et al. 2004, 2005).

An advantage of the NFW profile is that the total DM mass within r, $M_{NFW}(< r)$ (which is the 70-80% of the total cluster mass, DM+gas+galaxies) is given by a simple analytical formula:

$$M_{NFW}(< r) = 4\pi\rho_c\delta_c r_s^3\Big[ln(1 + r/r_s) + (1/(1 + r/r_s)) - 1\Big], \qquad (1.22)$$

So far we have presented two techniques to determine the total cluster mass: the first based on the X-ray measurements of intracluster gas (Eq.1.9) and its combination with the β-model (Eq.1.17), and the second based on the optical measurements of distribution and velocity dispersion of cluster galaxies (Eq.1.19). A third independent method is based on strong and weak gravitational lensing, *i.e.,* on the images of distant galaxies behind clusters which result distorted by the cluster gravity. In principle, strong gravitational lensing furnishes a simple yet efficient way to measure the projected cluster mass along the line of sight. A simple spherical lensing model provides a good estimate of the projected cluster mass within the position (r_{arc}) of the arc-like image, as (*e.g.,* Bartelmann 2003):

$$M_{lens}(< r_{arc}) \approx \pi r_{arc}^2 \Sigma_{crit} \qquad (1.23)$$

where $\Sigma_{crit} = (c^2/4\pi G)(D_s/D_d D_{ds})$ is the critical surface mass density and $D_{d,ds,s}$ are three characteristic distances of the lens system: from the observer to the lens, from the lens to the source and from the observer to the source, respectively. Observations of week lensing by galaxy clusters aim at reconstructing the cluster mass distribution from the appearance of arclet, *i.e.* weakly distorted images of faint background galaxies. This thechnique uses ellipticities of sources but since the sources are not intrinsically circular week-lensing needs several source images to be averaged under the assumption of random orientation of these sources. In principle, the week lensing techniques allow the surface density distribution of clusters to be mapped with angular resolution determined by the number density of background galaxies (see Bartelmann 2003, for a review).

While the traditional cluster mass estimators using optical/X-ray observations of galaxies/gas in clusters rely strongly upon the assumption of hydrostatic equilibrium, the strong and week gravitational lensing methods are not based on any assumption about the dynamical equilibrium of the cluster. It turns out that there is a good agreement between the gravitational lensing, X-ray and optically determined cluster masses on scales larger than the X-ray core radii, within which the X-ray method is likely to underestimate cluster masses by a factor of 2-4 (*e.g.,* Wu 1994; Allen 1998; Wu et al. 1998). A number of resons have been proposed to explain

this mass discrepancy, but a satisfactory explanation has not yet been achieved. Oversimplification of strong lensing models for the central mass distribution of clusters or the non general validity of the hydrostatic equilibrium hypothesis in the central region of clusters are among the generally quoted arguments (*e.g.,* Hicks 2002; Wu 2000).

1.4 Hierarchical Formation of Galaxy Clusters

Galaxy clusters occupy a special position in the hierarchy of cosmic structures being the largest bound structure in the Universe. In the framework of the hierarchical model for the formation of cosmic structures, galaxy clusters are supposed to form by accretion of smaller units (galaxies, groups, etc). In the paradigm of structure formation the universe is composed mainly by non-baryonic DM (the baryons are only $\Omega_b \sim 0.023 - 0.032h^{-2}$). Cosmic structures form by gravitational instability driven by the gravity of the DM component and thus the first non-linear system to form, by gravitational collapse, are dark matter halos. Galaxies and other luminous objects are assumed to form by cooling and condensation of baryons within the gravitational potential well created by the DM halos (White & Rees 1978).

Recent observations, based on the relative orientation of substructures within clusters (West et al. 1995) and on the relation between their dynamical status and the large scale environment (Plionis & Basilakos 2002), do support the hierarchical scenario. In the last decades, due to the increased spatial resolution in X-ray imaging (ROSAT/PSPC & HRI) and to the availability of wide-field cameras, many of the previous thought "regular" clusters have shown to be clumpy to some level and this is even more so in the *Chandra* and *XMM* era. The physical properties of galaxy clusters, such as the fraction of dynamically young clusters, the luminosity and temperature functions, the radial structure of both dark and baryonic components, constitute a challenging test for our current understanding of how these objects grow from primordial density fluctuations.

There are different ways to model the cosmic structure formation: analytic, semi-analytic and numerical techniques. The analytic techniques, first developed in the '70 years, pose the basis of the present models of the galaxy formation (White & Rees 1978; Fall & Efstathiou 1980). The numerical techniques, from pure N-body simulations (Davis et al. 1985) to the more recent N-body plus hydrodynamic

simulations (Steinmetz & Muller 1995; Katz et al. 1996), allow a detailed study of the relevant physical process, but also these techniques are subject to different approximations or ad hoc assumptions. The semi-analytic techniques consider the overall processes leading to the galaxies and galaxy clusters formations, but these processes are simplified in order to have a general parametric model, justified by analytic models and calibrated on results of numerical simulations. These models (Cole 1991; White & Frenk 1991; Kauffmann et al. 1993; Cole et al. 1994) are based on the model of the gravitational clustering by Press & Schechter (1974, hereafter PS74) and its extensions (Bower 1991; Bond et al. 1991; Lacey & Cole 1993, ; hereafter LC93). This formalism is extensively used to build up, via Montecarlo techniques, synthetic populations of dark matter halos which evolve in time due to mergers and hierarchical clustering. These techniques have been also extensively developed in order to study the evolution and formation of galaxies (*e.g.,* Kauffmann et al. 1993, 1999; Menci et al. 2004).

In the following we will discuss in some detail the Extended Press & Schechter (EPS) theory (LC93) for structure formations and some of its basis as the spherical collapse model. Finally we will briefly discuss the main numerical techniques. We will focus on the case of galaxy clusters which will be of interest in this Thesis.

1.4.1 Linear theory for structure formation

Observations of the Cosmic Microwave Background (CMB) radiation (*e.g.,* Bennett et al. 1996) show that the universe at recombination was extremely uniform, but with spatial fluctuations in the energy density and gravitational potential of roughly one part in 10^5. Such small fluctuations, generated in the early universe, grow over time due to gravitational instability, and eventually lead to the formation of galaxies and the large scale structure observed in the present universe. The gravitational instability is based on the following demonstration: starting from an homogeneous and isotropic "mean" fluid, small fluctuations in the density, $\delta\rho$, and in the velocity , δv, can grow with time if the self-gravitating force overcome the pressure force. This occurs if the typical lenghtscale of the fluctuation is greater than the Jeans length scale, λ_J, for the fluid.

There are two different regimes of growth of the perturbations: linear and non-linear. The two regimes can be distinguished defining the density fluctuation, or the

overdensity:

$$\delta = \frac{\rho - \overline{\rho}}{\overline{\rho}} = \frac{\delta\rho}{\overline{\rho}} \tag{1.24}$$

where ρ is the density of the universe at a given position (for simplicity of notation we neglect the coordinate dependence) and $\overline{\rho}$ is the mean unperturbed density of the universe. The linear regime acts as long as $\delta << 1$. The fluid is described by the continuity, the Euler, the Poisson and the entropy conservation equations (*e.g.,* Peebles 1993; Coles & Lucchin 1995):

$$\frac{\partial\rho}{\partial t} + \overrightarrow{\nabla} \cdot (\rho\overrightarrow{v}) = 0 \tag{1.25}$$

$$\frac{\partial\overrightarrow{v}}{\partial t} + (\overrightarrow{v} \cdot \overrightarrow{\nabla})\overrightarrow{v} + \frac{1}{\rho}\overrightarrow{\nabla}p + \overrightarrow{\nabla}\phi = 0 \tag{1.26}$$

$$\nabla^2\phi - 4\pi G\rho = 0 \tag{1.27}$$

$$\frac{\partial s}{\partial t} + \overrightarrow{v} \cdot \overrightarrow{\nabla}s = 0 \tag{1.28}$$

These equations, expanded in coomoving coordinates for the perturbed quantities ($\rho + \delta\rho$, $v + \delta v$, and so on) and linearized to search for solutions in the form of plane waves, give:

$$\ddot{\delta} + 2\frac{\dot{a}}{a}\dot{\delta} + \left[c_s^2\frac{k^2}{a^2} - 4\pi G\overline{\rho}\right]\delta = 0 \tag{1.29}$$

where k is the wave number, $c_s = (\partial p/\partial\rho)^{1/2}$ is the sound speed and a is the scale factor of the Universe. The solution for δ depends on the quantity in bracket which represent the combined contribution of pressure and gravity. The Jeans length scale can be defined as:

$$\lambda_J \equiv c_s\sqrt{\frac{\pi}{G\overline{\rho}}} \tag{1.30}$$

Perturbations with $\lambda >> \lambda_J$ (or $(c_s k/a)^2 << 4\pi G\overline{\rho}$) are unstable and their growth will depend on the geometry of the universe:

$$\ddot{\delta} + 2\frac{\dot{a}}{a}\dot{\delta} - 4\pi G\overline{\rho}\delta = 0 \tag{1.31}$$

which yields a growing and the decaying mode. For a Einstein-de Sitter universe one has:

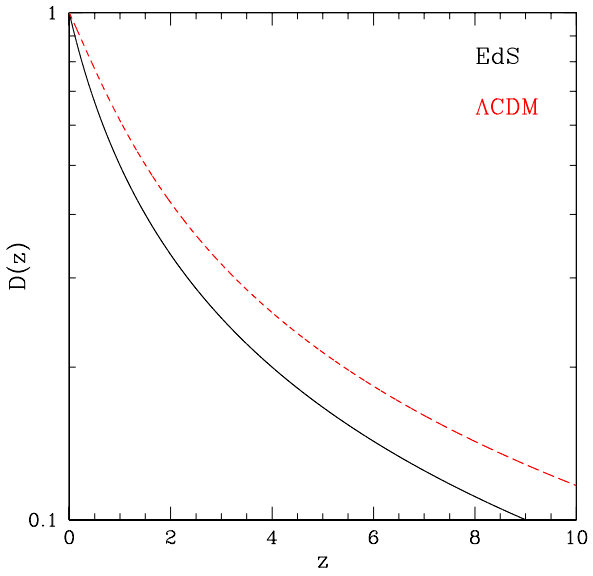

Figure 1.1: The redshift dependence of the linear growth factor of perturbation for an EdS model,$\Omega_m = 1$ (black solid curve) and for a flat model, $\Omega_m = 0.3$, with cosmological constant (red dashed curve).

$$\overline{\rho} = \frac{1}{6\pi G t^2} \tag{1.32}$$

$$a = a_0 (\frac{t}{t_0})^{2/3} \tag{1.33}$$

$$\frac{\dot{a}}{a} = \frac{2}{3t} \tag{1.34}$$

and Eq.1.31 has two trial solutions: $\delta_+ \propto t^{2/3} \propto a$ and $\delta_- \propto t^{-1} \propto a^{-2/3}$ for the growing and decaying mode, respectively.

It is helpful to introduce the linear growth factor $D(z)$ which gives the growth of fluctuations (normalized to the present epoch) as a function of redshift z. In the case of a EdS universe $D(z) = 1/(1+z) = (t/t_0)^{2/3} \propto a$. In a model with $\Omega_m \neq 1$ and with a cosmological constant $\Omega_\Lambda \neq 0$ (a ΛCDM model) a remarkable approximation formula for $D(z)$ is given by (*e.g.,* Carroll et al. 1992) :

$$D(z) = \frac{1}{(1+z)} \frac{g(z)}{g(z=0)} \tag{1.35}$$

where $g(z)$ is given by:

$$g(z) = \frac{5}{2}\Omega_m(z)\Big[\Omega_m(z)^{4/7} - \Omega_\lambda(z) + (1 + \frac{\Omega_m(z)}{2})(1 + \frac{\Omega_\Lambda(z)}{70})\Big]^{-1} \tag{1.36}$$

In Fig.1.1 we report $D(z)$ for an EdS model and for a ΛCDM model ($\Omega_m = 0.3$ and $\Omega_\Lambda = 0.7$). It is evident that the EdS has the faster evolution (*i.e.,* $D(z)$ is steeper), while in a ΛCDM model the evolution is less rapid due to the fact that at some point the cosmic expansion takes place at a quicker rate than the gravitational instability, and this freezes the perturbation growth.

The density fluctuations in a given region obeys these simple relations until the perturbation δ becomes of order of unity, at which point non-linear effects become important, and the linear theory cannot be applied.

1.4.2 Spherical collapse model

In the strongly non-linear regime, $\delta >> 1$ (a cluster of galaxies, for example, corresponds to δ of order of several hundred), it is necessary to develop techniques for studying the non-linear evolution of perturbations.

The spherical collapse model follows the evolution of a spherically symmetric perturbation with constant density. At the initial time, $t_i \simeq t_{rec}$ (t_{rec} being the recombination time), the perturbation has an amplitude $0 < |\delta_i| << 1$ and is taken to be expanding with the background universe in such a way that the initial peculiar velocity, V_i, is zero. At the beginning of its evolution the perturbation can still be described by the quasi-linear theory which in the case of an EdS Universe gives:

$$\delta = \delta_+(t_i)(\frac{t}{t_i})^{2/3} + \delta_-(t_i)(\frac{t}{t_i})^{-1} \tag{1.37}$$

$$V = \frac{i}{k_i t_i}\Big[\frac{2}{3}\delta_+(t_i)(\frac{t}{t_i})^{1/3} - \delta_-(t_i)(\frac{t}{t_i})^{-4/3}\Big] \tag{1.38}$$

where i is the imaginary unit. The condition $V_i = 0$ implies $\delta_+(t_i) = 3\delta_i/5$. After a short time, the decaying mode δ_- will become negligible and the perturbation will grow. The spherical symmetry of the perturbation implies that it can be treated as a separate universe and, if pressure gradients are negligible, the perturbation evolves like a Friedmann model whose initial density parameter is given by:

$$\Omega_p(t_i) = \frac{\rho(t_i)(1+\delta_i)}{\rho_c(t_i)} = \Omega(t_i)(1+\delta_i) \tag{1.39}$$

where the suffix p denotes quantities relative to the perturbation, while $\rho(t_i)$ and $\Omega(t_i)$ refer to the unperturbed underground universe ($\Omega(t_i) = 1$ in a EdS model). Structures will be formed if, at some time t_m, the spherical region ceases to expand with the background universe and begins to collapse and this will happen to any perturbation with $\Omega_p(t_i) > 1$. This implies the condition for the initial collapse:

$$\delta_+(t_i) > \frac{3}{5}\frac{1-\Omega}{\Omega(1+z_i)} \tag{1.40}$$

where Ω is the present value of the density parameter. Obviously, in a EdS ($\Omega = 1$) universe any $\delta_i > 0$ will collapse, while in the case $\Omega < 1$, the initial perturbation must exceed some critical value.

The evolution of the perturbation with $\Omega_p > 1$ is described by a Friedmann model with $\Omega_p > 1$:

$$(\frac{\dot{a}}{a})^2 = H_i^2\Big[\Omega_p(t_i)\frac{a_i}{a} + 1 - \Omega_p(t_i)\Big] \tag{1.41}$$

where H_i is the initial value of the Hubble expansion parameter. At time t_m the perturbation will reach the maximum expansion (*e.g.,* Coles & Lucchin 1995):

$$t_m = \frac{\pi}{2H_i}\frac{\Omega_p(t_i)}{(\Omega_p(t_i)-1)^{3/2}} \tag{1.42}$$

$$a_m \equiv a(t_m) = a_i\frac{\Omega_p(t_i)}{\Omega_p(t_i)-1} \tag{1.43}$$

which correspond to a minimal density ($\rho \propto a^{-3}$):

$$\rho_p(t_m) = \rho_p(t_i)\Big(\frac{\Omega_p(t_i)-1}{\Omega_p(t_i)}\Big)^3 = \rho_c(t_i)\Omega_p(t_i)\Big(\frac{\Omega_p(t_i)-1}{\Omega_p(t_i)}\Big)^3 \tag{1.44}$$

and, using Eq.1.44 and taking $\rho_c(t_i) = 3H_i/8\pi G$, one also finds:

$$t_m = \frac{\pi}{2H_i}\Big[\frac{\rho_c(t_i)}{\rho_p(t_m)}\Big]^{1/2} = \Big[\frac{3\pi}{32G\rho_p(t_m)}\Big]^{1/2} \tag{1.45}$$

In a EdS universe the matter density evolves with time according to Eq.1.32 and (from Eq.1.45 and Eq.1.32) it is:

$$\frac{\rho_p(t_m)}{\rho(t_m)} = \chi = (\frac{3\pi}{4})^2 \simeq 5.6 \tag{1.46}$$

which correspond to a perturbation $\delta_+(t_m) = \chi - 1 \simeq 4.6$. We notice that the extrapolation of the linear growth law would have yielded:

$$\delta_+(t_m) = \delta_+(t_i)(\frac{t_m}{t_i})^{2/3} \simeq \frac{3}{5}(\frac{3\pi}{4})^{2/3} \simeq 1.07 \tag{1.47}$$

corresponding to $\rho_p(t_m)/\rho(t_m) \simeq 1 + \delta_+(t_m) \simeq 2.07$.

The perturbation at $t > t_m$ will subsequently collapse and formally reach an infinite density at the center in a time $t_c \simeq 2t_m$. However, when the density becomes high, slight departure from this symmetry will results in formation of shocks and pressure gradients which convert some of the kinetic energy of the collapse into heat yielding a final virial-equilibrium state at $t_v \approx t_c$ with radius R_v and mass M. From the virial theorem the total energy of the fluctuation is:

$$E_v = \frac{U}{2} = -\frac{1}{2}\frac{3GM^2}{5R_v} \tag{1.48}$$

and, if the system is closed (mass and energy conservation), at time t_m, when the perturbation is at its maximum size, R_m, the energy is given by:

$$E_m = U = -\frac{3}{5}\frac{GM^2}{R_m} \tag{1.49}$$

and from Eq.1.48 and Eq.1.49 one has the simple relation between the virial and maximum radius of the perturbation, $R_m = 2R_v$, which allows to compute the overdensity at the collapse-virial time, t_v:

$$\frac{\rho_p(t_v)}{\rho(t_v)} = (\frac{R_m}{R_v})^3(\frac{t_v}{t_m})^2\chi = 8 \cdot 2^2 \cdot (\frac{3\pi}{4})^2 = 18\pi^2 \simeq 178 \tag{1.50}$$

Thus DM halos with an overdensity of ~ 200 are usually considered to have reached the condition of virial equilibrium. We notice that an extrapolation of linear perturbation theory would have given:

$$\delta_+(t_v) = \delta_+(t_m)(\frac{t_v}{t_m})^{2/3} = \frac{3(12\pi)^{2/3}}{20} \simeq 1.69 \tag{1.51}$$

which is an important number that will be used in next Section in order to characterize the mass function of virialized halos. While the above derivation holds

for an EdS Universe, for $\Omega_m < 1$ the increased expansion rate of the universe causes a faster dilution of the cosmic density from t_m to t_v and, as a consequence, a larger value of the overdensity is obtained at the virialization epoch. In the following we will indicate with Δ_v the overdensity at virial equilibrium, computed with respect to the background density. According to this definition the masses and radii of a virialized clusters are related as:

$$R_v = \left[\frac{3M_v}{4\pi\Delta_v(z)\overline{\rho}_m(z)}\right]^{1/3} \tag{1.52}$$

where $\overline{\rho}_m(z) = 2.78 \times 10^{11}\,\Omega_m\,(1+z)^3\,h^2\,M_\odot Mpc^{-3}$ is the mean mass density of the universe at redshift z. The quantity $\Delta_v(z)$ depends on the cosmological model. For an EdS model $\Delta_v(z) = 18\pi^2 \simeq 178$ (Eq.1.50), while in the ΛCDM cosmology $\Delta_v(z)$ depends on z and is given by Kitayama & Suto (1996):

$$\Delta_v(z) = 18\pi^2(1 + 0.4093\omega(z)^{0.9052}), \tag{1.53}$$

where $\omega(z) \equiv \Omega_f(z)^{-1} - 1$ and:

$$\Omega_f(z) = \frac{\Omega_{m,0}(1+z)^3}{\Omega_{m,0}(1+z)^3 + \Omega_\Lambda}, \tag{1.54}$$

in this case the value of Δ_v at redshift zero is ~ 330.

1.4.3 Excursion set and the mass function of collapsed halos

What we have discussed so far is useful only to estimate the scale of the formation of non-linear structures and the properties of the objects which undergo a spherical collapse. To follow the hierarchical evolution of a population of dark matter halos it is necessary to adopt a theory and, with semi-analytic techniques, this is only possible by making use of the quasi linear theory. Here we will present the EPS theory (*e.g.,* Bond et al. 1991; Lacey & Cole 1993) which will be extensively used in this PhD thesis.

At the begininning of this evolution, when the amplitude of the density perturbations is small, $\delta << 1$, these perturbations grow according to the linear theory (see Sec.1.4.1) and $\delta(\mathbf{x}, t) = \delta(\mathbf{x}, t_0) \cdot D(t)/D(t_0)$ ($\mathbf{x}$ being the comoving coordinate). As discussed in the previous sections, the evolution of δ can be

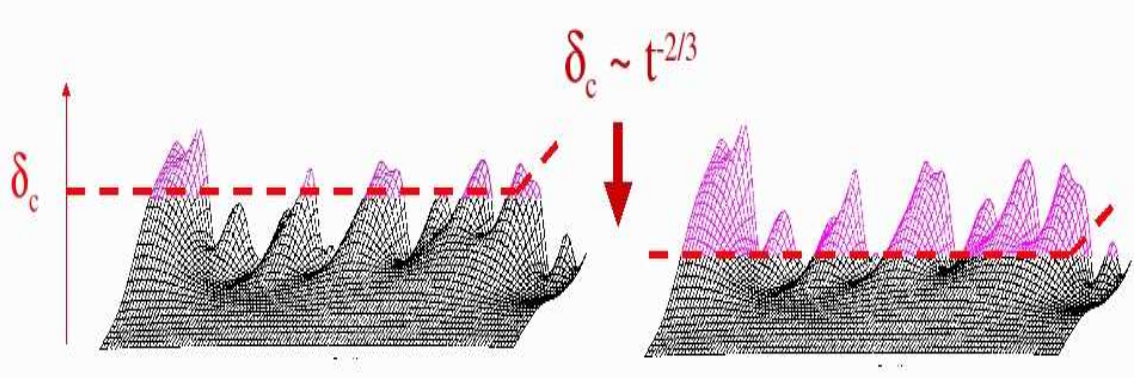

Figure 1.2: Realization of one-dimensional Gaussian random density field filtered on a scale k_s; in abscissa there is the position x; in depth the filtering radius (small k ahead); in ordinate the amplitude of the field $\delta_(x, R)$ (Bond et al. 1991).

described by the linear theory until $\delta(\mathbf{x}, t)$ approach unity, at which point non-linear effects become important and the region ceases to expand, turns around, and collapses to form a virialized halo. At this point the density contrast estimated by the linear theory will have reached a critical value δ_c, estimated from the evolution of an isolated spherical overdense region (see Sec.1.4.2, Eq.1.51; here we will use the suffix c instead of v for 'critical'), while mass and virial radius of the collapsed halos can be estimated by Eq.1.52 with Δ_c given by Eq.1.50 and Eq.1.53 in a EdS a ΛCDM cosmology respectively.

A useful way of viewing this evolution is to simply consider the linear density field $\delta(\mathbf{x}) \equiv \delta(\mathbf{x}, t_o)$ at t_o, the present time, and a critical threshold $\delta_c(t) = \delta_c \cdot \frac{D(t_o)}{D(t)}$ that is progressively lowered with increasing cosmic time allowing to collapse first the perturbations on small scales and then the perturbations on scales larger and larger (see Fig.1.2). More accurately in a EdS universe one can identify the regions which will have collapsed to form virialized halos at time t as those region in the linear density field for which δ is larger than:

$$\delta_c(t) = \delta_c \cdot \frac{D(t_0)}{D(t)} = \frac{3(12\pi)^{2/3}}{20}(\frac{t_0}{t})^{2/3} \tag{1.55}$$

while in the case of a ΛCDM universe it is (Kitayama & Suto 1996):

$$\delta_c(t) = \delta_c \cdot \frac{D(t_0)}{D(t)} = \frac{D(t_0)}{D(t)}\Big(1 + 0.0123 log\Omega_m(z)\Big) \tag{1.56}$$

where $\Omega_m(z)$ is given by:

$$\Omega_m(z) = \frac{\Omega_m(0)(1+z)^3}{\Omega_m(0)(1+z)^3 + \Omega_\Lambda(0)} \tag{1.57}$$

and the linear growth factor in Eq.(1.56) is given by Eqs.1.35 and Eq.1.36.
In order to follow the collapse of the evolving perturbations in terms of halo masses it is necessary to introduce a smoothing scale and a mass of a halo: the infinitesimal mass element in $\mathbf{x}$ will be part of a halo of mass $\geq M$ at time t if the linear density field $\delta(\mathbf{x}; R)$, centred in $\mathbf{x}$ and smoothed (averaged) on a sphere of radius $R \propto M^{1/3}$, exceeds the threshold for collapse at time t, $\delta_c(t)$. Thus, in order to obtain the mass of the collapsed halos at time t one considers the largest M for which $\delta(M) \geq \delta_c(t)$. This idea was first proposed by PS74, and subsequently developed by Bond et al. (1991) and LC93 for a semi-analytic description of the merging and appears to be in good agreement with the hierarchical mergers synthesized in cosmological N-body simulations.

The density field smoothed on a scale R, $\delta(\mathbf{x}, R)$, is the convolution of the density field in $\mathbf{x}$, $\delta(\mathbf{x})$, with a window function $W_M(r)$ of typical extent R. It is costumary to consider the Fourier decomposition of the linear density field:

$$\delta(\mathbf{x}) = \sum_{\mathbf{k}} \delta_{\mathbf{k}} \exp(i\mathbf{k} \cdot \mathbf{x}) \tag{1.58}$$

Applying the convolution to the Fourier series, the smoothed field can be expressed as:

$$\delta(\mathbf{x}, R) = \int W_M(|\mathbf{x} - \mathbf{y}|)\delta(\mathbf{y}) d^3\mathbf{y} = \sum_{\mathbf{k}} \delta_{\mathbf{k}} \widehat{W}_M(\mathbf{k}) \exp(i\mathbf{k} \cdot \mathbf{x}) \tag{1.59}$$

where $\widehat{W}_M(\mathbf{k})$ is the Fourier transform of the spatial window function $W_M(r)$. At a fixed $\mathbf{x}$ Eq.1.59 gives $\delta(M)$. The simplest form of $W_M(r)$ is the top-hat filtering which is constant inside a sphere and zero outside; correspondingly, $\widehat{W}_M(\mathbf{k})$ is a step function in k-space:

$$\widehat{W}_M(\mathbf{k}) = \begin{cases} 1 \ \text{ for } k << k_s \\ \\ 0 \ \text{ for } k >> k_s \end{cases} \tag{1.60}$$

where $k_s \propto 1/R$ is the wave number corresponding to the filtering radius R; thus the perturbations that contribute to $\delta(R)$ will only be those with $\lambda \sim k^{-1} > R$, the others will delete each other. The problem of reconstructing the mass function of

the evolving perturbations is complex since it depends on $\mathbf{x}$ and on the spectrum of the perturbations $P(\mathbf{k}) = |\delta_k|^2$. It is necessary to define a new variable, the mass variance of the linear density field smoothed with the window function of size R, $S(M)$:

$$S(M) = \sigma^2(M) = \langle|\delta(M, \mathbf{x})|^2\rangle = \Sigma_k \langle|\delta_\mathbf{k}|^2\rangle \widehat{W}_M^2(\mathbf{k}) \tag{1.61}$$

In the cases of interest S is a monotonically decreasing function of M and, if the smoothing mass scale is sufficiently large, S (and thus $\delta(S, \mathbf{x})$) will tend to zero. It can be noted that the mass variance does not depend on the coordinates and thus it does not give us information about the spatial distribution of the perturbations, but given that the perturbations evolve with time, the mass variance depends on time and gives us information on the amplitude of the dishomogeneities.

In standard models, the inflation produces a primordial power-law spectrum $P(k) \propto \langle|\delta_\mathbf{k}|^2\rangle \propto k^n$, the variance as a function of mass is simply $\sigma^2(M) \equiv \langle|\delta_\mathbf{k}|^2\rangle \sim \int P(k)k^2dk \sim k^{n+3} \sim M^{-\frac{n+3}{3}}$ (*e.g.,* Coles & Lucchin 1995). In this case the mass variance assumes large values on small scales, and thus the first structures to form are those on small scale, then these structures merge to form halos of larger mass (see also Fig.1.2); this is what happen in a hierarchical model of structures formation.

For a given realization of the density field, *i.e.* a given set of $\delta_\mathbf{k}$, $S(M)$ and $\delta(\mathbf{x}, M)$ at different locations $\mathbf{x}$ are determined. It is customary to fix the location $\mathbf{x}$ and to obtain different realizations of $\delta_\mathbf{k}$ so that $S(M)$ and $\delta(\mathbf{x}, M)$ can be considered as random. For a given realization of $\delta_\mathbf{k}$, $\delta(S) = 0$ at $S = 0$, corresponding to a null fluctuation at an infinite radius, and then $\delta(S)$ stochastically changes as S increases. It can be shown that, in the case in which $W_M(r)$ is a step function in the Fourier space (Eq.1.60), the variations $\delta(M)$-$S(M)$ can be considered as a Brownian random walk in the bidimensional space $(S, \delta(S))$ where S is the "time" equivalent variable and $\delta(S)$ is the "space". This "motion" can be described by a simple diffusion equation (*e.g.,* Lacey & Cole 1993):

$$\frac{\partial Q}{\partial S} = \frac{1}{2}\frac{\partial^2 Q}{\partial \delta^2} \tag{1.62}$$

where $Q(\delta, S)$ is the probability distribution of "trajectories" at S in the interval δ to $\delta + d\delta$. In the case of a Brownian motion, the solution is a simple Gaussian probability distribution:

$$Q(\delta, S) = \frac{1}{\sqrt{2\pi S}} \exp -(\frac{\delta^2}{2S}) \tag{1.63}$$

The use of the Brownian walks in the space (S, δ) is a fundamental point as this allows to formulate the model of the *excursion sets*, first proposed by Bond et al. (1991). The basic idea of this model is the following: the "trajectories" that, starting from the origin ($S = 0$), touch for the first time at S the ordinate $\delta = \delta_c(t)$ are fluid elements which at the time t belong to halos of mass $M(S)$. In other words: each time t determinates a threshold, or barrier, $\delta_c(t)$ which will be crossed for the first time in a point corresponding to an abscissa S. Thus, at the time t the mass element associated to this "trajectory" will become part of a halo of mass $M(S)$.

It is important to note that the request that the "trajectory" touches the threshold $\delta_c(t)$ for the first time corresponds to selecting the minimum value of S and thus the maximum filtering radius $R = R_{max}$ for which the sphere of radius R at time t has an overdensity $\delta(M) \geq \delta_c(t)$. To compute the mass function of the virialized structures at the time t it is necessary to consider the fraction of "trajectories" that are above the threshold $\delta_c(t)$ at some mass scale M but are below this threshold for all largeer values of M. The solution of Eq.1.62 is (Chandrasekhar, 1943):

$$Q(\delta, S, \delta_c(t)) = \frac{1}{\sqrt{2\pi S}} \Big[\exp\Big(-\frac{\delta^2}{2S} \Big) - \exp\Big(-\frac{(\delta - 2\delta_c(t))^2}{2S} \Big) \Big] \tag{1.64}$$

and this gives the fraction of the "trajectories" that are above the threshold $\delta_c(t)$ at some mass M but are below this threshold for all large values of M (or small values of S).

The probability that at time t a fluid element belongs to a halo of mass around M is the probability that a particular "trajectory" will be absorbed by the barrier at time t around S and this is equal to the reduction in the number of "trajectories" surviving below the barrier (LC93):

$$f_S(S, \delta_c(t)) = -\frac{\partial}{\partial S} \int_{-\infty}^{\delta_c(t)} Q d\delta = -\Big[\frac{1}{2} \frac{\partial Q}{\partial \delta} \Big]_{-\infty}^{\delta_c(t)} = \frac{\delta_c(t)}{\sqrt{2\pi S^3}} \exp\big[-\frac{\delta_c(t)^2}{2S} \big] \tag{1.65}$$

where the second equality follow from Eq.1.62 and the third equality is obtained from Eq.1.64. The comoving number density of halos of mass M at time t is obtained from Eq. 1.65 in the form:

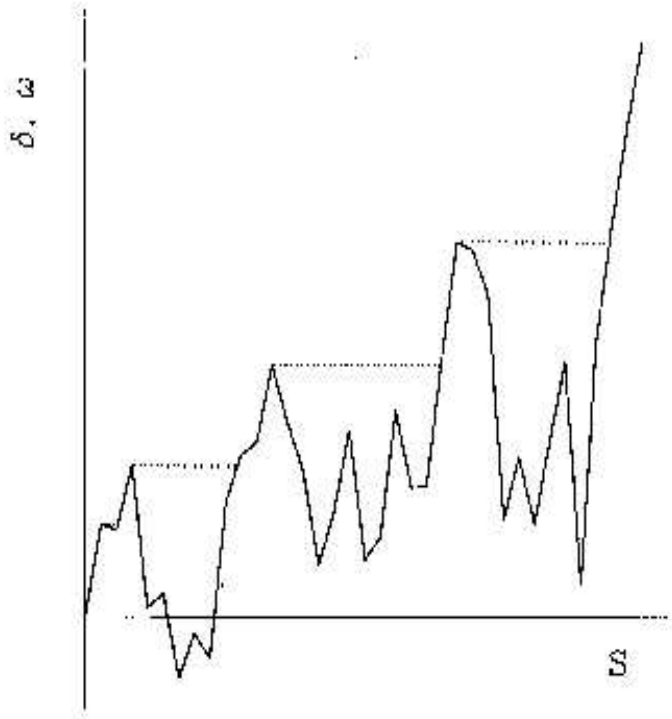

Figure 1.3: A "trajectory" $\delta(S)$ and the corresponding halo merger history. The solid line shows the "trajectory" for the overdensity δ as the smoothing scale is varied. The dotted line shows the "trajectory" for the halo mass, represented by a function $S(\omega)$ with $\omega = \delta_c(t)$. Where δ is increasing with S, the dotted line coincides with the solid line (by Lacey & Cole 1993).

$$\frac{dn}{dM}(M,t)dM = \frac{\overline{\rho}(t)}{M} f_S(S,\delta_c(t)) \left|\frac{dS}{dM}\right| dM = \\ = \left(\frac{2}{\pi}\right)^{1/2} \frac{\overline{\rho}(t)}{M^2} \frac{\delta_c(t)}{\sigma(M)} \left|\frac{d\ln\sigma}{d\ln M}\right| \exp\Big[-\frac{\delta_c(t)^2}{2\sigma^2(M)}\Big] dM \qquad (1.66)$$

where $\overline{\rho}(t)$ is the mean mass density of the universe at the time t. This expression for the mass function was originally proposed by PS74.

1.4.4 Extended Press-Schechter model and merger trees

The *excursion set* theory is also useful to describe the properties of the merging history of dark halos. These results are often referred to as *Extended Press-Schechter model* developed by LC93. Each "trajectory" $\delta(S)$ describes the merging history for a given particle: the hierarchical merging process, in the normal temporal sequence of increasing mass M as t increases, corresponds to the process of starting from large value of S and $\delta_c(t)$ and following the track down and to the left in Fig.1.3. The solid line in Fig.1.3 gives an example of "trajectory" $\delta(S)$, while the dotted line shows the merging history $S(\delta_c(t))$ for that "trajectory": at a given time (and thus $\delta_c(t)$) the fluid element associated to the "trajectory" is part of a halo with a mass M which corresponds to the smaller value of S in which the "trajectory" crosses the threshold $\delta_c(t)$.

With increasing time, from early epoch to the present time, $\delta_c(t)$ decreases and the minimum value of S at which the "trajectory" crosses the barrier gradually diminishes giving the mass grow process of halos ("accretion"). However when a new peak of the "trajectory" crosses the barrier at smaller values of S, the evolution of S makes horizontal jumps (as represented in Fig.1.3) and these correspond to sudden jumps in the mass of the halos ("merger" events).

The conditional probability that a "parent" cluster of mass M_1 at a time t_1 had a progenitor of mass in the range $M_2 \rightarrow M_2 + dM_2$ at some earlier time t_2, with $M_1 > M_2$ and $t_1 > t_2$ can be obtained from Eq.1.65 but with the starting point of "trajectories" not in the origin ($S = 0$, $\delta(S) = 0$) but in the point (S_1, $\delta_c(t_1)$). This is given by (e.g., LC93, Randall, Sarazin & Ricker 2002):

$$\mathcal{P}(M_2,t_2|M_1,t_1)dM_1 = \frac{1}{\sqrt{2\pi}} \frac{M_1}{M_2} \frac{\delta_{c2}-\delta_{c1}}{(\sigma_2^2-\sigma_1^2)^{3/2}} \left|\frac{d\sigma_2^2}{dM_2}\right| \times$$

$$\exp\left[-\frac{(\delta_{c2}-\delta_{c1})^2}{2(\sigma_2^2-\sigma_1^2)}\right] dM_2\,, \tag{1.67}$$

$\delta_{c1} \equiv \delta_c(t=t_1)$ and $\sigma_1 \equiv \sigma(M_1)$, with similar definitions for δ_{c2} and σ_2. $\delta_c(z)$ is given by Eq.1.55 and Eq.1.56 for an EdS and a ΛCDM model respectively; $\sigma(M) = S^{1/2}$ is the rms density fluctuation within a sphere of mean mass M.

Over the range of scales of interest for cluster studies it can be sufficient to consider a power-law spectrum of the density perturbation given by (Randall, Sarazin & Ricker 2002):

$$\sigma(M) = \sigma_8 \left(\frac{M}{M_8}\right)^{-\alpha}\,, \tag{1.68}$$

where σ_8 is the present epoch rms density fluctuation on a scale of 8 h^{-1} Mpc, $M_8 = (4\pi/3)(8\,h^{-1}\,\mathrm{Mpc})^3\bar{\rho}$ is the mass contained in a sphere of radius 8 h^{-1} Mpc ($\bar{\rho}$ is the present epoch mean density of the Universe), $\alpha = (n+3)/6$ (Bahcall & Fan 1998) and $\sigma_8 = 0.514$ for the EdS models (Randall, Sarazin & Ricker 2002).

It is convenient (LC93) to replace the mass M and time t (or redshift z) with the suitable variables $S \equiv \sigma^2(M)$ and $x \equiv \delta_c(t)$ (S decreases as the mass M increases, and x decreases with increase cosmic time t).

So that Eq.1.67 is written in the form:

$$K(\Delta S, \Delta x)d\Delta S = \frac{1}{\sqrt{2\pi}}\frac{\Delta x}{(\Delta S)^{3/2}}\exp\left[-\frac{(\Delta x)^2}{2\Delta S}\right] d\Delta S \tag{1.69}$$

where $\Delta S = \sigma_2^2 - \sigma_1^2$ and $\Delta x = \delta_{c2} - \delta_{c1}$. This expression will be used in Cap.5 to construct merger trees via Monte Carlo techniques.

1.4.5 Numerical simulations of cluster formation

While the initial, linear growth rate of density perturbations can be calculated analytically, and the Extended Press & Schechter theory can provide a reference frame to study the merging rate and history of clusters, the details of the collapse of fluctuations and the hierarchical build-up of structures requires an extensive use of numerical simulations. This simulations are indeed the main theoretical tool for studying this nonlinear phase and for testing theory of the early universe against observational data. The resulting matter distribution in the simulated universe has a complex topology, often described as a "cosmic web", which is clearly visible in Fig.1.4, a slice through the dark matter density field at redshift $z = 0$ taken from the

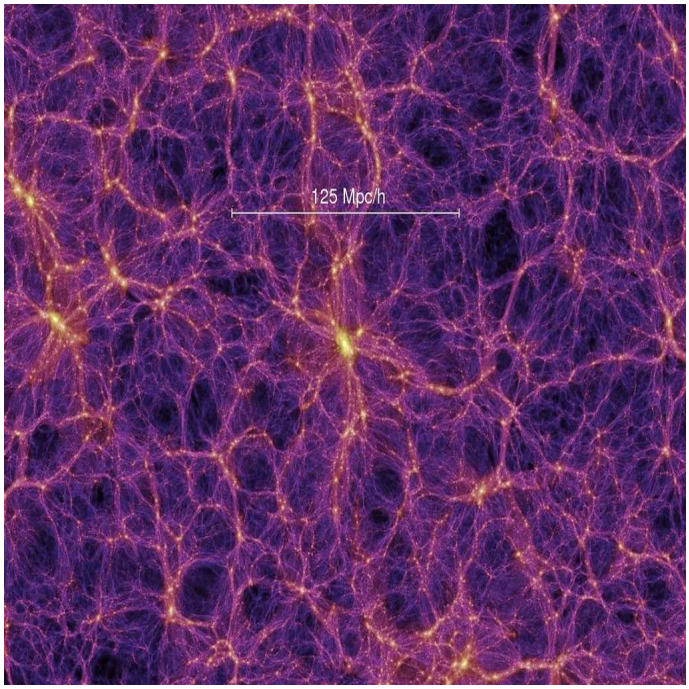

Figure 1.4: A slice of thickness $15\,h^{-1}$ Mpc through the dark matter density field of the *Millennium Simulation* at redshift $z = 0$ (Springel et al. 2005).

Millennium Simulation (by Springel et al. 2005). A tight network of cold dark matter clusters and filaments of characteristic size $\sim 100\,h^{-1}$ Mpc is visible, while on large scales there is little discernible structure and the distribution appears homogeneous and isotropic.

Dark matter in numerical simulations is assumed to be cold and made of elementary particles (N-body) that currently interact only gravitationally. This approach proved powerful enough to reject the idea that the dark matter consists of massive neutrinos and to establish the viability of the alternative hypothesis that the dark matter is made up of cold collisionless particles (see Ostriker & Steinhardt 2003, for a review). N-body simulations are now well understood and the validity of analytic approximations is often gauged by reference to simulation results.

Gasdynamical simulations are based on a particle representation of Lagrangian gas elements using the smoothed particle hydrodynamics (SPH) techniques (Lucy 1977; Gingold & Monaghan 1977; Evrard 1988), or are based on fixed-mesh Eulerian methods (Cen et al. 1990; Cen 1992), or on Eulerian methods with submeshing (Bryan & Norman 1995).

SPH algorithms use particles to approximate the behavior of the gas, treating

gas particles as moving interpolation centers for quantities such as the gas pressure. Typically SPH codes, tanks to their Lagrangian nature, allow a locally changing resolution that "automatically" follows the local mass density, in this way they achieved spatial resolution in high-density regions but handle shocks and low-density regions poorly. Examples of cosmological hydrodynamics codes based on SPH include those of Evrard (1988), Hernquist & Katz (1989), Navarro & White (1993), Couchman et al. (1995), Steinmetz (1996) and Springel et al. (2001) (Gadget-1), Springel (2005) (Gadget-2). Grid-based methods suffer from more limited resolution, but they handle high-density and low-density regions equally well, and they also handle shocks extremely well. Example of grid-based cosmological hydrodynamics codes are that of Cen (1992), the TVD code of Ryu et al. (1993), Bryan & Norman (1995), Gheller et al. (1998). Afterward, the code of Bryan & Norman (1995) has been extended to include adaptive mesh refinement (AMR) (ENZO, Norman & Bryan 1999).

A comparison of various cosmological particle- and grid-based codes have been performed, "The Santa Barbara cluster comparison project" in Frenk et al. (1999). The properties of the cluster dark matter were found to be gratifyingly similar in all the models, with a total mass and velocity dispersion agreement better than 5%, while less agreement was observed for the gas properties of the cluster with the largest discrepancies occurring in the predicted cluster X-ray luminosities of clusters (best agreement was within a factor of ~ 2).

The numerical cosmological simulations are important tools to study the observed scaling relations for galaxy clusters (the $L_x - T$, $M - T$, $M - L_x$, and so on), and the comparison between the simulated and observed clusters properties can allow to better constrain the physics to be included in simulations (*e.g.,* Borgani et al. 2004). Usually the predicted scaling relations reproduce observational data reasonably well for massive clusters, where the effects of additional physical processes are expected to play a minor role (*e.g.,* Rosati et al. 2002).

Another important point of interest in this PhD thesis is the comparison between the properties of statistical quantities as the halo mass functions expected in numerical simulations and from PS thequineques. It is found that the PS mass function (Eq.1.66), while qualitatively correct, shows some deviation from the exact numerical results, specifically the PS formula overestimates abundance of halos in

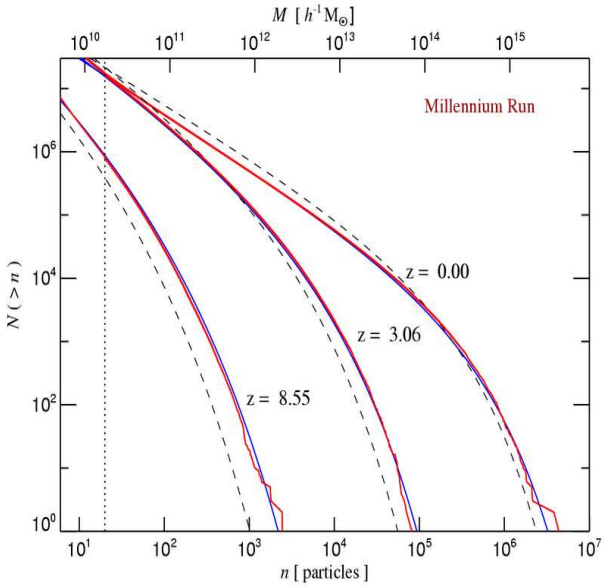

Figure 1.5: Non-linear halo mass function of the *Millennium Simulation* Millennium simulation at different times, (Springel et al. 2005). The number of dark matter halos above a given mass threshold, shown at three different times. The blue line is an analytic fitting function by Sheth & Tormen, while the dashed line is the Press & Schechter mass function. The vertical dotted line marks the halo resolution limit of the simulation.

the lower-mass tail and underestimates the number of clusters in the high-mass tail (*e.g.,* Efstathiou & Rees 1988; Lacey & Cole 1994; Eke et al. 1996). Such deviations are usually interpreted in terms of inaccuracy of the PS approach. Evolutions of the PS approach which incorporate the effect of a non-spherical collapse (Sheth & Tormen 1999, ;ST) provide a better agreement with N-body simulations. In Fig.1.5 we report a comparison from the *Millennium simulation* between different mass functions. It is important to note that the agreement between the PS mass function and the numerical mass function is satisfactory towards low redshifts and for masses typical of galaxy clusters $10^{14} - 10^{15}\, h^{-1} M_{\odot}$. This is the range of z and masses in which the present PhD work focuses on and thus we will use the PS massfuction in the next part of this work.

1.5 Physics of cluster mergers

Observations of cluster mergers

For many years clusters were thought to be dynamically relaxed systems evolving slowly after an initial, short-lived episode of violent relaxation. Many papers in the

1980's, exploited the imaging of the Einstein Observatory and showed the rich and complex structure of present epoch galaxy clusters (*e.g.,* Jones et al. 1979; Jones & Forman 1984; Mohr et al. 1993, 1995). Along with the X-ray observations, optical surveys delineated the large scale structure and elucidated the filamentary structure of the Universe (*e.g.,* de Lapparent et al. 1986). ROSAT and ASCA provided a detailed view of rich physics of cluster mergers (*e.g.,* Briel et al. 1991; Böhringer et al. 1994; Markevitch et al. 1999; Henriksen et al. 2000). These observations reveal that many clusters may grow from accretion of relatively small mass concentrations along filamentary structures (van Haarlem & van de Weygaert 1993) and other may undergo major mergers of two nearly equal components. Major cluster mergers are energetic events in which clusters collide at velocities of $\sim$ 2000 km/s, releasing binding gravitational energies of $\gtrsim 10^{64}$ ergs. During merger shocks are driven in the ICM and, in the case of major merger, they dissipate energies of $\sim 3 \cdot 10^{63}$ ergs which are mainly converted in the heating of the X-ray emitting gas.

Chandra's high angular resolution has provided further insight of the merging process and of the complexity of the ICM, revealing for the first time the unequivocal signature of a few shocks fronts (Markevitch 2006; Markevitch et al. 2005). Also "cold" fronts, sharp gas density discontinuities between a dense cold cloud, associated with a merging subcluster, and the hot cluster gas (*e.g.,* Vikhlinin et al. 2001) are evidences of mergers as they are interpreted as the low-entropy remnants of recently merged substructures (Markevitch et al. 2000).

Basic kinematics of cluster mergers

There are some simple analytical arguments which can be used to estimate the kinematics of an individual binary merger collision. The picture is that of two subclusters with mass M_{max} and M_{min} that merge at some time t_m and which have fallen together from a large distance d_0 with nonzero angular momentum. It can be assumed that the two subclusters are point masses initially expanding away from one another in the Hubble flow and that their radial velocity was zero at their largest separation d_0. The collapse can be treated as the orbit of two point masses, and their largest separation will be given by the Kepler's third Law as:

$$d_0 \simeq \left(2G(M_{max} + M_{min})\right)^{1/3} \left(\frac{t_m}{\pi}\right)^{2/3} \tag{1.70}$$

The exact value of d_0 does not significantly affect the collision velocity as long as d_0 is large and the infall velocity approaches free-fall from infinity. At the separation d_0 the orbital angular momentum and energy are:

$$\begin{aligned} J_{orbit} &\approx m\, v_0\, d_0 \\ E_{orbit} &\approx \frac{1}{2} m\, v_0^2 - \frac{G M_{max} M_{min}}{d_0} \end{aligned} \tag{1.71}$$

where $m = M_{max}M_{min}/(M_{max} + M_{min})$ is the reduced mass and v_0 is the initial relative transverse velocity. At a distance (between the centers) of the order of the virial radius of the most massive cluster, R_{max}, the relative impact velocity v_i and the impact parameter b are given by:

$$\begin{aligned} J_{orbit} &\approx m\, v_i\, b \\ E_{orbit} &\approx \frac{1}{2} m\, v_i^2 - \frac{G M_{max} M_{min}}{R_{max}} \end{aligned} \tag{1.72}$$

Conserving angular momentum and energy, and eliminating v_0 one finds (e.g., Sarazin 2002):

$$v_i \simeq (2G(M_{max} + M_{min}))^{1/2} \Big(\frac{1}{R_{max}} - \frac{1}{d_0} \Big)^{1/2} \Big[1 - (\frac{b}{d_0})^2 \Big]^{-1/2}. \tag{1.73}$$

and in the simplest case of central collision ($b = 0$):

$$v_i \simeq \left(2G \frac{(M_{max} + M_{min})}{R_{max}} \Big(1 - \frac{1}{\eta_v} \Big) \right)^{1/2} \tag{1.74}$$

where $\eta_v = d_0/R_{max} \simeq 4(\frac{M_{max}+M_{min}}{M_{max}})^{1/3}$ and the masses and virial radii of clusters can be taken from the spherical collapse model according to Eq.1.52; Eq.1.74 will be used to calculate the impact velocity between clusters in Chap.5.

Shocks

The virial theorem implies that the square of the thermal velocity (sound speed) of the ICM scales with the gravitational potential. During a merger, the infall velocity of the subclusters are thus comparable to the escape velocity which is a factor of $1.5 - 2$ the sound speed. This implies that the motions in cluster mergers are expected to be moderately supersonic.

Shocks are thus important imprints of cluster mergers and their study is of great importance. Semi-analytic calculations of merger related shocks in the hierarchical picture of structure formation showed that the bulk of the shocks in galaxy clusters should have a Mach number ($\mathcal{M} \equiv v_s/c_s$) $\mathcal{M} \sim 1.5$ Gabici & Balsi (2003). Recent cosmological simulations (Ryu et al. 2003; Pfrommer et al. 2006) confirmed this but also allow to study the higher Mach-number tail of shocks. Stronger shocks may indeed occur under some circumstance, such us in the outer part of the clusters where gas is not virialized. These external shocks are crucial for understanding the role of cosmic rays in large scale structure, because most cosmic rays accelerated in the outskirts are then advected in the central parts, were they get confined for cosmological times (Völk et al. 1996; Berezinsky et al. 1997).

Chapter 2

Non-thermal Phenomena in Galaxy Clusters: Observations

There is now firm evidence that the ICM is a mixture of hot gas, magnetic fields and relativistic particles.

The most important evidence for relativistic electrons in clusters of galaxies comes from the diffuse synchrotron radio emission observed in a growing number of massive clusters. The diffuse emissions are referred to as radio halos and/or radio mini–halos when they appear confined to the center of the cluster, while they are called relics when they are found in the cluster periphery (*e.g.,* Feretti 2003).

Diffuse radio emission is not the only evidence of non-thermal activity in the ICM. Additional evidence comes from the detection of hard X-ray (HXR) excess emission discovered in few galaxy clusters (Fusco-Femiano et al. 1999, 2000, 2003, 2004; Rephaeli et al. 1999; Rephaeli & Gruber 2002, 2003) which may be explained in terms of IC scattering of relativistic electrons off the photons of the cosmic microwave background (CMB)

The presence of high energy hadrons is not yet proven, but in principle, due to confinement of cosmic rays over cosmological time scales (*e.g.,* Völk et al. 1996; Berezinsky et al. 1997, Chapt. 3), the hadron content of the intracluster medium might be appreciable and may be constrained by future gamma–ray observations (*e.g.,* Blasi 2003; Blasi et al. 2007; Miniati 2003).

In this Chapter we will discuss the main properties of the non-thermal emission and magnetic fields in galaxy clusters from an observational point of view.

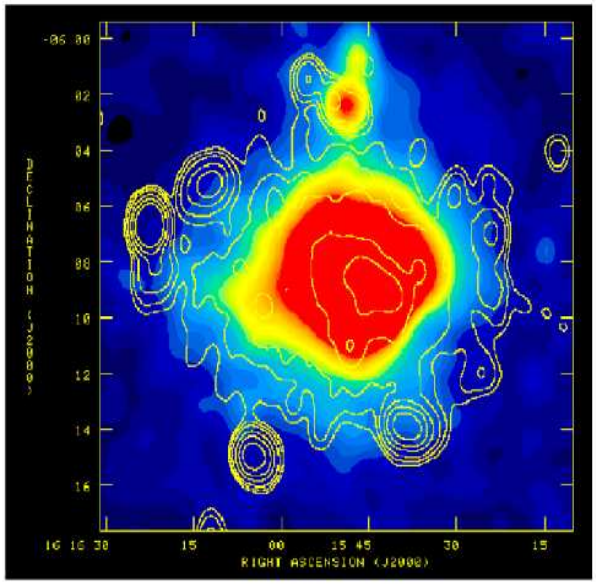

Figure 2.1: The cluster A2163: radio contours at 1.4 GHz overlaid on the ROSAT X-ray emission (Feretti 2001).

2.1 Diffuse Radio emission in galaxy clusters

2.1.1 Giant Radio Halos, Relics and mini-halos

According to definitions given in literature, *radio halos* (RH hereafter) are large diffuse non-thermal radio source permeating the cluster centers which are not associated with any single active galaxy but rather with the diffuse ICM. Large-scale RH show a generally regular shape, low surface brightness ($\sim \mu$Jy/arcsec^2 at 1.4 GHz), with typical luminosity of $\sim 5 \cdot 10^{23} - 5 \cdot 10^{25}\, h_{70}^{-2}$ Watt/Hz at 1.4 GHz, and typical size of $\gtrsim 1$ Mpc. They have a steep radio spectrum and show low or negligible polarized emission ($< 10\%$)[1]. One of the most impressive, powerful and extended RH is found in the galaxy cluster A2163 (see Fig.2.1; Feretti et al. 2001, 2004).

These sources are difficult to detect because of their low surface brightness and large size: their detection is limited by the surface brightness sensitivity coupled with the relatively high resolution needed to separate such sources from the embedded discrete sources. Because of their steep spectrum they are better detected at lower frequencies, thus future low-frequency radio instruments, such as LOFAR

[1]The only exception being the RH in A2255 which shows a filamentary structure strongly polarized (Govoni et al. 2005).

and LWA, will probably provides a step forward in the discovery of new RHs. Despite the observational difficulties, several surveys were undertaken to detected RHs and determine how common they are (*e.g.,* Jaffe & Rudnick 1979; Cane et al. 1981; Hanish 1982). The general conclusion was that such sources are very rare (*e.g.,* Feretti & Giovannini 1996). With the aim to build a larger sample of halos and relics Giovannini, Tordi & Feretti (1999, hereafter GTF99) undertook a search for new halos and relic candidates using the NRAO VLA Sky Survey (NVSS, Condon et al. 1998). As a parent cluster sample they used the X-ray-brightest Abell-type clusters (XBACs, Ebeling et al. 1996). The cross correlation between the XBACs and the radio survey NVSS provided a list of ~ 29 candidates for diffuse cluster-wide sources. Kempner & Sarazin (2001) made a search for radio halos and relics in all Abell clusters present in the Westerbork Northern Sky Survey (WENSS, Rengelink et al. 1997) at 327 MHz and they found 18 candidates, all showing evidence of a recent or ongoing merger.

Several of the candidates selected from these surveys were subsequently confirmed by radio follow-up. So far the number of well known radio halos is ~ 20. Apart Coma, they are: the powerful radio halos in the hottest known cluster 1E 0657-56 (the so called "bullet cluster", Liang et al. 2000); A2163 (Feretti et al. 2001); A2744, A520, A2254 and A773 (Govoni et al. 2001a); A2219, A1941, A545 and A754 (Bacchi et al. 2003); A665 and possible CL0016+16, at $z \simeq 0.55$ (Giovannini & Feretti 2000); A2256, A2319, A1300 (Feretti 2000). Very recently radio halos have been discovered in : RXCJ1314.4-2515 (Feretti et al. 2005; Venturi et al. 2007); RXCJ2003.5-2323 (Venturi et al. 2007) and A209 (Giovannini et al. 2006; Venturi et al. 2007).

The prototype of this class of sources and the best studied one is Coma C in the Coma cluster, discovered 30 years ago (Willson 1970; Schlickeiser et al. 1987; Kim et al. 1990; Giovannini et al. 1993; Deiss et al. 1997; Thierbach et al. 2003). The total (integrated) radio spectrum of the Coma halo is a steep power law with $\alpha \sim 1.2$ at frequency below 1.4 GHz, while observations at higher frequencies reveal the presence of a spectral steepening (Schlickeiser et al. 1987 at 2.7 GHz and Thierbach et al. 2003 at 2.675 and 4.85 GHz; Fig.2.2) which can be interpreted due to the presence of a break in the spectrum of the emitting electrons (see Chapt. 4). High sensitivity radio images of the Coma halo exist at both 327 MHz (Venturi et al. 1990)

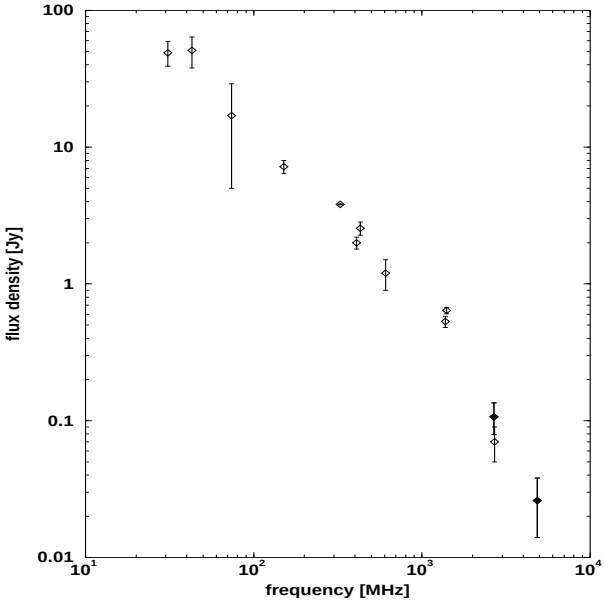

Figure 2.2: Total radio spectrum of the radio halo Coma C (from Thierbach et al. 2003).

and at 1.38 GHz (Kim et al. 1990), by applying Gaussian fits, it has been found that the 327-MHz FWHM ($28 \times 20\text{arcmin}^2$) is significantly larger than that at 1.38 GHz ($18.7 \times 13.7\text{arcmin}^2$) and this implies a steepening of the synchrotron spectral index with distance from the cluster centre. The spectral index distribution of Coma C between 327-1380 MHz shows a central plateau with $\alpha \sim 0.8$, and an outer region with a steeper spectrum, up to $\alpha \sim 1.8$ beyond a region of 10 arcmin (Giovannini et al. 1993). The increasing of the size of Coma C at lower radio frequencies is also consistent with the analysis of less recent images taken at 43 MHz and 150 Mhz (*e.g.,* Hanisch & Erickson 1980 at 43 MHz; Cordey 1985 at 151 MHz) and the steepening of the spectral index with radius has also been confirmed by 1.4 GHz data from Effelsberg single-dish 100-m telescope (Deiss et al. 1997).

In addition, spectral index maps obtainded for some other RHs (Feretti et al. 2004; Orrù et al. 2007) indicate the existence of patches of different spectra. This suggests a complex shape of the electron spectrum, as generally expected in the case of particle re-acceleration.

It is not clear whether the complex spectral properties of the Coma C are common among the class of RHs, yet these properties can be used to constrain the origin of the emitting particles (Chap. 3).

Radio relics are similar to RHs in the low surface brightness, large size and

lumiositis of $\sim 10^{23} - 10^{25}\,h_{70}^{-2}$ Watt/Hz at 1.4 GHz and steep spectrum, but are generally elongated in shape. They are located in cluster peripheral region and are generally linearly polarized at a livel of 10-30% at 1.4 Ghz (*e.g.,* Giovannini & Feretti 2004).

It should be pointed out that while the class of giant RHs is a well defined one, the classification of radio relics is more complicated because they are made of different objects, which may have a different origin and this complicates any present effort aimed to a statistical analysis of these sources. Govoni & Feretti (2004) divided the known relic sources in different class according to their observational structure and location, without relating them to physically different classes. Currently the total number of the relic sources is ~ 30 but, in addition to the classical peripheral elongated radio sources, they include also objects like extended radio sources near the central cD galaxy, but not clearly related to it; radio sources at the cluster periphery, but with a mostly circular shape; and extended radio sources very distant from the nearest cluster centre.

A prototype of the relic source class is the diffuse source, named 1253+275, in the Coma cluster. This source is located at $\sim 2.7\,h_{50}^{-1}$ Mpc from the cluster centre, and has size and brightness similar to those of Coma C, but shows an elongated shape, 30% polarization level at 1.4 GHz and its spectrum does not steepen at higher frequencies.

A spectacular example of two almost symmetric relics in the same cluster can be found in A3667 (Röttgering et al. 1997). Remarkably, in some clusters both radio halos and relics have been detected, *e.g.,* in Coma, A2255, A2256, A1300, A2744 and RXCJ1314.4-2515.

Mini-halos are diffuse extended radio sources of moderate sizes ($500\,h_{50}^{-1}$ kpc) surrounding a dominant powerful radio galaxies at the cluster centre. Example of this class are found in Perseus (Burns et al. 1992; Sijbring 1993) and Virgo (Owen et al. 2000) clusters. Although these sources could be related to a central radio source, it is worth noticing that these sources do not appear as extended lobes maintained by an Active Galactic Nucleus (AGN), as in classical radio galaxies, therefore their radio emission is indicative of the presence of diffuse relativistic particles and magnetic fields in the ICM at the cluster center. Radio mini-halos, are only observed in clusters with a cooling flow and their origin and connection with the cooling flow is

still poorly understood.

2.1.2 Connection to cluster mergers and statistical properties of Giant Radio Halos

The important results of the GTF99 work is that they found that only $\sim 5\%$ of clusters have a radio halo source and only $\sim 6\%$ a peripherical relic source. They also found that the detection rate of diffuse radio sources increases with the cluster X-ray luminosity reaching $\sim 33\%$ in clusters with X-ray luminosity larger than $10^{45}\, h_{50}^{-2}$ erg/s (luminoisity in the energy range 0.1-2.4 keV). Cluster hosting a RH have X-ray luminosities significantly higher than clusters without a diffuse source (Owen et al. 1999; Giovannini et al. 1999), implying that these clusters also have higher temperature ($KT \gtrsim 6$ keV) and larger virial masses ($M_v \gtrsim 10^{15}\, h_{70}^{-1}\, M_{\odot}$).

How the increase of the occurrence of RHs with the X-ray luminosity is affected by brightness detection limit of present surveys is still not completely clear. However, Feretti (2005) and Clarke (2005), have already concluded that the typical brightness of the powerful and giant RHs are well above the detection limit of the NVSS; on the other hand, it is possible that low power RHs could be hosted by less luminous X-ray clusters and in this sense future radio instruments (LOFAR, LWA and SKA) will be crucial.

In many cases, radio structures of halos show close similarities to the X-ray structures, suggesting a causal connection between the hot and relativistic plasma (Deiss et al. 1997; Feretti 2000; Liang et al. 2000). This similarity was quantitatively confirmed by Govoni et al. (2001b) by comparing the point-to-point surface brightness of the radio and X-ray emission in four cluster of galaxies (Coma, A2255, A2319 and A2744). This study leads to a correlation between the radio and the X-ray brightness in all the analyzed clusters: a higher X-ray brightness is associated with a higher radio brightness. A correlation seem to exist between the largest radio size of diffuse sources and the cluster X-ray luminosity, with more X-ray luminous clusters hosting larger radio diffuse sources (Feretti 2000).

Colafrancesco (1999) and Liang et al. (2000) found a correlation between the radio power of radio halos and the cluster temperature in the form $P_{1.4} \propto T^{6.25^{+6.25}_{-2.08}}$. This correlation is consistent with the fact that the monochromatic radio power at 1.4 GHz of halos increases with the bolometric X-ray luminosity of the parent clusters (Liang et al. 2000; Feretti 2000, 2003; Enßlin and Röttgering 2002).

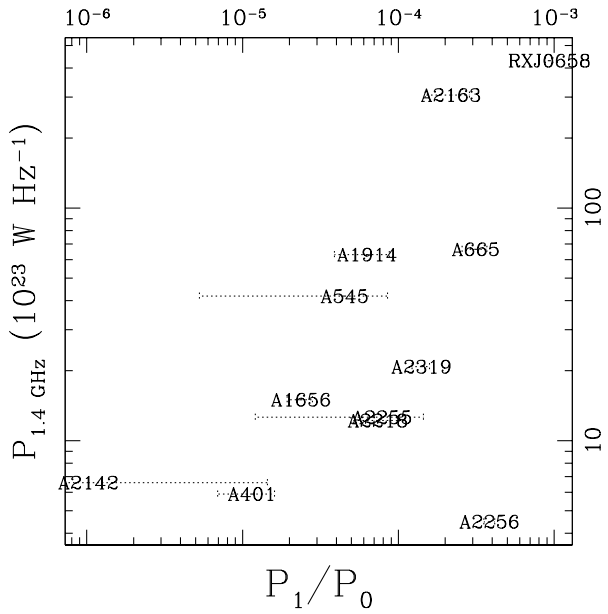

Figure 2.3: From Buote (2001): Radio power ($P_{1.4}$ - 1.4 GHz rest frame) of radio halos versus dipole power ratio (P_1/P_0). The power ratios are computed within a 0.5 Mpc aperture centered on the X-ray emission peak with estimated 1σ errors shown.

Since in clusters the X-ray luminosity and mass are correlated, as well as the temperature and the mass (*e.g.,* Neumann & Arnaud 1999, 2001), it follows that radio halos power correlates with the cluster mass. By analyzing 6 radio halo clusters, Govoni et al. (2001a) found $P_{1.4} \propto M^{2.2}$, where M was the total gravitational mass inside the Abell radius ($\sim 3\,h_{50}^{-1}$ Mpc)

All clusters hosting halos and relics are characterized by dynamical activity related to merging processes. These clusters indeed show: substructures and distorsions in the X-ray brightness distribution (Schuecker et al. 2001); temperature gradients (Markevitch et al. 1998; Govoni et al. 2004) and shocks and cold fronts (Markevitch et al. 2002); absence of strong cooling flows (Edge et al. 1992; Feretti 2000); optical substructures (Boschin et al. 2004). Although there is evidence for a connection between cluster merging and radio halos, it has been argued (*e.g.,* Giovannini & Feretti 2000; Liang et al. 2000; Feretti 2000) that merging cannot be the solely responsible for the formation of radio halos because at least 50% of clusters show evidence for X-ray substructure (Jones & Forman 1999) whereas only a small fraction possess radio halos. Unfortunately, it is difficult to interpret the importance of merging without making use of a quantitative measure of the

deviation of an individual cluster from a virialized state. A method to measure the dynamical states of clusters from X-ray images quantifying the cluster morphology is the "power ratio" method (Buote & Tsai 1995, 1996; Buote 1998). The power ratio are constructed from the moments of the two-dimensional gravitational potential due to matter interior to a circle of radius R centred on the peak of the X-ray emission. In particular the power ratio P_1/P_0 provides structural information related to potential fluctuations which are related to the dynamical status of the cluster. Buote (2001) used power ratio to provide the first quantitative comparison of the dynamical states of clusters possessing radio halos. A correlation between the 1.4 GHz power ($P_{1.4}$) of the radio halos and the magnitude of the dipole power ratio (P_1/P_0) was discovered such that approximately $P_{1.4} \propto P_1/P_0$ (see Fig.2.3) This correlation not only confirmed previous circumstantial evidences relating the presence of radio halos to mergers but established for the first time a quantitative relationship between the "strength" of radio halos ($P_{1.4}$) and the "strength" of mergers (P_1/P_0). The merger-RH connection is a fundamental point in our present understanding of the origin of RH and represents a major issue of the present PhD work (Chap. 5).

2.2 Cluster Magnetic Field: Observations

The existence of magnetic fields associated with the ICM in cluster of galaxies is now well established through different methods of analysis which substantially lead typical field strengths of order $\approx \mu$G. In some locations, such as the cores of "cooling flow" clusters, the magnetic fields reach levels of 10–40 μG and may be dynamically important. Even though in most clusters magnetic fields are not dynamically important, with magnetic pressures one to two orders of magnitude below thermal gas pressures, in all clusters the magnetic fields have a significant effect on energy transport in the ICM (Sarazin 1986; Tribble 1989) and significant implications for the lifetimes of relativistic particles in the ICM. Moreover, the magnetic suppression of thermal conductivity in the ICM, verified by the recent discovery of "cold fronts" in galaxy clusters (Markevitch et al. 2000; Vikhlinin et al. 2001), may play an important role in understanding the common occurrence of "cooling flow" clusters.

Direct evidence of the presence of intra-cluster magnetic fields (ICMFs) is provided by observations of extended radio halos in galaxy clusters. Their radiation

can only be due to synchrotron emission of relativistic electrons in the ICM. The strength of the ICMFs can be estimated from the intensity of the observed radio emission, either assuming the minimum energy condition, giving $\langle B \rangle \sim 0.1 - 1\,\mu$G (Feretti 2000; Giovannini et al. 1993), or by an independent determination of the density of relativistic electrons. The former is frequently used in the literature but it has to be understood as an order of magnitude approach, as there is no compelling physical reason why one should expect the magnetic field to be in equipartition. The latter is made possible for a few clusters by the observation of hard X-ray (HXR) emission that, if interpreted as the outcome of inverse Compton (IC) scattering of relativistic electrons on CMB photons, implies an average magnetic field strength within the emitting volume in the range of $0.2 - 0.4\ \mu$G (Fusco-Femiano et al. 1999; Rephaeli et al. 1999).

Additionally Faraday rotation measurements (RMs) of polarized radio sources placed within the cluster, or in the background, provide significant evidence for the presence of stronger magnetic fields, in the range $1 - 10\ \mu$G in the core of non cooling-flow clusters, and of even larger strength in cooling-flow clusters (*e.g.,* Kim et al. 1991; Clarke et al. 2001; Taylor et al. 2001; Vogt & Enßlin 2003; Govoni 2006): still these values come from the interpretation of RMs observations and are rather model dependent (Newman et al. 2002). Investigations of RMs of elongated radio-sources within galaxy clusters may also provide invaluable information on the geometrical structure of magnetic fields, which cannot be provided by radio-halo observations alone. The data on RMs are incompatible with uniformly oriented magnetic fields, rather, a typical length-scale of $\approx 5 - 15$ kpc has been inferred. Also, evidence is accumulating that there is no unique length-scale for the ICMFs, and that a successful interpretation of the RMs requires the adoption of a power-law spectrum, even though the power law index (somewhere in the range -1.5 to -4) is so far only very weakly constrained (Enßlin & Vogt 2003; Vogt & Enßlin 2003; Murgia et al. 2004).

Another crucial issue in the present context concerns the radial profile of ICMF in the external regions of galaxy clusters. Recent work based on radio emission (Brunetti et al. 2001a) as well as RMs (Dolag et al. 2001) indicates that the intracluster magnetic field decline in strength with radius, with a radial profile that appears to be similar to that of the gas density.

2.3 Extreme Ultraviolet, Hard X-Ray and Gamma Ray Emission

Additional spectral components of galaxy clusters, potentially of non-thermal origin have been discovered in the soft X–rays (EUV excess) detected by *EUVE* (Lieu et al. 1996a) and *ROSAT* (*e.g.,* Bonamente et al. 2002), and in the hard X-rays (HXR excess) detected by *BeppoSAX* (Fusco-Femiano et al. 1999) and *RXTE* (Rephaeli et al. 1999). No detection of galaxy clusters has been obtained in gamma rays so far (Reimer et al. 2003). In this Section we will briefly discuss the observational picture. Upper limits in gamma rays could be extremely important for discreminating among different scenarios for the origin of non-thermal components in galaxy clusters and will be considered in Chap. 3.

2.3.1 EUV/Soft X-Ray Emission

Clusters of galaxies are strong emitters of X–rays, which originate from a diffuse and hot phase of the ICM (see Sect.1.2). At the typical temperatures of $T \sim (1-10)\times 10^7$ K, the bulk of the hot ICM radiation is detected at few keV, while Galactic absorption could be responsible for a substantial reduction of the flux below ~ 1 keV. The soft X–ray band around 0.25 keV and the EUV band offer a unique windows to investigate the presence of other emitting/absorbing phases of the ICM. With advent of more sensitive low-energy X-ray instrumentation (*ROSAT-PSPC* and *EUVE, Extreme Ultraviolet Explorer*) it was found that some clusters contained soft excess emission in excess from the extrapolation of the contribution from the X-ray emitting ICM. Such a soft component has been seen first in the Virgo (Lieu et al. 1996a; Bowyer et al. 1996) and Coma clusters of galaxies (Lieu et al. 1996b) in both EUVE detector and ROSAT PSPC observations, and then found in other clusters (*e.g.,* Mittaz et al. 1998; Bowyer et al. 1998). In the most cases, at an EUV excess is associated a soft X-ray excess seen in the *ROSAT* PSPC spectra of the clusters.

The EUV-excess in rich clusters has luminosities of $\sim 10^{44}$ erg/s, and this have spectral component declines rapidly in going from the EUV to the X-ray band. The problem of its physical origin is still matter of debate.

The excess EUV emission can be interpreted as due to two principal different mechanisms: thermal radiation from a warm ($10^5 - 10^6$K) gas, as first suggested

by Lieu et al. (1996a), or IC emission of relativistic electrons on the CMB photons (Hwang 1997; Ensslin & Biermann 1998; Sarazin & Lieu 1998).

The main concern with the "thermal" hypothesis is that at these temperature the gas cooling is particulary efficient requiring a substantial energy input to sustain the gas at these temperatures. On the other hand, non–thermal models (Sarazin & Lieu 1998; Bowyer & Berghöfer 1998; Lieu et al. 1999; Enßlin et al. 1999; Atoyan & Völk 2000; Brunetti et al. 2001b) are potentially able to account for the excess EUV emission.

Due to the large amount of data, the Coma cluster represents the best case to compare model predictions with observations. It was soon realized that, since the EUV profiles was narrower than the radio one, it cannot be accounted for by IC emission of the low energy tails of electrons producing radio halo with the CMB photons (Bowyer & Berghöfer 1998). Low energy, $\gamma \approx 100 - 300$, electrons in the ICM are large living and could be injected in the ICM by supernovae, radio galaxies or by intracluster shocks; these particles may IC scatter off CMB photons to the soft X-rays (Sarazin & Lieu 1998; Brunetti et al. (2001b)

Another possibility is provided by the contribution from 'warm-hot' intergalactic medium", WHIM filaments with $T \simeq 10^5 - 10^7\,\mathrm{K}$ projecting themselves onto the galaxy clusters (*e.g.,* Bonamente et al. 2002), however the details of the soft X-ray emission from such filaments heavily depend on their temperature, density and metal abundances, which at the moment can only be predicted within orders of magnitude.

A step forward in this research has been made recently by the advent of XMM-Newton which allows to study clusters of galaxies at low energy with moderate spectral resolution ($\sim 60eV$) and good sensitivity. A number of studies have been performed using the XMM-Newton EPIC detector (*e.g.,* Kaastra et al. 2003, 2004; Nevalainen et al. 2003) which confirm the presence of the soft X-ray emission in several clusters. The spectral analysis (Kaastra 2004) shows signature of thermal emission in several cases (A1795, Sersic 159-03, A2052, MKW 3s and A2199) and controversial results in other cases (Coma and A3112). The thermal signature is present in form of line emission at 0.57 keV, identified with the (unresolved) triplet of O VII, in addition to an unresolved soft-excess below an energy of 0.3 keV. This warm gas (Kaastra et al. 2003, 2004; Finoguenov et al. 2003) typically extend on

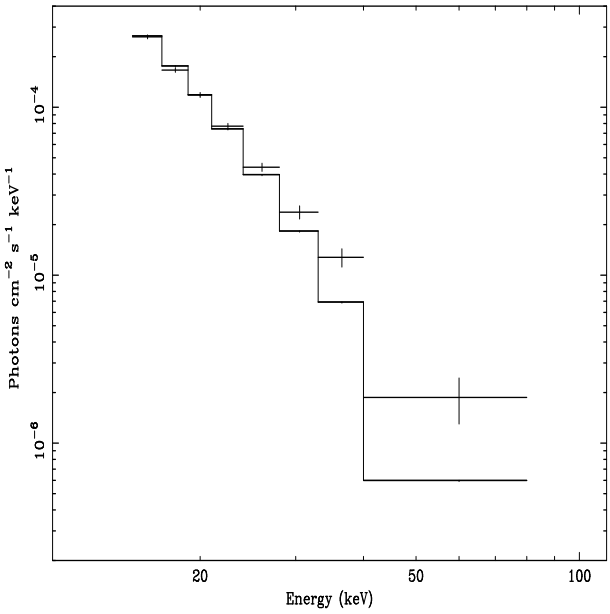

Figure 2.4: PDS combined spectrum of the Coma cluster obtained with the XAS package (Fusco-Femiano et al. 2004). The continuous line represents the best fit with a thermal component at the average cluster gas temperature of 8.11 keV (David et al. 1993). The error bars are quoted at the 1σ level. The spectrum starts at 15 keV.

2-6 Mpc and has temperature of $\sim 2 \times 10^6$ K.

Still due to the difficulty of the observations and data analysis, no general consensus is achieved on the origin of this emission. In principle, if the above discovery of O VII line emission in the outskirts of some clusters support the contribution from WHIM, on the other hand the possibility of a non-thermal origin cannot be excluded yet.

2.3.2 Hard X-Ray Emission

Non–thermal hard X–ray radiation (HXR) was predicted in 1970's in galaxy clusters showing extended radio emission, because of IC scattering of CMB photons by the same radio synchrotron electrons (*e.g.,* Rephaeli 1979).

The CMB photons give an IC-equivalent field $B_{cmb} \sim 3\mu$G which is likely to dominate the energy losses of relativistic electrons (Chap. 3) and thus most of the energy of the relativistic electrons will be radiated via inverse Compton (IC) scattering of the CMB photons, producing a broad hard X-ray spectral component with a flux higher than that of radio radiation.

While the detectability of such spectral component would be easiest in the soft

X-ray range, where very sensitive imaging instruments are available, in reality, in this range, the prominent thermal bremsstrahlung emission completely mask this component.

Recently HXR emission (in the 20 to 80 keV range) at significant levels above that expected from the thermal gas was detected by instruments on board *BeppoSAX* and *Rossi X-ray Timing Explorer* (*RXTE*) satellites from Coma, reported in Fig.2.4 (Fusco-Femiano et al. 1999; Rephaeli et al. 1999; Rephaeli & Gruber 2002; Fusco-Femiano et al. 2004), Abell 2256 (Fusco-Femiano et al. 2000; Rephaeli & Gruber 2003; Fusco-Femiano et al. 2005), Abell 2319 (Gruber & Rephaeli 2002), and a marginally ($\sim 3\sigma$) in Abell 754 (Fusco-Femiano et al. 2003) and in 1E0657-56 (Petrosian et al. 2006). *BeppoSAX* observed also A2163, A1367, A3667 (Fusco-Femiano et al. 2001) and A119 (Fusco-Femiano et al. 2003) reporting only upper limit to the non-thermal flux.

As stated above electrons of similar energies, $\gamma \sim 10^4$, can be responsible for both the IC−HXR and for the synchrotron−radio emission and the ratio of these fluxes depends primarily on the ratio of the photon (CMB in this case) to magnetic field energy densities. The luminosity of Coma in the 20-80 keV range is $L_{\rm HXR} \sim 4 \times 10^{43}$ erg/s which is much larger than the radio synchrotron luminosity implying a volume average magnetic field $\overline{B} \sim 0.1\,\mu$G. On the other hand, Faraday rotation measure are interpreted with line-of-sight average field of $\overline{B}_l \sim 3\,\mu$G (*e.g.,* Eilek 1999; Giovannini et al. 1993; Kim et al. 1990; Clarke et al. 2001; Clarke 2003), and $\sim \mu$G fields in galaxy clusters are commonly derived from RM-tecniques (*e.g.,* Govoni & Feretti 2004). As explained in Chap.3, this discrepancy can be significally reduced by more complex modelling of radio and IC emission from galaxy clusters.

An additional possibility to explain HXR-excess in clusters is via supra-thermal bremmstralhung (Blasi 2000; Dogiel 2000) although these models are sfavored being very inefficient and requiring a large (problematic) energy budjet (Petrosian 2001). The issue of non–thermal radiation is clearly related to the problem of acceleration of particles: we will discuss this important issue in Chapt.3.

Chapter 3

Physics & Models of non-thermal components in the ICM

As discussed in the previous Chapter the diffuse radio (synchrotron) emission from halos and relics and the hard X-ray (inverse Compton) radiation (and eventually EUV/Soft X-ray, inverse Compton, radiation) demonstrate that the ICM consist not only of the hot gas emitting thermal X-rays, but also of *non-thermal components*, *i.e.,* relativistic particles and magnetic fields.

Understanding the energetics and physical properties of these "new" components is important not only to get the picture of the non-thermal phenomena in galaxy clusters but also to understand how these components may eventually affect the physics of the thermal ICM.

In this Chapter we will discuss the basic physics of relativistic particles in the ICM with particular attention to their evolution, energy losses, acceleration and injection. Then we will give some basic information about our present knowledge of the properties of the magnetic field in galaxy clusters. Finally, we will briefly discuss the present models for the non-thermal emission from galaxy clusters; details on the re-acceleration model are given in Sect. 3.4.

3.1 Relativistic particles in the ICM

3.1.1 Injection

Clusters of galaxies should host a large number of sources of cosmic rays. They contain AGNs (radio loud and radio quite) which may produce and distribute cosmic rays throughout the cluster volume. These AGNs indeed inject in the ICM a considerable amount of energy in relativistic particles and also in magnetic fields,

likely extracted from the accretion power of their central black hole (Ensslin et al. 1997).

Powerful Galactic Winds (GW) can inject relativistic particles and magnetic fields in the ICM (Völk & Atoyan 1999). Although the present day level of starburst activity is low and thus this mechanism is not expected to produce a significant contribution, it is expected that these winds were more powerful during early starburst activity. Some evidence that powerful GW were more frequent in the past comes from the observed iron abundance in galaxy clusters (Völk et al. 1996).

In addition to galaxies and AGNs, cluster formation is also believed to provide a contribution to the injection of cosmic rays in the ICM due to the formation of shocks which may accelerate relativistic particles (Blasi 2001; Takizawa & Naito 2000; Miniati et al. 2001; Fujita & Sarazin 2001). The efficiency of this mechanism is related to the Mach number of these shocks which is an issue still under debate. Semi–analytical calculations based on PS-Monte Carlo techniques (Gabici & Balsi 2003; Berrington & Dermer 2003) find that the bulk of the shocks have Mach numbers of order ~ 1.4.

First cosmological numerical simulations found that the distribution of Mach numbers of merger shocks peaked at $\mathcal{M} \sim 5$ (Miniati et al. 2000), and that the bulk of the energy was dissipated at $4 \leq \mathcal{M} \leq 10$ shocks (Miniati 2002). On the other hand, more recent numerical simulations mitigated the discrepancy between semi-analytical approaches and numerical simulations, finding more weak shocks and that the bulk of the energy dissipation (thermal energy and cosmic rays) at internal shocks was associated with shocks with $2 \leq \mathcal{M} \leq 4$ (Ryu et al. 2003). These results have been confirmed by Pfrommer et al. (2006), where energy is found to be mostly dissipated at shocks with moderate Mach number $\mathcal{M} \simeq 2 - 3$.

In addition to mergers, structure formation proceeds also through *accretion* on already formed objects. Accretion shocks form outside the virialized regions, where the gas is much less dense and at lower temperatures. The low temperature of the gas implies that accretion shocks are always rather strong, with Mach number that may exceed ~ 10.

In the context of the linear theory of shock acceleration the spectrum of the accelerated particles is a power-law $N(E) \propto E^{-\delta}$, with a slope which is determined uniquely by the Mach number $\mathcal{M}$ of the shock, $\delta = 2\frac{\mathcal{M}^2+1}{\mathcal{M}^2-1}$ (*e.g.,* Eilek & Hughes

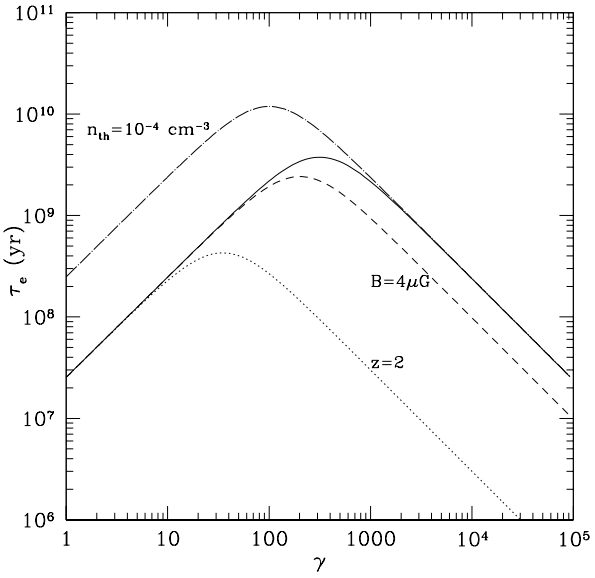

Figure 3.1: Instantaneous loss timescale (Eq.3.3) as a function of γ for electrons in a cluster with an electron density of $n_{th} = 10^{-3} cm^{-3}$, a magnetic field of $B = 0.5\mu$G at redshift z=0 (solid curve); an electron density of $n_{th} = 10^{-4} cm^{-3}$ (dot-dashed curve); a magnetic field of $B = 4\mu$G (dashed curve) and a redshift $z = 2$ (dot curve).

1991). For shocks with $\mathcal{M} = 2 - 4$. the spectrum of the accelerated particles varies between $\delta = 3.33 - 2.27$. For $\mathcal{M} = 1.4$ where the peak of the merger related shocks was found, the spectrum is as steep as $N(E) \propto E^{-6.2}$ and such shocks are irrelevant for particle acceleration.

3.1.2 Energy losses

In this Section we briefly review the most important channels of energy losses for electrons/positrons and protons.

Electrons

Relativistic electrons with momentum $p_{\rm e} = m_{\rm e} c\gamma$ in the ICM lose energy through ionization losses and Coulomb collisions (Sarazin 1999):

$$\left(\frac{dp}{dt}\right)_{\rm c} = -3.3 \times 10^{-29} n_{\rm th} \left[1 + \frac{\ln(\gamma/n_{\rm th})}{75}\right] \tag{3.1}$$

where $n_{\rm th}$ is the number density of the thermal plasma.

Relativistic electrons also lose energy via synchrotron emission and inverse Compton scattering off the CMB photons:

$$\left(\frac{dp}{dt}\right)_{\rm rad} = -4.8\times10^{-4}p^2\left[\left(\frac{B_{\mu G}}{3.2}\right)^2\frac{\sin^2\theta}{2/3}+(1+z)^4\right] = -\frac{\beta_{rad}p^2}{m_e\,c} \qquad (3.2)$$

where $B_{\mu G}$ is the magnetic field strength in μG and θ is the pitch angle of the emitting electrons; in case of efficient isotropization of the electron momenta it is possible to average over all possible pitch angles, so that $< \sin^2\theta >= 2/3$. It is well known that in the typical conditions of the ICM radiation losses are the most important for electrons with Lorentz factor $\gamma \gg 100$ while Coulomb losses dominate at lower energies (Sarazin 1999; Brunetti 2002). The lifetime of relativistic electrons, defined as $\tau \sim \gamma/\dot{\gamma}$, can be easily estimated from Eqs.(3.1–3.2) as:

$$\tau_{\rm e}({\rm Gyr}) \sim 4\times\Big\{\frac{1}{3}\Big(\frac{\gamma}{300}\Big)\left[\left(\frac{B_{\mu G}}{3.2}\right)^2\frac{\sin^2\theta}{2/3}+(1+z)^4\right] + \Big(\frac{n_{\rm th}}{10^{-3}}\Big)\Big(\frac{\gamma}{300}\Big)^{-1}\left[1.2+\frac{1}{75}\ln\Big(\frac{\gamma/300}{n_{\rm th}/10^{-3}}\Big)\right]\Big\}^{-1}. \qquad (3.3)$$

We stress that Eq. 3.3 can be used to obtain the maximum life time of particles with energy $m_e\,c^2\,\gamma$ by taking $B = 0$; n_{th} being measured by X-ray observations. As an example in Fig.3.1 we report the lifetime of relativistic electrons for typical physical conditions of ICM.

Protons

The main channel of energy losses for relativistic protons is represented by inelastic proton-proton collisions, which is a threshold reaction that requires cosmic ray protons with kinetic energy larger than ~ 300 MeV. The timescale associated with this process is :

$$\tau_{pp} = \frac{1}{n_{\rm th}\sigma_{\rm pp}c} \sim 10^{18}\Big(\frac{n_{\rm th}}{10^{-3}}\Big)^{-1}. \qquad (3.4)$$

Inelastic pp scattering is weak enough to allow for the accumulation of protons over cosmological times (Berezinsky et al. 1997).

Protons which are more energetic than the thermal electrons, namely protons with velocity $\beta_p > \beta_c = (3/2m_e/m_p)^{1/2}\beta_e$ (β_e here is the velocity of the thermal electrons, $\beta_e \simeq 0.18(T/10^8K)^{1/2}$) lose energy due to Coulomb interactions. If we define $x_m = \left(\frac{3\sqrt{\pi}}{4}\right)^{1/3}\beta_e$, we can write (*e.g.,* Schlickeiser 2002):

$$\frac{dp}{dt} \simeq -1.7 \times 10^{-29} \left(\frac{n_{\rm th}}{10^{-3}}\right) \frac{\beta_p}{x_m^3 + \beta_p^3} \tag{3.5}$$

with the following asymptotic behavior:

$$\frac{dp}{dt} \propto \left(\frac{n_{\rm th}}{10^{-3}}\right) \times \begin{cases} \text{Const.} & \text{for} \quad p >> mc \\ p^{-2} & \text{for} \quad mcx_m < p << mc \\ p & \text{for} \quad mc\beta_c < p < mcx_m \end{cases} \tag{3.6}$$

The timescale associated with Coulomb collisions (in the case $mcx_m < p \ll mc$) can be therefore written as:

$$\tau_C \sim 2.5 \times \tau_{pp} \Big(\frac{p}{m_{\rm p}c}\Big)^3. \tag{3.7}$$

For trans-relativistic and sub-relativistic protons this channel can easily become the main channel of energy losses in the ICM.

3.1.3 Confinement

In this Section we briefly discuss the CR confinement in galaxy clusters: for most of the cosmic ray protons in the ICM both the timescales of energy losses (Sec.3.1.2) and diffusion out of the cluster volume are larger than the Hubble time (Berezinsky et al. 1997; Völk et al. 1996).

The minimum possible diffusion coefficient in a magnetized medium can be estimated assuming that the mean free path of particles is comparable to the their Larmor radius R_L. This is known as *Böhm diffusion*, and the related diffusion coefficient $D_B(E)$ for typical ICM conditions is given by (*e.g.,* Blasi 2001):

$$D_B(E) = 3.3 \cdot 10^{22} \Big(\frac{B}{1\mu\rm G}\Big)^{-1} \Big(\frac{E}{1\rm GeV}\Big)\, \rm cm^2 s^{-1} \tag{3.8}$$

If the power spectrum of the magnetic field irregularities is described by a Kolmogorov law $P(k) \propto k^{-5/3}$, then the diffusion coefficient for typical ICM conditions can be written as (*e.g.,* Blasi 2001):

$$D_K(E) = 2.3 \cdot 10^{29} \Big(\frac{B}{1\mu\rm G}\Big)^{-1/3} \Big(\frac{L_{max}}{20\rm kpc}\Big)^{2/3} \Big(\frac{E}{1\rm GeV}\Big)^{1/3} \rm cm^2 s^{-1} \tag{3.9}$$

where L_{max} is the maximum coherent scale of the magnetic field. Following Berezinsky et al. (1997) one can use these expressions to estimate the escape time scale, defined as $\tau_{esc} \sim R_v^2/6D(E)$, for a relativistic particle with energy E from a Coma-like cluster with mass $\sim 10^{15}\, M_\odot$ and virial radius $R_v \sim 3$ Mpc:

$$\tau_{esc}(E) = \begin{cases} 1.4 \cdot 10^{10} (\frac{R_v}{3\mathrm{M}pc})^2 (\frac{B}{1\mu\mathrm{G}}) (\frac{E}{1\mathrm{G}eV})^{-1}\,\mathrm{G}yr & \text{Böhm} \\ 2.0 \cdot 10^{3} (\frac{R_v}{3\mathrm{M}pc})^2 (\frac{B}{1\mu\mathrm{G}})^{1/3} (\frac{L_{max}}{20\mathrm{k}pc})^{-2/3} (\frac{E}{1\mathrm{G}eV})^{-1/3}\,\mathrm{G}yr & \text{Kolomogorov} \end{cases}$$

All the particles having escape times longer than the cluster life time, which can be assumed to be roughly equal to the Hubble time $t_H \sim 13$ Gyr, remain trapped within the cluster volume. The maximum particle energy for which the confinement is effective, is obtained making equal the escape times obtained above to t_H. This depends on the diffusion coefficient which is rather uncertain, still under ICM conditions one finds that this maximum energy is $\sim 10^9$ GeV for a Böhm diffusion and $\sim 4 \cdot 10^6$ Gev for a Kolmogorov diffusion coefficient; and thus the bulk of cosmic rays are expected to remain confined in the ICM for cosmological times. This argument is important for protons, which are only marginally affected by energy losses (Sect.3.1.2), and thus once injected in the ICM these protons should remain confined and accumulate in the ICM during the cluster lifetime. This fact may have important consequences for the expected non-thermal emission from clusters, as we will discuss in Sec.3.3.1.

3.1.4 Evolution

In this Section we introduce the formalism used to describe particle evolution in the presence of energy losses and acceleration (stochastic acceleration) mechanisms. In order to consider the evolution of the particle spectrum a kinetic theory approach is suitable (*e.g.,* Blandford 1986; Eilek & Hughes 1991). Let $f(\mathbf{p})$ be the distribution function (with implicit time dependence) so that $f(\mathbf{p})d\mathbf{p}$ is the number of particles in the element $d\mathbf{p}$ of the momentum space. The evolution of this distribution function is described by the Boltzmann equation:

$$\frac{\mathrm{d}f(\mathbf{p})}{\mathrm{d}t} = \left(\frac{\partial f}{\partial t}\right)_{\mathrm{coll}} + \left(\frac{\partial f}{\partial t}\right)_{\mathrm{diff}} \tag{3.10}$$

where f may be a function of momentum $\mathbf{p}$, position $\mathbf{r}$ and time t, and thus the total time derivative is to be interpreted according to (*e.g.,* Eilek & Hughes 1991):

$$\frac{\mathrm{d}}{\mathrm{d}t} \rightarrow \frac{\partial}{\partial t} + \mathbf{v} \cdot \frac{\partial}{\partial \mathbf{r}} + \mathbf{F} \cdot \frac{\partial}{\partial \mathbf{p}} \tag{3.11}$$

where $\mathbf{v} = \mathrm{d}\mathbf{r}/\mathrm{d}t$ is the particle velocity, and $\mathbf{F} = \mathrm{d}\mathbf{p}/\mathrm{d}t$ the force acting on the particles.

The *diffusion* term in Eq.(3.10) describes spatial diffusion, while the *collision* term accounts for all the physics of collisions and scattering (*e.g.,* radiative losses, interaction with waves and shocks, Coulomb collisions). A stochastic acceleration process may be thought of as a diffusion in momentum space, characterized by a diffusion coefficient $D_{\mathbf{pp}}$, so that

$$\left(\frac{\partial f}{\partial t}\right)_{\mathrm{coll}} = \frac{\partial}{\partial \mathbf{p}}\left(D_{\mathbf{pp}} \cdot \frac{\partial f(\mathbf{p})}{\partial \mathbf{p}}\right) \tag{3.12}$$

the diffusion coefficient contains the detail of the wave spectrum and the wave-particle interactions. Under the assumption of isotropy one has $f(\mathbf{p})d\mathbf{p} = 4\pi p^2 f(p)dp$. If one adds a radiative loss term, so that the losses for one particle are $dp/dt = -b(p)$, and an isotropic phase-space particle source term $q_s(p)$, in the case that only collision contribute to $\partial f/\partial t$ the Boltzmann equation is:

$$\frac{\partial f(p)}{\partial t} = \frac{1}{p^2}\frac{\partial}{\partial p}\left(p^2 D_{pp}(p)\frac{\partial f(p)}{\partial p} + p^2 b(p) f(p)\right) + q_s(p) \tag{3.13}$$

which is colled "Fokker-Planck" equation (e.g., Tsytovich 1966; Borovsky & Eilek 1986). Eq.3.13 can be transformed from a diffusion equation in the particle phase-space density, $f(\mathbf{p})$, into an equation in the particle number density, $N(p)$. For an isotropic distribution of the particle momenta, the number density $N(p)$ is related to the phase-space density by $N(p)dp = f(\mathbf{p})d\mathbf{p} = 4\pi p^2 f(p)dp$, and the source term becomes $Q_s(p) = 4\pi p^2 q_s(p)$; using these relations Eq.3.13 becomes:

$$\frac{\partial N(p)}{\partial t} = \frac{\partial}{\partial p}\left[N(p)\left(b(p) - \frac{2}{p}D_{pp}(p)\right)\right] + \frac{\partial}{\partial p}\left[D_{pp}(p)\frac{\partial N(p)}{\partial p}\right] + Q_s(p) \tag{3.14}$$

This basic equation describes the evolution of a distribution of highly relativistic particles subject to particular acceleration processes (accounted for by $D_{pp}(p)$) and loss processes (accounted for by $b(p)$).

In the case of of relativistic electrons Eq.3.14 is:

$$\frac{\partial N(p,t)}{\partial t} = \frac{\partial}{\partial p}\left[N(p,t)\left(\left|\frac{dp}{dt}\right|_{\mathrm{rad}} + \left|\frac{dp}{dt}\right|_{\mathrm{c}} - \frac{2}{p}D_{\mathrm{pp}}\right)\right] + \frac{\partial}{\partial p}\left[D_{\mathrm{pp}}\frac{\partial N(p,t)}{\partial p}\right] + Q_e(p,t) \tag{3.15}$$

where $D_{\rm pp}$ is the electron diffusion coefficient in the momentum space, $dp/dt_{\rm i}$ and $dp/dt_{\rm rad}$ are the terms due to ionization and radiative losses given by Eq.3.1 and Eq.3.2 respectively, and Q_e is an isotropic electron source term.

In the case of relativistic protons Eq.3.14 is:

$$\frac{\partial N(p,t)}{\partial t} = \frac{\partial}{\partial p}\left[N(p,t)\left(|\frac{dp}{dt}|_{\rm i} - \frac{2}{p}D_{\rm pp}\right)\right] + \frac{\partial}{\partial p}\left[D_{\rm pp}\frac{\partial N(p,t)}{\partial p}\right] + Q_p(p,t) \quad (3.16)$$

where $(dp/dt)_i$ is given by Eq.3.5.

3.2 Magnetic fields in the ICM

3.2.1 Origin of magnetic fields in galaxy clusters

The existence of μG magnetic fields associated with the ICM in cluster of galaxies is now well established (see Sec. 2.2), but the origin of the intra-cluster magnetic fields (ICMFs) is still poorly understood. The combination of relatively "high", μG level, field and the fact that RM suggest a complex topology of ICMF up to large scales, requires a non-linear amplification of the ICMFs which probably happens during the process of cluster formation. The complex dynamics of the gas during the accretion of matter and cluster mergers can indeed provides a non-linear amplification of the field in the ICM. Still a seed magnetic field to be amplified is required in galaxy clusters and we can distinguish three main classes of models that have been proposed to explain the origin of this seed field.

In the first, extragalactic magnetic fields are assumed to be produced 'locally' and at relatively low redshift ($z \sim 2-3$) by the ejecta of galaxies (*e.g.,* Völk & Atoyan 2000) or AGNs (*e.g.,* Furlanetto & Loeb 2001). One of the main arguments in favor of these models is that the high metallicity observed in the ICM suggests that a significant enrichment driven by galactic winds or AGN must have taken place in the past, together with a possibly magnetic pollution. While it was shown that winds from ordinary galaxies give rise to magnetic fields which are far weaker than those observed in galaxy clusters, magnetic fields in the ICM produced by the ejecta of starburst galaxies can be as large as 0.1 μG. Clearly, this class of models predicts that extragalactic magnetic fields are mainly concentrated in galaxy clusters. These fields will be amplified by both the adiabatic compression of the proto-cluster region

and by shear flows, turbulent motions, and merging events during the formation of the galaxy clusters.

In the second class of models, the seeds of extragalactic magnetic fields are assumed to be produced at higher redshift, before galaxy clusters form as gravitationally bound systems. Although the strength of the seed fields is expected to be considerably smaller than in the previous scenario, the adiabatic compression of the gas and the shear flows driven by the accretion of structures may still give rise to a considerable amplification of the magnetic field up to the observed value. Several mechanisms have been proposed to explain the origin of magnetic seed fields at high redshift. Some of these models are similar to those discussed above, differing only in the time at which the magnetic pollution is assumed to take place. In some models the magnetic field seeds are supposed to be expelled by an early population of dwarf starburst galaxies or by AGNs at a high redshift between 4 and 6 (Kronberg et al. 1999), allowing them to magnetize a large fraction of the volume. Other models invoke processes which took place in the early universe (see Grasso & Rubinstein 2001, for a review). Indeed, the ubiquity of magnetic fields in the universe suggests that they may have a cosmological origin. In general, all 'high-z models' predict magnetic field seeds that fill the entire volume of the Universe. Another (speculative) possibility is that the seed field was produced during inflation.

The third scenario assumes that the seeds of ICM magnetic field were produced by the so-called Biermann battery (Kulsrud et al. 1997; Ryu et al. 1998) effect. The idea here is that merger shocks produced by the hierarchical structure formation process give rise to small thermionic electric currents which, in turn, may generate magnetic fields. The battery process has the attractive feature to be independent of unknown physics at high redshift. Its drawback is that, due to the large conductivity of the intergalactic medium, it can give rise to at most very tiny magnetic field, of order 10^{-21} G. One therefore needs to invoke a subsequent turbulent dynamo to boost the field strength to the observed level. But, lacking a theoretical understanding of the turbulent amplification, it is therefore not straightforward to relate the very week seed fields produced by the battery process with the magnetic fields observed today.

3.2.2 Magnetic fields amplification and simulations

As discussed above, a magnetic seed field generated at higher redshift is expected to be amplified during the formation of galaxy clusters due to the complex dynamics of the gas in which the magnetic field is frozen in. This complex process has been simulated in different works (Röttiger et al. 1999; Dolag et al. 1999, 2002, 2004; Brüggen et al. 2005).

These studies have shown that magnetic field amplification takes place due to both adiabatic compression and magnetic induction, with the latter being driven by shear flows (Birk et al. 1999) that are ultimately powered by anisotropic accretion and merger events. The fact that the anisotropy of the collapse of galaxy clusters gives rise to additional amplification of magnetic fields has also been demonstrated with analytic models (Bruni et al. 2003).

By using synthetic ("simulated") RM maps obtained from simulations, Dolag et al. (2001) found a nearly linear correlation between the X-ray flux of the simulated clusters and RMs, which was nicely confirmed by observations, together with the predicted radial profiles of RMs. The strength of the uniform seed field required to reach this agreement was $(1-5)\times 10^{-9}\,\mathrm{G}$ at redshift $z_* \simeq 20$ which is within the range of values expected from the models for magnetic seed field injection that we have discussed in the previous section.

It is important to note that due to the chaotic nature of the process of matter accretion process on clusters, no memory of the initial field configuration is expected (Dolag et al. 2002). Also, since most of the magnetic field amplification takes place at low redshift ($z \lesssim 3$), the result of the simulations does not crucially depend on the precise cosmological epoch at which the seed field is injected, provided it is generated before the first significant major merger events.

Predicted MF scalings in galaxy clusters

An important expectation of MHD simulations is that the magnetic field decreases with increasing cluster-centric distance. In Fig. 3.2 (Dolag et al. 2005b, taken from), it is reported the radial profiles of the mass-weighted averages of the gas density, of the magnetic field strength and of the temperature. The median density profile is compatible with the canonical β-model (Eq.1.16). Depending on the cluster and its dynamical state, the slope of the magnetic profile in the outer parts and in the

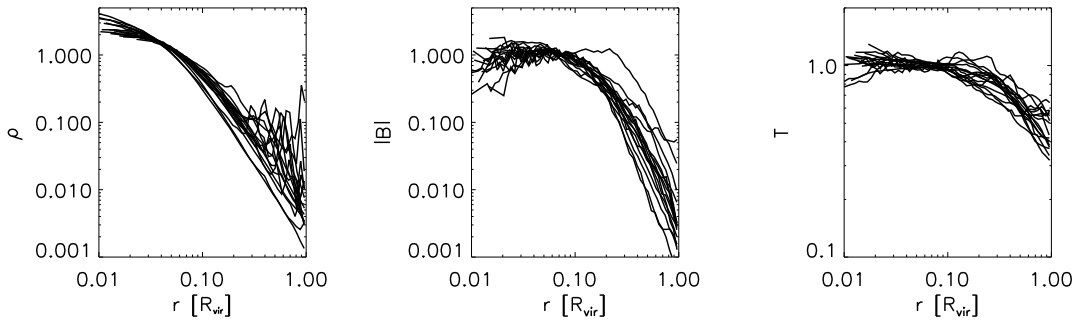

Figure 3.2: Spherically averaged profiles of gas density (left panel), magnetic field strength (middle panel) and temperature (right panel, mass-weighted) for the 16 most massive clusters extracted from the simulation. The profiles are scaled to $R_{\rm vir}$ and normalized to have the same mean value within $0.1 \times R_{\rm vir}$.

cluster cores scatters. On average, however, the magnetic field profiles follow the density profiles of clusters in their outer parts, whereas in the central regions the magnetic field profiles flatten. This flattening is presumably a direct consequence of the lower gas velocities in the cluster cores, and of the increase of the Alfvénvelocity in these regions, which make magnetic induction less effective.

As discussed in the previous section, the amplification of the magnetic field within these simulations is not only due to the adiabatic compression of the gas but this is dominated by the magnetic induction driven by shear flows. Thus a clear expectation of this scenario is that the final value of the magnetic field in galaxy clusters should depend on their merging history. In particular, more massive clusters, which undergo more numerous and more energetic merger events, should have a higher magnetic field in their cores than less massive ones (Dolag et al. 1999, 2005b).

Figure 3.3 (taken by Dolag et al. 2005) reports the mass-averaged magnetic field calculated within $0.1 \times R_{\rm vir}$ as a function of the gas temperature in the cores of simulated clusters: a strong dependence of $\langle B \rangle$ on temperature is expected. This scaling is fitted by a power-law, $\langle B \rangle \propto T^{\alpha}$ with $\alpha \approx 2$ (Dolag et al. 2002, 2005b).

3.3 Models for the non-thermal emission of ICM

Here we will give a brief description of the theoretical scenarios proposed to explain the observed non-thermal broad band spectrum of galaxy clusters. We treat this argument by describing the modeling of selected phenomena (RH, relics, mini-halos,

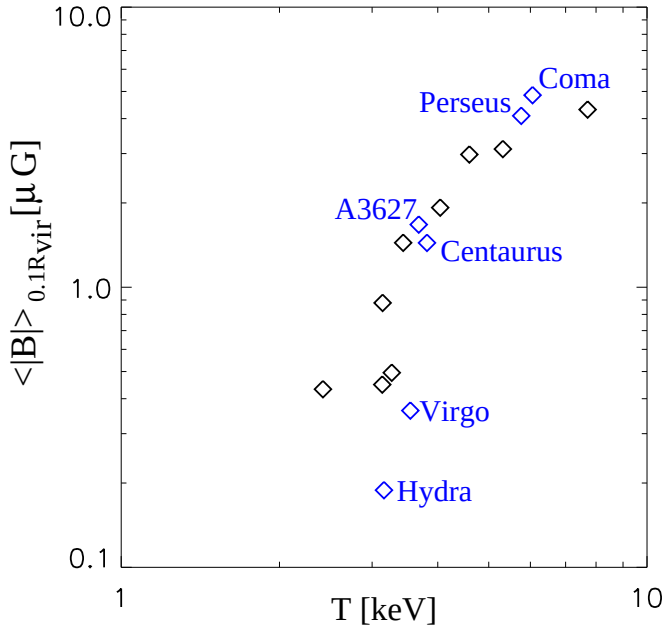

Figure 3.3: Magnetic field strength versus temperature for the most massive clusters of the simulation by Dolag et al. (2005b). The labels refer to halos that are identified with actual clusters. The magnetic field has been mass-averaged within $0.1 \times R_{\rm vir}$, resulting in mean values representative for the cluster cores.

HXR tails and so on) still, as it will become clear to the reader, in same cases different phenomena may be consequence of a single scenario (p−p collisions in the ICM, merger-driven particle acceleration, etc . . .).

3.3.1 Radio Halos

The radio emission observed in a growing number of galaxy clusters in the form of RHs (Sect. 2.1.1) is certainly the most importante evidence for the existence of relativistic electrons diffused on cluster scales and thus our present understanding of the non-thermal activity in the ICM is mostly based on the modelling of this component. The main difficulty in explaining the extended radio halos arises from the combination of their $\sim$ Mpc size, and the relatively short radiative lifetime of the radio emitting electrons (Fig. 3.1). Indeed, the diffusion time necessary for the radio electrons to cover such distances is orders of magnitude larger than their radiative lifetime. Indeed radio emission at ~ 1 GHz is typically due to electrons with energy of $\approx 10 B_{\mu\rm G}^{-1/2}$ GeV, which have a radiative lifetime of $\sim 10^8$ yrs (Sec.3.1.2) and can diffuse only for some tens of kpc during this time-scale. This diffusion distance is

several order of magnitude smaller than the typical size of RHs and this argument lead to the requirement that electrons should be generated or accelerated everywhere in the cluster (Jaffe 1977). Two main possibilities have been discussed for the origin of the emitting electrons: either the radiating electrons have a secondary origin, being produced by *pp* scattering (Dennison 1980; Blasi & Colafrancesco 1999), or they are continuously re-accelerated *in situ* through Fermi-like processes associated with merger events (Schlickeiser et al. 1987; Tribble 1993; Brunetti et al. 2001a; Petrosian 2001). More recently Brunetti & Blasi (2005) have developed *Hybrid Models* calculations, which include, in a self-consistent way, secondary electrons, MHD waves and primary electrons and protons.

In the following we will discuss the case of secondary models, while *the case of the re-acceleration model, which is the leading scenario adopted in this PhD work, will be discussed in more detail in Sect. 3.4.*

Secondary Models

As discussed in Sec.3.1.3 relativistic protons injected in the ICM during the whole cluster life remain confined and accumulate there, due to their negligible energy losses. Due to this confinement the probability of having inelastic proton-proton scattering in enhanced. The process is efficient enough to the continuous production of neutral and charged pions, which in turn decay into gamma rays, electrons and positrons ("secondary") through the decay chain (Blasi & Colafrancesco 1999):

$$p + p \rightarrow \pi^0 + \pi^+ + \pi^- + \text{anything}$$

$$\pi^0 \rightarrow \gamma\gamma$$

$$\pi^\pm \rightarrow \mu + \nu_\mu \quad \mu^\pm \rightarrow e^\pm \nu_\mu \nu_e.$$

The spectrum of secondary electrons and positrons with energy E_e is given by the convolution of the spectra of protons, $N(E_p)$, with the spectrum of pions, $F_\pi(E_\pi, E_p)$, produced in a single cosmic ray interaction at energy E_p, and with the distribution of leptons from the pion decay, $F_e^\pm(E_e, E_\pi)$, (*e.g.,* Moskalenko & Strong 1998):

$$Q_e^\pm[p,t;N_p] = n_{th}^p c \int_{E_{tr}} dE_p \beta_p N(E_p) \sigma_\pi^\pm(E_p) \int dE_\pi F_\pi(E_\pi, E_p) F_e^\pm(E_e, E_\pi), \quad (3.17)$$

where $\sigma^{\pm}(E_p)$ is the inclusive cross section for pion production, E_{tr} is the threshold energy for the process to occur and the distribution of electrons and positrons is given by :

$$F_e^{\pm}(E_e, E_{\pi^{\pm}}) = \int dE_\mu F_e^{\pm}(E_e, E_\mu, E_\pi), \tag{3.18}$$

where $F_e^{\pm}(E_e, E_\mu, E_\pi)$ is the spectrum of electrons/positrons from the decay of a muon of energy E_μ produced in the decay of a pion with energy E_π. For the detail on the expressions of the distribution functions of different particle species we refer the reeder to the specific papers (*e.g.,* Blasi & Colafrancesco 1999; Brunetti & Blasi 2005; Kelner et al. 2006).

Secondary electron models were first proposed by Dennison (1980) to explain RHs and considered in detail by Blasi & Colafrancesco (1999). More recently these models have been revived by many authors in the framework of numerical simulations (Dolag & Enßlin 2000; Miniati et al. 2001) where they can be easily implemented. There is general agreement on the fact that although the general features of the observed RHs could be reproduced by secondary electron models, some of the spectral, morphological and statistical properties of RHs are hard to be explained by these models.

Within the cluster there are many potential sources of cosmic ray protons which eventually would injected secondary $e^{\pm}$ in the ICM (Berezinsky et al. 1997): normal galaxies, active galaxies and shock waves associated with cluster formation (the last two are expected to be the dominant sources of cosmic rays in clusters). In all these cases the maximum energies of the accelerated protons are expected to be large enough ($>>$ 100 GeV) On the other hand the presence of a synchrotron break in the integrated spectrum of a few RHs (*e.g.,* Coma Schlickeiser et al. 1987, Thierbach et al. 2003 and A 3562 Giacintucci et al. 2005) and the evidence for a radial spectral steepening and/or patchiness which come from maps of synchrotron spectral index of a few RHs (Giovannini et al. 1993; Feretti et al. 2004; Orrù et al. 2007) can only be explained under the hypothesis of a break at $\approx$ GeV energy in the spectrum of the emitting electrons (*e.g.,* Brunetti 2001a; Blasi 2004). Also the broad synchrotron profiles of some giant RHs (*e.g.,* Abell 2163) are challenging for secondary models: in order to reproduce this very broad radio-profile with an energy budget of relativistic hadrons significantly below that of the thermal pool the strength of the magnetic

field in the ICM should be almost constant on scales comparable to the cluster size (Brunetti 2003, 2004; Marchegiani et al. 2007), which contrasts with the scenario of the amplification of magnetic field in galaxy clusters (see Sec.2.2, Fig. 3.2).

Finally, there is an increasing evidence that RHs are associated to ongoing cluster mergers, the secondary electron models have the problem that the radio emission would be dominated at any time by the pile up of cosmic ray protons during the merger history of the cluster, rather than by the last merger event, and in this case no correlations with cluster merger is expected. In particular, present radio data allow to conclude that the typical life–time of RHs should be of the order of 1 Gyr (Kuo et al. 2004), in contrast with a secondary origin of the emitting electrons which would produce very long living RHs.

The importance of all the above points deserve additional observations to better understand the spectral and morphological properties of RHs and to test the radio halos–cluster merger connection, still in this PhD work we will focus on the re-acceleration scenario which potentially does not suffer of these challenges (Sect. 3.4).

3.3.2 Radio Mini-Halos

Theoretically it is not clear whether radio mini-halos (RMH) are a different class of sources or whether they are simply smaller RHs, or RHs at an early stage of their evolution. Clearly classical RMH are always found in cooling-flow clusters with a dominant central radio sources while RHs are found in merging clusters without cooling-flow. Because a "diffusion-problem" similar to that of RHs also holds in the case of the classical RMHs (*e.g.,* Perseus RMH), two scenarios have been proposed to explain their origin. RMHs may originate due to particle acceleration by MHD turbulence in the cooling-flow region (Gitti et al. 2002) or they may be due to synchrotron emission from secondary $e^{\pm}$ injected during p−p collisions in the dense cooling-flow region (Pfrommer & Enßlin 2004).

3.3.3 Radio Relics

Radio Relics are usually interpreted in terms of the interaction of shocks with thermal or ghost plasma in the ICM. As discussed in Sec.1.5 mergers occur at supersonic relative speed, therefore implying the formation of shock waves. If a fraction of this energy can be converted at the shocks into non-thermal particles

through a first order Fermi process, then the ICM may be populated with a large amount of non-thermal particles. Shocks cannot be the responsible for the formation of RHs as the resulting non-thermal emission should have a filamentary structure tracing the position of the shock (Miniati et al. 2001), rather then the regular, symmetric structure observed in RHs. This is because, as discussed above, electrons cannot diffuse away from the re-acceleration site, due to their short cooling time. Two competing physical mechanisms to accelerate the radio-emitting electrons have been proposed: diffusive shock acceleration (Fermi I) (Ensslin et al. 1998; Röttiger et al. 1999) and adiabatic compression of fossil radio plasma by merger shock waves (Enßlin & Gopal-Krishna 2001; Enßlin & Brüggen 2002).

3.3.4 Hard X-ray emission

The origin of the hard X-ray (HXR) excess is still debated. As already anticipated in Sec.2.3.2 the HXR photons may be generated by IC scattering of relativistic electrons off the CMB photons (Rephaeli et al. 1999; Rephaeli & Gruber 2003; Fusco-Femiano et al. 1999, 2000, 2004; Völk & Atoyan 1999; Brunetti et al. 2001a; Petrosian 2001; Fujita & Sarazin 2001). Because electrons of similar energies are also responsible for the synchrotron−radio emission, by assuming that the synchrotron and IC emission are co-spatial, from the ratio of the HXR and radio flux it is possible to estimate the ICM magnetic field (see also Sec.2.3.2). The strength of the magnetic field inferred from the IC method are much smaller than those inferred from the interpretation of RMs. This discrepancy can be mitigated in the presence of a break in the spectrum of the emitting electrons and by considering a profile of the magnetic field strength which decreases with distance from the cluster center: in this case the bulk of the radio emission comes from the cluster central regions while that of the IC emission comes from the external regions (Brunetti et al. 2001a; Brunetti 2003, 2004; Petrosian 2001; Colafrancesco et al. 2005). The uncertainties in the IC modelling and those in the interpretation of the RM data (Newman et al. 2002) leave the magnetic field discrepancy still an open issue.

IC emission in the hard X-rays has been discussed in the framework of the re-acceleration model in which case present radio and hard X-ray data may be successfully reproduced (Sect. 3.4). On the other hand, at least for the Coma cluster, in the case of a secondary origin of the emitting electrons it is not possible

to reproduce at the same time the radio flux of the RH (in terms of synchrotron emission) and the HXR data (in terms of IC emission) without exceeding the EGRET gamma ray upper limit (Blasi & Colafrancesco 1999) and thus the HXR excess cannot be of IC origin.

Alternative explanations of the HXR excess have also been proposed. One possibility is non-thermal bremsstrahlung radiation (Enßlin et al. 1999; Blasi 2000; Dogiel 2000; Sarazin & Kempner 2000). However, this is an extremely inefficient process and would require an input in energy which will approximately double the ICM temperature every $\approx 10^8$ yr so that it can apply only in the case that the HXR emission is short living, $< 3 \times 10^7$ yr (Petrosian 2001).

An additional proposed explanation is related to the possibility that Ultra High Energy (UHE) protons ($E \sim 10^{18} - 10^{19}$ eV) are accelerated in the clusters by strong accretion shocks. Such protons interact with the CMB photons and can produce very high energy electron-positron pairs, which then radiate synchrotron and IC emission, with the synchrotron radiation peaking at hard X-rays (Inoue et al. 2005). The emission should spatially trace the morphology of the accretion shock. This model predicts the bulk of the radiation at TeV energy, and thus may eventually be tested by future Cherenkov telescopes.

3.3.5 Gamma ray emission

At present no cluster of galaxies has been detected in gamma rays (Reimer et al. 2003). However, as already discussed, it is expected that the bulk of cosmic rays accelerated within the cluster volume would be confined there for cosmological times (*e.g.,* Berezinsky et al. 1997; see also Sec.3.1.3), thereby enhancing the possibility of inelastic proton-proton collisions and consequent gamma ray production through the decay of neutral pions (*e.g.,* Enßlin et al. 1997; Blasi & Colafrancesco 1999; Blasi 1999; Atoyan & Völk 2000; Pfrommer & Enßlin 2004; Miniati 2003, Blasi et al. 2007). In such a case radio emission at some level should be produced by secondary electrons and this, under the assumption that the observed RH are not of secondary origin, can be used to impose limits on the amount of hadronic cosmic rays in the ICM, and therefore on the flux of gamma rays due to π^0 decay that may be expected (Reimer et al. 2004). Current EGRET-limits on gamma rays suggest that not more than $\sim 10 \div 30\%$ of the cluster thermal energy may be in form of relativistic particles

(Colafrancesco & Blasi 1998; Reimer et al. 2004; Pfrommer & Enßlin 2004), while future observations with GLAST will put more stringent limits (or detect a number of clusters) in the energy range 100 MeV–10 GeV. In addition, in Loeb & Waxman (2000) it was recognized that large scale shocks associated with structure formation, merger and accretion shocks, may accelerate electrons to TeV energies, implying that high energy emission would occur due IC scattering of these electrons off the CMB photons. In this case the detectability of the gamma ray signal depends on the strength of the shocks, only strong shocks can accelerate particles with spectra hard enough to result in an appreciable gamma ray emission. For instance Gabici & Blasi (2004) assumed a constant efficiency of electron acceleration of 5% and found that ~ 50 galaxy clusters should be detected by GLAST. It is worth stressing that the electrons accelerated according to this recipe provide a negligible contribution to radio and HXR emissions.

Another channel for the production of gamma rays in the ICM is related to the possibility that the UHE protons ($E > 10^{18}$ eV) may be injected in the ICM by cluster accretion shocks, and, as discussed for the HXR emission, these could interact with the CMB photons, producing electron-positron pairs which produce TeV gamma ray emission via IC scattering with the CMB photons (Inoue et al. 2005). However the resulting gamma ray flux is extremely uncertain due also to the absence of an efficient confinement of cosmic rays up to such high energies.

3.4 The re-acceleration scenario

It is believed by several authors that the bulk of present-day radio data requires the presence of particle turbulent-acceleration in the ICM (see reviews by Brunetti 2003, 2004; Petrosian 2003; Blasi 2004; Hwang 2004; Feretti 2005; Dolag et al. 2005b).

This PhD work is based on the re-acceleration scenario. According to this scenario a fraction of the energy dissipated during cluster-cluster mergers is channeled into MHD turbulence and this turbulence may re-accelerate a relic population of relativistic particles (*e.g.,* Brunetti et al. 2001a; Petrosian 2001) or secondary particles (Brunetti & Blasi 2005). The synchrotron and IC emission from the re-accelerated electrons give rise to the RH and HXR, respectively, whereas in the framework of this scenario gamma ray emission may also be produced by π^0-decay and IC emission from the secondary $e^{\pm}$ produced during p$-$p collisions of

high energy CR protons with thermal protons (Brunetti & Blasi 2005).

Although the physics of particle acceleration is a challenging problem and the model details are difficult to test, it should be stressed that the re-acceleration model clearly predicts simple properties of RHs which are almost independent of the details of the adopted physics:

- in these models, the accelerated electrons have a maximum Lorentz factor γ_{max} below a few times 10^4, and this produces a high frequency cut-off in the synchrotron spectral distribution (Schlickeiser et al. 1987; Brunetti et al. 2001a; Petrosian 2001) which provides a unique possibility to explain the steepening of the integrated synchrotron spectrum claimed in several RHs (*e.g.,* Thierbach et al. 2003; Feretti 2005) and the complex behavior observed in the spectral index maps of RHs (Feretti et al. 2004; Orrù et al. 2007);

- the maximum energy of the radiating electrons is determined by the balance between the energy gains (re–acceleration processes) and synchrotron and inverse Compton losses and accordingly, the detection of a RHs critically depends on cut–off frequency which should be sufficiently larger than the observing frequency. As a consequence, there is a threshold in the efficiency which should be overcome by the re–acceleration processes in order to accelerate the electrons at the energies necessary to produce radio emission at the observed frequency in the clusters' magnetic fields.

- a relatively thigh connection of RHs with cluster mergers is a very "natural" expectation of these models as turbulence is assumed to be injected during cluster mergers in Mpc^3 regions (*e.g.,* Tribble 1993; Röttiger et al. 1997, Ricker & Sarazin 2001). As a matter of fact RHs are preferentially found in dynamically disturbed systems (*e.g.,* Buote 2001; Govoni et al. 2004).

- most importantly, RHs should be *transient phenomena* in dynamically disturbed clusters. The time scale of the RH phenomena comes from the combination of the time necessary for the cascading of the turbulence from cluster scales to the smaller scales relevant for particle acceleration, of the time–scale for dissipation of the turbulence and of the cluster–cluster crossing time. As a matter of fact, present observations suggest that indeed RHs are short living (≤ 1 Gyr; *e.g.,* Kuo et al. 2004).

In this Section we will discuss in some detail the physics of electron *re-acceleration model*. We will start illustrating the basic properties of the ICM turbulence and then we will explain the main channels of interaction of that turbulence with the relativistic particles in the ICM.

3.4.1 Turbulence in the ICM

Cluster mergers and accretion of matter at the virial radius may induce large–scale motions with $V_L \sim 1000$ km s^{-1} in massive clusters. Numerical simulations suggest that turbulence may store an appreciable fraction, 5–30%, of the thermal energy of the ICM (*e.g.,* Sunyaev et 2003; Dolag et al. 2005b; Vazza et al. 2006). Simulations of merging clusters provide an insight into the gas dynamics during a merger event (*e.g.,* Röttiger, Burns & Loken 1996; Röttiger et al. 1997; **?**): sub–clusters generate laminar bulk flows through the swept volume of the main clusters which inject turbulence via e.g. Kelvin–Helmholtz instabilities at the interface of the bulk flows and the primary cluster gas. The largest turbulent eddies decay into smaller and turbulent velocity fields and eventually develop a turbulent cascade.

Merger-turbulence in the ICM is expected to be a transient phenomena being mostly injected during the most massive mergers. However, since more frequent, minor mergers may also contribute to the injection of such turbulence, some minimum level of turbulence should be rather ubiquitous in the ICM (Cassano & Brunetti 2005, Chapt.5).

In spite of obvious observational challenges, indications of some level ($\approx$ 10–20% of the thermal energy) of turbulence in the ICM comes from gas–pressure maps in the X–rays (Schuecker et al. 2004), and also from the lack of resonant scattering from X–ray spectra (Churazov et al. 2004; Gastaldello & Molendi 2004).
Interestingly enough, also upper limits to the turbulent–energy content in the ICM were obtained in a few nearby galaxy clusters from kinematical arguments related to the properties of Hα and X–ray filaments (*e.g.,* Fabian et al. 2003; Crawford et al. 2005; Sun et al. 2006). Assuming that turbulence is driven at hundred–kpc scales the above upper limits actually can be used to place upper limits on the intensity of strong turbulence in the ICM (supersonic or trans–sonic turbulence).

Theoretically, a fluid becomes turbulent when the rate of viscous dissipation at the injection scale, L_o, is much smaller than the energy transfer rate, i.e. when the

Reynolds number is $Re = V_L L_o/\nu_K \gg 1$, where V_L is the injection velocity and ν_K is the kinetic fluid viscosity. Without considering the effect of magnetic fields the viscosity is given by $\nu_K \sim l_{mfp} v_i/3$ (v_i and l_{mfp} being the velocity of thermal ions and the ion–ion mean free path, respectively) and the Reynolds number in the ICM is given by (*e.g.,* Braginskii 1965):

$$Re \sim 52 \left(\frac{V_L}{1000\,\mathrm{km/s}}\right)\left(\frac{L_o}{300\,\mathrm{kpc}}\right)\left(\frac{n_{\mathrm{th}}}{10^{-3}\mathrm{cm}^{-3}}\right)\left(\frac{T}{8\,\mathrm{keV}}\right)^{-5/2}\left(\frac{\ln\Lambda}{40}\right) \tag{3.19}$$

where $\ln\Lambda$ is the Coulomb logarithm. This value for the Reynolds number would be formally just sufficient for initiating the developing of turbulence. However, the ICM is magnetized and in the presence of a magnetic field the Reynolds number may get extremely high (*e.g.,* Braginskii 1965). Turbulence injected in the ICM by merger events is super-Alfvénic turbulence (*i.e.,* the injection velocity $V_L \simeq 1000 - 1500$ km/s is greater than the Alfvén one $v_A = B/\sqrt{4\pi\rho} \sim 50 - 80$ km/s) and in this case the magnetic field lines are easily bended by the motion of turbulent eddies. Under these circumstances ion diffusion is driven by the bending of the field lines and the viscosity is expected to be suppressed implying that the effective Reynolds number in the ICM is much larger than that estimated in the unmagnetized case (Brunetti & Lazarian 2007). Additional mechanisms may affect the value of the particle mean free path in the ICM, for example plasma instabilities may reduce the effective mean free path and this should further increase the value of the Reynolds number (*e.g.,* Schekochihin et al. 2005, Lazarian & Beresnyak 2006).

It is believed that the magnetic field suppression of the viscosity in the ICM would allow turbulence cascade to reach the collisionless regime without being significantly dissipated by viscosity (*e.g.,* Brunetti & Lazarian 2007). When the frequency of the turbulent modes is larger then the ion–ion collision frequency starts the *collisionless regime* and the main source of turbulent dissipation is collisionless damping with particles in the ICM, *i.e.,* particle acceleration. In this case the time evolution of waves in the wavenumber space, $W_{\mathrm{k}}(t)$, is given by a kinetic equation which in the quasi linear regime reads (*e.g.,* Eilek 1979):

$$\frac{\partial W_{\mathrm{k}}(t)}{\partial t} = \frac{\partial}{\partial k}\left(D_{\mathrm{kk}}\frac{\partial W_{\mathrm{k}}(t)}{\partial k}\right) - \sum_{i=1}^{n}\Gamma^{\mathrm{i}}(k)W_{\mathrm{k}}(t) + I_{\mathrm{k}}(t) \tag{3.20}$$

The first term on the right hand describes the wave–wave interaction (here we take a one-dimensional form of the wave-wave coefficient; see Miller et al. 1996; Brunetti & Lazarian 2007), with diffusion coefficient $D_{\rm kk} = k^2/\tau_s$ (with τ_s the spectral energy transfer time). The second term in Eq.(3.20) describes the damping with the relativistic and thermal particles in the ICM, while $I_{\rm k}(t)$ accounts for the turbulent injection term.

3.4.2 Stochastic particle acceleration

Re–acceleration models are basically models of second order Fermi acceleration, in which charged particles are accelerated stochastically due to random interaction of the particles with the perturbations (waves) in the structure of the magnetic field. The scenarios of particle acceleration are based on particle interaction with either large scale compressible (magnetosonic) modes or small scale Alfv́en modes.

Alfv́en waves

Alfvén waves are circular polarized, transverse waves which propagate along or at an angle to the magnetic field. They look like transverse oscillation of the field lines. In the MHD approach the dispersion relation for Alfvén waves with a frequency ω and wavenumber projected along the magnetic field $k_{\|}$ is :$\omega \simeq |k_{\|}|v_{\rm A}$, where $v_{\rm A} = B/(4\pi\rho)^{1/2}$ is the Alfvén speed.

Alfvén waves efficiently accelerate relativistic particles via resonant interaction. The condition for resonance between a wave of frequency ω and wavenumber projected along the magnetic field $k_{\|}$, and a particle of type α with energy E_α and projected velocity $v_{\|} = v\mu$ is (Melrose 1968; Eilek 1979):

$$\omega - n\frac{\Omega_\alpha}{\gamma} - k_{\|}v_{\|} = 0 \qquad (3.21)$$

where Ω_α/γ is the relativistic gyrofrequency. The most important resonance for electron interaction with Alfvén waves is the $n = -1$ resonance, while for protons $n = +1$ is the most important (Melrose 1968). Combining the dispersion relation of the waves with the resonant condition, Eq. (3.21), one can derive the resonant wavenumber, k_{res}, for a given momentum ($p = mv\gamma$) and pitch angle cosine (μ) of the particles:

$$k_{res} \sim |k_{\parallel}| = \frac{\Omega m}{p} \frac{1}{\left(\mu \pm \frac{v_{\rm A}}{v}\right)}, \tag{3.22}$$

where the upper and lower signs refer to protons and electrons respectively. We can see that there is a correspondence between the particle energy and the wavelength with which it can resonate. The particles does not "see" all turbulent wavenumber, but only those above:

$$k_{min} = \frac{\Omega m}{p} \frac{1}{\left(1 \pm \frac{v_{\rm A}}{v}\right)} \tag{3.23}$$

and below k_{max}, which is given by the largest wavenumber of the Alfvén waves, limited by the fact that the frequency of the waves cannot exceed the proton cyclotron frequency, namely $\omega < \Omega_p$. It follows that $k_{max} \sim \Omega_p / v_A$ or $k_{max} \sim \Omega_p / v_M$, v_M being the magnetosonic velocity. *We stress that these waves coupled with relativistic electrons (and protons) at very small scales $l \sim 2\pi p/(\Omega m)$ and thus the cascading process should be very efficient if the turbulence injection process happens at large scales, or these waves should be injected at these small resonant scales.*

In an isotropic distribution of waves and particles, the particle diffusion coefficient in momentum space is given by (Eilek & Henriksen 1984):

$$D_{\rm pp}(p,t) = \frac{2\pi^2 e^2 v_{\rm A}^2}{c^3} \int_{k_{min}}^{k_{max}} \frac{W_k(t)}{k} \Big[1 - \Big(\frac{v_{\rm A}}{c} \mp \frac{\Omega m}{pk}\Big)^2\Big] dk, \tag{3.24}$$

In Chapt.4 we will present an application of particle acceleration by Alfvén waves in galaxy clusters.

Magnetosonic waves

Magnetosonic (MS) waves are compressive waves which propagate across or at an angle to the magnetic field. The MHD dispersion relation of these modes is given by $\omega = v_M k$, where the phase velocity v_M is given by (*e.g.,* Krall & Trivelpiece 1973) :

$$v_{\rm M}^2 = \frac{c_s^2 + v_A^2}{2} \left\{ 1 \pm \sqrt{1 - 4 \left(\frac{k_{\parallel}}{k}\right)^2 \frac{c_s^2 v_A^2}{(c_s^2 + v_A^2)^2}} \right\} \tag{3.25}$$

The fast MS waves are those with higher frequency, corresponding to the (+) expression in Eq.3.25, while the slow mode are those corresponding to the (−)

expression in Eq.3.25. In the ICM where $c_s >> v_A$ the phase velocity of fast modes is the sound speed, while slow modes have the dispersion relation of the Alfvén modes.

Large scale MS waves can interact with particle through the $n = 0$ resonance (Melrose 1968; Eilek 1979), $\omega - k_{\parallel} v_{\parallel} = 0$ which is called transit-time damping (TTD; *e.g.,* Eilek 1979; Schlickeiser & Miller 1998). This resonance depends only on pitch-angle, so that all wavenumbers can interact with a given particle energy. An important aspect of this interaction is that it is effective only in the case of isotropization of particle momenta during the acceleration. This is because the rate of energy gain for a given particle depend on the component of the momentum perpendicular to the magnetic field, but the energy gain goes all to the component parallel to the field (Achterberg 1981). This would cause an increasing degree of anisotropy of the particle distribution and thus the deriving acceleration would become less and less efficient with time. However, in general, there are several processes in the ICM which can provide particle-pitch angle scattering.

In this PhD thesis we will widely use the compressible modes (fast modes in the MHD regime) (see Sec.3.4.2), which *do not require an injection process at small spatial scales of the modes* (as in the case of Alfvén modes), *since it is expected that a significant fraction of the ICM turbulence* (given the high β plasma of the ICM) *is in the form of large scale compressible isotropic modes* (*e.g.,* Brunetti & Lazarian 2007).

Chapter 4

Alfv́enic re-acceleration of relativistic particles in galaxy clusters

As discussed in the previous Chapter, re–acceleration of a population of relic electrons by turbulence powered by major mergers is suitable to explain the very large scale of the observed radio emission and is also a promising possibility to account for the fine radio structure of the diffuse emission (Brunetti et al. 2001a; Petrosian 2001; Brunetti 2004). Alfvén waves are likely to be able to transfer most of their energy into relativistic particles and they have received much attention in the last few years. In this framework for instance Ohno et al. (2002) developed a time-independent model for the acceleration of the relativistic electrons expected in radio halos through magnetic turbulence. The authors studied the acceleration of continuously injected relativistic electrons by Alfvén waves with a power law spectrum and applied this model to the case of the radio halo in the Coma cluster. More recently, Fujita et al. (2003) studied the effect of Alfvénic acceleration of relativistic electrons in clusters of galaxies. These authors invoked the *Lighthill* theory to establish a connection between the large scale fluid turbulence and the radiated MHD waves. The electron and MHD-wave spectra adopted by Fujita et al.(2003) are obtained via a self-similar approach by requiring that the spectra are described by two power laws. These approaches have two intrinsic limitations: the first one is in the assumption that all spectra are time-independent and that the turbulence spectrum is a power law. The second is that they neglect, the effect of relativistic hadrons in the ICM: it is well known that the interaction of the Alfvén waves with relativistic particles is, in general, more effective for protons

than for electrons (e.g., Eilek 1979). It is also well known that the presence of a significant energy budget in the form of relativistic particles can significantly affect the spectrum of the Alfvén waves through damping. In fact, this damping occurs even on the thermal protons in the ICM, another effect which was never included in previous calculations.

The news about the calculations presented in this Chapter is that Alfvénic acceleration is studied in the most general situation in which relativistic electrons and positrons, thermal and relativistic protons exist in the ICM. In these calculations the interaction of all components with the waves, as well as the turbulent cascading and damping process of Alfvén waves, will be treated in a fully time-dependent way in order to calculate the spectra of electrons, positrons, protons and waves at any fixed time. These calculations are published in Brunetti, Blasi, Cassano & Gabici (2004) and in this Chapter we report the main results from this paper.

4.1 Preliminary consideration on cosmic ray electrons and protons in the ICM

The first ingredient in our calculations is given by cosmic ray (CR) electrons and protons. In this Section we report some preliminary considerations on the properties of these CR before the re-acceleration process in the ICM is started.

4.1.1 The need for seed relativistic electrons

As seen in Sec.3.4.2, Alfvén waves may accelerate particles via resonance interection. In Sec.3.4.2 we give the resonance condition (Eq.3.21) and the expression for the *diffusion coefficient in momentum space* $D_{pp}(p,t)$ (Eq.3.24).

The momentum of electrons and protons which can resonate with waves of a given wavenumber k depends on the pitch angle cosine μ (see Eq.3.22). This resonant momentum can be written as:

$$p = \frac{\Omega_e m_e}{k} \frac{1}{\mu - \frac{v_A}{v}}. \tag{4.1}$$

The minimum momentum of the electrons for which resonance with waves of a given wavenumber k can occur is obtained from Eq.4.1 substituting $v = P/m_e$ and taking $\mu \sim 1$:

$$p_{min} = \frac{m_e}{k}\Big(\Omega_e + v_A k\Big), \tag{4.2}$$

Since the wavenumber of Alfvén waves in a plasma is limited by $\omega < \Omega_p$, from Eq. (4.2), one has that the minimum momentum of the electrons which can resonate with Alfvén waves is:

$$p_{min} = p_{th}\frac{v_A}{v_{th}}\Big(\frac{m_p}{m_e} + 1\Big), \tag{4.3}$$

which, in general, gives $p_{min} >> p_{th}$, $p_{th} = m_e v_{th}$ being the momentum of the thermal electrons. *It follows the well known result that thermal electrons cannot resonate with Alfvén waves* (Hamilton & Petrosian 1992, and references therein). This important limitation of Alfvén waves as particle accelerators *forces us to consider the situation in which a relic population of relativistic electrons exists in the ICM.*

The situation is different for protons. In fact, in this case, the minimum momentum of the protons which may resonate with waves of wavenumber k is given by:

$$p_{min} = p_{th}\frac{v_A}{v_{th}}\Big(\frac{\Omega_p}{\omega} - 1\Big). \tag{4.4}$$

Since $\omega < \Omega_p$, this basically means that thermal protons can efficiently resonate with Alfvén waves (Hamilton & Petrosian 1992).

4.1.2 On the initial spectrum of seed relativistic electrons and protons

After having pointed out that a population of seed relativistic electrons is necessary to have efficient Alfvénic re-acceleration in the ICM, in this Section we briefly discuss the shape of the spectrum of the relic population and of the CR protons accumulated in the ICM. As shown in the previous Chapter several mechanisms can inject electrons and protons in the ICM, and the injection spectrum from a single mechanism can be assumed to be a power-law in momentum, $Q(p) \propto p^{-\delta}$.

As seen in Sec.3.1.2, once injected the relativistic electrons lose energy via Coulomb collisions, IC and synchrotron emission (Eq.3.1, 3.2 respectively). The evolution of a population of relativistic electrons subject *only to energy losses* is obtained by solving the so-called Fokker-Planck equation (Eq.3.15) *neglecting the acceleration terms.* As an example in Fig.4.1 we report the spectra at z=0 of

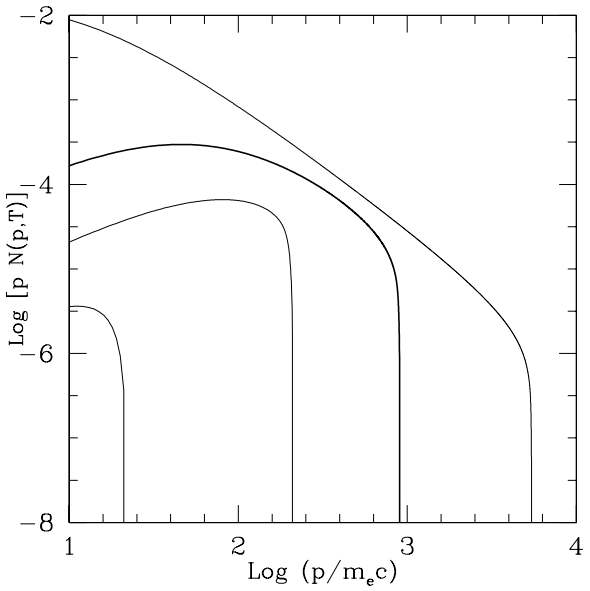

Figure 4.1: Electron spectrum at $z = 0$ injected as a single burst at z_i =0.01, 0.1, 0.3, 0.5 (from right to left) adopting injection spectrum $Q(p) \propto p^{-2.5}$ and maximum Lorentz factor $\gamma_{max} = 10^4$. The calculations are carried out for $n_{th} = 10^{-3}\mathrm{cm}^{-3}$ and $B = 1\mu$G.

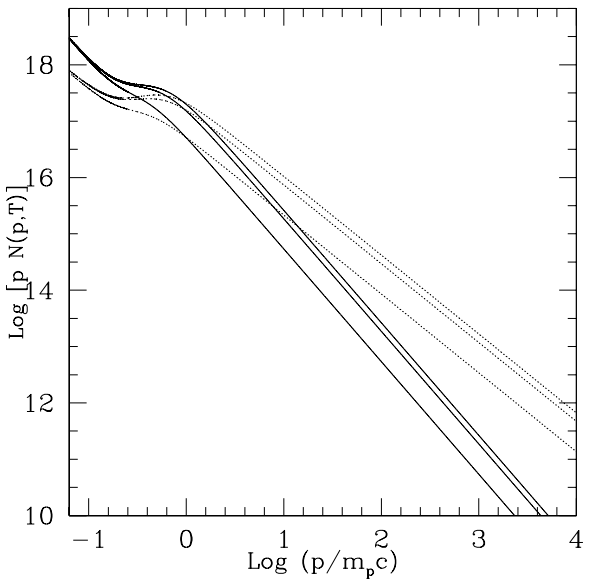

Figure 4.2: Present-epoch spectrum of the cosmic ray protons continuously injected (with $p > 0.1\, m_p c$) in the ICM starting from z_i. The spectra are plotted for s =2.4 (dotted lines) and 3.0 (solid lines) and for z_i =0.1, 0.5, 1 (from bottom to top). Calculations are carried out assuming $n_{th} = 10^{-3}\mathrm{cm}^{-3}$.

electrons injected as a single burst at redshift z=0.5, 0.3, 0.1, 0.01 with an initial power law momentum distribution $p^{-2.5}$ and with maximum Lorentz factor $\gamma = 10^4$; it is evident that most electrons injected at $z \gtrsim 0.2$ get thermalized.

As discussed in the previous Chapter, relativistic protons are confined for cosmological times in the cluster volume and, given that the loss time due to inelastic collisions with thermal protons is greater than the Hubble time, their spectrum is unaffected by energy losses. On the contrary the spectrum at mildly and sub-relativistic energies can be significantly modified by Coulomb interactions (Eq.3.5, Sec.3.1.2). As for the relativistic electrons, the evolution of the proton spectra can be calculated by solving the Fokker-Planck equation (Eq.3.16) neglecting the acceleration terms. In Fig.4.2 we report the present day spectrum of protons if a time independent continuous injection $Q(p) \propto p^{-s}$ is assumed (for different values of the slope s and of the redshift at which the injection starts); spectra show a large modification at low energy due to Coulomb losses.

4.2 From fluid turbulence to Alfvén waves: the *Lighthill* mechanism

In this Section we discuss the basic physics of the second main ingredient of our calculations: the Alfvén waves.

4.2.1 Injection

We assume that fluid turbulence is present in the cluster volume with a power spectrum

$$W_{\rm f}(x_{\rm f}) = W_{\rm f}^{\rm o} x_{\rm f}^{-{\rm m}} \tag{4.5}$$

in the range $x_{\rm f}^{\rm min} < x_{\rm f} < x_{\rm f}^{\rm max}$, where $x_{\rm f}^{\rm min}$ is the wavenumber corresponding to the maximum scale of injection of the turbulence and the maximum wavenumber is that at which the effect of fluid viscosity starts to be important and it is of the order of $x_{\rm f}^{\rm max} \sim x_{\rm f}^{\rm min}(Re)^{-3/4}$ (*e.g.,* Landau & Lifshitz 1959), Re being the Reynolds' number. Since most of the energy of fluid turbulence resides in the largest scale, the total energy density of the fluid turbulence is given by $\mathcal{E}_t \sim \rho v_f^2$, where ρ is the fluid density and v_f is the turbulent velocity of the largest scale $\sim 2\pi/x_{\rm f}^{\rm min}$.
For Kolmogorov turbulence one has m = 5/3, while for Kraichnan turbulence (Kraichnan 1965) one has m = 3/2.

Here we investigate the connection between the fluid turbulence that we start with and the MHD waves that we use as particle accelerators. Fluid turbulence can radiate MHD modes (Kato 1968) via the Lighthill process. A fluid eddy may be thought of as radiating MHD waves in the mode j at a wavenumber $k = (v_{\rm f}(x)/v_j)x_{\rm f}$, where v_j is the velocity of the j–mode wave. The MHD modes are expected to be driven only for $x > x_{\rm T}$, $x_{\rm T}$ being the wavenumber at which the transition from large–scale ordered turbulence to small–scale disordered turbulence occurs. Following previous works in the literature (Eilek & Henriksen 1984; Fujita et al. 2003), we adopt the Taylor wavenumber as an estimate of this transition scale, namely:

$$l_{\rm T} = \frac{2\pi}{x_{\rm T}} \sim \Big[< v_{\rm f,i}^2 > / < \Big(\frac{\partial v_{{\rm f},i}}{\partial x_i}\Big)^2 > \Big]^{1/2} \sim l_o(15/Re)^{1/2}, \tag{4.6}$$

where the Reynolds number is given by $Re = l_o v_{\rm f}/\nu_{\rm K}$, and $\nu_{\rm K}$ is the kinetic viscosity. The energy rate radiated via the *Lighthill* mechanism into waves of mode j and wavenumber k is given by (*e.g.,* Eilek & Henriksen 1984):

$$I_j(k) = I_{j,{\rm o}}\Big(\frac{k}{x_{\rm T}}\Big)^{-y_j}, \tag{4.7}$$

It can be shown that the injection rate of Alfvén waves is given by (see Brunetti et al. 2004, for details):

$$I_k \simeq 2\Big|\frac{3-2m}{3-m}\Big|\rho v_{\rm A}^3\Big(\frac{v_{\rm f}^2}{v_{\rm A}^2 R}\Big)^{\frac{3}{3-m}} k^{-3\frac{m-1}{3-m}}. \tag{4.8}$$

i.e., $I_k \propto k^{-3/2}$ for a Kolmogorov spectrum of fluid turbulence ($m = 5/3$) and $I_k \propto k^{-1}$ for a Kraichnan spectrum ($m = 3/2$).

4.2.2 Evolution of Alfvénic turbulence

In our calculations we assume for simplicity that Alfvén waves propagate isotropically in the cluster volume and thus $k \simeq |k_\parallel|$. The spectrum of Alfvén waves driven by the fluid turbulence evolves as a result of wave–wave and wave–particle coupling. In particular, the wave–particle involves the thermal and relativistic particles. The combination of these processes produces a modified, time–dependent spectrum of Alfvén waves, $W_{\rm k}(t)$, which can be calculated by solving the continuity equation (Eq.3.20) in which one consider the wave–wave interaction and the damping with the relativistic and thermal particles in the ICM.

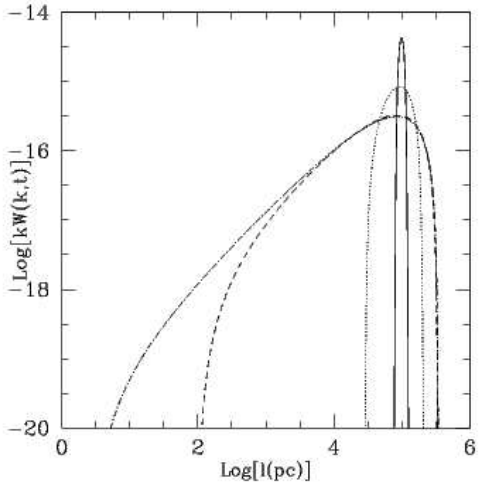

Figure 4.3: Time evolution of the spectrum of Alfvén waves injected in a single burst at a given scale. The spectra are plotted for 10^{14} (solid line), 5×10^{15} (dotted line), 3×10^{16} (dashed line), and 3.2×10^{16} s (dot-dashed line) after the injection event. In the calculations, a Kolmogorov diffusion coefficient is adopted. The temperature of the gas, the magnetic field and the gas density are $T = 10^8$K, $B = 1\mu$G, and $n_{th} = 10^{-4}$cm^{-3} respectively.

Turbulent cascade

The turbulent cascading process is described by the kinetic equation (Eq.3.20) neglecting the terms which describe damping processes and wave injection. The cascade timescale at a given wavelength is $\tau_{\rm kk} \sim k^2/D_{\rm kk}$. By adopting the expression for the diffusion coefficient, $D_{\rm kk}$, in the Kolmogorov and Kraichnan regime (see Brunetti et al. 2004), one has:

$$\tau_{\rm kk}(l) \simeq \frac{2\times10^8{\rm yr}}{B_{\mu G}}\Big(\frac{l_{100}}{\rm kpc}\Big)\Big(\frac{n_{\rm th}}{10^{-3}}\Big)^{\frac{1}{2}} \begin{cases} \sqrt{2}\Big(\frac{\delta B_{>k}}{B}\Big)^{-1} \\ ({\rm Kolmogorov}) \\ \\ 2\Big(\frac{\delta B_{>k}}{B}\Big)^{-2} \\ ({\rm Kraichnan}) \end{cases} \tag{4.9}$$

where we define $\delta B_{>k} \sim \sqrt{8\pi k W_k}$. It is worth noticing that the cascade timescale in the Kolmogorov regime does not depend on the value of the magnetic field strength. We also notice that $\tau_{\rm kk}$ is smaller in low density regions. Most importantly, it can be show that, for typical conditions of the ICM, the wave–wave time scale below 1 pc, namely on the scale relevant for wave–particle interaction, is considerably shorter

than 10^7yr.

As an example in Fig. 4.3 we plot the time evolution of the spectrum of Alfvén waves injected at a given scale in the Kolmogorov phenomenology (see caption for details); the broadening of the waves distribution at scales larger than the injection scale is due to stochastic wave-wave diffusion.

Damping processes

In the case of nearly parallel wave propagation ($k_\perp << m\Omega/p$, $k \simeq |k_\parallel|$) and isotropic distribution of particles of type α, the cyclotron damping rate for Alfvén waves is given by (Melrose 1968):

$$\Gamma^\alpha_{\rm k}(t) = -\frac{4\pi^3 e^2 v_{\rm A}^2}{kc^2}\int_{p_{\rm min}}^{p_{\rm max}} p^2(1-\mu_\alpha^2)\frac{\partial f_\alpha(p,t)}{\partial p}dp = \frac{\pi^2 e^2 v_{\rm A}^2}{kc^2}\int_{p_{\rm min}}^{p_{\rm max}}(1-\mu_\alpha^2)\left(2\frac{N_\alpha(p,t)}{p} - \frac{\partial N_\alpha(p,t)}{\partial p}\right)dp, \quad (4.10)$$

where, for relativistic particles, one has :

$$\mu_\alpha^{\rm rel} = \frac{v_{\rm A}}{c} \pm \frac{\Omega_\alpha {\rm m}_\alpha}{pk}, \quad (4.11)$$

while for sub–relativistic particles:

$$\mu_\alpha^{\rm th} = \frac{v_{\rm A}{\rm m}_\alpha}{p} \pm \frac{\Omega_\alpha {\rm m}_\alpha}{pk}. \quad (4.12)$$

Here the upper and lower signs are for negative and positive charged particles respectively.

Alfvén waves can be damped in their interaction with thermal and relativistic protons and relativistic electrons, so that the global damping time can be written as the sum of three different contributions:

$$\tau_{\rm d} = \Big(\sum_{j=1}^{3}\Gamma_k^j\Big)^{-1}. \quad (4.13)$$

We refer the reader to Brunetti et al. (2004) for the detailed expressions of the damping terms obtained from Eq.4.10. For typical conditions in the ICM, the damping time on the thermal proton gas is $< 10^5$sec (but the process is efficient only for $k/k_{\rm max} > 0.1$). The damping time on the relativistic component (especially protons) is usually $> 10^8$sec.

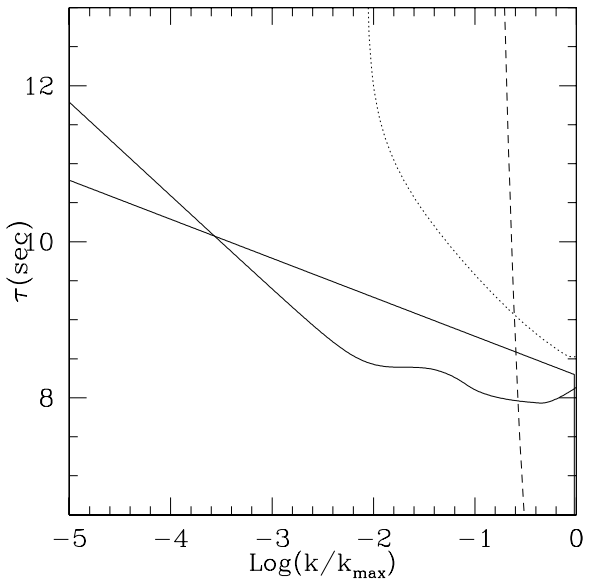

Figure 4.4: Comparison between cascade-time (solid straight line) and damping time-scales on the thermal gas (dashed line), on relativistic electrons (dotted line), and on relativistic protons (solid line). Calculations are carried out assuming a Kolmogorov diffusion coefficient, and adopting $T = 10^8$K, $n_{th} = 10^{-3}$cm^{-3}, and $d(\delta B)^2/dt = 3.3\times10^{-15}(\mu\mathrm{G})^2/\mathrm{s}$.

Damping versus Cascading

When the damping time-scale is shorter than the cascading time-scale a break is established in the spectrum of the waves and the cascade at smaller scales is suppressed.

The time scale for the development of the wave-wave cascade depends on the wave-wave diffusion coefficient, D_{kk}, and thus on the energy density of the waves. Given a spectrum of injection of waves per unit time, I_k, one simple possibility to estimate the cascade time scale, and thus to compare it with the time scale of the damping processes, is to use the spectrum of the waves under stationary conditions and without damping processes, namely

$$W_k \sim \frac{1}{k} \begin{cases} \left(\frac{B^2}{4\pi}\frac{I_k^2}{v_A^2}\right)^{1/3}, \text{ (Kolmogorov)} \\ \\ \left(\frac{B^2}{4\pi}\frac{I_k}{v_A}\right)^{1/2}, \text{ (Kraichnan)} \end{cases} \tag{4.14}$$

The wave-wave time scale is therefore given by :

$$\tau_s = \frac{k^2}{D_{kk}} \sim \frac{1}{k} \begin{cases} \left(\frac{B^2}{4\pi}\right)^{1/3} / \left(v_A^{2/3} I_k^{1/3}\right), \text{ (Kolmogorov)} \\ \left(\frac{B^2}{4\pi}\right)^{1/2} / \left(v_A^{1/2} I_k^{1/2}\right), \text{ (Kraichnan)} \end{cases} \tag{4.15}$$

A comparison between the time scales of the damping processes and of the wave-wave cascade is given in Fig.4.4 for typical values of the parameters (see caption). We assume that the energy in relativistic protons and electrons is respectively ~ 1 and 0.1 per cent that of the total thermal energy. Protons are injected starting from $z = 1$ with a spectrum $s = 2.2$. Fig.4.4 shows that the time scale due to the damping with the thermal pool is considerably shorter than the cascade time scale for $k/k_{max} >> 0.1$ so that a break or a cutoff in the spectrum of the waves is expected at large wavenumbers. However, the most important result illustrated in Fig.4.4 is that, if a relatively large number of relativistic protons is present in the ICM, the resulting damping time scale can become comparable with or shorter than the wave-wave cascade time scale. This means that, at the corresponding wavenumbers, the spectrum of the waves is modified by the effect of the dampings and therefore that a power law approximation for the spectrum of the MHD waves cannot be achieved. We also note that the effect of the damping due to relativistic protons is particularly evident at those wavenumbers that can exhibit a resonance with the bulk of the relativistic electrons in the ICM (those with $\gamma \sim 200 - 1000$) and thus that this effect may have important consequences for the acceleration of the relativistic electrons.

Thus the damping of the relativistic protons on the Alfvén waves modifies the spectrum of the waves and therefore it may indirectly affect the acceleration of electrons. The damping of the waves at a given wavenumber basically depends on the number of protons with momentum that can resonate with such waves. At fixed number of relativistic protons with supposedly a power law spectrum $N(p) \propto p^{-s}$, the damping rate at wavenumbers corresponding to $p >> p_{\rm low}$ ($p_{\rm low}$ being the minimum momentum in the proton spectrum) decreases with increasing s.

4.3 Quasi Stationary Solutions

Given the injection rate of the Alfvén waves in the ICM, the evolution of the spectra of electrons, protons and waves can be calculated by coupling the relative Fokker-

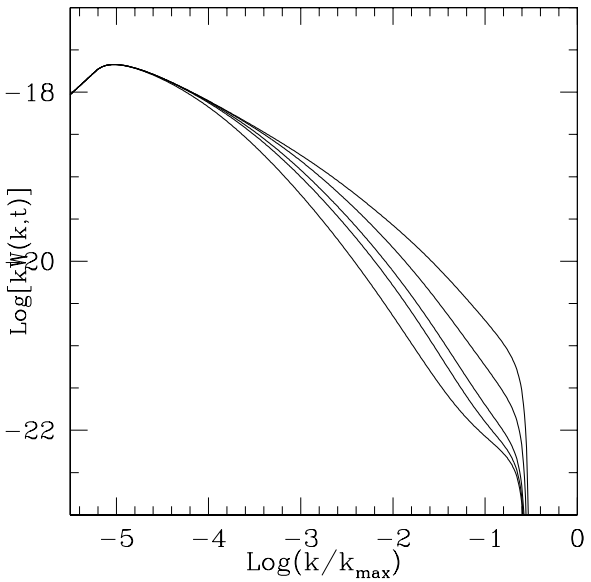

Figure 4.5: Temporal evolution of the spectrum of the Alfvén waves at times 2×10^{15}, 5×10^{15}, 8×10^{15}, 10^{16}, and 1.5×10^{16}sec after the beginning of the acceleration (from top to bottom). The calculations are carried out for a Kolmogorov spectrum of the fluid turbulence (i.e., $y_j = 3/2$), a Kolmogorov diffusion coefficient $d(\delta B)^2/dt = 3.3 \times 10^{-15}(\mu\mathrm{G})^2/\mathrm{s}$, $T = 10^8$K, $n_{th} = 10^{-3}\mathrm{cm}^{-3}$, $B = 0.5\mu$G, $\mathcal{E}_e = 0.001 \times \mathcal{E}_{th}$, $\mathcal{E}_p = 0.005 \times \mathcal{E}_{th}$, $s = 3.2$, $z_i = 1.0$ and $p_{inj} > 0.1\, m_p c$. The Taylor scale is at $k \sim 10^{-5} k_{\max}$.

Planck and kinetic equations, Eqs. 3.15 (with $Q_e = 0$), 3.16 and 3.20.

The spectra of electrons, protons and waves, as discussed above, result from a coupling between all these components: the spectrum of the waves develops in time due to the turbulent cascade until damping becomes efficient and particle acceleration occurs. It is worth noticing that the time scales for the processes of damping and cascading are quite different from those related to particle losses and transport mechanisms. While the wave spectrum develops over $\sim 10^7$ sec, particle acceleration occurs on time scales of $\geq 10^{14}$sec, and we are interested in following the particle evolution for a typical time of $\geq 10^{15}$sec. Based on these considerations we shall use a *quasi stationary approach*, in which it is assumed that at each time-step the spectrum of the waves approaches a stationary solution and that this solution changes with time due to the evolution of the spectrum of the accelerated electrons and protons.

Intermittent injection of turbulence in the ICM may occur on time–scales $\geq 10^7 - 10^8$ yrs which are much longer than the time–scales of damping and cascading,

and thus the quasi–stationary approach discussed above remains applicable.

In the following we will consider the case in which the turbulent energy is always smaller then the thermal energy and thus we can safely assume that the thermal distribution of protons in the ICM is not appreciably affected by the interaction with the waves.

4.3.1 The spectrum of Alfvén Waves

The shape of the spectrum of waves at any time is determined by the damping of these waves, mainly on protons. The proton spectrum in turn changes because of acceleration, and backreacts upon the spectrum of waves: *this implies that even for a time-independent rate of continuous injection of waves, the strength of the damping rates and the spectrum of the MHD waves are expected to change with time.*

In particular, we found that the damping rate increases with time, as a consequence of the fact that most of the energy injected in MHD waves is channelled into relativistic protons.

A relevant example of the time evolution of the spectrum of waves is illustrated in Fig. 4.5: as expected, the energy associated with MHD waves which contribute to the acceleration of the bulk of the relativistic electrons ($k/k_{max} \sim 10^{-3} - 10^{-1}$) decreases with time. In addition, we note that the spectrum is not a simple power law; the spectrum has a low-k cutoff due to the maximum injection scale, close to the Taylor scale; it has also a high-k cutoff generated by the damping with the thermal particles.

4.3.2 Electron acceleration

The initial stage of reacceleration of relic relativistic electrons (i.e. $\gamma \sim 100 - 1000$ electrons) is mainly affected by the competition between Coulomb losses and acceleration due to the Alfvén waves, while later stages of further acceleration to the highest allowed energies are limited by radiative losses.

We found that the time scale for electron acceleration depends on proton spectra injected in the ICM. In particular, for steep proton spectra (with a fixed total number of protons), the electron acceleration is more efficient because less energy gets channelled into the proton component. In general, hard proton spectra make the acceleration of electrons to Lorentz factors $\gamma > 10^3$ relatively difficult (see Fig.4.6).

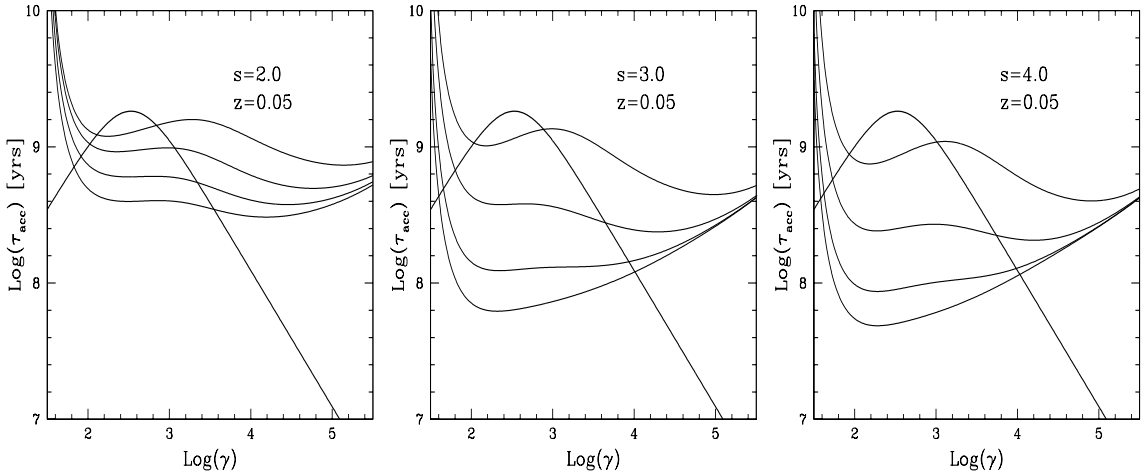

Figure 4.6: Acceleration time–scale (thin lines) and time–scale for energy losses (thick lines) for relativistic electrons as a function of the Lorentz factor. From bottom to top, the acceleration time–scales are calculated at 2×10^{15}, 5×10^{15}, 10^{16}, and 2×10^{16}sec after the beginning of the acceleration. The following values of the parameters are adopted: $d(\delta B)^2/dt = 3.3 \times 10^{-15}(\mu\mathrm{G})^2/\mathrm{s}$, $T = 10^8\mathrm{K}$, $n_{th} = 10^{-3}\mathrm{cm}^{-3}$, $B = 0.5\mu\mathrm{G}$, and $\mathcal{E}_e = 0.001 \times \mathcal{E}_{th}$. **Left Panel**: $\mathcal{E}_p = 0.2 \times \mathcal{E}_{th}$, $s = 2.0$ and $z_i = 1.0$; **Central Panel**: $\mathcal{E}_p = 0.025 \times \mathcal{E}_{th}$, $s = 3.0$ and $z_i = 1.0$; **Right Panel**: $\mathcal{E}_p = 0.002 \times \mathcal{E}_{th}$, $s = 4.0$ and $z_i = 1.0$;

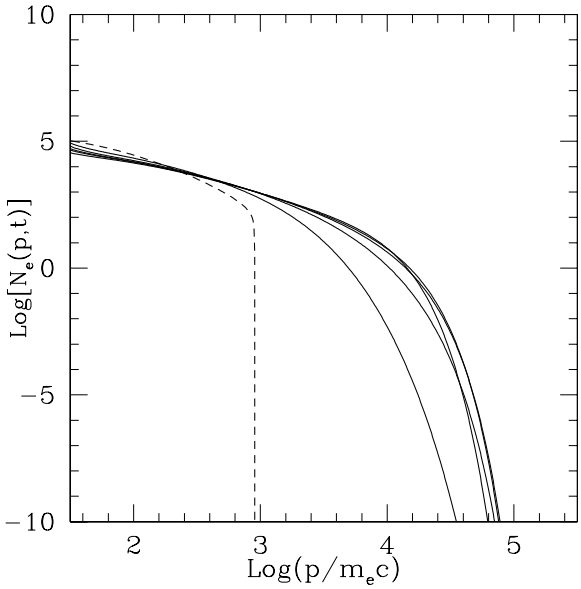

Figure 4.7: Time evolution of the spectrum of relativistic electrons as a function of p obtained after 2×10^{15}, 5×10^{15}, 8×10^{15}, 10^{16}, and 1.5×10^{16} sec from the beginning of the acceleration. The values of the parameters are as in Fig. 4.5.

This is true in the initial stage of evolution of the system: after about $\sim 0.5-0.7$ Gyr, relativistic protons have accumulated enough of the waves energy that the damping of the waves becomes even more efficient and further acceleration of electrons is prevented, independently of the injected proton spectra.
In fig.4.7 we report the evolution of the electrons spectra. It is clear that the bulk of the relativistic electrons, initially at $\gamma \sim 10^2$, can be energized up to $\gamma > 10^4$. We also note that, with increasing time, the efficiency of electron acceleration is lowered because of the damping of relativistic protons on the waves. The continuous backreaction between waves and protons creates a sort of *wave-proton boiler* that in a way is self-regulated.

If the injection of fluid turbulence is intermittent on time scales of the order of the cooling time of electrons with Lorentz factors $\gamma \sim 10^3 - 10^4$, then the effect of the *wave-proton boiler* on the electron acceleration may be reduced. The reason for this is that for a given reacceleration rate, the accumulation of energy in the form of relativistic protons requires longer times and the electron acceleration remains efficient for ~ 1 Gyr.

4.3.3 Proton acceleration

We consider the case in which the energy injected in Alfvén waves is significantly larger than that stored by the relativistic protons at the beginning of the acceleration phase, in this case the spectrum of protons is expected to be considerably modified. In Fig. 4.8 we report the evolution of the spectrum of the relativistic protons; it is clear that the spectrum flattens and a bump develops.
The prominence of this bump increases with time as the energy absorbed by relativistic protons also increases. Moreover, the bump moves toward larger momenta of the particles during the acceleration time.

4.3.4 The Wave-Proton Boiler

One of the most important results of our investigation is the quantitative treatment of the backreaction of the accelerated protons on the waves and in turn on the electrons. Qualitatively, given typical conditions in the ICM, we can identify three main temporal stages of the acceleration process:

1) Cascading stage:

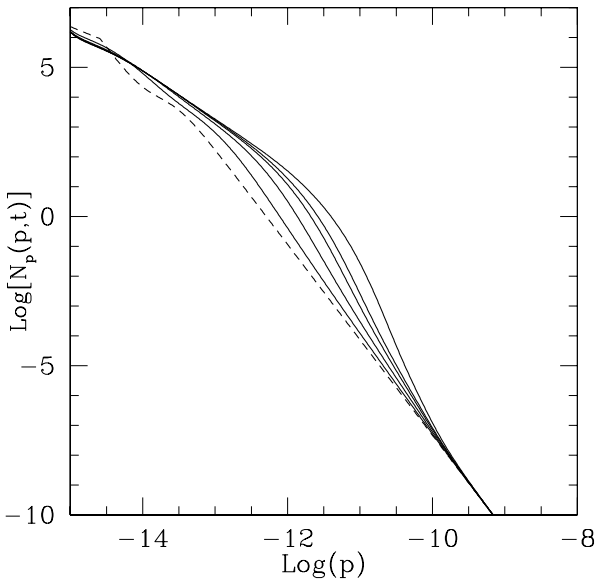

Figure 4.8: Time evolution of the spectrum of cosmic ray protons as a function of p. From bottom to top, the curves are obtained at times 2×10^{15}, 5×10^{15}, 8×10^{15}, 10^{16}, and 1.5×10^{16} sec after the beginning of acceleration. The initial proton spectrum is plotted as a dashed line. The values of the parameters are as in Fig. **??**.

For a non negligible rate of energy injection in the form of Alfvén waves, the cascade time is shorter than the damping time. This remains true up to some critical wavenumber, which depends on energetics and spectrum of protons, where damping starts to be relevant. If such a wavenumber is larger than about $10^{-2}k_{max}$, then enough energy is left in the form of waves at the scales which may resonate with relic relativistic electrons. In this case electrons are effectively re-energized.

2) Stage of proton backreaction:

Once the Alfvén waves start to accelerate electrons and protons to higher energies, the spectrum of protons and electrons becomes harder and the fraction of the energy stored in non-thermal particles starts to be large enough to make damping more severe. As a consequence, the rate of electron acceleration is reduced.

3) End of acceleration:

At the beginning of the acceleration phase, the bulk of protons is located at supra-thermal or trans-relativistic energies: however, it can be shown (see

Fig.16 in Brunetti et al. 2004, for details) that in few 10^8 yrs these protons can be energized to higher energies. After about $0.5-0.7$ Gyr the acceleration time scale of relativistic protons has increased by about one order of magnitude and at this point the acceleration stage of protons and electrons can be considered as concluded, unless the injection of turbulence occurs intermittently .

After the end of the third stage, the electrons cool due to radiative and Coulomb losses, while the Alfvén acceleration is only able to prevent the thermalization of these particles maintaining their Lorentz factor around $\gamma \sim 100 - 1000$.

4.4 Non-thermal emission from galaxy clusters

In this Section we specifically apply the previous findings to the case of merger driven turbulence in galaxy clusters and calculate the non-thermal spectrum.

4.4.1 Cluster mergers and turbulence

We assume that turbulence in the ICM is injected by cluster-cluster mergers. The bulk of the turbulence is most likely injected on scales ≥ 100 kpc due to the motion of the subclusters. Afterwards this turbulence eventually cascades toward smaller scales. As discussed in Sect.4.2, when the turbulent cascade reaches scales close to the Taylor scale, a fraction of the energy flux of the fluid turbulence can be transferred to MHD waves which in turn can accelerate fast particles via gyro-resonance.

For simplicity, we assume here that the bulk of the fluid turbulence in a given point of the cluster volume is injected at the scale l_o for a time τ_i of the order of the time necessary for the subclump to cross the scale l_o:

$$\tau_i(\mathrm{Gyr}) \sim 0.3\xi\Big(\frac{l_o}{300}\Big)\Big(\frac{v_c}{10^3}\Big)^{-1}, \tag{4.16}$$

where v_c is the velocity of the subclump in the host cluster and ξ is a parameter of the order of a few. With these assumptions the injection rate of energy in the form of fluid turbulence is given by :

$$F_f \sim \frac{2.3\times 10^{-27}}{\xi}\Big(\frac{n_{\rm th}}{10^{-3}}\Big)\Big(\frac{T}{10^8}\Big)\Big(\frac{l_o}{300}\Big)^{-1}\Big(\frac{v_c}{10^3}\Big)\frac{\mathcal{E}_t}{\mathcal{E}_{th}}, \tag{4.17}$$

where $\mathcal{E}_{\rm th}$ is the local energy density of the ICM in the form of thermal gas and $\mathcal{E}_{\rm t}$ is that in the form of turbulence. The bulk of the fluid turbulence at the scale l_o then cascades toward smaller scales producing a spectrum of the fluid turbulence that we write as $W_f(x) \propto x^{-m}$ (Sect.4.2). Assuming a Kolmogorov phenomenology (this is indeed appropiate for Alfvénic turbulence) for the wave-wave diffusion in $k-$space, the time scale for the cascade can be estimated from Eq. (4.15) with $I_{x_o} \sim x_o^{-1} F_f$:

$$\tau_s({\rm Gyr}) \sim 0.2 \Big(\frac{l_o}{300}\Big)\Big(\frac{10^8}{T}\Big)^{1/3}\Big(\frac{10^3}{v_c}\Big)^{1/3}\xi^{1/3}\Big(\frac{0.1}{\mathcal{E}_t/\mathcal{E}_{th}}\Big)^{1/3}. \qquad (4.18)$$

In our simple approach, this is the time delay between the merger event and the development of the turbulence at small scales (and thus the production of MHD waves). The power injected in Alfvén waves in the case of a Kolmogorov phenomenology is (from Eq.4.8):

$$P_A = \int I(k)dk \simeq 1.5 \times 10^{-29} B_{\mu G}^{-1}\Big(\frac{n_{\rm th}}{10^{-3}}\Big)^{\frac{3}{2}}\Big(\frac{l_o}{300}\Big)^{-1}\Big(\frac{Re}{10^{16}}\Big)^{-1/6}\Big(\frac{v_{\rm f}}{400}\Big)^4 \qquad (4.19)$$

All the quantities involved in the calculation of Eq.4.19 can be relatively well modelled, the only parameter, which is very difficult to estimate is the value of the Reynolds number, Re, at these small scales. (see discussion in Brunetti et al. 2004).

4.4.2 Constraining the model parameters

One may obtain some constraints on the physical conditions in the ICM which are necessary to have a reacceleration efficiency sufficient to explain the observed non–thermal emission. Here we report the main results and refer the reader to Brunetti et al. (2004) for the details of the calculations:

i) By balancing the energy losses and gains one may obtain the maximum energy, γ_{max}, of the accelerated electrons. It can be show that in order to obtain $\gamma_{max} >> 1000$, needed to explain the synchrotron emission at GHz frequency as well as the IC hard X–ray photons, the energy density in relativistic protons should be less than 3% the thermal energy density($\mathcal{E}_p \leq 3\%\,\mathcal{E}_{th}$) for physical conditions typical of the central cluster regions. Such a stringent limit is the consequence of the effective damping of Alfvén waves upon the relativistic proton component,

which inhibits the acceleration of electrons. In the periphery of the cluster, where the magnetic field is expected to be lower, the conditions to obtain high energy electrons are less stringent. It remains true however that *no more than a few percent of the thermal energy of the cluster can be in the form of relativistic protons if we want to interpret the observed non-thermal phenomena as the result of radiative processes of high energy electrons accelerated via Alfvén waves.*

ii) Another crucial parameter in the modeling of the non–thermal phenomena in galaxy clusters is the strength of the magnetic field in the ICM. There is still debate on whether this field is of several μG or rather fractions of μG (see Sect.2.2). In order to illustrate the effect of the magnetic field strength we evaluate the synchrotron cut–off frequency as a function of the magnetic field strength. Given the shape of the spectrum of the accelerated electrons, a synchrotron cut–off at $\geq 200-300$ MHz is required to account for the synchrotron radiation observed in the form of radio halos. From one hand a low value of B implies that very high energy particles are necessary to get the observed radio spectrum, on the other hand a value of B larger than the equivalent magnetic field strength of the CMB, considerably affects the strength of radiative losses and implies a large acceleration efficiency to mantain the emitting electrons. Thus, for typical condition of the cluster cores, by requiring a cut–off frequency $\geq 200-300$ MHz, Alfvénic reacceleration of relic electrons cannot be an efficient process for $B \gg 4\mu$G and for $B \ll 0.5\mu$G. These constraints become less stringent in the case of low density regions.

4.4.3 A simplified models for Radio Halos and Hard X–ray emission

In this section we apply the formalism described in previous sections in order to show that for the conditions realized in the ICM, Alfvénic reacceleration of relic electrons may generate the observed radiation, provided the energy content in the form of relativistic protons is not too large.

Our simple model for the ICM assumes a *β-model* (Chap.1, Eq.1.16; Cavaliere & Fusco-Femiano 1976) for the radial density profile of the thermal gas in the ICM, with $\beta = 0.8$. The magnetic field is assumed to scale with density according with flux conservation:

$$B(r) = B(r=0)\Big(\frac{n_{th}(r)}{n_{th}(r=0)}\Big)^{2/3}. \tag{4.20}$$

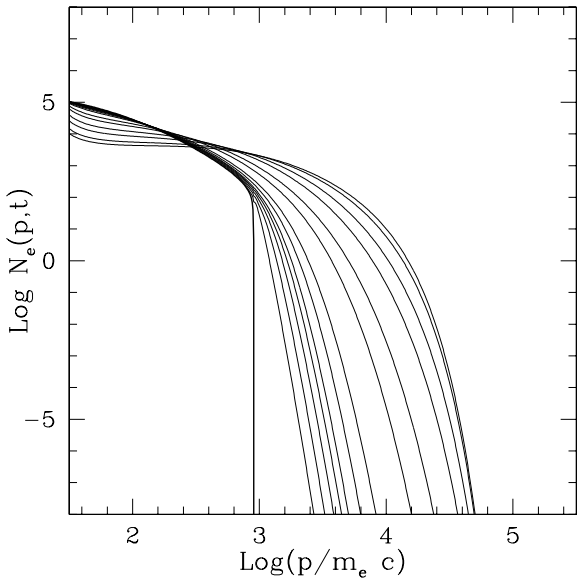

Figure 4.9: Temporal evolution of the accelerated electron spectra after 0, 10^{14}, ..., 5×10^{15}, 7×10^{15}, 10^{16}, and 1.2×10^{16}sec from the beginning of the acceleration stage. The following values of the parameters have been used: $d(\delta B)^2/dt = 1.6\times10^{-15}(\mu\mathrm{G})^2/\mathrm{s}$, $B = 0.5\mu$G, $T = 10^8$K, $n_{th} = 10^{-3}\mathrm{cm}^{-3}$, $\mathcal{E}_e = 0.001\times\mathcal{E}_{th}$, $\mathcal{E}_p = 0.01\times\mathcal{E}_{th}$, $s = 2.2$ and $z_i = 1.0$.

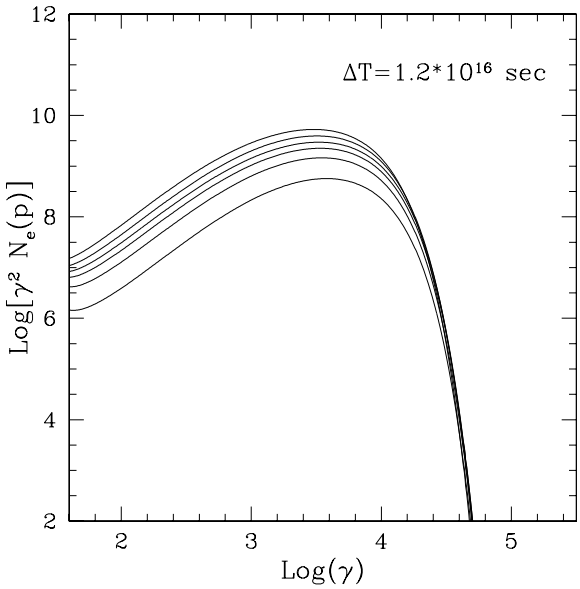

Figure 4.10: Spectra of electrons accelerated for 1.2×10^{16}sec at different distances from the cluster center: r =0.3, 0.6, 0.9, 1.2, 1.4, $2.1r_c$ (from top of the diagram). The central values assumed in the calculations are : $n_{th}(0) = 1.5\times10^{-3}\mathrm{cm}^{-3}$, $B(0) = 1.5\mu$G, $d(\delta B(0))^2/dt = 2.2\times10^{-15}(\mu\mathrm{G})^2/\mathrm{s}$.

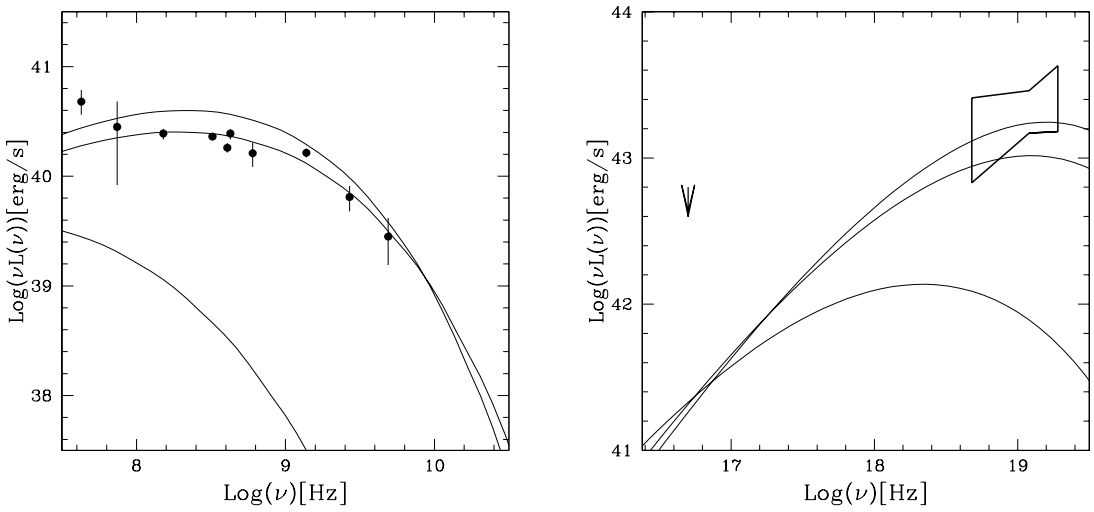

Figure 4.11: Temporal evolution of the synchrotron (**Left Panel**) and ICS (**Right Panel**) spectra from the cluster model given in Sect. 6.3 (integrating the emissivities up to $5 \times r_c$). Spectra are shown at 5×10^{15}, 1.2×10^{16} and 1.7×10^{16}sec from the beginning of the acceleration (from bottom to top). In the calculations $\mathcal{E}_e = 5 \times 10^{-5} \mathcal{E}_{th}$ has been adopted. Radio data are taken from Thierbach et al. (2003), EUV from Bowyer et al. (1999; here reported as an upper limit, see text), XHR from Fusco–Femiano et al. (2004).

Based on the constraints given in the previous Section we adopt $B(r = 0) \sim 0.5 - 4\mu$G. Finally, we assume that the ratio between the energy density of the relic relativistic particles (at the beginning of the acceleration phase) and that of the thermal plasma is constant in the cluster volume; that the maximum injection scale of the turbulence, the Reynolds number and the velocity of the turbulent eddies are independent of the location within the cluster volume.

Using the scaling relationship for the magnetic field, Eq. 4.20, and the expression for the injection power in the form of Alfvén waves, Eq. 4.19, we obtain:

$$P_A(r) = P_A(r = 0)\Big(\frac{n_{th}(r)}{n_{th}(r = 0)}\Big)^{5/6}. \tag{4.21}$$

The time evolution of the re-accelerated spectrum of the relativistic electrons in the core region is plotted in Fig.4.9. We can see that the bulk of relativistic electrons, initially at $\gamma \sim 10^2$, can be energized up to $\gamma \sim 10^4$ for a relatively long time.
Eq.4.21 indicates that, in our simple approach, the power injected in the form of Alfvén waves decreases with increasing distance from the cluster center. Since radio halos have a considerable size, it is needed to check that our model provides enough

energy in the outskirts of clusters. In Fig. 4.10 we plot the electron spectra at different distances from the cluster center (see caption). *At large distances the effect of acceleration is even stronger than in the central region and the electron spectra peak at slightly higher energies than in the core. This is due to the fact that in the outskirts the damping rate is reduced more than the rate of injection of turbulence.*

The corresponding synchrotron and IC spectra integrated over the cluster volume are plotted in Fig.4.11 at different times, for a central magnetic field $B(r = 0) \simeq 1\mu G$. The spectra are compared with that observed for the radio halo in the Coma cluster : an initial energy density in the relic relativistic electrons of the order of $5 \times 10^{-5}\mathcal{E}_{th}$ is required to account for the data. In Fig. 4.11 we also report the luminosity of the EUV excess in the Coma cluster as an upper limit (as the origin of the EUV excess is not directly related to the same electron population responsible for the radio and possibly for the HXR emission; Bowyer & Berghöfer 1998; Ensslin et al. 1999; Atoyan & Völk 2000; Brunetti et al. 2001b; Tsay et al. 2002). Here we stress that Fig.4.11 is just a comparison between data and time evolution of the emitted spectra resulting from the very simple scaling of the parameters described above. On the other hand, it should also be stressed that the time evolution of the synchrotron and IC spectra reported in Fig.4.11 is generated via the first fully self-consistent calculation of particle acceleration in galaxy clusters. Thus, *provided that the energy of relativistic protons in galaxy clusters is not larger than a few percent of the thermal energy, Fig.4.11 proves, the possibility to obtain the observed magnitude of the non–thermal emission in these objects via Alfvénic acceleration.*

4.5 Conclusions

In this Chapter we have presented a full account of the time-dependent injection of fluid turbulence, its cascade to smaller scales, the injection of Alfvén waves through the *Lighthill* mechanism, the resonant interaction of these waves with electrons and protons (namely their acceleration) and the backreaction of the accelerated particles on the waves. The solution of the coupled evolution equations for the electrons, protons and waves has revealed several new interesting effects resulting from the interaction among all these components:

i) Alfvén waves are injected by the fluid turbulence through the *Lighthill* mechanism. This allows us to establish a direct connection between the fluid turbulence likely to be excited during cluster mergers, and the MHD turbulence that may resonate with particles in the ICM.

ii) Previous calculations looked for self-similar solutions for the spectra of electrons and MHD waves in the form of power laws. *The solutions obtained in the present Chapter show that in Nature these self-similar solutions are not necessarily achieved.* In general *the system evolves toward complex spectra of electrons and MHD waves with a bump in the electron spectrum*, that moves in time toward an increasingly large particle momentum.

iii) The main damping of Alfvén waves occurs on relativistic protons, if there are enough of them. The spectrum of the waves is cutoff at small scales due to the damping of these waves. The damping moves energy from the waves to the particles, determining their acceleration/heating.

iv) The importance of the presence of the relativistic protons for the acceleration of electrons is one of the most relevant new results of this Chapter. A large fraction of the thermal energy in the form of relativistic protons enhances the damping rates of Alfvén waves, suppressing the possibility of resonant interaction of these waves with electrons. Since electrons are the particles that radiate the most, a too large fraction of relativistic protons suppresses non-thermal phenomena directly related to electron reacceleration via Alfvén resonance. *Our results show that no more than a few percent of the thermal energy density of the cluster can be in the form of relativistic protons if we want to interpret the diffuse radio and hard X-ray emissions as the result of synchrotron and IC radiation of relic electrons re-accelerated through Alfvén waves.* This appears as a stringent constraint on the combination of proton number and spectrum since the accumulation of large number of protons in the ICM (see also Sec.3.1.3) is predicted by both analytical calculations (Berezinsky et al. 1997) and numerical simulations (Ryu et al. 2003). Both the energy and spectrum of the cosmic rays stored in the ICM affect the temporal evolution of Alfvén waves and their ability to re-accelerate relic electrons.

If future observations will unveil the presence of a population of relativistic protons in the ICM with $> 5-10\%$ *of the thermal energy, then Alfvénic reacceleration of relativistic electrons in galaxy clusters will be discarded as a possible explanation*

of non-thermal phenomena in the ICM. On the other hand, similar reacceleration phenomena can be driven by MHD waves other than Alfvén waves, for which the energy transfer does not occur preferentially toward protons (see Chapt. 5). In this case, the bounds presented here on the allowed energy density in the form of relativistic protons in the ICM could be substantially relaxed.

v) By assuming that protons have a relatively flat spectrum ($s \sim 2.2$) and that they contain up to a few percent of the thermal energy, we used a simple but phenomenologically well motivated model for the density and magnetic field in a cluster of galaxies in order to calculate the expected non-thermal radio and hard X-ray activity of the cluster as a function of time. *For the first time we performed a fully self consistent calculation and showed that the reacceleration of relic electrons through resonant interaction with Alfvén waves can explain very well the observed phenomena, including the extended diffuse appearance of this emission.* In passing, without considering the case of the HXR emission, we also showed that a magnetic field strength in the range $0.5 - 4\mu$G in the cluster cores allow electron acceleration efficient enough to produce GHz synchrotron emission. These conditions are less stringent in the outermost regions of the clusters.

vi) In our calculations we adopted a constant injection rate of turbulence during particle acceleration. In this case, even assuming $\mathcal{E}_p < 0.1 \times \mathcal{E}_{th}$, we find that after a few 10^8yrs of acceleration the backreaction of protons on MHD waves can suppress the acceleration of energetic electrons : this provides a limit on the duration of the non-thermal phenomena in galaxy clusters. It is possible to extend the duration of non-thermal activity assuming that injection of turbulence occurs in relatively short bursts of duration comparable with the life–time of electrons. On the other hand, independently on the assumptions, our results show that if particle acceleration is mainly due to Alfvén waves, then the existence of radio halos and HXR tails in massive clusters should be limited to achieve periods of $< 10\%$ of the Hubble time.

vii) The temporal duration of the process of turbulent cascade and the acceleration time scale of electrons are estimated to be about one order of magnitude shorter than the dynamical time-scale of a merger event. This implies that a temporal correlation is still expected between merging processes and the rise of the non-thermal phenomena in galaxy clusters.

Chapter 5

A first approach to the calculation of the statistical properties of RHs

Although the physics of particle acceleration due to turbulence generated in merging clusters has been investigated in some detail (*e.g.,* Schlickeiser et al. 1987; Petrosian 2001; Fujita et al. 2003; Brunetti et al. 2004; Brunetti & Blasi 2005; Brunetti & Lazarian 2007) and the model expectations for the origin of RHs seem to reproduce the observed radio morphologies and spectral features, and possibly also the hard X–rays (*e.g.,* Brunetti et al. 2001a; Kuo et al. 2003; Brunetti 2004; Hwang 2004), a *theoretical investigation of the statistical properties of the Mpc diffuse emission in galaxy clusters in the framework of the re-acceleration model has not been carried out extensively as yet.* In particular, the fact that giant radio halos are always associated to massive galaxy clusters and the presence of a trend between their radio power and the mass (temperature, X-ray luminosity) of the parent clusters may be powerful tools to test and constrain present models.

So far two works have modeled the statistics of the formation of radio halos.

Enßlin & Röttgering (2002) calculated the radio luminosity function of cluster radio halos (RHLF). These calculations can be considered as an extrapolation of present radio data toward clusters with smaller mass and different z. In a first modelling, they obtained RHLF by combining the X-ray cluster luminosity function with the radio–halo luminosity – X–ray luminosity correlation, assuming that a fraction, $f_{rh} \simeq \frac{1}{3}$, of galaxy cluster have radio halos; this fraction being calibrated with observational findings of massive clusters. Then, in a slightly more accurate modelling, f_{rh} was assumed to be equal to the fraction of clusters that have recently undergone a strong mass increase and the radio halo luminosity of a cluster was

assumed to scale with $(1+z)^{-4}$ (due to the increasing IC-losses).

In a more recent paper, Kuo et al. (2004) calculated the formation rate and the comoving number density of radio halos in the hierarchical clustering scheme. The model was based on two morphological criteria to define the conditions necessary to the formation of radio halos : 1) the cluster mass must be greater than or equal to a threshold mass adjusted to observations (Giovannini et al. 1999); 2) the merger process must be violent enough to disrupt the cluster core, and thus the relative mass increase was required to be $\Delta_m \equiv (\Delta M/M)_{th} = 0.6$ according to numerical simulations (Salvador-Sole et al. 1998). Given the above criteria and making use of the PS formalism these authors found that a duration of the radio halo phenomenon of the order of 1 Gyr would result to be in good agreement with the observed occurrence of radio halos.

As already pointed out, all these approaches are based on assumptions in defining the conditions of formations of radio halos based on observational correlations and/or mass thresholds. On the other hand, no effort has been done so far to model the formation of radio halos and HXR tails in a self-consistent approach, *i.e.,* an approach which should model, at the same time, the evolution of the thermal properties of the ICM of the host galaxy clusters and the generation and evolution of the non-thermal phenomena.

As mentioned above, one of the ideas that is producing the most promising results for the interpretation of non-thermal phenomena in galaxy clusters consists in the turbulent re-acceleration of relic relativistic electrons leftover of the past activity occurred within the ICM.

In this Chapter we describe the formalism and relative calculations of the statistical properties of giant RHs and HXR tails in the framework of this electron re-acceleration scenario.

In order to have a straightforward comparison with published observational constraints, in this Chapter we focus on a Einstein de Sitter (EdS) cosmology ($H_o = 50$ km s^{-1}Mpc^{-1}, $q_o = 0.5$) and discuss the case of the ΛCDM model at the end of the Chapter.

The results presented in this Chapter are published in: Cassano & Brunetti (2005; CB05) and Vazza et al. 2006.

5.1 Focus & Main Questions

In this Chapter we will assume the re-acceleration scenario and address the following points:

- Is it possible to model "self-consistently" the evolution of non-thermal radio (and HXR) emission and the hierarchical process of formation of the clusters?
- Which are the physical requirements in terms of density of relativistic electrons and of turbulence to reproduce the basic observed properties of RHs and HXR tails?
- Is it possible, in the framework of the re-acceleration model, to reproduce in a natural and straightforward way the increase of the fraction of probability to find RHs in galaxy clusters with increasing the cluster mass?

Addressing, for the first time, these points will be crucial to test the viability of the re-acceleration model, and to a first quantitative understanding of the merger–non-thermal emission connection.

5.2 The Model: Outline

In this Section we outline the formalism and procedures used to develop our statistical calculations. The major steps can be sketched as follows :

i) Cluster formation: The evolution and formation of galaxy clusters is computed making use of the extended Press & Schechter (1974, hearafter PS; Lacey & Cole 1993) semi-analytic procedure based on the hierarchical theory of cluster formation (Sec.1.4). Given a present day mass and temperature of the parent clusters, the cosmological evolution (back in time) of the cluster properties (merger trees) are obtained making use of Monte Carlo simulations. A suitable large number of trees allows us to describe the statistical cosmological evolution of galaxy clusters.

ii) Turbulence in Galaxy Clusters: The turbulence in galaxy clusters is supposed to be injected during cluster mergers and dissipated in a time-scale of the order of the cluster-cluster crossing time.

The energetics of the turbulence injected in the ICM is "calibrated" with the PdV work done by the infalling subclusters in passing through the volume of the most massive one; it basically depends on the density of the ICM and on the velocity between the two colliding subclusters. The sweeped volume in which turbulence is injected is estimated from the *Ram Pressure Stripping* (*e.g.,* Sarazin 2002, ; and ref. therein). We assume that a relatively large fraction of the turbulence developed during these mergers is in the form of *fast magneto–acoustic waves* (MS waves). We use these waves since their damping rate and time evolution basically depend on the properties of the thermal plasma which are provided by our merger trees for each simulated cluster.

The shape of the spectrum of the MS waves depends on many unknown quantities thus we adopt two extreme scenarios: the first one assumes a broad band injection of MHD waves (Sec.5.4.2), the second one assumes that turbulence is injected at a single scale (Sect.5.9.1). In both cases the spectrum of MS waves is calculated solving a turbulent-diffusion equation in the wavenumber assuming that the turbulence, injected in the cluster volume for each merger event, is injected for- and thus dissipated in a dynamical crossing time.

iii) Particle Acceleration: We focus on the electron component only because the major damping of MS waves (which determines the spectrum of these waves and thus the efficiency of the particle acceleration), is due to thermal electrons and thus hadrons cannot significantly affect the electron–acceleration process [1]. We assume a continuous injection of relativistic electrons in the ICM due to AGNs and/or Galactic Winds; this injection is necessary to provide the pool of supra-thermal electrons to be re-accelerated. At each time step, given the spectrum of MS waves and the physical conditions in the ICM, we compute the time evolution of relativistic electrons by solving a Fokker-Planck equation including the effect of electron acceleration due to the coupling between MS waves and particles, and the relevant energy losses.

Given a population of galaxy clusters by combining *i)-iii)* we are thus able *to follow in a statistical way the cosmological evolution of the spectrum of the relativistic*

[1]This is different from the case of Alfvén waves whose damping may be indeed dominated by the presence of relativistic hadrons (Brunetti et al. 2004); Sec. **??**).

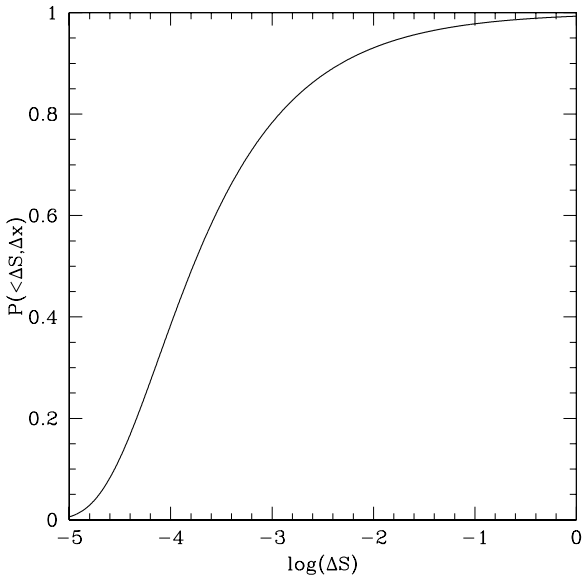

Figure 5.1: Cumulative probability distribution $\mathcal{P}(< \Delta S, \Delta x)$ as a function of $log(\Delta S)$.

electrons in the volume of these clusters and the properties of the thermal ICM.

5.3 Monte Carlo Technique and Merger Trees

Based on the extended PS formalism (see Sec.1.4.4) and following a relatively standard procedure adopted in the literature (*e.g.,* Randall et al. 2002; Gabici & Balsi 2003), we employ a Monte Carlo technique to construct merger trees. Each tree starts at the present time with a cluster of mass M and temperature T. Following Sec.1.4.4 we replace the mass M and time t (or redshift z) with the suitable variables $S \equiv \sigma^2(M)$ and $x \equiv \delta_c(t)$. We step each simulated cluster back in time, using a small but finite time step corresponding to a positive increase Δx. The step size determines the value of the minimum mass increment of the cluster, ΔM_c, which is due essentially to a single merger event (Lacey & Cole 1993) :

$$(\Delta x)^2 \lesssim \left|\frac{d\ln\sigma^2}{d\ln M}\right| \left(\frac{\Delta M_c}{M}\right) S\,, \tag{5.1}$$

where M is the mass of the cluster at the current time step. The value ΔM_c gives the mass of the smallest merging subcluster we can resolve individually in our trees; we choose $\Delta M_c \simeq 10^{12} h^{-1} M_\odot$. Thus mass increments smaller than this value are considered to be part of the continuous mass accretion process in galaxy clusters.

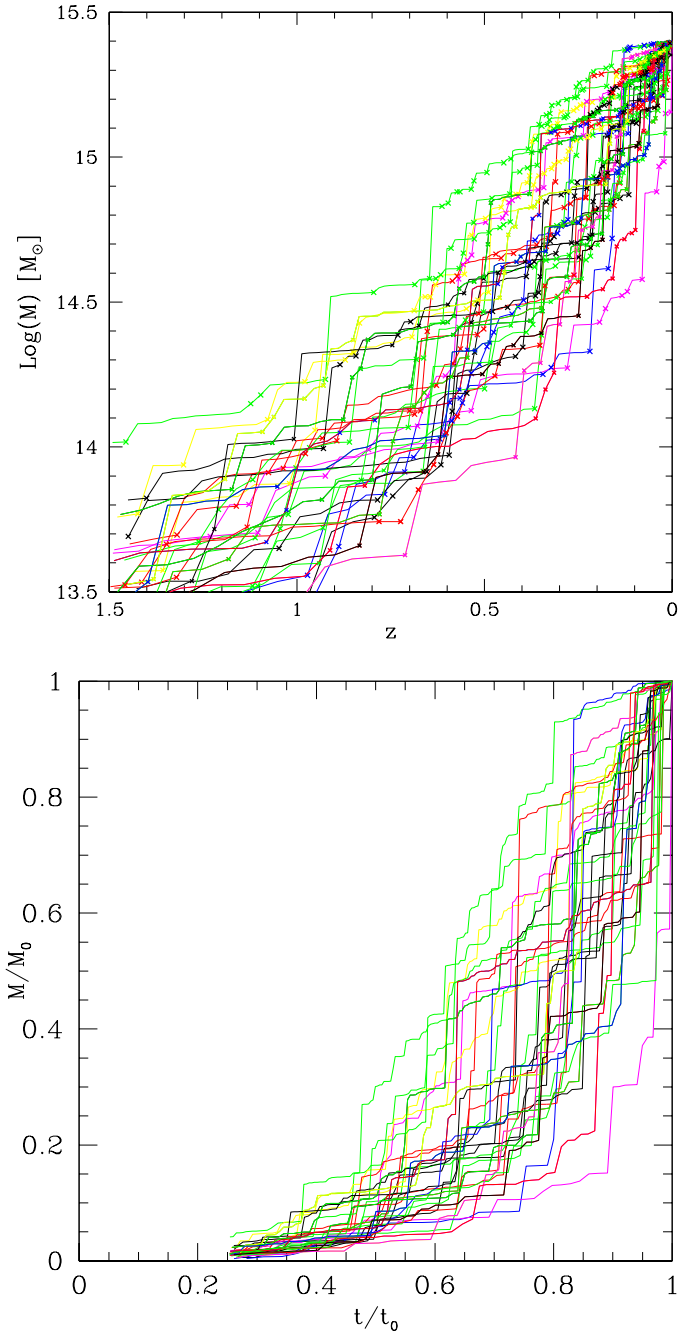

Figure 5.2: Example of Merger Trees obtained from Monte Carlo simulation in a EdS universe for clusters with present day mass $M_0 = 2.5 \times 10^{15} M_\odot$: a) $Log(M) - z$; b) $M/M_0 - t/t_0$ with t cosmic time; t_0 present time.

In order to follow the probability that a merger with a given ΔS (*i.e.* ΔM) occurs at a given time we make use of the cumulative probability distribution of subcluster masses:

$$\mathcal{P}(<\Delta S, \Delta x) = \int_0^{\Delta S} K(\Delta S', \Delta x)\, d\Delta S' = \mathrm{erfc}\left(\frac{\Delta x}{\sqrt{2\Delta S}}\right) \tag{5.2}$$

where erfc() is the complementary error function and $K(\Delta S', \Delta x)\, d\Delta S'$ is given in Eq.1.69. The cumulative probability distribution (Fig. 5.1) is defined such that $\mathcal{P}(<\Delta S, \Delta x) \rightarrow 1$ for $\Delta S \rightarrow \infty$.

The Monte Carlo procedure selects a uniformly-distributed random number, r, in the range 0–1, then it determines the corresponding value of ΔS solving numerically the equation $\mathcal{P}(<\Delta S, \Delta x) = r$ (Fig. 5.1). The value of S_2 of the progenitor is given by $S_2 = S_1 + \Delta S$. The mass of one of the subclusters is given by solving $\sigma^2(M_2) = S_2$, where $\sigma(M_2)$ is given by Eq.(1.68), whereas the mass of the other subcluster is $\Delta M = M_1 - M_2$. We define $M_{min} \equiv \min(M_2, \Delta M)$ and $M_{max} \equiv \max(M_2, \Delta M)$. In order to speed up the computational procedures, without significantly affecting the results, we consider two cases :

i) If $M_{min} < 1 \times 10^{13} M_\odot$ the event is considered a very minor merger and its contribution to the injection of cluster turbulence (Sec. 5.4.1) is neglected [2]. The mass of the parent cluster is simply reduced to $M_2 = M_1 - M_{min}$ and the next back in time-step in the merger tree starts from M_2.

ii) if $M_{min} > 1 \times 10^{13} M_\odot$ then the event is treated as a merger and we calculate all the physical quantities useful for the computation of the energy of the turbulence generated during this event (Sec. 5.4.1). In this case, if M_{min} is also greater than a given value of interest we follow back in time the evolution of both the subclusters (*i.e.,* M_{min} and M_{max}) constructing the merger tree for each subcluster.

This procedure is thus iterated until either the mass of the larger cluster drops below ΔM_c or a maximum redshift of interest z_{max} is reached. An example of a merger tree obtained from our procedure (tracing the evolution of the M_{max} clusters only) is shown in Fig. 5.2 as a function of both look back time and redshift.

[2] Note that we are interested in describing mergers of typically $> 5 \times 10^{14} \mathrm{M}_\odot$, Sec. 5.7.

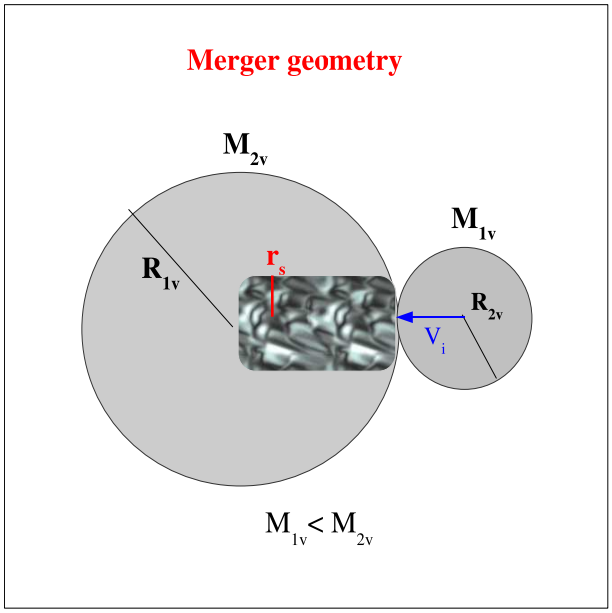

Figure 5.3: Cartoon of the assumed geometry for the binary cluster mergers.

Our procedure is basically a *Binary Merger Tree Method* which does not allow to describe multiple nearly simultaneous mergers. This simple procedure, however, is sufficient for our purposes since multiple mergers mainly affect the evolution of low mass halos at relatively high redshift which are not interesting for the study of the non-thermal phenomena. The implementation of more complicated *N-Branch Tree Methods* can be found in Somerville & Kolatt (1999).

5.4 Ram Pressure Stripping, turbulence and MHD waves

5.4.1 Turbulence injection rate

The passage of the infalling subhalos through the main cluster during mergers induces large–scale bulk flows with velocities of the order of ~ 1000 km s^{-1} or larger. Numerical simulations of merging clusters (*e.g.,* Röttiger et al. 1997; Ricker & Sarazin 2001; Tormen et al. 2004) provide a detailed description of the gasdynamics during a merger event. It has been found that subclusters generate laminar bulk flows through the swept volume of the main clusters which inject eddies via Kelvin–Helmholtz instabilities at the interface of the bulk flows and the primary cluster gas. Finally these eddies redistribute their energy through the cluster volume in a few Gyrs by injecting random and turbulent velocity fields.

The impact velocity between the subclusters increases at the beginning of the merger and then it saturates when the subclusters interpenetrate each other. Depending on the initial conditions and on the mass ratio of the two subclusters, during the merging process the infalling halos may be efficiently stripped due to the ram–pressure. However, the numerical simulations show that the efficiency of the ram pressure stripping is reduced by the formation of a bow shock on the leading age of the subcluster. This bow shock forms an oblique boundary layer which slows the gas flow and redirects it around the core of the subcluster so that, at least in the case of mergers with mass ratios < 10, a significant amount of the subcluster gas is found to be still self–bounded after the first passage through the central regions of the main cluster (Röttiger et al. 1997; Tormen et al. 2004).

Due to the complicated physics involved in these events, the details of the injection and evolution of turbulent motions in galaxy clusters during merging processes are still unexplored. However, turbulence should be basically driven by the PdV work done by the infalling halos through the volume of the primary cluster and the turbulent motions should be initially injected within the volume swept by the passage of the subhalos (*e.g.,* Fujita et al. 2003). Following this simple scenario, in this Section we estimate the rate of turbulence injected during a merger event. As a necessary approximation (due to the PS formalism) in the calculations, we assume that subclusters undergo only central collisions (See Fig.5.3 for an illustrative picture of the merger geometry).

The relative impact velocity of two subclusters with mass M_{max} and M_{min} which collide (at a distance R_{max} between the centers) starting from an initial distance d_o with zero velocity is given by Eq.1.74 in Sect.1.5 (*e.g.,* Sarazin 2002).

While the smaller subcluster crosses the larger one, it is stripped due to the effect of the ram–pressure. The stripping is efficient outside a radius r_s (stripping radius) at which equipartition between static and ram–pressure is established, *i.e.* :

$$\overline{\rho}_{max} v_i^2 = \frac{\rho_{min}(r_s) K_B T_{min}}{\mu m_p} \tag{5.3}$$

where, as an approximation, $\overline{\rho}_{max}$ is fixed at the average density of the ICM of the larger subcluster :

$$\overline{\rho}_{max} = \left(\frac{M_{max}}{\frac{4}{3}\pi R_{max}^3} \right) \times f_b \,, \tag{5.4}$$

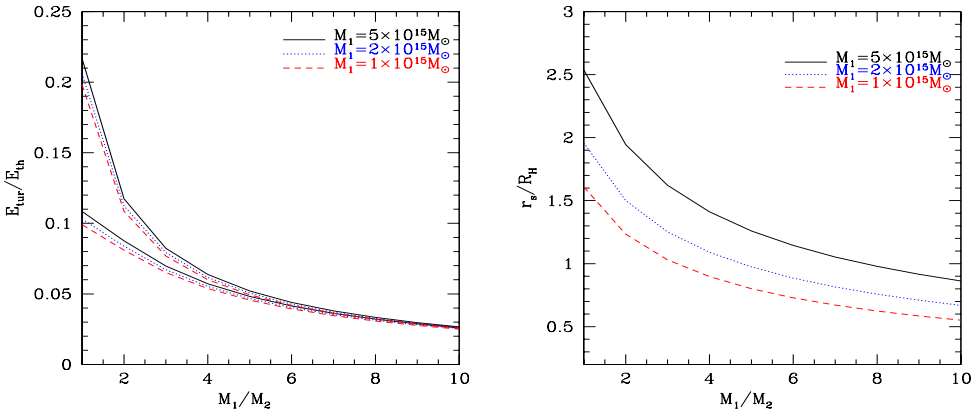

Figure 5.4: **Panel a)**: Ratio between the energy injected in form of turbulence and the thermal energy of the system as a function of the mass ratio of the two subclusters. Thermal energy is calculated for both the sum of the two subclusters (lower lines) and for the main cluster alone (upper lines). We stress that in the case of a mass ratio ≤ 1.5 our approach is quite inadequate because essentially no primary cluster exists, however these mergers are very rare events and do not dominate the injection of turbulence in our model. **Panel b)**: Ratio between the stripping radius and the radius of the radio halos (assuming $R_H = 500 h_{50}^{-1}$ kpc) reported as a function of the mass ratio of the two subclusters. In both panels calculations are obtained following the recipes given in Sect. 4.1 for a $M = 5$, (solid lines), 2 (dotted lines), and $1 \times 10^{15} M_\odot$ (dashed lines) clusters.

with $f_b = 0.25\,(\frac{h}{0.5})^{-3/2}$ the observed barion fraction of clusters (Ettori & Fabian 1999, Arnaud & Evrard 1999). We solve Eq.(5.3) numerically at each merger event assuming that the density profile of the ICM of the smaller cluster, ρ_{min}, is described by a β-model (Cavaliere & Fusco-Femiano, 1976), Eq.1.16, and the normalization is given by:

$$\rho_{min}(0) = \frac{f_b M_{min}}{4\pi} \left\{ \int_0^{R_v^{M_{min}}} dr r^2 \left[1 + (\frac{r}{r_c})^2 \right]^{-3\beta_x/2} \right\}^{-1} \qquad (5.5)$$

a core radius $r_c = 0.1\ R_{min}$ and $\beta_x \simeq 0.8$ are assumed. The temperature of the smaller cluster, T_{min}, in Eq.(5.3) is estimated by making use of the observed M-T relationship (*e.g.,* Nevalainen et al. 2000). As a general remark we stress that the value of the stripping radius obtained above would give the mean value of r_s during a merger and it is not the minimum r_s. In qualitatively agreement with numerical simulations, this approach yields $r_s \to 0$ in the case of mergers with large mass ratios between the two colliding subclusters.

The motion of the smaller cluster through the ICM of the main one generates fluid turbulence. Following Fujita et al. (2003) we assume that turbulence is initially

injected in the swept volume, $V_t \sim \pi r_s^2 R_{max}$, with a maximum turbulence length scale of the order of $\approx 2 \times r_s$ (see Fig. 5.3). The total energy injected in turbulence during a merger event is thus $E_t \simeq \overline{\rho}_{max,s}\, v_i^2 V_t$, where $\overline{\rho}_{max,s}$ is the ICM density of the main cluster averaged on the swept cylinder. We assume that the duration of the injection is of the order of a crossing time, $\tau_{cros} \simeq R_{max}/v_i$, then the turbulence is dissipated in a relatively short time.

The use of the averaged density of the ICM of the primary cluster, $\overline{\rho}_{max}$, of the initial impact velocity between the subclusters, v_i, and of the density of the main cluster averaged on the swept cylinder, $\overline{\rho}_{max,s}$ in the calculations of the injected turbulence is a necessary simplification which however guarantees a basic estimate of the averaged injected turbulence in the ICM and which does not depend on essentially unknown details. For seek of completeness, in Fig. 5.4a we report the typical ratio between turbulent energy injected by a merger event and the thermal energy of the system as a function of the mass ratio between the two colliding subclusters; it is found that major mergers may channel about 10-15 % of the thermal energy in the form of large scale turbulence. In Fig. 5.4b we also report the value of the stripping radius as a function of the mass ratio of the two colliding subclusters. It is found that r_s (*i.e.,* the mean value of r_s during a merger event) is typically larger than the radius of the radio halos, R_H, for the merger events which mainly contribute to the injection of cluster turbulence in our model. If the swept volume is smaller than that of the radio halo, we assume that the injected turbulence is diffused over the volume of the radio halo, $V_H = \frac{4}{3}\pi R_H^3$, which is basically equivalent to assume that the integral cross section of the ensemble of minor mergers which occur in a time interval of ∼Gyr is comparable to R_H.

Under these hypothesis, the injection rate per unit volume of turbulence is given by :

$$\frac{E_t}{\tau_{cros} \times V_H} \simeq \frac{\overline{\rho}_{max,s}}{R_{max}} v_i^3 \left(\frac{V_t}{V_H}\right) \tag{5.6}$$

As a relevant example, in Fig. 5.5a we report the cosmological evolution of the thermal energy of galaxy clusters with different masses, together with the total energy injected up to that z in form of turbulence in the ICM. The energy in turbulence is calculated by integrating the contributions from all the merger events. The thermal energy of the considered clusters, calculated assuming the observed M-

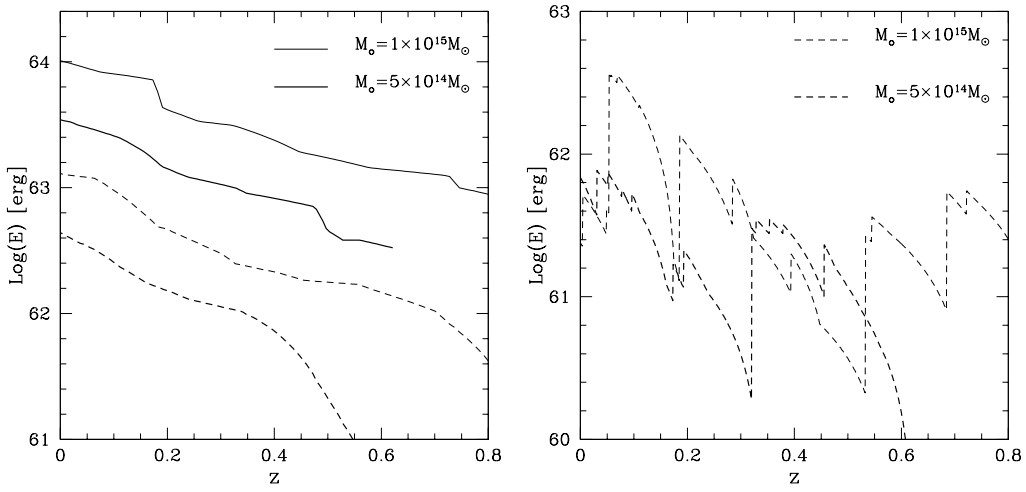

Figure 5.5: **a)** Evolution of the thermal energy (solid lines) and of the energy injected in fluid turbulence (dashed lines) integrated during cluster life (at redshift z) in typical galaxy clusters. **b)** Evolution of the differential turbulent energy (turbulent energy present at the redshift z) as a function of z for the same two clusters in panel **a)**. In both panels the thin lines are for a cluster with present time $M_0 = 10^{15} M_\odot$ and the thick lines are for a cluster with present time $M_0 = 5 \times 10^{14} M_\odot$.

T relation (*e.g.,* Nevalainen et al. 2000), increases from about 10^{62}erg at $z \sim 1$ to a few 10^{64}erg at the present epoch depending on the mass of the cluster. As it should be, we note that the energy budget injected in turbulence during cluster formation is well below the thermal energy; this indicates the consistency of our calculations.

While in Fig.5.5a we report the cumulative contributions to the injection of turbulent energy from all merger events experienced from the formation of the cluster up to redshift z, in Fig. 5.5b we report for the same clusters of Fig.5.5a the differential turbulent energy, *i.e.,* the energy present in the form of turbulence at a given z, and this is associated with recent merging processes. We would to point out that since turbulence is assumed to dissipate in a typical crossing time (Sec.5.2 *ii)*), turbulence due to cluster-cluster mergers is a *transient* phenomena (with a tipical time scale of the order of the cluster-cluster crossing time) which is intrinsically related to the merger history of the cluster.

From Fig. 5.5a we note that the turbulent energy is found to be $\sim 15\%$ that of the thermal energy in agreement with recent numerical simulations (Sunyaev et al. 2003) and with very recent observational claims (Schuecker et al. 2004). Finally, as reasonably expected, the energy injected in turbulence calculated with our approach is found to roughly scale with the thermal energy of the clusters. Indeed, since the

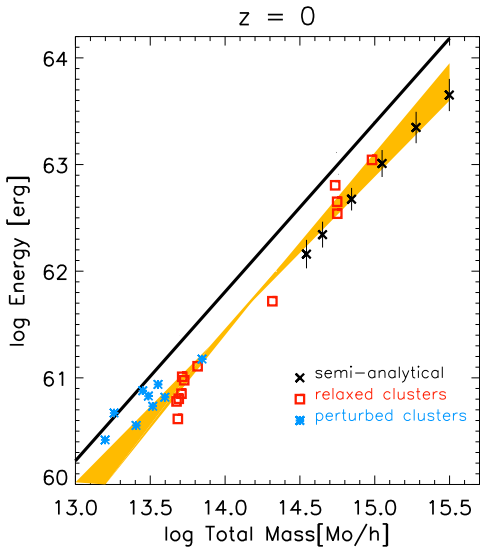

Figure 5.6: Comparison between the thermal and turbulent scaling at zero redshift, for 12 "relaxed" (*i.e.* $\xi < 0.5$) galaxy clusters, 9 "perturbed" (*i.e.* $\xi \geq 0.5$) clusters and semi-analytical average data with 1σ errors. The black line shows the thermal scaling of the whole simulated sample, while the orange band encloses, within 1σ errors, the scaling of the "relaxed" sample alone and the scaling with the 9 "perturbed" object added (Vazza et al. 2006).

infalling sub-clusters are driven by the gravitational potential, the velocity of the infall should be $\sim 1.5-2$ times the sound speed of the main cluster amd consequently the energy density of the turbulence injected during the cluster–crossing should be proportional to the thermal energy density of the main cluster. In addition, the fraction of the volume of the main cluster in which turbulence is injected (the volume swept by the infalling subclusters) depends only on the mass ratio of the two merging clusters. Thus, provided that the distribution of the accreted mass–fraction does not strongly depend on the cluster mass (Lacey & Cole 1993), the combination of the above two items yields a self–similarity in the injection of turbulence in the ICM: the energy of such turbulence should scale with the cluster thermal energy, and thus, in the case of a self similar scaling $M \propto T^{3/2}$, the turbulent energy should scale with virial mass with a slope $\simeq 5/3 \simeq 1.67$.

The issue of the injected budget of energy in the form of turbulence in galaxy clusters during cluster formation is an important issue and our simplified approach may require a test with numerical simulations. A first test of our expected scaling between thermal and turbulent energy in galaxy clusters has been done in a recent

work (Vazza et al. 2006) where we present a study of the turbulent velocity fields in the ICM of a sample of 21 galaxy clusters. The cluster sample consists of 9 resimulations with 21 galaxy clusters and groups simulated with the tree N-body–SPH code Gadget2 (Springel et al. 2005). The cluster regions were extracted from a dark matter only simulation with box of $479\,h^{-1}$Mpc on a side and in the context of a ΛCDM model with $\Omega_0 = 0.3$, $h = 0.7$, $\sigma_8 = 0.9$ and $\Omega_{\rm b} = 0.04$ (Yoshida et al. 2001). Adopting the 'Zoomed Initial Conditions' technique (Tormen et al. 1997) the regions were re–simulated in order to achieve higher mass and force resolution. The sample is a non-radiative SPH subset where an improved recipe for the numerical viscosity of gas–particles is used (for a more detailed discussion about this method we address the reader to Dolag et al. (2005a). The turbulent motions in the ICM of simulated clusters are detected with a novel method devised to better disentangle laminar bulk motions from chaotic ones. We focus on the scaling law between the turbulent energy content of the gas particles and the total mass, and confirm that the energy in the form of turbulence scales approximatively with the thermal energy of clusters. This is reported in Fig.5.6 where we show the integral of the turbulent energy (injected in the ICM up to the present time) versus the cluster mass, as estimated with semi-analytical calculations with 360 merging trees of massive galaxy clusters in a ΛCDM cosmology and the measures obtained for the simulated clusters. The two approaches are complementary, since semi–analytical calculations can follow the properties of $> 10^{15}$M$_\odot$ clusters which are rare in numerical simulations due to the limited simulated cosmic volume; thus when plotted together the data of the two independent methods prove the scaling over more than two order of magnitude in mass. In addition, semi-analytical calculations give a simple physical explanation of the scaling laws in term of the PdV work done by the infalling subclusters through the main ones, and strengthen the physical nature, in terms of gravitational driven, of the turbulent velocity fields found in simulations.

5.4.2 Spectrum of the magnetosonic waves

As already discussed cluster mergers are likely to generate turbulence, the fraction (η_t) of the turbulent energy which goes in magnetosonic (MS) waves and the spectrum of these waves depend on the details of the turbulent driving at large scales, and this clearly requires future detailed studies.

In the conservative case of solenoidal forcing (and beta of plasma >> 1) this fraction is expected to scale with $\mathcal{M}_s^2\,\mathcal{R}_e$ (with $\mathcal{M}_s < 1$, the turbulent Mach number) for $\mathcal{M}_s^2\,\mathcal{R}_e < 10$ and with a flatter slope for larger values (Bertoglio et al. 2001). Assuming a Reynolds number (at the injection scale, *i.e.,* hundreds of Kpc) in hot and magnetized galaxy clusters $\mathcal{R}_e \gtrsim 10^3$ (see discussion in Lazarian 2006; Brunetti 2006; Brunetti & Lazarian 2007) and a turbulent energy of the order of $\sim$ 20% of the thermal energy (as reported in Sec.5.4.1), from Fig. 8 in Bertoglio et al. (2001) one finds a reference value $\eta_t \sim 0.1$ which may be even larger in the case of compressible driving; this value sholud be taken as a viable reference value in what follows.

As a reasonable attempt we assume that a fraction, η_t, of the energy of the turbulence is in the form of MS waves. We shall consider two extreme scenarios:

i) in the first one we assume that MS waves are driven by the plasma instabilities (*e.g.,* Eilek 1979, and ref. therein) which develop in the turbulent field generated during cluster mergers. In this case MS waves may be injected over a broad range of scales. Here, we shall adopt a simple power law injection spectrum of these waves: $I(k) = I_o k^{-a}$ for $k > k_{min} \sim \pi/r_s$;

ii) in the second one, we assume that MS waves are basically injected at a single scale, $k = k_{min} \sim \pi/r_s$, from which a MHD turbulence cascade is originated.

In both cases the decay time of the MHD turbulence at the maximum/injection scale, $L_{inj} \sim 2r_s$, can be estimated as (*e.g.,* Sect.5.9.1) $\tau_{kk}(L_{inj}) \sim \frac{r_s}{\eta_t v_i}$, one has :

$$\tau_{kk}(\mathrm{Gyr}) \sim 1 \times (\frac{v_i}{2 \cdot 10^3 \mathrm{km/s}})^{-1} (\frac{r_s}{500\mathrm{kpc}}) (\frac{\eta_t}{0.25})^{-1} \tag{5.7}$$

which is of the order of a crossing time and thus allows the MHD turbulence to diffuse filling a volume of the order of that of radio halos (or larger) with a fairly uniform intensity.

In the following we focus on the first scenario, while in Sect. 5.9.1 we consider the second picture. Sect. 5.9.1 demonstrates that these two extreme scenarios lead to very similar results and thus that, in our model, the details of the injection process of the MS waves do not appreciably change the conclusions.

In the case in which a power law spectrum of MS waves is injected in the ICM, one has :

$$\int_{k_{min}}^{k_{max}} I_o k^{-a} dk = \eta_t \frac{E_t}{\tau_{cros} \times V_H} \tag{5.8}$$

with $k_{min} \sim \pi/r_s$ and $k_{max} = \Omega_p/v_M$ Ω_p being the proton cyclotron frequency and v_M the magnetosonic velocity (Eq. **??**). From Eq. (5.8) we find:

$$I_o = \begin{cases} \frac{E_{MS}}{\tau_{cros}} \times \frac{(a-1)}{V_H} k_{min}^{-(1-a)} & (r_s \leq R_H) \\ \\ \frac{E_{MS}}{\tau_{cros}} \times \frac{(a-1)}{V_H} k_{min}^{-(1-a)} \times (\frac{R_H}{r_s})^2 & (r_s > R_H) \end{cases} \tag{5.9}$$

Thus, the injection of the MS waves is obtained by combining Eqs.(5.6) and (5.9). η_t is the first free parameter of our model, in order to have a self–consistent modelling it should be $\eta_t < 1$.

In general, the spectrum of MHD waves injected in the ICM evolves due to wave–wave and wave–particle coupling. The combination of these processes produces a modified spectrum of the waves, $W_{\rm k}(t)$. As discussed in Sec.3.4.1, in the quasi linear regime the spectrum of the waves can be calculated solving a continuity equation in the wavenumber space (see Eq.3.20 in Sec.3.4.1) that here we report for seek of clarity:

$$\frac{\partial W_{\rm k}(t)}{\partial t} \frac{\partial}{\partial k} \left(D_{\rm kk} \frac{\partial W_{\rm k}(t)}{\partial k} \right) - \sum_{i=1}^{n} \Gamma^{\rm i}(k) W_{\rm k}(t) + I_{\rm k}(t)$$

In the following, we shall neglect the term due to the wave–wave interaction, $D_{\rm kk} = 0$, this is justified provided that the time–scale of the dampings, Γ, are smaller than that of the wave–wave cascade (or comparable), at least for the range of scales which contribute to the acceleration process. Under physical conditions typical of the ICM the most important damping in the collisionless regime is that with the thermal electrons (*e.g.,* Eilek 1979). An estimate of this damping rate via TTD (see Sec.3.4.2) (for $v_A < v_M$ as in the ICM) is given by Eilek (1979); a relatively simple formula that we obtain, consistent whitin a 10% with the Eilek's results [3], is:

$$\Gamma_{th,e} = \sqrt{32\pi^3}\, n_{th}\, (m_e K_B T)^{1/2} (\frac{v_M}{B})^2 \frac{W_k^B}{W_k}\, \mathcal{I}(x)\, k \tag{5.10}$$

[3]Brunetti (2006) and Brunetti & Lazarian (2007) recently derive the exact equation for the damping rate via TTD collisionless resonance which is consistent within a factor of ≈ 2 with this equation

where n_{th} is the number density of the thermal electrons, W_k^B is the turbulent magnetic energy density, $W_k^B = W_k \times (1 + 8\pi P/B^2)^{-1}$, with $P \simeq 2 n_{th} K_B T$ the thermal pressure, B the plasma magnetic field (*e.g.,* Barnes & Scargle 1973) and $\mathcal{I}(x)$ is a numerical value given by :

$$\mathcal{I}(x) = 2 \int_1^{+\infty} dx \left(\frac{1}{x} - \frac{1}{x^3}\right) e^{-[x^2 (\frac{v_M}{v_{th}})^2]} \tag{5.11}$$

where $x = \frac{p_\parallel}{m_e v_M}$, with $p_\parallel$ the component of the momentum of the thermal electrons along the magnetic field lines and $v_{th} = (2\, K_B\, T/m_e)^{1/2}$.

Since for each merger event we are interested in the evolution of the spectrum of the injected waves on a time scale of ~ 1 Gyr, which is orders of magnitude longer than the typical time scales of the damping processes, the spectrum of the waves is expected to approach a stationary solution ($\partial W_{\rm k}/\partial t = 0$). From Eq. (3.20) this solution is given by :

$$W_{\rm k} \simeq \frac{I({\rm k})}{\Gamma_{\rm th,e}(k)} = \frac{I({\rm k})}{f(T)\, k} \tag{5.12}$$

In Sect. 5.5 we will derive the efficiency of electron acceleration due to the MS waves. Here we would just point out that the acceleration time, $\tau_{\rm acc}$, depends on:

$$\tau_{\rm acc}^{-1} \propto \int_{k_{min}}^{k_{max}} k W_{\rm k} dk \tag{5.13}$$

which leads (making use of Eqs. 5.9 and 5.12) to the nice result that the acceleration time in our model, and under our assumptions, does not depend on the slope of the injection spectrum of MS waves (which depends on basically–unknown details of the injection mechanism) and on the value of k_{min}.

5.4.3 Spectrum of MS waves during cluster formation

In this Section we estimate the spectrum of MS waves resulting from the combination of the contributions of several mergers during the process of cluster formation. For a given galaxy cluster, we define z_i^j to be the redshift at which the j^{th} merger event starts. For an Einstein-De Sitter model, the corresponding time, t_i^j, is :

$$t_i^j = \frac{2}{3H_o} \frac{1}{(1 + z_i^j)^{3/2}} \tag{5.14}$$

In our simple modelling we assume that the duration time of a merger is of the order of a crossing time, $\Delta t = t^j_{cros}$, and that turbulence is injected during this time interval and then suddenly dissipated via damping processes [4]. Thus the turbulence injected during the j^{th} merger is dissipated at time $t^j_f = t^j_i + t^j_{cross}$ and the corresponding redshift is given by :

$$z^j_f = (\frac{2}{3H_o t^j_f})^{2/3} - 1 \tag{5.15}$$

We describe the spectrum of the MS–waves established during the j^{th} merger event as :

$$W^j_k(z) = W^j_k(z^j_i) \times S^j(z) \tag{5.16}$$

were $S^j(z)$ is a step function defined as :

$$S^j(z) = \begin{cases} 1 & (z^j_f < z < z^j_i) \\ \\ 0 & (\text{otherwise}) \end{cases} \tag{5.17}$$

According to the hierarchical scenario adopted in this paper, clusters undergo several merger events which contribute to the injection of turbulence yielding a combined spectrum of MS–waves. Since under stationary conditions and neglecting the wave–wave interaction term, the equation that describe the evolution of MS waves (Eq. 3.20) is a linear differential equation, and the spectrum of the MS–waves resulting from the combination of the different merger events is given by the sum of all the contributions (Eq.5.16), *i.e.,* :

$$\mathcal{W}_{\rm k}(z) = \sum_j W^j_k(z^j_i) \times S^j(z) \tag{5.18}$$

5.5 Particle Evolution and Acceleration

As discussed in Sec.3.1.3 the diffusion of relativistic particles in the ICM is negligible, so that we can safely assume that electrons injected by some mechanism in the ICM simply follow the thermal plasma and magnetic field. Under this condition, the time

[4]Note that if the injection time is slightly longer than t_{cros} then the probability to combine the effect of several mergers increases and the efficiency of the model would slightly increase (see above, Eq.5.18).

evolution of relativistic electrons with isotropic momentum distribution is provided by a Fokker-Planck equation for the electron number density, Eq.3.15, that here we report for sake of clarity:

$$\frac{\partial N(p,t)}{\partial t} = \frac{\partial}{\partial p}\left[N(p,t)\left(|\frac{dp}{dt}|_{\rm rad} + |\frac{dp}{dt}|_{\rm c} - \frac{2}{p}D_{\rm pp}\right)\right] + \frac{\partial}{\partial p}\left[D_{\rm pp}\frac{\partial N(p,t)}{\partial p}\right] + Q_e(p,t)$$

Here we consider the case of the MS waves, thus the term due to statistic energization of particles, $D_{\rm pp}$, in Eq.3.15 is the electron diffusion coefficient in the momentum space due to the interaction with the MS waves, the terms $dp/dt_{\rm i}$ and $dp/dt_{\rm rad}$ are the terms due to ionization and radiative losses (see Sec.3.1.2), and Q_e is an isotropic electron source term.

Independently from the specific scenario adopted for the injection of relativistic particles (see Sec.3.1.1), a power law spectrum for the injection rate of relativistic electrons up to a maximum momentum, $p_{\rm max}$, can be reasonably assumed in the form:

$$Q_{\rm e}(p,t) = K_{\rm e}(t)p^{-s} \tag{5.19}$$

This injection is necessary to merely provide a reservoir of supra-thermal electrons to be re-accelerated. We parameterize the injection rate by assuming that the total energy injected in cosmic ray electrons (for $p > p_{\rm min}$) during the cluster life up to the present epoch, is a fraction, η_e, of the total thermal energy of the cluster at $z = 0$, *i.e.,* :

$$\eta_e = \frac{c}{\mathcal{E}_{\rm th}}\int_{t=t(z)}^{t=t(0)} d\tau \int_{p_{\rm min}}^{p_{\rm max}} Q_e(p,\tau)\, p\, dp \tag{5.20}$$

where $\mathcal{E}_{\rm th}$ is the present day thermal energy density of the ICM. The injection rate should depend on the number and energetics of AGNs and GWs in galaxy clusters which are expected to be considerably larger at high redshifts. However, since electrons injected at relatively high redshifts cool very rapidly because of the combination of high energy losses and low efficiency of the particle acceleration mechsnism (Fig. 5.7), only the electrons injected at relatively low redshifts can be re-accelerated and therefore contribute to the non-thermal emission observed at low redshift ($z < 0.2$) which is the focus of this Chapter. As a simplification, we adopt

a constant injection rate of electrons so that (for $s > 2$) the normalization of the spectrum of the injection rate is simply given by :

$$K_{\rm e} \sim \frac{s-2}{c} \eta_e \mathcal{E}_{\rm th} p_{\rm min}^{s-2} \tau_H^{-1} \tag{5.21}$$

where τ_H is the Hubble time. η_e is the second free parameter in our model. In the following we use $s = 2.5$, $p_{\rm min}/mc = 60$, and $p_{\rm max}/mc = 10^4$; as we will discussed in Sect. 5.8 the basic results of our model do not depend on the values adopted for these parameters.

In a isotropic distribution of waves and particle momenta the diffusion coefficient in the momentum space, for $v_A < v_M$, is given by Eilek (1979). This can be expressed as[5]:

$$D_{\rm pp}(p,t) \simeq 4.45\,\pi^2\,\frac{v_M^2}{c}\,\frac{p^2}{B^2}\int_{k_{min}}^{k_{max}} k \mathcal{W}_k^B(t) dk \tag{5.22}$$

Where $\mathcal{W}_k^B = \mathcal{W}_k \times (1 + 8\pi P/B^2)^{-1}$ with $\mathcal{W}_k$ given by Eq. 5.18. The acceleration time scale, which in this case does not depend of the particle energy, is given by :

$$\tau_{\rm acc}^{-1} = \chi \simeq 4\frac{D_{\rm pp}}{p^2} \tag{5.23}$$

and thus the systematic energy gain of particles interacting with MS waves is given by :

$$\left(\frac{dp}{dt}\right)_{\rm acc}^{sys} = \chi\, p \tag{5.24}$$

In our calculations we focus on the population of relativistic electrons, do not consider proton acceleration, and neglect the effect of these particles on the efficiency of the electron acceleration. The resonance condition $v_M k = k_\parallel v_\parallel$ implies that only a very small fraction of MS waves (those making an angle ∼89–91 degrees with the local B-field) cannot be damped by the thermal electrons, but only by the relativistic particles (protons and electrons), while outside this narrow cone the damping due to the thermal electrons should be the strongest one (*e.g.,* Eilek 1979, see also Brunetti & Lazarian 2007 for a detailed discussion). As a consequence, since in our calculations we assume a continuous pitch angle isotropization (*e.g.,* Miller et

[5]Most recently Brunetti & Lazarian (2007) calculated the exact expression for $D_{\rm pp}$ due to TTD collisionless resonance. In the typical physical conditions of the ICM their derivation is equivalent for physical dependences with Eq.5.22 and is also consistent within a factor of ≈ 2 in normalization.

al. 1996) and an isotropic distribution of MS waves which propagate in a complex geometry of the field lines, the damping of MS waves should be dominated by the effect due to the thermal electrons in the ICM.

As an example, we assume that MS waves are injected in the central $\sim$1 Mpc^3 of a massive cluster for 0.5–1 Gyr with a total energy budget of the order of that of the thermal ICM within the same region. We calculate particle acceleration and find that about $\sim 4-10\%$ of the energy flux of these waves is channelled into the acceleration of relativistic protons (assuming an initial energy density of these particles of the order of few % of the thermal energy density and $N_p(p) \propto p^{-2.2}$): this corresponds to $\leq 1\%$ of the total thermal energy of the cluster. At the same time, we find that only $\sim 0.1\%$ of the energy flux of the MS waves should be channelled into the acceleration of relativistic electrons to produce an HXR luminosity of $\sim 10^{43}$erg s^{-1} from the same volume ($\eta_e \sim 0.003$, Fig.5.8). Consequently the $90-95\%$ of the energy flux of the MS waves is channelled into the thermal electrons and thus the resulting spectrum of these waves may be estimated with good approximation by Eq.(5.12).

Detailed time dependent calculations which include electron and proton acceleration due to MS waves and a comparison with the case of Alfvén waves can be found in Brunetti & Lazarian (2007).

5.6 Radio Halos and HXR tails

5.6.1 Cluster evolution and electron spectrum

In this Section we combine the formalism developed for the evolution of the turbulence (Sects. 5.3 & 5.4) with the recipes for particle acceleration and evolution (Sec. 5.5) to model the cosmological evolution of the spectrum of the relativistic electrons in galaxy clusters.

The electron–acceleration coefficient, due to the effect of MS waves at redshift z, is obtained by combining Eq. (5.23) with Eqs. (5.22, 5.9, 5.12, 5.18):

$$\chi(z) \simeq \frac{2.23\times10^{-16}\eta_t}{(R_H/500\mathrm{kpc})^3}\sum_j\left[\left(\frac{M_{max}+M_{min}}{2\times10^{15}M_\odot}\,\frac{2.6\mathrm{Mpc}}{R_{max}}\right)^{3/2}\times\frac{(r_s/500\mathrm{kpc})^2}{(kT/7\mathrm{keV})^{1/2}}\right]_j\times\left\{\begin{array}{ll}1 & \text{if } r_s\leq R_H\\ (R_H/r_s)^2 & \text{if } r_s>R_H\end{array}\right\}_j \tag{5.25}$$

where only mergers which contribute to the turbulence spectrum at redshift z (Sect. 5.4.3, Eq.5.18) are considered. The evolution of the electron spectrum is thus obtained from the numerical solution of the Fokker-Planck equation (Eq. 3.15) by adopting the values of the coefficient D_{pp} (Eq. 5.23 and Eq. 5.25) and of the energy loss terms (Eqs. 3.1–3.2) at each redshift.

In Fig. 5.7 we report an example of the time evolution of the electron–acceleration coefficient obtained for a typical massive cluster (top panel) and the corresponding spectra of the electrons at different relevant times (bottom panel): an increase of the acceleration coefficient produces an increase of the maximum energy of the electrons. The reported results indicate that cluster–merger activity at low redshift can generate an increse of the cluster turbulence which may be sufficient to accelerate electrons up to $\gamma >> 10^3$, necessary to produce synchrotron radiation in the radio band. It should be noticed that electrons are accelerated (and cool) with a delay time (of the order of the corresponding electron–acceleration time $\sim \chi^{-1}$) with respect to the abrupt increases (decreases) of the values of the acceleration coefficient. *We also noticed that the electron number density at* $\gamma \geq 10^3$ *during the re-acceleration period is boosted by 2-3 order of magnitude with respect to the injection case without re-acceleration* ($z = 0.01$ or $z = 0.02$ versus $z = 0.45$ in Fig.5.7).

In Fig.(5.8) we show the broad band non–thermal emission (synchrotron and IC) from the galaxy cluster reported in Fig. 5.7 assuming $\eta_e = 0.003$ and $B = 0.5\mu$ G. *The aim of this Figure is to show that synchrotron (and IC) luminosities of the order of those of the most luminous radio halos can be reasonably obtained* (see Sec.5.8). On the other hand, it should be stressed that the synchrotron spectrum reported in Fig.(5.8) is obtained assuming a constant value of B through the cluster volume. More reasonable calculations should assume a radial gradient of the magnetic field strength which causes a stretching in frequencies of the synchrotron spectral shape with respect to that of Fig.(5.8) (*e.g.,* Brunetti et al. 2001a; Kuo et al. 2003).

The synchrotron emitted power from radio halos is expected to increase with increasing the mass of the parent clusters. Indeed the bolometric synchrotron power roughly scales as $P_{\rm R} \propto B^2 \gamma_{\rm b}^2 n_{\rm e} R_H^3$, where $\gamma_b = \chi/\beta$ is the maximum energy of the accelerated electrons (β is the total energy–loss coefficient, Eq. 3.2) and $n_{\rm e}$ is the number density of relativistic electrons in the cluster emitting volume. During major

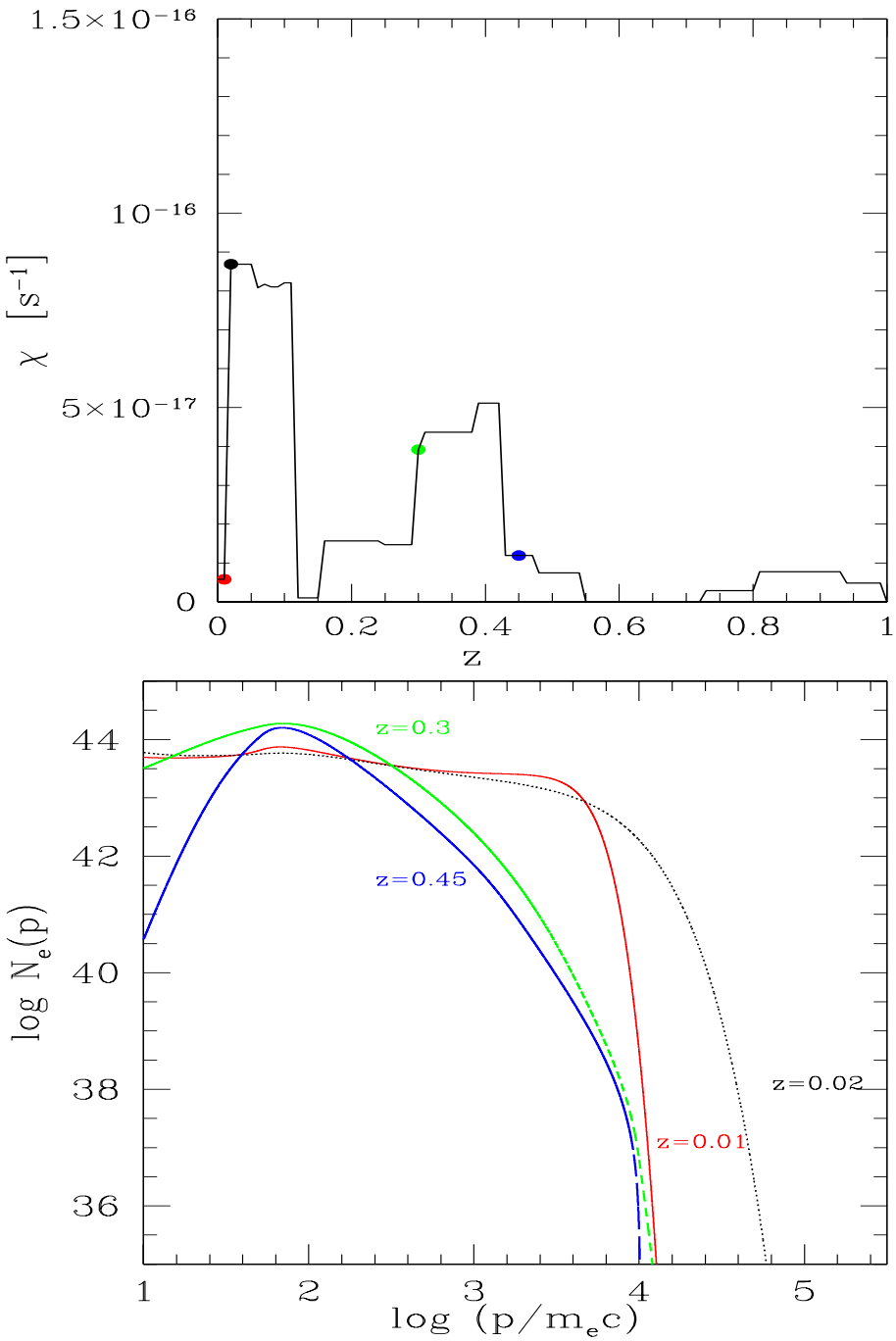

Figure 5.7: **Top panel**: evolution with redshift of the electron-acceleration coefficient due to MS waves as obtained from Eq.5.25 for a cluster of $M_0 = 1\times10^{15} M_\odot$ at the present time. **Bottom panel**: electrons spectra (in arbitrary units) calculated at different redshifts (also marked in the top panel) for the same cluster. Calculations are performed for $s = 2.5$, $B = 0.5\mu$G, and $\eta_t = 0.26$.

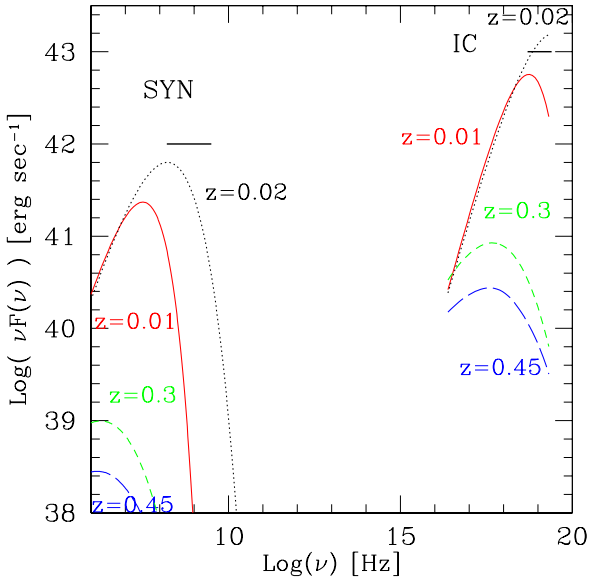

Figure 5.8: Broad band synchrotron (SYN) and Inverse Compton (IC) spectra calculated for the case reported in Fig.5.7 and for $\eta_e = 0.003$, $R_H = 500$ kpc, and $B = 0.5\mu$G. Horizontal bars give the radio (used for radio halos) and HXR observational range of frequencies.

mergers, from Eq.(5.25, with $T \propto M^{\Gamma}$, $\Gamma \sim 0.56 - 0.67$) one has :

$$P_{\rm R} \propto \frac{n_{\rm e} M_v^{2-\Gamma}\, B^2}{(B^2 + B^2_{\rm cmb})^2}\, g(r_s, R_H) \qquad (5.26)$$

where $g(rs, R_H)$ ($g = r_s^4/R_H^3$ for $r_s \leq R_H$ and $g = R_H$ for $r_s > R_H$) is a slightly increasing function of cluster mass. We will further investigate the expected correlations for giant RHs in the framework of the re-acceleration model in the next Chapter.

5.6.2 Basic constraints on the required values of η_t and η_e

As stressed in Sec.5.1 it is important to understand which are the physical requirements in the model in order to match the basic properties of RHs & HXR tails. In this Section we derive the range of values of the two free parameters of our model, η_t and η_e, which provide a reasonable agreement with the general properties of radio halos. In order to check the reliability of the obtained values, these are then compared with independent findings and general expectations from both analytical and numerical calculations.

The first free parameter is η_t which is defined as the fraction of the fluid turbulence in MS waves. The value of η_t drives the efficiency of the electron acceleration and thus the resulting maximum energy of electrons, $\gamma_b = \frac{\chi}{\beta}$, ($\beta$ is the total energy–loss coefficient, Eq. 3.2), and the maximum synchrotron emitted frequency $\nu_b = \frac{3}{4\pi}\frac{eB}{m_e c}\gamma_b^2$. Under the assumption that the losses of the electrons are dominated by the IC mechanism, the acceleration coefficient is thus related to the break frequency by :

$$\chi \simeq 6.3 \times 10^{-21} \nu_b^{1/2} B_{\mu G}^{-1/2} (1+z)^4 \tag{5.27}$$

The values of η_t are constrained by requiring that the accelerated electrons can produce synchrotron radiation in the radio band with the spectral shape observed in the case of radio halos, *i.e.,* with spectral index $\alpha = 1.1 - 1.5$ between 327 and 1400 MHz (*e.g.,* Kempner & Sarazin 2001). The synchrotron spectral index between two fixed frequencies depends on the value of ν_b and also on the shape of the spectrum of the emitting electrons. Given the typical shape of the spectrum of the emitting electrons accelerated during cluster mergers in our calculations, we are able to estimate the minimum typical value of ν_b necessary to account for the spectral indices of the observed radio halos: $\nu_b > 200$ MHz is obtained. From Eq. (5.27), this limit translates into a limit on χ (given in Eq.5.25) :

$$\chi(\eta_t) \gtrsim \chi_{min} = 7.4 \times 10^{-17} (1+z)^4 \left(\frac{B_{\mu G}}{0.5}\right)^{-1/2} s^{-1} \tag{5.28}$$

Radio halos have a typical radius $R_H \sim$500 Kpc and they are found in massive galaxy clusters (M $\gtrsim 10^{15} M_\odot$). Thus we derive the value of χ for these typical clusters in our synthetic population and find that $\eta_t = 0.2 - 0.3$ is required to satisfy the condition of Eq. (5.28) during major mergers (at $z < 0.2$; $B \sim 0.5\mu$G is adopted). This is the first important result of our modelling since *it basically proves that if a fraction of the kinetic energy of cluster mergers is channelled into MS waves then this is sufficient to power particle acceleration in the ICM with the efficiency requested in the case of radio halos.* Although there are no numerical studies which are aimed at a detailed investigation of the cluster turbulence injected during merging processes, a general finding of high resolution numerical simulations

[5] $\nu_b > 200$ MHz gives $\alpha_{327}^{1400} \sim 1.5$ for a typical re-accelerated electron spectrum.

is that a relevant fraction (10-30 %) of the thermal energy in galaxy clusters is in the form of compressible plasma turbulence (*e.g.,* Sunyaev et al. 2003 and ref. therein).

The second free parameter in our model is η_e which gives the ratio between the energy injected in relativistic electrons during the cluster life and the present day thermal energy of the ICM. The values of η_e can be constrained by requiring that the model reproduces the typical radio (L_R) and hard-X ray (L_{HX}) luminosities observed in galaxy clusters: $L_R = 10^{40} - 10^{41}\mathrm{erg}s^{-1}$ (Feretti 2003) and $L_{HX} = 10^{43} - 10^{44}\mathrm{erg}s^{-1}$ (Fusco-Femiano et al. 2003). We derive the requested values for typical massive galaxy clusters in our synthetic population during the time intervals in which the condition of Eq. (5.28) is satisfied; we find that $\eta_e = 10^{-4} - 10^{-3}$ is sufficient to match the observed luminosities at $z < 0.2$ ($B \sim 0.5\mu$G is assumed). *The above η_e–values are very reasonable for massive clusters (e.g., Sect.3.1.1) and they are also much smaller than those assumed in other modellings of non–thermal emission from galaxy clusters* (*e.g.,* $\eta_e \simeq 0.1$, Sarazin 1999). This is mainly because in our model the resulting spectrum of the emitting electrons during an efficient acceleration period is not a simple power law, but it is peaked at the energies required to emit the synchrotron and IC radiation (*e.g.,* Fig. 5.8) and this strongly increases the emitting efficiency (see also Sec.5.8) at a given frequency.

5.7 Statistics and Comparison with Observations

As discussed in Sec.5.1 it is important to compare the results based on the re-acceleration model with the observed occurrence of RHs. *In Sec. 5.6.2 we have essentially derived a criterion for radio halo formation: clusters may have radio halos if $\chi(\eta_t) \geq \chi_{min}$.* With the observing frequency fixed at $\approx$ 1 GHz smaller values of χ will generate RHs with a spectrum too steep (essentially above a cut-off) and they cannot be detected in present surveys. By making use of this criterion, the goal of this Section is to calculate the formation probability of radio halos with cluster mass and to compare expectations with observational constraints.

In order to have a prompt comparison with observations we calculate the formation probability in the redshift bin z=0–0.2 for three mass bins of the parent clusters ΔM: $< 9 \times 10^{14} M_\odot$, $9 \times 10^{14} < M < 1.8 \times 10^{15} M_\odot$, and $1.8 \times 10^{15} < M < 3.6 \times 10^{15} M_\odot$, which are consistent with the luminosity bins adopted to draw the observed statistics (Giovannini et al. 1999; Giovannini & Feretti 2002, ; Sect.).

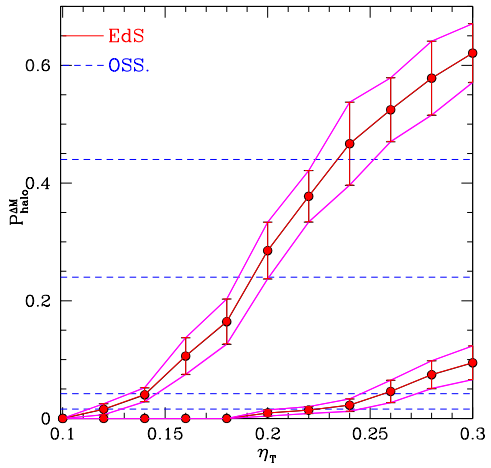

Figure 5.9: Expected formation probability of radio halos ($R_H \simeq 500$ kpc, $B \sim 0.5\mu$G) in a EdS cosmology as a function of parameter η_t in two different mass bins (solid lines with error bars): binA= $[1.8 - 3.6]\,10^{15} M_\odot$ and binB= $[0.9 - 1.8]\,10^{15} M_\odot$. The two bottom dashed lines mark the observed probabilities for radio halos in the mass binB while the two top dashed lines mark the observed probabilities in the mass binA. The two reported observational ranges account for 1σ errors. The theoretical errors are estimated by extracting sub-samples of galaxy clusters from the synthetic population with a Monte Carlo procedure.

First we run a large number, $\mathcal{N}$, of trees for different cluster masses at $z = 0$, ranging from $\sim 10^{14} M_\odot$ to $\sim 10^{16} M_\odot$. Thus, for each M, we estimate the formation probability of radio halos in the mass bin ΔM as :

$$f_M^{\Delta M,\,\Delta z} = \frac{\sum_{j=1}^{\mathcal{N}} t_u^j}{\sum_{j=1}^{\mathcal{N}} (t_u^j + t_d^j)} \tag{5.29}$$

where t_u is the time that the cluster spends at $z < 0.2$ in the mass bin ΔM with $\chi \geq \chi_{min}$[6] and t_d is the time that the same cluster spends in ΔM with $\chi < \chi_{min}$.

Thus the total probability of halo formation in the mass bin ΔM is obtained by combining all the contributions (Eq. 5.29) weighted with the present day mass function of clusters.

We consider two possible cluster mass functions: the PS mass function (Eq.1.66) and the Sheth & Tormen (1999, ST) mass function, which is obtained from a fit to numerical simulations and which predicts smaller and larger values of the cluster number density for small and large masses, respectively (see also Sec. 1.4.5). We

[6]Since clusters in our synthetic population never have $\chi >> \chi_{min}$, the condition $\chi \geq \chi_{min}$ guarantees a synchrotron spectral index compatible with that of radio halos.

checked that the probability to have a radio halo obtained by making use of the PS and ST mass functions are consistent within few percent for the considered mass bins.

In Fig. 5.9 we plot the occurrence of radio halos with a typical radius $R_H \sim 500$ kpc as a function of η_t compared with the observated statistics (see caption). We find that the relatively high occurence of radio halos observed in massive clusters can be well reproduced by our modelling under very reasonable conditions, *i.e.* that a fraction of 20-30% of the energy of the turbulent motions (about few percent of the thermal energy) is in the form of compressible MS waves. In addition, we find that there is a range of values of the parameter η_t ($0.2 \leq \eta_t \leq 0.26$, for $B \sim 0.5\mu$G) for which the theoretical expectations are in agreement with the observed statistics in both the considered mass bins: $\sim 30\%$ and $\sim 4\%$ in the high and medium mass bins considered, respectively. Finally, we find that the expected probability to form giant radio halos in smaller clusters (not reported in Fig. 5.9) is negligible, in agreement with present observations.

5.7.1 The case of a ΛCDM cosmology

We compare the model results obtained with a EdS cosmology with those obtained assuming a ΛCDM cosmology. In particular we use $\Omega_m(0) = 0.3$, $\Omega_\Lambda(0) = 0.7$, $\sigma_8 = 0.9$ and $h_0 = 0.7$ and discuss the differences with the EdS case.

In the ΛCDM cosmology the critical overdensity as a function of the cosmic time which enter in the equation for the computation of the merger trees (in Eq.1.67 in Sect.1.4.4) is given by Eq.1.56 and the ratio of the average density of the cluster to the mean density of the universe at a given z, $\Delta_c(z)$ (in Eq.(1.52)), in the ΛCDM model is given by Eq.1.53.

Following the procedures adopted in the case of the EdS cosmology, we compute merger trees (Sect. 5.3), turbulence injection rate and spectrum of the MS waves (Sect. 5.4), particle evolution (Sect. 5.5) and non-thermal emission (Sect. 5.6) from galaxy clusters and thus the expected formation probability of radio halos for $z < 0.2$ (Sect. 5.7). In Fig.5.10, we report the comparison between the probability to form radio halos obtained in the two cosmologies. The comparison is derived by converting the virial mass of the clusters from a EdS into a ΛCDM model:

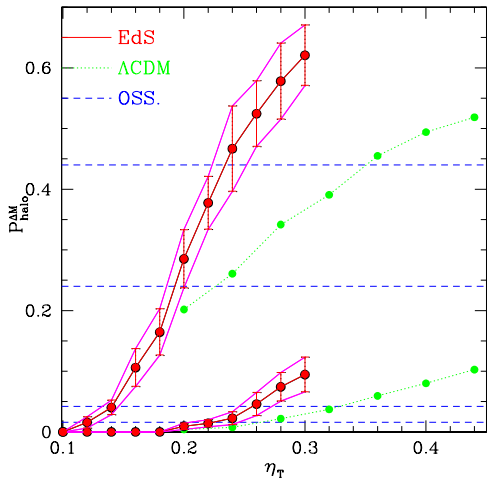

Figure 5.10: Expected formation probability of RHs ($R_H \simeq 500 h_{50}^{-1}$kpc, $B \sim 0.5\mu$G) as a function of parameter η_t in a EdS cosmology (solid lines with error bars) and in a ΛCDM cosmology (dotted lines) in the mass bins: binA=$[1.8 - 3.6]\, 10^{15} M_\odot\, h_{50}^{-1}$ and binB=$[0.9 - 1.8]\, 10^{15} M_\odot\, h_{50}^{-1}$ for EdS case and binA=$[1.9 - 3.8] \cdot 10^{15}$ $M_\odot h_{70}^{-1}$ and binB=$[0.945 - 1.9] \cdot 10^{15}$ $M_\odot h_{70}^{-1}$ for the ΛCDM model. The two bottom dashed lines mark the observed probabilities for radio halos in the mass binB while the two top dashed lines mark the observed probabilities in the mass binA; observational regions account for 1σ errors.

$$M_v^\Lambda = M_v^{EdS} \times \left(\frac{[\Delta_c(t)\rho_m(t)]_{EdS}}{[\Delta_c(t)\rho_m(t)]_\Lambda} \right)^{1/2} \tag{5.30}$$

where ρ_m is the mean mass density of the Universe. Thus the calculations with a ΛCDM model are performed for the mass bins $[0.945 - 1.9] \cdot 10^{15}$ $M_\odot h_{70}^{-1}$ and $[1.9 - 3.8] \cdot 10^{15}$ $M_\odot h_{70}^{-1}$.

As expected, we find that at $z < 0.2$ *the results are relatively independent from the considered cosmology*, with the ΛCDM model being only slightly less efficient. In particular, as in the EdS case we note that it is possible to find a unique interval in η_t in which the model reproduces the observed halo formation probability for both the cluster-mass bins.

In the ΛCDM Universe the structures start to grow at early time with respect to the EdS case (see also Sec.1.4.1), the merging rate at $z < 0.2$ is consequently reduced, and thus particle acceleration is less efficient. However, this is roughly compensated by the fact that in a ΛCDM Universe ($H_o = 70$ km s^{-1}Mpc^{-1}) the observed radio halos are "smaller" and "less luminous" than in our EdS case ($H_o = 50$ km s^{-1}Mpc^{-1}).

5.8 Summary and Discussion

Crucial constraints on the origin of radio halos are provided by statistical studies which show a connection between the formation of these sources and cluster mergers, and also find an abrupt increase of the occurence of radio halos with the mass of the parent clusters.

- The first goal of the this Chapter was to check if cluster turbulence generated during mergers may be able to drive efficient particle acceleration processes in the ICM.

- The second goal, in the framework of the turbulent-acceleration hypothesis, was to investigate if the hierarchical formation process of galaxy clusters can naturally account for the increase of the radio halos' occurrence with cluster mass.

To achieve these goals we have developed a statistical method based on the following steps :

i) Extensive merger trees of galaxy clusters with different present day masses are obtained. The trees are calculated making use of a procedure of *Binary Merger Tree Method* which is based on the extended PS formalism (Sec. 1.4.4). The temperature of the ICM is estimated at each redshift from the observed M-T relationships.

ii) Cluster turbulence is assumed to be injected during cluster mergers by the crossing of the infalling subclusters into the larger ones. To be conservative, turbulence is assumed to be injected in the major subcluster only within the volume sweeped by the minor subcluster (Sec. 5.4). The injection rate of MS waves is assumed to be a fraction, $\eta_{\mathbf{t}}$, of the turbulence injection rate. Although cluster-cluster mergers are the best candidates to the injection of turbulence on large scales, it should be noticed that additional events (*e.g.,* AGN, galaxies; Deiss & Just (1996)) might inject an additional turbulent component, thus our scenario should be considered as "conservative".

The injection spectrum of MS waves is assumed to be a simple power law which extends over a broad range of scales (Sec. 5.4), or a delta–function from which turbulent cascade is originated (Sect.5.9.1). In both cases the maximum/injection scale is fixed at $L_{inj} \sim 2r_s$. The resulting spectrum of MS waves is then calculated assuming stationary conditions within a crossing time

for each merger and by taking into account the relevant damping processes (or cascading processes) in the ICM (Sec. 5.4). The evolution of the spectrum of MS waves during cluster formation is calculated by combining the effect of all mergers.

iii) The evolution of relativistic electrons in galaxy clusters is calculated considering the acceleration by MS waves and the energy losses. Relativistic electrons are assumed to be continuously injected in the ICM by shocks, AGNs and star forming galaxies in the clusters during their life, and this provide the necessary budget of supra-thermal electrons to be re-accelerated. The total energy injected in the relativistic electrons during the cluster life up to $z = 0$ is assumed to be a fraction, $\eta_{\mathbf{e}}$, of the thermal energy of the clusters at the present epoch. We do not follow the evolution of the relativistic hadronic component since the most important damping of MS waves is with thermal electrons (Sec. 3.4.2) and thus the relativistic hadrons do not affect significantly the electron-acceleration process.

To match the redshift range spanned by observational studies we calculate the model expectations for $z < 0.2$. The comparison between model and observations is performed in two main steps :

i) First we consider the case of a typical massive cluster of our synthetic population and calculate the expected synchrotron and inverse Compton emission as a function of η_t and η_e. We find that *the typical radio luminosity of radio halos and the HXR luminosities can be obtained by our model provided that a fraction of the cluster turbulence,* $\eta_t \sim [0.2 - 0.3]\,(B_{\mu G}/0.5)^{-1/2}$ ($B_{\mu G}$ being the volume averaged field strength within R_H in units of μG), *is channeled into MS waves during major mergers and that the energy injected into relativistic electrons is* $10^{-3} - 10^{-4}$ *times the present energy of the thermal pool* (Sec.5.6.2, see also the discussion below).

ii) Then, we compute the occurence of radio halos with the mass of the parent clusters. More specifically, we estimate a threshold for the particle acceleration coefficient, χ_{min}, which is required to efficiently boost the accelerated electron population and produce radio emission with the spectral slope typical of radio halos. We thus identify the galaxy clusters containing a radio halo as

those clusters in our synthetic population for which $\chi \geq \chi_{min}$ (see Sec. 5.7 for details). The radio halos' occurrence is calculated in three mass bins consistent with those adopted in observational studies ($< 9 \cdot 10^{14} \mathrm{M}_{\odot} \mathrm{h}_{50}^{-1}$, $9 \cdot 10^{14} - 1.8 \cdot 10^{15} \mathrm{M}_{\odot} \mathrm{h}_{50}^{-1}$, and $1.8 \cdot 10^{15} - 3.6 \cdot 10^{15} \mathrm{M}_{\odot} \mathrm{h}_{50}^{-1}$). We find that *for a single range of values of η_t it is possible to account for the observed probabilities in all the three mass bins: about $\sim 30\%$ and $\sim 4\%$ in the larger and medium mass bins, respectively, while the probability to find a radio halo in a cluster with mass $< 9 \cdot 10^{14} M_{\odot} h_{50}^{-1}$ is found to be negligible.*

As a general conclusion *we find that the model expectations are in good agreement with the observational constraints for viable values of the two free model parameters: η_t, η_e.*

We also find that given these parameters and the physical conditions in the ICM, the cascade time of the largest eddies of the MHD turbulence is of the order of $\sim$1 Gyr. Consequently the diffusion and transport of these large scale eddies and waves may give a fairly uniform turbulent intensity within a relatively large volume ($\geq R_H$). Finally, we find that the two extreme scenarios considered in our model, *i.e.* an injection of the MS waves with a power law spectrum, or with a single scale delta–function, provides very similar results since the process of particle acceleration basically depends on the energy flux injected into MS waves (which is dissipated at collisionless scales) and on the physical conditions in the ICM (Sect. 5.9.1).

Thus, although the necessary approximations adopted in our formalism, we have shown that particle acceleration processes, which are invoked to explain the morphological and spectral properties of RHs, can also account "self-consistently" for the statistical properties of this class of objects.

The following important items need some further discussion:

• Why the occurrence of RHs increases with cluster mass?

An important finding of our calculations is that only massive clusters can host giant radio halos ($R_H \geq 500$ kpc) and that the probabilty to form these diffuse radio sources presents an abrupt increase for clusters with about $M \geq 2 \times 10^{15} M_{\odot}$.

Fig. 5.3and Fig. 5.5a show that the energy of the turbulence injected in galaxy clusters is expected to roughly scale with the thermal energy of the clusters. This seems a reasonable finding which immediately implies that the energy density of the turbulence is an increasing function of the mass of the clusters, $\mathcal{E}_t \propto T \propto M^a$. In

addition, in the case of clusters with mass $M < 10^{15} M_{\odot}$ the infall of subclusters through the main one injects turbulence in a volume V_t smaller than that of giant radio halos, V_H, and thus the efficiency of the mechanism is reduced by about a factor of V_t/V_H (Sect. 5.4.1). On the other hand, major mergers between massive subclusters are expected to inject turbulence on larger volumes, of the order of V_H (or larger, *e.g.,* Fig. 5.4b), and thus the efficiency of the generation of radio halos is not reduced.

More quantitatively, focussing for simplicity on what happens during a single merger event, the efficiency of the particle acceleration in the fixed volume $V_H = 4\pi R_H^3/3$ can be derived from Eq.(5.25) : $\chi \propto g(r_s, R_H)(M/R)^{3/2}/\sqrt{T}$, where the term $T^{-1/2}$ is due to the stronger damping of MS waves on thermal electrons with increasing the temperature of the ICM (Eq. 5.10). Thus the acceleration efficiency within V_H is found to scale about with $\chi \propto M^{1-a/2} g(r_s, R_H) \propto M^{0.75-1.25}$ (0.75 for $M \geq 3 \cdot 10^{15} M_{\odot}$, 1.25 for $M < 10^{15} M_{\odot}$) and is thus an increasing function of cluster mass.

Future radio studies (with LOFAR, LWA and SKA) will be crucial to constrain the occurrence and evolution of the observed non–thermal diffuse emission in galaxy clusters expecially in the case of less massive clusters, and thus to perform a more stringent comparison between observations and model expectations.

• Turbulence on scale larger than R_H and HXR tails.

Several mechanisms can provide injection of turbulence in the ICM during cluster mergers. We have just followed a simple approach which allows us to estimate the injection of turbulence during the crossing of smaller clusters through the more massive ones. It should be reminded that in the calculations we have adopted a typical radius of a radio halo, $R_H \sim 500$ kpc, and assumed that turbulence injected in a smaller volume is diffused on the scales of the radio halo, while the effect of the turbulence injected outside R_H is not considered. However, the stripping radius, in the case of major mergers between very massive subclusters, can be larger than $R_H \sim 500$ kpc and thus the turbulence injected by these massive mergers can power particle acceleration also on larger scales. *The relativistic electrons accelerated at these scales can significantly contribute to the IC spectrum and thus the IC luminosities given in this Chapter (e.g., Fig. 5.8) may be underestimated.* On the other hand, the volume integrated synchrotron spectra should be mainly

contributed by the emission produced within R_H due to the expected decrease of the magnetic field strength with radius. Thus our results, which are essentially based on the synchrotron properties of radio halos, should not be affected by the presence of non–thermal emission from very large scales.

• How many energy in relativistic electrons is really necessary?
An important result of this work is that the energy which should be injected in relativistic electrons in the volume of galaxy clusters is of the order of a few $10^{-4} \times (B_{\mu G}/0.5)^{-2}$ of the present day thermal energy of the ICM. This value basically depends on the balance between the electrons' energy losses and the turbulent–acceleration efficiency which is experienced by the relativistic electrons injected in the ICM during the last few Gyrs. Since our calculations are performed by assuming the physical conditions of the ICM as averaged over the cluster volume, the required injected energy in relativistic electrons may be substantially higher in the central regions of the clusters where the high density of the thermal plasma causes stronger Coulomb losses. We notice that the required values of η_e can be easily provided by considering the injection of relativistic electrons in the ICM from AGNs, galactic winds, and large scale shocks (*e.g.,* Biermann et al. 2003 for a review).

The requested values of the energy injected in relativistic electrons in the ICM are calculated thorugh the paper by assuming $s = 2.5$ and $p_{\rm min}/mc = 60$. The results however should not be very sensitive to these assumptions, and they would be only sensitive to the total number of relativistic electrons injected in the ICM during the cluster life. Indeed, the turbulence experienced in the ICM basically increases the cooling time of the injected electrons which are then mantained at the peak of their *cooling–time curve* (*i.e.,* at $\gamma \sim 100 - 200$, *e.g.,* Sarazin 1999) and thus boosted at higher energies during an efficient re–acceleration period. In order to test the poor dependence of our results on the assumptions on s and $p_{\rm min}$, we re–calculate the value of η_e by assuming $s = 2.2 - 3.0$ and $p_{\rm min}/mc = 20 - 100$. We find that different assumptions require values of η_e within a factor of ~ 3 to reproduce a given synchrotron power. In particular we find that η_e decreases with increasing s (or with decreasing $p_{\rm min}$).

It should be stressed that the amount of injection of relativistic electrons required by our model is orders of magnitude smaller than that needed by models which

assume a simple continuous injection of a power law energy distribution of the emitting electrons in the ICM (*e.g.,* Sarazin 1999). This is mainly because during an efficient acceleration period the spectrum of the relativistic electrons is not a steep power law in which the bulk of the electrons is at low energies. During this period the bulk of the electrons, accumulated at $\gamma \sim 100 - 300$, is boosted at higher energies and essentially piled up in the energy range responsible for the synchrotron emission in the radio band.

• Comments on the magnetic field

Since the present work is not aimed at reproducing in detail the properties of radio halos, in our calculations we assume that the magnetic field strength (within R_H) is roughly constant ($B \sim 0.5\mu$G is assumed to constrain η_t and η_e). Larger values of B (but still under the conditions in which the radiative cooling of electrons is dominated by IC emission, *i.e.* $B < 3\mu$G) would allow to radiate the synchrotron photons at higher frequencies (Eq. 5.28) and this would imply that lower values of η_t ($\eta_t \propto B^{-1/2}$, Sec. 5.6.2) are required to form radio halos. On the other hand, the discovery of HXR tails in galaxy clusters has revealed that the non–thermal spectra of these objects are dominated by the IC component which has a luminosity $\sim 10^3$ times larger than the synchrotron component. These observations indicate that the volume–averaged magnetic field strength should be $< 0.5\mu$G (*e.g.,* Fusco–Femiano et al., 2003). However, as discussed above, a relevant contribution to the IC spectrum of galaxy clusters can be provided by electrons accelerated by turbulence injected in the outer regions ($\geq R_H$) and thus values $B \gtrsim 1\mu$G in the synchrotron emitting volume may be still compatible with the observed IC components. A detailed investigations of the dependence of the ratio between synchrotron and IC power can be found in Brunetti et al. (2001a), Brunetti (2003), Kuo et al. (2003), Colafrancesco et al. (2005).

• Size of RHs versus cluster mass

As already stated in the model calculations we have assumed a typical mean radius of the radio halos and a value of the magnetic field strength B which are independent from the mass of the parent clusters. If radio halos in more massive clusters are larger than those in smaller ones (see Sec.**??**), then this approach should underproduce the expected probability to find radio halos in the smaller clusters with respect to the larger ones. *The fact that the values of η_t required to match observations in the*

intermediate mass bin are found to be slightly larger than those in the more massive bin (Figs.5.9 and 5.10) *may reflect this effect.* On the other hand, if B increases with the mass of the parent clusters (with $B \leq 3\mu$G) then the synchrotron emission would be boosted at higher frequencies and the expected probability to find radio halos in the case of larger clusters would be slightly increased with respect to our present expectations. In the next Chapter we will model the more complex case of a B which scale with cluster mass.

• **Cosmology**

Finally, the model results obtained with a EdS cosmology have been compared with those obtained assuming a ΛCDM cosmology. We find that the possibility to explain the observations in the redshift bin $0-0.2$ does not depend critically on the adopted cosmology. In particular, although the model is found to be slightly less efficient in a ΛCDM cosmology, also in this case the occurence of radio halos can be matched for viable values of the parameters, and a single range of η_t is found to be able to explain observations in all the mass bins. In the next Chapter all the calculations will be given in a "concordance" ΛCDM model.

5.9 Appendix

5.9.1 Turbulence injection at a single scale

In this Appendix we adopt the scenario in which MHD turbulence is injected in the ICM at a large single–scale, $k_{min} \sim \pi/r_s$, from which the MHD turbulence cascade is originated.

The mean free path, L_{mfp}, in the ICM marks the boundary between the collisionless regime ($k > 2\pi/L_{mfp}$) and the collisional regime ($k < 2\pi/L_{mfp}$). It is given by (*e.g.,* Braginskii 1965):

$$L_{mfp}(\mathrm{kpc}) \sim 300\Big(\frac{T}{10^8\mathrm{K}}\Big)^2\Big(\frac{n_{th}}{10^{-4}\mathrm{cm}^{-3}}\Big)^{-1} \tag{5.31}$$

which, for the typical values of the cluster temperatures and of the mean thermal density within V_H, is of the order of 100 kpc.

Once MS waves are injected at k_{min}, the process of wave–wave coupling generates a turbulence cascade. The cascade time of fast MS waves at the wavenumber k is given by (*e.g.,* Yan & Lazarian 2004):

$$\tau_{kk}(k) \sim \frac{v_M}{k v_k^2} \sim \frac{v_M \rho}{k^2 W_k} \tag{5.32}$$

so that the diffusion coefficient in Eq.(3.20) is given by :

$$D_{kk} \sim \frac{k^2}{\tau_{kk}} \sim \frac{v_A^2}{v_M} \frac{k^4 W_k}{2 W_B} \tag{5.33}$$

In the quasi linear regime and at scales where the diffusion processe is more efficient than the damping process, the spectrum of the waves due to the cascading process can be calculated solving Eq.(3.20) and neglecting the contribution due to the damping terms :

$$\frac{\partial W_{\rm k}(t)}{\partial t} = \frac{\partial}{\partial k} \left(D_{\rm kk} \frac{\partial W_{\rm k}(t)}{\partial k} \right) + I_{\rm k} \tag{5.34}$$

with $I_{\rm k} = I_o \delta(k - k_{min})$ and $I_o \simeq \eta_t v_i^3 \rho (\pi r_s^2 / V_H)$ (Sect. 4.1). The stady state solution of Eq.(5.34) is a Kraichnan–like spectrum :

$$W_{\rm k} \simeq \left(\frac{2 \rho I_o v_M}{3} \right)^{1/2} k^{-3/2} \tag{5.35}$$

This spectrum extends down to a truncation scale at which the cascading time, $\tau_{kk} \propto k^{-1/2}$, becomes substantially larger (*i.e.,* ξ times, $\xi \sim 1-3$) than the damping time scale, $\tau_d \sim \Gamma_{th,e}^{-1} \propto k^{-1}$ (Eq. 5.10). In the collisionless regime, this truncation scale, $L_{tr} \sim 2\pi / k_{tr}$, is obtained from Eqs.(5.10), (5.33), and (5.35), one has :

$$L_{tr} \simeq \frac{0.23}{\xi^2 \eta_t} \left(\frac{T}{10^8} \right)^{3/2} \left(\frac{v_i}{10^3 {\rm km/s}} \right)^{-3} \left(\frac{4}{3} \frac{R_H^3}{r_s^2} \right) \tag{5.36}$$

which typically falls in the range 10–30 kpc for our synthetic clusters (note that such scale is smaller than or comparable to the ion-ion mean fre path, L_{mfp}, and thus the estimate can be done under the assumption of a collisionless regime), *i.e.* a factor of 30–100 smaller than the value of the typical turbulence injection scale.

The picture of the model in this Appendix is thus that the injection of MHD turbulence occurs at a maximum scale of the order of 1 Mpc which is larger but relatively close to the scales typical of the collisionless regime. The wave-wave coupling then leads to a power-law inertial range with a Kraichnan spectrum which is approximatively mantained down to $\sim 10 - 30$ kpc. At these scales the damping

time with the thermal electrons becomes considerably shorter than the cascading time–scale and the turbulence cascade is broken [7].

Under these conditions the acceleration time of relativistic electrons, $\tau_{\rm acc}$, is dominated by the contribution from the spectrum of the waves at the truncation scale and it can be obtained from Eqs.(5.22) and (5.23) :

$$\tau_{\rm acc}^{-1} = \chi \propto v_M^2 W_k(k = k_{tr}) k_{tr}^2 \tag{5.37}$$

An important point is to check if the scenario adopted in Sect. 5.4.2 and that adopted in this Appendix give consistent results. In the scenario adopted in Sect. 5.4.2, the spectrum of the MS waves is approximately given by :

$$W_k \sim I_k \tau_d(k) \tag{5.38}$$

and thus, since $I_o = \int I_k dk$ and the damping time scale is $\tau_d(k) \sim \Gamma_{e,th}^{-1} \propto k^{-1}$, one has :

$$D_{pp} \sim c_{pp} \int W_k k dk \sim I_o \tau_d(k_{tr}) k_{tr} \tag{5.39}$$

where c_{pp} does not depend on the turbulence spectrum and energy (Eq. 5.22). On the other hand, in the scenario adopted in this Appendix the spectrum of the MS waves is approximately given by :

$$W_k \sim \frac{I_o}{k} \tau_{kk} \tag{5.40}$$

and thus, since the cascading time scale is $\tau_{kk} \propto k^{-1/2}$, one has :

$$D_{pp} \sim c_{pp} \int W_k k dk \sim 2\, I_o \tau_{kk}(k = k_{tr}) k_{tr} \tag{5.41}$$

as a consequence, since k_{tr} is the scale at which the damping time scale and the cascading time scale are comparable, we expect that the two scenarios would provide a similar acceleration efficiency.

More specifically, we can calculate the electron acceleration coefficient due to a single merger event (with $r_s \geq R_H$) in the framework of the scenario adopted in this Appendix. From Eqs.(5.35), (5.36), (5.37), (1.74), and the expression for I_o given in this Appendix, one finds :

[7] A detailed analysis of cascading turbulence in the ICM in the presence of the most important physical mechanism, including viscosity, can be found in Brunetti & Lazarian (2007).

$$\chi \sim 2 \times 10^{-16} \xi \eta_t \left(\frac{M}{2 \times 10^{15} M_\odot} \right)^{3/2} \left(\frac{kT}{7\, keV} \right)^{-1/2} \left[\frac{(r_s/500kpc)^2}{(R_H^3/500kpc)} \right] \tag{5.42}$$

which is close to the value given in Eq.(5.25), and thus proves the important point that the main results of our model do not crucially depend on the assumptions on the specific injection process (and spectrum) of the MS waves.

Chapter 6

Magnetic fieds, correlations, luminosity functions and number counts of giant RH

6.1 Introduction

In the Chapter 5 we have modelled the statistical properties of giant RHs in the framework of the merger–induced *in situ* particle re-acceleration scenario. By adopting the semi–analytic PS theory to follow the cosmic evolution and formation of a large synthetic population of galaxy clusters, it was assumed that the energy injected in the form of magnetosonic waves during merging events in clusters is a fraction, η_t, of the PdV work done by the infalling subclusters in passing through the most massive one. Then the processes of stochastic acceleration of the relativistic electrons by these waves, and the ensuing synchrotron emission properties, have been worked out under the *assumption that the magnetic field intensities have constant volume averaged values (within 1 Mpc^3)*. The main findings of these calculations was that giant RHs were *naturally* expected only in the more massive clusters, and that the expected fraction of clusters with RHs (at redshifts $z \lesssim 0.2$) can be reconciled with the observed one under viable assumptions ($\eta_t \simeq 0.24 - 0.34$). The increase of the probability with the cluster mass in the calculation in Chapt. 5 is essentially due to the increase of both the energy density of turbulence and of the turbulence injection volume with cluster mass (see Sec.5.8).

6.2 Main Questions and Aims

The present Chapter is a natual extension of the previous one, the most important difference being that here *we adopt a scaling law between the rms magnetic field strength (averaged in the synchrotron emitting volume) and the virial mass of the parent clusters,* $B \propto M_v^b$. Having in hand an extension of the Chapt. 5 the main questions of this Chapter are:

- Is it possible to reproduce the correlation between the radio power and the thermal properties of galaxy clusters found for giant RHs with the re-acceleration model?
- Is it possible to obtain viable constraints on the $B - M_v$ scaling from these correlations?

The main goals of this Chapter are:

- To obtain a complete description in terms of cosmological epochs of the occurrence of RH in galaxy clusters at different observing frequencies.
- To calculate the luminosity functions and number counts of RH at different observing frequencies.

6.3 Outline

In Sec. 6.4 we collect radio and X-ray data for well known giant RHs from the literature and derive radio–X-ray correlations.
In Sec. 6.5 we investigate the possibility to match the observed radio–X-ray correlations for giant RHs with electron acceleration models. *This comparison provides stringent constraints on the physical parameters in the ICM, in particular for the magnetic field in galaxy clusters.*
In Sec. 6.6 we derive the expected probability to form giant RHs as a function of M_v and z. This is done by adopting the same values of the physical parameters which allows to account for the observed radio–X-ray correlations.
In Sects.6.7–6.8 we finally calculate the expected luminosity functions and number counts of giant RHs at 1.4 GHz.

Table 6.1: Radio and X-ray properties of cluster with giant RHs (linear size $\sim 1\,h_{50}^{-1}$ Mpc) in a ΛCDM cosmology. In Col.(1): Cluster name. Col.(2): Cluster redshift. Col.(3): Cluster temperature given in keV. Col.(4): X-ray luminosity in the energy range $[0.1-2.4]$ keV in unit of $h_{70}^{-2}\,10^{44}$ erg/s. Col.(5): Bolometric X-ray luminosity in the energy range $[0.01-40]$ keV in unit of $h_{70}^{-2}\,10^{44}$ erg/s. Col.(6): Radio power at 1.4 GHz in unit of $h_{70}^{-2}\,10^{24}$ Watt/Hz.

cluster's name	z	T [keV]	L_X [10^{44} erg/s]	L_{bol} [10^{44} erg/s]	$P_{1.4}$ [10^{24} Watt/Hz]
1E50657-558	0.299	$13.59^{+0.71}_{-0.58}$(Z04)	23.32 ± 1.84(B04)	88.62 ± 7.00	28.21 ± 1.97(L00)
A2163	0.203	$13.29^{+0.64}_{-0.64}$(W00)	23.44 ± 1.50(B04)	82.02 ± 5.24	18.44 ± 0.24(FF01)
A2744	0.308	$8.65^{+0.43}_{-0.29}$(Z04)	13.06 ± 2.44(B04)	37.32 ± 6.97	17.16 ± 1.71(GFG01)
A2219	0.228	$9.52^{+0.55}_{-0.40}$(W00)	12.73 ± 0.98(E98)	40.29 ± 4.34	12.23 ± 0.59(B03)
CL0016+16	0.554	$9.13^{+0.24}_{-0.22}$(W00)	18.83 ± 1.88(T96)	51.63 ± 5.16	6.74 ± 0.67(GF00)
A1914	0.171	$10.53^{+0.51}_{-0.50}$(W00)	10.71 ± 1.02(E96)	33.74 ± 3.21	5.21 ± 0.24(B03)
A665	0.182	$8.40^{+1.0}_{-1.0}$(M96)	9.84 ± 0.98(E98)	25.13 ± 3.92	3.98 ± 0.39(GF00)
A520	0.201	$7.84^{+0.52}_{-0.52}$(m)	8.83 ± 0.79(E98)	22.84 ± 5.14	3.91 ± 0.39(GFG01)
A2254	0.178	$7.50^{+0.0}_{-0.0}$(e)	4.32 ± 0.26(E96)	11.08 ± 0.66	2.94 ± 0.29(GFG01)
A2256	0.058	$6.90^{+0.11}_{-0.11}$(W00)	3.81 ± 0.16(E96)	9.54 ± 0.42	0.24 ± 0.02(F00)
A773	0.217	$8.39^{+0.42}_{-0.42}$(m)	8.10 ± 0.65(E98)	21.73 ± 3.62	1.73 ± 0.17(GFG01)
A545	0.153	$5.50^{+6.20}_{-1.10}$(D93)	5.73 ± 0.50(B04)	12.61 ± 1.10	1.48 ± 0.06(B03)
A2319	0.056	$8.84^{+0.29}_{-0.24}$(M98)	7.40 ± 0.41(E96)	20.73 ± 1.14	1.12 ± 0.11(F00)
A1300	0.307	$9.42^{+0.26}_{-0.25}$(m1)	14.11 ± 2.08(B04)	33.87 ± 4.98	6.09 ± 0.61(F00)
A1656	0.023	$8.21^{+0.16}_{-0.16}$(H93)	3.77 ± 0.10(E96)	10.18 ± 0.26	$0.72^{+0.07}_{-0.04}$ (m2)
A2255	0.081	$6.87^{+0.20}_{-0.20}$(W00)	2.65 ± 0.12(E96)	6.61 ± 0.30	0.89 ± 0.05(G04)
A754	0.054	$9.38^{+0.27}_{-0.27}$(W00)	4.31 ± 0.33(E96)	12.95 ± 0.98	1.08 ± 0.06(B03)

Note. — Ref. for the temperature data in brackets: (Z04) Zhang al. 2004 (XMM); (W00) White 2000 (ASCA); (M96) Markevitch 1996 (ASCA); (m) mean value between Mushotzky & Scharf 1997 (ASCA) and Govoni et al. 2004 (Chandra); (e) Ebeling et al. 1996 (from L_x-T relation) ; (D93) David et al. 1993 (Einstein MPC+ Exosat + Ginga); (M98) Markevitch et al. 1998 (ASCA); (m1) mean value between Z04 and Pierre et al. 1999 (ASCA data); (H93) Hughes et al. 1993 (GINGA). Ref. for the X-ray luminosities in brackets: (B04) Boehringer et al 2004, (E98) Ebeling et al 1998, (E96) Ebeling et al 1996, (T96) Tsuru et al 1996, Ref. for the radio data in brackets: (L00) Liang et al. 2000 (ATCA) (F00) Feretti 2000, (B03) Bacchi et al 2003, (GF00) Giovannini & Feretti 2000, (V03) Venturi et al 2003, (GFG01) Govoni et al. 2001a, (G05) Govoni et al. 2005, (FF03) Feretti et al. 2001, (m2) mean value between Kim et al. 1990 and Deiss et al. 1997

In Sect.6.9 we extend calculations to the case of 150 MHz which is a frequency of interest for LOFAR.

As in Chapt. 5, we focus our attention on giant RHs only (linear size $\sim$1 h_{50}^{-1} Mpc). Here, the adopted cosmology is: ΛCDM ($H_o = 70$ Km s^{-1} Mpc^{-1}, $\Omega_{o,m} = 0.3$, $\Omega_\Lambda = 0.7$, $\sigma_8 = 0.9$).

Results reported in this Chapter are published in Cassano et al. (2006a) and Cassano et al. (2006b).

6.4 Observed Correlations

In this section we revise and discuss the observed correlations between the X-ray and the radio properties of clusters hosting giant RHs.
We collect galaxy clusters with known giant RHs from the literature obtaining a total sample of 17 clusters. In Tab. 6.1 we report the radio and X-ray properties of this sample in a ΛCDM cosmology. In order to have the best estimate of the X-ray temperatures we select results from XMM-Newton observations when available, otherwise we use ASCA results or combine ASCA and Chandra information. We investigate the correlations between the X-ray and the radio properties of the selected clusters by making use of a linear regression fit in log-log space following the procedures given in Akritas & Bershady (1996). This method allows for intrinsic scatter and errors in both variables.

6.4.1 Radio Power–X-ray luminosity correlation

The presence of a correlation between the radio powers and the X-ray luminosities is well known (Liang et al. 2000; Feretti 2000, 2003; Enßlin and Röttgering 2002).

In Fig.6.1 we report the correlation between the X-ray luminosity (in the 0.1-2.4 keV energy band) and the radio power at 1.4 GHz ($P_{1.4}$) for our sample of giant RHs. The fit has been performed by using the form:

$$\log\Big(\frac{P_{1.4\,GHz}}{3.16\cdot 10^{24}\,h_{70}^{-1}\,\frac{Watt}{Hz}}\Big) = A_f + b_f\,\log\Big[\frac{L_X}{10^{45}\,h_{70}^{-1}\,\frac{ergs}{s}}\Big] \qquad (6.1)$$

where the best fit parameters are: $A_f = 0.159 \pm 0.060$ and $b_f = 1.97 \pm 0.25$.
Our findings are consistent with those of Enßlin and Röttgering (2002) who used 14 clusters with radio halos and found a correlation of the form $P_{1.4\,GHz} \propto L_X^{1.94}$. By using 16 clusters with giant RHs Feretti (2003) found a correlation between the X-ray bolometric luminosity and the radio power at 1.4 GHz of the form $P_{1.4\,GHz} \propto (L_X^{bol})^{1.8\pm0.2}$. A consistent result is obtained with the data in Tab. 6.1, $P_{1.4\,GHz} \propto (L_X^{bol})^{1.74\pm0.21}$, which is shown in Fig.6.2.

6.4.2 Radio Power–ICM temperature correlation

We also investigate the correlation between the radio power at 1.4 GHz and the X-ray ICM temperature. A $P_{1.4} - T$ correlation was first noted by Liang (1999) and

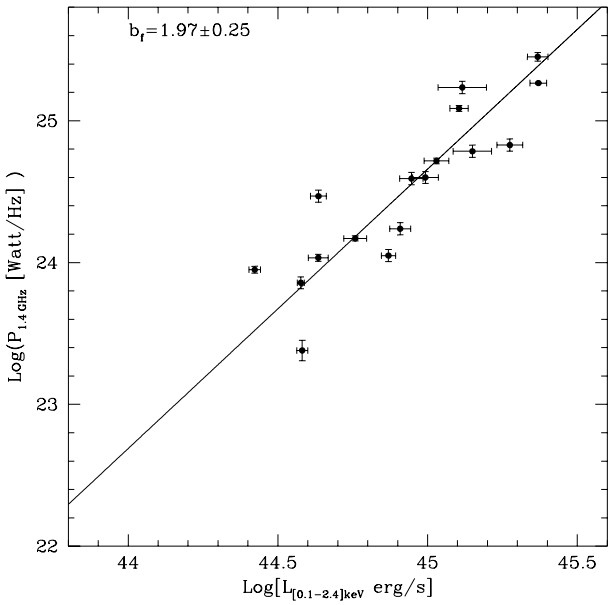

Figure 6.1: Correlation between the radio power at 1.4 GHz and the X-ray luminosity between [0.1-2.4] kev for the giant RHs.

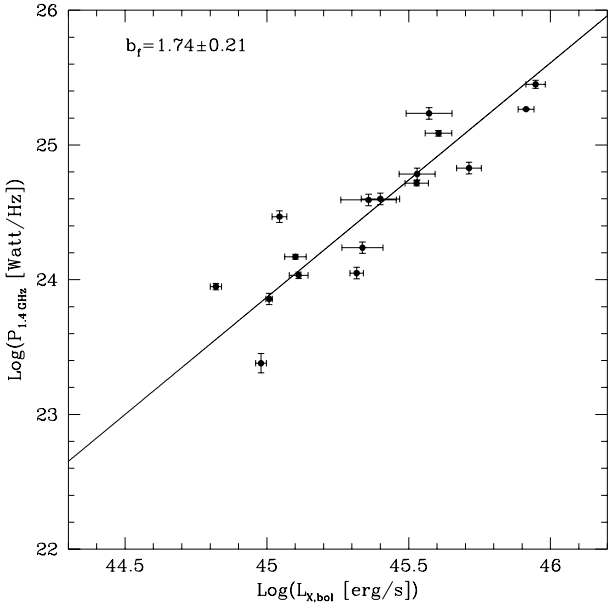

Figure 6.2: Correlation between the radio power at 1.4 GHz and the X-ray bolometric luminosity for the giant RHs.

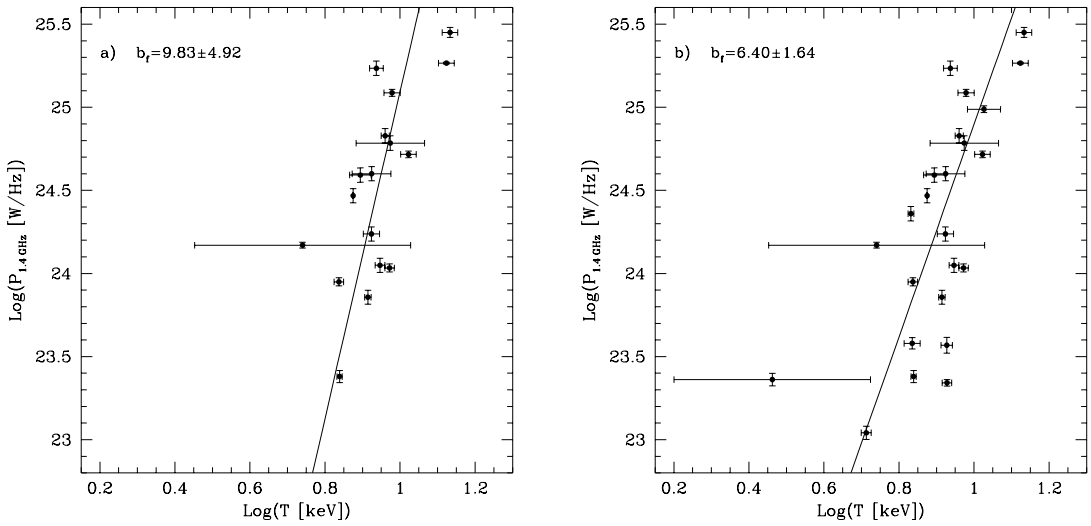

Figure 6.3: Panel a):correlation between the radio power at 1.4 GHz and the temperature for the giant RHs; Panel b): correlation between the radio power at 1.4 GHz and the X-ray temperature for a total sample of 24 cluster with a giant RHs or with a smaller size ($\sim 200 - 700$ kpc h_{50}^{-1}).

Colafrancesco (1999); with a sample of only 8 radio halos the last author obtained a steep trend of the form $P_{1.4} \propto T^{6.25^{+6.25}_{-2.08}}$. In Fig. 6.3a we report the best fit for our sample. The fit has been performed in the form:

$$\log\left[\frac{P_{1.4\,GHz}}{3.16\cdot 10^{24}\, h_{70}^{-1}\,\frac{Watt}{Hz}}\right] = A_f + b_f\,\log\left(\frac{T}{8\,keV}\right) \tag{6.2}$$

and best fit parameters are: $A_f = -0.390 \pm 0.139$ and $b_f = 9.83 \pm 4.92$. We note that the observed $P_{1.4} - T$ correlation is very steep, it seems rather a "wall" than a correlation and it is dominated by the large errors of the cluster temperatures avaiable to date. In order to test the strength of this correlation we included also 7 additional clusters with smaller (size $\sim 200 - 700$ kpc h_{50}^{-1}) radio halos. (Fig. 6.3b) and obtained a slope $b_f = 6.40 \pm 1.64$ which is consistent at the 1σ level with that in Fig. 6.3a.

6.4.3 Radio Power – virial mass correlation

The most important correlation for our study is that between the virial mass (M_v) of a cluster and the radio power at 1.4 GHz. This correlation is indeed extensively used in the calculations of the RHLFs and number counts (Sects. 6.7 and 6.8) and in constraining the values of the magnetic field in galaxy clusters to be used in our

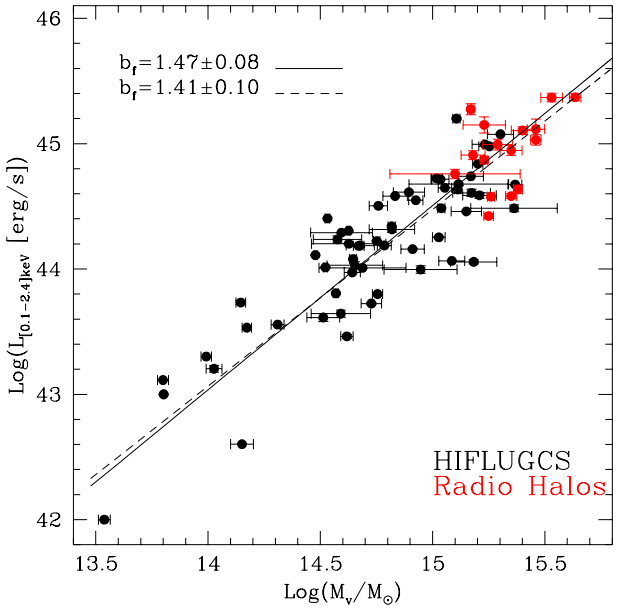

Figure 6.4: Correlation between the X-ray luminosity [0.1-2.4] keV and the virial cluster mass: for the HIFLUGCS sample (black points) plus the 16 clusters with giant RHs (red points, excluding A2254 for which no information on the β-model are available) (solid line) and for the HIFLUGCS sample alone (dashed line).

calculations (Sect. 6.5). On the other hand, this is also the most difficult correlation to derive since it is very difficult to measure the cluster masses. Govoni et al. (2001a) first obtained a correlation between the radio power and cluster gravitational mass (within 3 h_{50}^{-1} Mpc radius) estimated from the surface brightness profile of the X-ray image using 6 radio halo clusters. This correlation was confirmed by Feretti (2003) who extended the sample to 10 cluster radio halos and obtained a best fit of the form $P_{1.4} \propto M^{2.3}$, where M is, again, the gravitational mass computed within 3 h_{50}^{-1} Mpc from the cluster center. However as discussed in Chap.1 while the X-ray mass determination method gives good results in relaxed clusters, it may fail in the case of merging clusters due to possible deviation from hydrostic equilibrium and spherical symmetry.

The effect of the scattering produced by the mass uncertainties can hopefully be reduced by making use of large cluster samples. Thus, we choose to obtain the $P_{1.4\,GHz} - M_v$ correlation by combining the $L_x - M_v$ correlation, obtained for a large statistical sample of galaxy clusters, with the $P_{1.4} - L_x$ correlation previously derived (Eq.6.1, Fig. 6.1). We use a complete sample of the X-ray–brightest clusters

Table 6.2: Parameters of the β-fit and cluster mass estimated for the 16 galaxy clusters with giant RHs for which β-fits are avaiable. Col.(1): Cluster name. Col.(2): β-parameter value with 1σ error. Col.(3): Core radius in units of h_{70}^{-1} kpc and corresponding uncertainty. Col.(4): Virial mass and is uncertainty in units of $h_{70}^{-1}\,10^{15}\,M_{\odot}$. Col.(5): Virial radius in units of h_{70}^{-1} kpc. Col.(6): Mass estimated inside the core radius in units of $h_{70}^{-1}\,10^{13}\,M_{\odot}$.

cluster's name	β	r_c [kpc h_{70}^{-1}]	M_v [$10^{15}\ M_{\odot}$]	R_v [kpc h_{70}^{-1}]	M_c [$10^{13}\ M_{\odot}$]
1E50657-558(a)	0.70 ± 0.07	179 ± 18	3.43 ± 0.38	3301	9.50 ± 1.40
A2163 (b)	0.80 ± 0.03	371 ± 21	4.32 ± 0.26	3766	22.00 ± 1.84
A2744 (c)	1.00 ± 0.08	458 ± 46	2.87 ± 0.26	3096	22.10 ± 2.96
A2219 (d)	0.79 ± 0.08	343 ± 34	2.52 ± 0.28	3104	14.40 ± 2.16
CL0016+16 (e)	0.68 ± 0.01	237 ± 80	1.47 ± 0.05	2166	8.27 ± 0.38
A1914 (b)	0.75 ± 0.02	165 ± 80	2.90 ± 0.15	3356	7.28 ± 0.51
A665 (f)	0.74 ± 0.07	350 ± 35	1.97 ± 0.30	2933	12.10 ± 2.20
A520 (c)	0.87 ± 0.08	382 ± 50	2.22 ± 0.25	3018	14.50 ± 2.51
A2256 (b)	0.91 ± 0.05	419 ± 28	2.23 ± 0.13	3281	14.70 ± 1.28
A773 (c)	0.63 ± 0.07	160 ± 27	1.52 ± 0.19	2636	4.72 ± 0.98
A545 (d)	0.82 ± 0.08	286 ± 29	1.25 ± 0.84	2562	7.20 ± 4.89
A2319 (b)	0.59 ± 0.01	204 ± 10	1.71 ± 0.07	3009	5.95 ± 0.38
A1300 (g)	0.64 ± 0.01	171 ± 80	1.71 ± 0.06	2609	5.76 ± 0.33
A1656 (b)	0.65 ± 0.02	246 ± 15	1.83 ± 0.07	3136	7.38 ± 0.53
A2255 (b)	0.80 ± 0.05	419 ± 28	1.76 ± 0.12	2996	12.80 ± 1.22
A754 (b)	0.70 ± 0.03	171 ± 12	2.42 ± 0.11	3379	6.25 ± 0.52

Note. — Ref. for the (data) source in brackets: (a) Markevitch et. al 2002 (Chandra); (b) RB02 (ROSAT for β-fit and T as in table 1); (c) Govoni et al. 2001a (ROSAT); (d) Ettori & Fabian 1999 (ROSAT); (e) Ettori et. al 2004 (Chandra); (f) Feretti 2004 (Einstein); (g) Lemonon et al. 1997 (ROSAT).

(HIFLUGCS, the Highest X-ray FLUx Galaxy Cluster Sample) compiled by Reiprich & Böhringer (2002) (hereafter RB02). We use this sample of luminous clusters ($L_x \sim 10^{44} - 10^{45}$erg s^{-1}) since it is large and homogeneously studied. It consists of 63 bright clusters with galactic latitude $|b_{II}| > 20^o$, flux $f_X(0.1-2.4\,keV) \geq 2\times10^{-11}$ ergs s^{-1} cm^{-2} and it covers about 2/3 of the whole sky.

The clusters have been reanalyzed in detail by RB02 using mainly ROSAT PSPC pointed observations. RB02 fitted the X-ray brightness profiles of the 63 galaxy clusters by assuming a $\beta-$model profile (Sect. 1.2.2), and here we corrected the relevant parameters, β and the core radius r_c, for a ΛCDM cosmology. Then under the assumption that the intracluster gas is in hydrostatic equilibrium and isothermal (using the ideal gas equations), the gravitational cluster mass within the virial radius R_v can be computed according to Eq.1.17 in Sect.1.2.2.

In addition to the HIFLUGCS clusters we have searched in the literature for β-fit parameters and T of the clusters with giant RHs (ref. in Tab. 6.2) in order to estimate M_v also for these clusters. Since some clusters of the HIFLUGCS sample are also in our sample, we note that in the majority of these cases the fits to the mass profile (and T) given in RB02 leads to a virial mass which is consistent at 1σ level with the mass derived by making use of the parameters obtained from more recent observations in the literature (given in Tabs. 6.1, 6.2). The $L_x - M_v$ distribution of the combined sample is reported in Fig. 6.4. The presence of a relatively large dispersion indicates the difficulty in estimating the virial masses of the single objects and confirms the need of large samples in these studies. We note that the statistical distribution of clusters with giant RHs is not different from that of the HIFLUGCS sample. *On the other hand, we note that clusters with known giant RHs span a narrow range in mass which is comparable to the mass–dispersion in the HIFLUGCS sample, this further strengthens the need of the approach followed in this Section*, since a L_x (or $P_{1.4}$)–M_v fit based on giant RHs alone would be affected by large uncertainties.

In order to better sample the region of higher X-ray luminosities and masses (typical of clusters with giant RHs), we compute the L_x–M_v fit by combining the HIFLUGCS with the radio–halo sample. The fit has been performed using the form:

$$\log\left[\frac{L_X}{10^{44}\,h_{70}^{-1}\,\frac{ergs}{s}}\right] = A_f + b_f\,\log\Big(\frac{M_v}{3.16\times10^{14}\,h_{70}^{-1}\,M_\odot}\Big) \qquad (6.3)$$

The best fit values of the parameters are: $A_f = -0.229 \pm 0.051$ and $b_f = 1.47 \pm 0.08$ ($b_f = 1.41 \pm 0.10$ is obtained with HIFLUGCS sample only).

In order to derive the $P_{1.4\,GHz} - M_v$ correlation for giant RHs, we combine Eqs 6.3 and 6.1 and find :

$$\log\Big[\frac{P_{1.4}}{3.16 \cdot 10^{24}\, h_{70}^{-1}\, \frac{Watt}{Hz}}\Big] = (2.9 \pm 0.4) \log\Big[\frac{M_v}{10^{15}\, h_{70}^{-1}\, M_\odot}\Big] - (0.814 \pm 0.147) \quad (6.4)$$

Our $P_{1.4\,GHz} - M_v$ correlation is slightly steeper than that obtained with 10 clusters by Feretti (2003) ($P_{1.4\,GHz} \propto M^{2.3}$), which, however, was derived in an EdS cosmology by considering the mass within 3 h_{50}^{-1} Mpc from the cluster centers, and not the virial mass.

6.5 Expected correlations and magnetic field constraints

The main goal of this Section is to extract the values of the physical parameters, in particular of B and its scaling with cluster mass $B \propto M_v^b$, to be used in the model calculations of Sec. 6.6– 6.8. This is constrained by comparing the model expected and observed trends of the synchrotron power of giant RHs with the mass (and temperature) of the parent clusters.

6.5.1 Radio power–cluster mass correlation

In the previus Chapter (Sec.5.6) we derived an expected trend between the bolometric radio power, P_R, and the virial cluster's mass and/or temperature. In the case of the giant RHs, the mergers which mainly contribute to the injection of turbulence in the ICM are those with $r_s \geq R_H$, r_s being the stripping radius of the infalling sub–cluster. It can be shown that, as a first approximation and assuming a fixed emitting volume, the expected scaling $P_R - M_v$ is given by:

$$P_R \propto \frac{M_v^{2-\Gamma}\, B^2\, n_e}{(B^2 + B_{cmb}^2)^2} \quad (6.5)$$

where B is the rms magnetic field strength in the radio halo volume (particle pitch angle isotropitazion is assumed), $B_{cmb} = 3.2(1+z)^2 \mu G$ is the equivalent magnetic field strength of the CMB and n_e is the number density of relativistic electrons in the volume of the giant RH. The parameter Γ is defined by $T \propto M^\Gamma$; we consider $\Gamma \simeq 2/3$ (virial scaling) and $\Gamma \simeq 0.56$ (*e.g.,* Nevalainen et al. 2000).

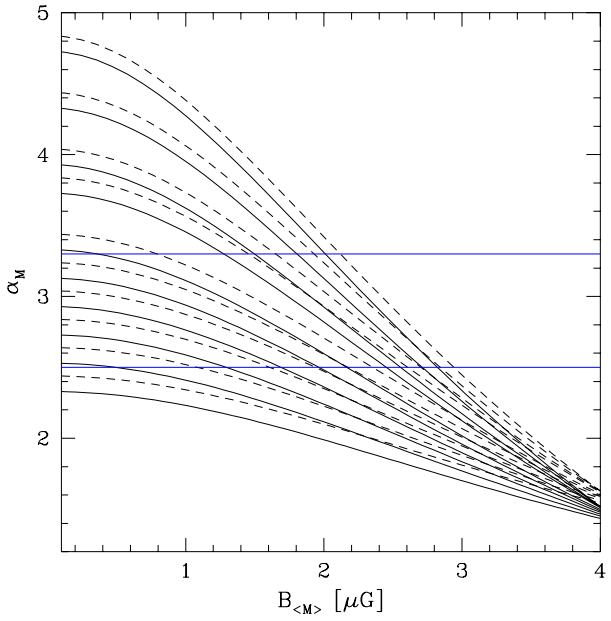

Figure 6.5: Expected slope of the $P_{1.4} - M_v$ correlation as a function of the magnetic field intensity in a cluster of mass $< M >= 1.6 \times 10^{15}\, M_{\odot}$. The calculations are obtained for b=0.5,0.6,0.7,0.8,0.9,1,1.2,1.3,1.5 and 1.7 (from bottom to top); $M_1 = 1.1 \times 10^{15}\, M_{\odot}$ and $M_2 = 2.5 \times 10^{15}\, M_{\odot}$ are adopted. The continuous lines are for $\Gamma \simeq 0.67$ and the dashed lines are for $\Gamma \simeq 0.56$. The two horizontal lines mark the 1 σ value of the observed slope.

In this paper we release the assumption adopted in Chapt.5 of a magnetic field independent of cluster mass and assume that the rms field in the emitting volume scales as $B = B_{<M>}(M/ < M >)^b$, with $b > 0$ and $B_{<M>}$ the value of the rms magnetic field associated to a cluster with mass equal to the mean mass $< M >$ of the clusters sample. A scaling of the magnetic field intensity with the cluster mass is indeed found in numerical cosmological MHD simulations (*e.g.,* Dolag et al. 2002, 2004). Dolag et al. (2002) found a scaling $B \propto T^2$ that would mean $B \propto M^{1.33}$ assuming the virial scaling or $B \propto M^{1.12}$ for $\Gamma \simeq 0.56$.

We assume that the number density of the relativistic electrons in galaxy clusters, n_e, does not depend on cluster mass. This is because there is no straightforward physical reason to believe that this value should scale systematically with M_v, and since only a relatively fast scaling of n_e with mass would significantly affect the radio power – mass trend (Eq. 6.5). It is indeed more likely that n_e may change from cluster to cluster, but in this case the major effect would simply be to drive some scattering on the $P_R - M_v$ trend (Eq. 6.5).

Given these assumptions Eq. 6.5 becomes:

$$P_R \propto \frac{M_v^{2-\Gamma}\, B^2_{<M>} \cdot (M_v/ < M >)^{2b}}{(B^2_{<M>} \cdot (M_v/ < M >)^{2\,b} + B^2_{cmb})^2} \tag{6.6}$$

which has two asymptotic behaviors: $P_R \propto M_v^{2-\Gamma+2b}$ for $B_{<M>} << B_{cmb}$ and $P_R \propto M_v^{2-\Gamma-2b}$ for $B_{<M>} >> B_{cmb}$. The observed correlations derived in Sect. 2 involve the monochromatic radio power at 1.4 GHz. How this monochromatic radio power can be scaled to P_R depends on the spectrum of radio halos. In the context of particle acceleration models (*e.g.,* Brunetti et al. 2001a, Ohno et al. 2002, Kuo et al. 2003) the spectrum of radio halos is given by the superposition of spectra emitted from regions in the emitting volume with different magnetic field strenghts. It is expected to reach a peack at ν_b and then gradually drop as a power-law which should further steepen at higher frequencies. The peack frequency can be expressed as a function of the cluster mass and of the rms field B in the emitting volume (Chapt.5):

$$\nu_b \propto M^{2-\Gamma} \frac{B\, \eta_t^2}{(B^2 + B^2_{cmb})^2} \tag{6.7}$$

If we adopt a power-law spectrum extending from the frequency of the peak to a few GHz, $P(\nu) \propto \nu^{-a}$, P_R and the monochromatic radio power at a fixed frequency ν_o ($\nu_o \geq \nu_b$) scale as $P(\nu_o)/P_R \propto (\frac{\nu_b}{\nu_o})^{a-1}$. This depends on the cluster mass (Eq.6.7):

$$\frac{P(\nu_o)}{P_R} \propto \frac{{M_v}^{(a-1)(2-\Gamma+b)}}{(B^2_{<M>}(M_v/ < M >)^{2b} + B^2_{cmb})^{2(a-1)}} \tag{6.8}$$

thus in the case $B << B_{cmb}$ one has $P(\nu_o)/P_R \propto (\frac{M}{<M>})^{(a-1)(2-\Gamma+b)}$, while in the case $B >> B_{cmb}$ one has $P(\nu_o)/P_R \propto (\frac{M}{<M>})^{(a-1)(2-\Gamma-3b)}$, which means that for $B << B_{cmb}$ the $P(\nu_o) - M$ trend is steeper than the $P_R - M$, while the opposite happens in the case $B >> B_{cmb}$ (the two scaling should be equal for continuity for $B \sim B_{cmb}$). On the other hand, the trends of $P(\nu_o)/P_R$ with the cluster mass in massive galaxy clusters is rather weak because the observed radio spectral index between 327–1400 MHz is $a \sim 1.2$ (*e.g.,* Feretti 2003) and because B in the most massive objects is probably close to B_{cmb} (Sec.3.3, Fig.6.7; Govoni & Feretti 2004). *Thus, in order to compare the model expectations with the observations, we will safely assume the same scaling for the monochromatic and for the total radio power.*

In order to have a prompt comparison with observations we calculate the slope α_M of the $P_{1.4} - M$ correlation between two points as:

$$\alpha_M = \frac{\log(P_1/P_2)}{\log(M_1/M_2)} \tag{6.9}$$

Eq.6.9 can be compared with the observed slope to constrain the value of the magnetic field and of the slope, b, of the scaling between B and the cluster mass. The M_1 and M_2 values give the representative mass range spanned by the bulk of clusters with giant RHs, while B_{cmb} should be calculated at the mean redshift of our sample ($< z > \simeq 0.19$). We point out that given $B_{<M>}$ and b, the values of B are fixed for all the values of the masses of the clusters in our sample.

In Fig.6.5 we report the expected slope α_M (Eq. 6.9) as a function of $B_{<M>}$. The different curves are obtained for different scaling-laws of the magnetic field with the cluster mass ($b = 0.5$ to 1.7, see caption). Dashed lines refer to $\Gamma \simeq 0.56$ and solid lines to the virial case. The two blue horizontal lines (Fig.6.5) indicate the range of the observed slope ($\alpha_M = 2.9 \pm 0.4$, Eq. 6.4).

Fig. 6.5 shows that there are values of $B_{<M>}$ and b for which the expected slope is consistent with the observed one. As a first result we find that with increasing b the values of $B_{<M>}$ should increase in order to match the observations (for example, $b \sim 0.6$ requires $B_{<M>} \sim 0.2 - 1.4\ \mu$G while $b \sim 1.7$ requires $B_{<M>} \sim 2 - 3\ \mu$G). Finally, the asymptotic behavior of Eq.6.6, combined with the observed correlation (Eq. 6.4) allows to immediately constrain b: for $B_{<M>} << B_{cmb}$ one has $0.58(0.53) < b < 0.98(0.93)$ for the virial (non-virial) case, whereas in the case of $B_{<M>} >> B_{cmb}$ the model expectations cannot be reconciled with the observations.

6.5.2 Radio power–cluster temperature correlation

Since the temperature is related to the cluster mass, the radio power – mass correlation also implies a correlation between synchrotron radio power and cluster temperature. Thus, in order to maximize the observational constraints, an analysis similar to that of Sect. 6.5.1 can also be done for the radio power – temperature correlation ($P_R - T$). Combining Eq. 6.6 with the $M - T$ scaling law ($T \propto M^{2/3}$ for the virial case and $T \propto M^{0.56}$) one has:

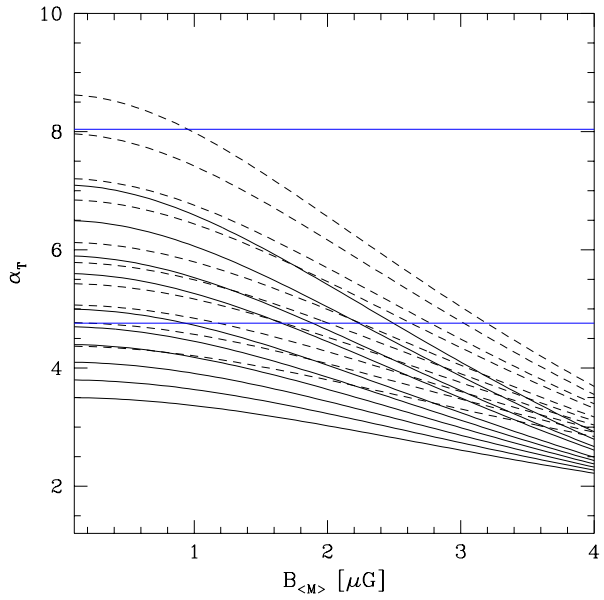

Figure 6.6: Expected slope of the $P_{1.4} - T$ correlation as a function of the magnetic field intensity in a cluster with temperature $< T >= 8$ keV. The calculations are obtained for b=0.5,0.6,0.7,0.8,0.9,1,1.2,1.3,1.5 and 1.7 (from bottom to top); $T_1 = 6$ keV and $T_2 = 10$ keV are adopted. The continuous lines are for $\Gamma \simeq 0.67$ and the dashed lines are for $\Gamma \simeq 0.56$. The two horizontal lines mark the 1 σ value of the observed slope.

$$P_R \propto \frac{T^{\frac{2}{\Gamma}-1}\, B^2_{<M>}\, (T/ < T >)^{2\, b_T}}{(B^2_{<M>} \cdot (T/ < T >)^{2\, b_T} + B^2_{cmb})^2} \tag{6.10}$$

where $b_T = b/\Gamma$ with $\Gamma \simeq 2/3$ (virial case) or $\Gamma \simeq 0.56$ (non-virial case). The asymptotic behaviors of Eq. 6.10 are given by $P_R \propto T^{2/\Gamma-1+2b_T}$ ($B_{<M>} << B_{cmb}$) and $P_R \propto M_v^{2\Gamma-1-2b_T}$ ($B_{<M>} >> B_{cmb}$).

As in Sec. 6.5.1, here we can adopt the same scaling with T for both P_R and $P_{1.4}$ and compare the values of the expected slope with those of the observed one. We can calculate the slope α_T of the $P_{1.4} - T$ correlation between two points as:

$$\alpha_T = \frac{\log(P_1/P_2)}{\log(T_1/T_2)} \tag{6.11}$$

where T_1 and T_2 define the interval of temperature of our sample, $< T >= 8$ keV is the mean temperature, and B_{cmb} is evaluated at $< z >\simeq 0.19$. In Fig. 6.6 we report the slope α_T of the $P_{1.4} - T$ correlation as a function of the magnetic field strength in a cluster with average mass, $B_{<M>}$. The different curves are obtained for different scaling-laws of the cluster magnetic fields with mass (*i.e.,* temperature)

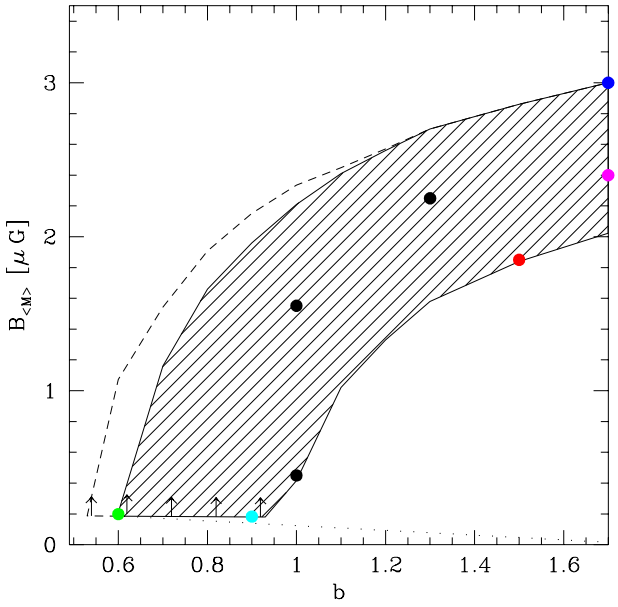

Figure 6.7: The region in the plane ($B_{<M>}$,b) allowed from the observed $P_{1.4} - M_v$ and $P_{1.4} - T$ correlations is reported as a shadowed area; $< M >= 1.6 \times 10^{15} M_{\odot}$. The dashed line indicate the upper bound of the allowed region obtained considering only the $P_{1.4} - M_v$ correlation. The coloured points indicate the relevant configurations of the parameters used in the statistical calculations in Sec.4-6 (Tab. 6.3). The vertical arrows indicate the IC limits on B.

(b=0.5 to 1.7). Dashed lines are for $\Gamma \simeq 0.65$ and continuous lines are for the virial case.

The horizontal blue lines mark the lower limit $\alpha_T \simeq 4.76$ and the upper limit $\alpha_T \simeq 8.05$ of the observed correlation. Fig. 6.6 shows that there is a range of values of the parameters $(B_{<M>}, b)$ for which the model is consistent with the observed slope. *The relevant point is that, similarly to the case of the $P_{1.4} - M$ correlations, also in this case values of $B_{<M>} >> B_{cmb}$ cannot be reconciled with observations: a clear upper boundary at $B < 3\mu G$ is obtained for $B_{<M>}$.*

6.5.3 Constraining the magnetic field

We combine the results obtained from the observed correlations (both $P_{1.4} - M_v$ and $P_{1.4} - T$) and the model expected trends to selects the allowed region of the ($B_{<M>}$, b) parameters. In order to improve the statistical constraint, we consider the slope of the $P_{1.4} - T$ correlation $\alpha_T \simeq 6.4 \pm 1.64$ as derived for the extended sample (Sect. 6.4.2).

In Fig.6.7 we report the region of the plane $(B_{<M>}, b)$ allowed by the observed slopes at 1σ level. The lower bound of the ($B_{<M>}$,b) region is due to the $P_{1.4} - M_v$ correlation while the upper bound is mostly due to the $P_{1.4} - T$ correlation which is poorly constrained because of the very large statistical errors. This bound is however also limited by the $P_{1.4} - M_v$ correlation (Fig.6.7, dashed line).

An additional limit on $B_{<M>}$, also reported in Fig.6.7 (vertical arrows), can be obtained from inverse Compton (IC) arguments. Indeed a lower bound to the magnetic field strength can be inferred in order to not overproduce, via IC scattering of the photons of the CMB radiation, the hard-X ray excess fluxes observed up to now in a few clusters (*e.g.,* Rephaeli & Gruber 2003, Fusco-Femiano et al 2003). In this case the value of the mean magnetic field intensity in the cluster volume can be estimated from the ratio between the hard-X ray and radio emission. The resulting value of the magnetic field should be considered as a lower limit because the IC emission may come from more external region with respect to the synchrotron emission (*e.g.,* Brunetti et al. 2001a, Kuo et al. 2003, Colafrancesco et al. 2005) and also because, in principle, additional mechanisms may contribute to the hard-X ray fluxes (*e.g.,* Fusco-Femiano et al. 2003). One of the best studied cases is that of the Coma cluster for which an average magnetic field intensity of the order of $B_{IC} \simeq 0.2\,\mu G$ was derived (Fusco-Femiano et al. 2004). As a first approximation we can use this value to obtain the lower bound of B for each cluster mass from the scaling $B = B_{<M>}(M/ < M >)^b$.

The resulting ($B_{<M>}$,b) region resulting from the match between model and observed scalings *spans a wide range of values of B and b.* An inspection of Fig.6.7 immediately identifies two allowed regimes: a super-linear scaling ($b > 1$) with relatively high values of B and a sub-linear scaling ($b < 1$) with lower values of B.

All the calculations we will report in the following sections are carried out by assuming representative values of ($B_{<M>}$,b) inside the constrained region (Fig. 6.7 coloured filled dots and Tab.6.3).

6.6 Probability to form giant radio halos

6.6.1 Probability of radio halos and constraining η_t

In this Section we derive the probability, as a function of cluster mass, to find giant RHs in the redshift range z=0–0.2. *The byproduct of the Section is to*

calibrate the model by requiring that the expected fraction of cluster with giant RHs is consistent with the observational constraints. This allows to select a range of values of the parameter η_t, which is the ratio between the energy injected in the form of magnetosonic waves and the PdV work done by the infalling subclusters in passing through the most massive one (Sect. 5.4). η_t is a free parameter in our calculations since the fraction of the energy which goes into the form of compressible modes is likely to depend on the details of the driving turbulent force.

As in Sect. 5.6.2 RHs are identified with those objects in a synthetic cluster population with a synchrotron peack frequency (Eq.6.7) $\nu_b \gtrsim 200$ MHz in a region of 1 $Mpc\ h_{50}^{-1}$ size. In Chapt. 5 it was assumed that the magnetic field in the radio halo volume is independent from the cluster mass and it is $B \simeq 0.5\mu G$. Then $\nu_b \propto M^{2-\Gamma}$ and consequently massive clusters are expected to be favourite in forming giant RHs. In Chapt. 5 indeed *we show that the expected fraction of clusters with giant RHs naturally shows an abrupt increase with cluster mass, and that the observed fractions* (20-30 % for $M > 2 \times 10^{15}\, M_\odot$ clusters, 2-5 % for $M \sim 10^{15}\, M_\odot$ clusters and negligible for less massive objects) *can be well reconciled with the model expectations by assuming* $\eta_t \sim 0.24 - 0.34$.

In this Chapter we assume that the rms magnetic field depends on the cluster mass and, although this cannot affect the general expectation of an increasing probability to form RHs in most massive clusters (Chapt. 5, *the magnetic field should affect the synchrotron break frequency (Eq. 6.7) and the details of the occurrence of giant RHs with cluster mass.* On the other hand, in Sect. 6.5 we have also shown that the comparison between the expected and observed trends between radio power and cluster mass (and temperature) helps in constraining the range of values which can be assigned to the magnetic field in clusters.

Thus our calculations of the occurrence of giant RHs ($z \leq 0.2$) and the selection of the values of η_t necessary to reproduce the observations should be performed within the dashed region in Fig.6.7.

To calculate the expected probabilities to form radio halos we first run a large number, $\mathcal{N}$, of trees for different cluster masses at $z = 0$, ranging from $\sim 5 \times 10^{14} M_\odot$ to $\sim 6 \times 10^{15} M_\odot$. Then we choose different mass bins ΔM and redshift bins Δz in which to perform our calculations. Thus, for each mass M, the formation probability of giant RHs in the mass bin ΔM and in the redshift bin Δz is computed

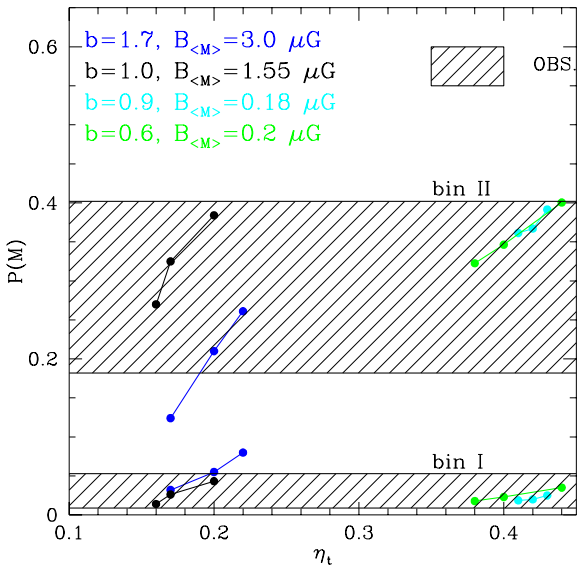

Figure 6.8: Probability to form giant RHs at $0.05 \leq z \leq 0.15$ in the observed mass bin I: $0.95 - 1.9 \times 10^{15} M_{\odot}$ and at $0.05 \leq z \leq 0.2$ in bin II: $1.9 - 3.8 \times 10^{15} M_{\odot}$ as a function of η_t. The calculations are reported for the following representative cases: $b = 1.7$, $B_{<M>} = 3.0\mu$G (blue points); $b = 1.0$, $B_{<M>} = 1.55\mu$G (black points); $b = 0.9$, $B_{<M>} = 0.18\mu$G (cyan points) and $b = 0.6$, $B_{<M>} = 0.2\mu$G (green points). The bottom shadowed region marks the observed probability for giant RHs in the mass bin I while the top shadowed region marks that in the mass bin II. The values of the observed probabilities are obtained by combining the results from Giovannini et al. 1999, Giovannini & Feretti 2000, and Feretti 2002. The observed probabilities for the bin I are calculated up to $z \leq 0.15$ to minimize the effect due to the incompleteness of the X–ray and radio catalogs used by these authors.

according to Eq. 5.29 (Chapt.5). The total probability of formation of giant RHs in the mass bin ΔM and in the redshift bin Δz is obtained by combining all the contributions (Eq. 5.29) weighted with the local cluster mass function, we use the Press & Schecther mass function.

To have a prompt comparison with present observational constraints, we calculate the probability to form giant RHs at $z \lesssim 0.2$ in the two observed mass bins: bin I ($[0.95 - 1.9] \times 10^{15} M_{\odot}$) and bin II ($[1.9 - 3.8] \times 10^{15} M_{\odot}$).

As an example, in Fig. 6.8 we report these probabilities in both bin I and bin II as a function of η_t for three representative cases which nicely sample the region in Fig.6.7: $b = 1.7$, $B_{<M>} = 3.0\mu$G (blue points); $b = 1.0$, $B_{<M>} = 1.55\mu$G (black points); $b = 0.9$, $B_{<M>} = 0.18\mu$G (cyan points); $b = 0.6$, $B_{<M>} = 0.2\mu$G (green points).

Table 6.3: Values of α_M and η_t derived for relevant sets of b, $B_{<M>}[\mu G]$ parameters.

b	$B_{<M>}[\mu G]$	α_M	η_{min}	η_{max}
1.7	3.0	2.5	0.19	0.2
1.7	2.2	3.22	0.17	0.2
1.5	1.9	3.3	0.15	0.2
1.3	2.25	2.84	0.15	0.2
1.0	1.55	2.96	0.16	0.21
1.0	0.45	3.3	0.29	0.33
0.9	0.18	3.23	0.39	0.44
0.6	0.2	2.63	0.38	0.44

The bottom shadowed region in Fig. 6.8 marks the observed probability for giant RHs in the mass bin I while the top shadowed region marks that in the mass bin II. Fig. 6.8 shows that *it is possible to find a range of values of the parameter η_t for which the theoretical expectations are consistent with the observed statistics in both the mass bins.* However we note that the requirement in terms of energy of the MS modes increases with decreasing the magnetic field: it goes from $\eta_t \sim 0.15 - 0.2$ for intermediate–large values of B up to $\eta_t \sim 0.5$ at the lower bound of the allowed B strengths.

The fact that the magnetic field depends on the cluster mass is reflected in the different behavior that the models based on different configurations of parameters have in the two mass bins of Fig. 6.8: model-configuration may be favoured in a mass bin with respect to another configuration but disfavoured in the other mass bin. This is *related to the transition from IC dominance ($B < B_{cmb}$) to synchrotron dominance ($B > B_{cmb}$) that occurs in going from the bin I to the more massive clusters of bin II.* In the case of IC dominance an increase of B does not significantly affect the particle energy losses, it causes an increase of ν_b (Eq.6.7) and thus an increase of the probability to have giant RHs. On the other hand, in the case of synchrotron dominance the particle energy losses increase and consequently ν_b decreases (Eq.6.7) as well as the probability to form giant RHs.

For this reason, *given η_t, the ratio between the probability to form giant RHs in the bin I and in the bin II is expected to decrease with increasing b, as larger values of b yield a more rapid increase of B with cluster mass* (Fig.6.8).

In Tab.6.3 we report the maximum and the minimum values of η_t ($\eta_{t,max}$ and

$\eta_{t,min}$) for which the model reproduces the observed probabilities (1 σ limits) in both the mass bins. The results are given for the relevant ($B_{<M>}, b$) configurations reported in Fig. 6.7. In agreement with the above discussions, one might notice that in the case of IC dominance a larger magnetic field implies a smaller energetic request (smaller $\eta_{t,max}$). Finally we point out that the values of η_t do not strongly depend on model parameters as they also appear similar to those obtained in the more simple calculations of Chapt. 5.

6.6.2 Probability of radio halos with M_v and evolution with z

In this Section we calculate the expected differential probability to form giant RHs with cluster mass and redshift without restricting ourselves to the mass and redshift bins covered by present observations (bin I and bin II in Fig. 6.8). In doing these calculations we use the values of η_t as constrained in Tab.6.3 within the region ($B_{<M>}$,b) of Fig.6.7, and *make the viable (and necessary) assumption that the value of η_t (i.e., efficiency of turbulence in going into MS modes) is constant with redshift.*

The detailed calculation of the acceleration efficiency and of the probability to have giant RHs requires extensive Montecarlo calculations (see Sec. 5.6 and 5.7) essentially because at each redshift the acceleration is driven by MS modes injected in the ICM from the mergers that the cluster experienced in the last few Gyr at that redshift. All the reported results make use of these calculations. However, to readily understand and comment the model results reported in the following, we may use the simplified formula Eq. (6.7) which describes the approximate trend of the break frequency with cluster mass. The adopted scaling $B \propto M^b$ implies that the synchrotron losses overcome the IC losses first in the more massive objects. Clusters of smaller mass in our synthetic populations have $B << B_{cmb}$ and this implies (Eq.6.7) $\nu_b \propto M^{2-\Gamma+b}\,(1+z)^{-8}$ so that the probability to form giant RHs in these clusters is expected to increase with the cluster mass ($2-\Gamma+b>0$ always) and to decrease with redshift. In the case of more massive clusters the situation may be more complicated. Indeed for these clusters there is a value of the mass, M_*, for which the cluster magnetic field becomes equal to B_{cmb}. For $M > M_*(z)$ it is $\nu_b \propto M^{2-\Gamma-3b}$ (Eq. 6.7) and thus the probability to form giant RHs would decrease as the mass becomes larger (given the lower bound of the slope b as constrained in Fig. 6.7, it is $2-\Gamma-3b<0$). In these cases, at variance with the smaller clusters, the

occurrence of giant RHs with z is only driven by the cosmological evolution of the cluster-merger history (which drives the injection of turbulence) rather than by the dependence of the IC losses with z (at least up to a redshift for which $B \sim B_{cmb}(z)$). As a consequence, the general picture is that going from smaller to larger masses, the probability should reach a max value around M_* for which $B \sim B_{cmb}(z)$, and then it should start to smoothly decrease. The value of this mass increases with z and depends on the scaling law of B with M. It is:

$$M_*(z) \simeq < M > \left(\frac{3.2\,(1+z)^2}{B_{<M>}(\mu G)} \right)^{1/b} \tag{6.12}$$

In order to show in some detail this complex behavior in the following we analyze two relevant examples.

An example with super-linear scaling: large B

As a first example we focus on the case of a super-linear scaling. In Fig. 6.9, we report the occurrence of giant RHs as a function of the cluster mass in three redshift bins (panel a)) and the occurrence of giant RHs as a function of redshift in two mass bins (panel b)). These calculations have been performed using $b = 1.7$ and $B_{<M>} = 3\mu$G which are allowed from the observed correlations. We adopt $\eta_t = 0.2$ which is in the corresponding range of values obtained in Sec. 6.6 (see Tab. 6.3) in order to reproduce the observed mean probability of giant RHs at $z < 0.2$. One finds that at lower redshifts ($z \lesssim 0.1$) the probability to form giant RHs increases with the mass of the clusters up to $M_* \sim 2 \times 10^{15}\, M_\odot$, while for $M \gtrsim M_*$ synchrotron losses become dominant and this causes the decrease of the probability for $M \gtrsim M_*$. The mass at which $B \sim B_{cmb}(z)$ increases as $(1+z)^{2/b}$ and this causes the shift with z of the value of the cluster mass at which the maximum of the probability is reached.

Fig.6.9b shows the occurrence of giant RHs with z. In the higher mass bin ($2 \cdot 10^{15} \leq M \leq 4.5 \cdot 10^{15}$) the occurrence increases up to $z \sim 0.4$ and than starts to drop. In this very massive clusters the magnetic field is larger than $B_{cmb}(z)$ at any redshift and thus the synchrotron losses are always the dominant loss term. The behavior of the probability with z in this case is essentially due to the fact that the bulk of turbulence in these massive clusters is injected preferentially between $z \sim 0.2 - 0.4$. A different behavior is observed in the lower mass bin

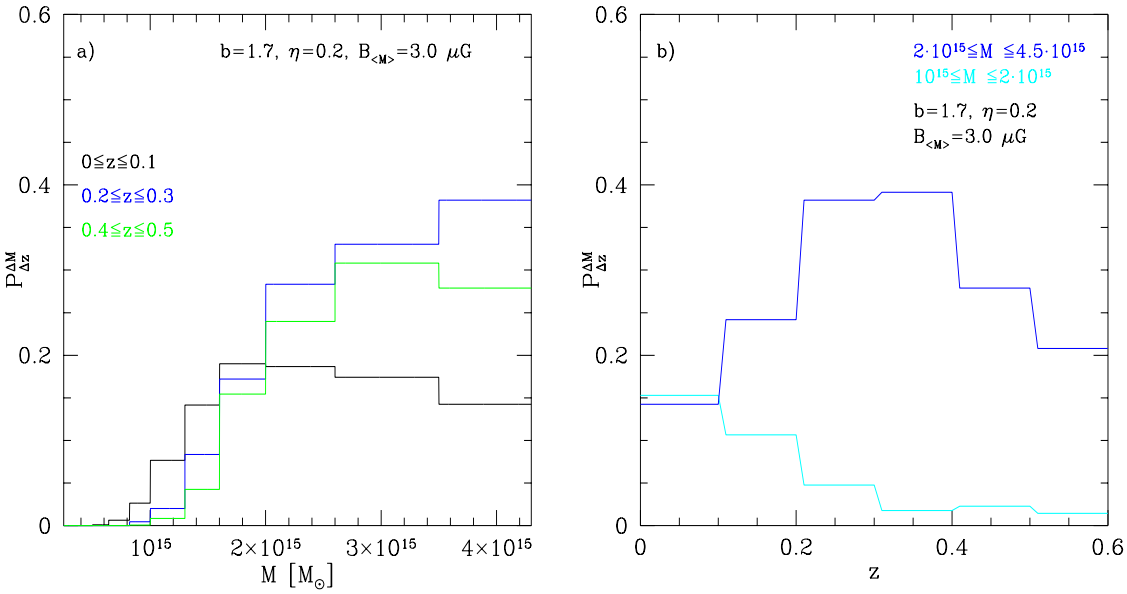

Figure 6.9: a) Occurrence of giant RHs as a function of the cluster mass in three redshift bins:0-0.1 (black line),0.2-0.3 (blue line), 0.4-0.5 (green line). b) Occurrence of giant RHs as a function of redshift in two mass bins: $[1\text{-}2]\times10^{15}M_{\odot}$ (cyan line) and $[2\text{-}4.5]\times10^{15}M_{\odot}$ (blue line). The calculation have been performed assuming: b=1.7, $B_{<M>} = 3.0\mu$G, $\eta_t = 0.2$ in both panels.

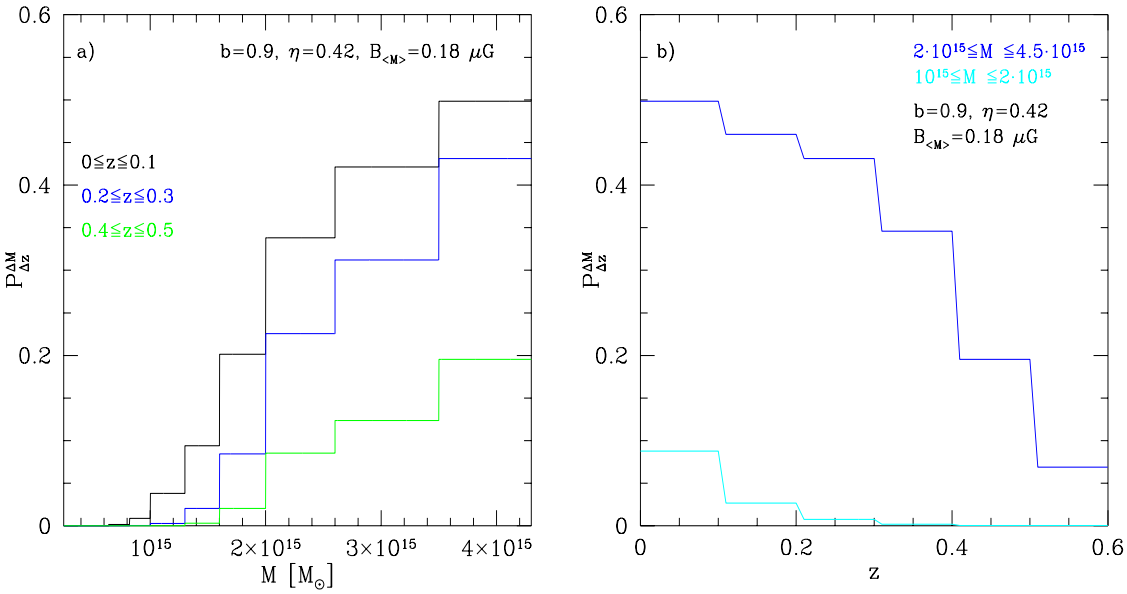

Figure 6.10: a) Occurrence of giant RHs as a function of the cluster mass in three redshift bins: 0-0.1 (black line),0.2-0.3 (blue line), 0.4-0.5 (green line). b) Occurrence of giant RHs as a function of redshift in two mass bins: $[1\text{-}2]\times10^{15}M_{\odot}$ (cyan line) and $[2\text{-}4.5]\times10^{15}M_{\odot}$ (blue line). The calculation have been performed assuming: b=0.9, $B_{<M>} = 0.2\mu$G, $\eta_t = 0.42$ in both panels.

($10^{15} \leq M \leq 2 \cdot 10^{15}$) where the occurrence of giant RHs decreases with redshift. This is because clusters with these lower masses have always $B < B_{cmb}(z)$.

An example with sub-linear scaling: small B

As a second example we focus on a sublinear scaling. In Fig. 6.10 we report the occurrence of giant RHs as a function of the cluster mass in three redshift bins (panel a)) and the occurrence of gint RHs as a function of redshift in two mass bins (panel b)). The calculations have been performed using $b = 0.9$ and $B_{<M>} = 0.2\mu$G, which are allowed from the correlations, and adopting a corresponding $\eta_t = 0.42$, which is within the range of values obtained in Sec. 6.6 (see Tab. 6.3) in order to reproduce the observed mean probability of formation of giant RHs at redshift $z < 0.2$. In this case at any redshift the probability to form giant RHs increases with the mass of the clusters. Indeed the magnetic field in these clusters is always $B << B_{cmb}(z)$ (for all redshifts and masses) and the IC losses are always the dominant loss term. In addition, as expected, in both the considered mass bins the probability to form giant RHs decreases as a function of redshift, due to the increase of the IC losses (Fig. 6.10, panel b)).

6.7 Luminosity Functions of Giant Radio Halos

In this Section we derive the expected luminosity functions of giant radio halos (RHLFs). Calculations for the RHLFs are carried out within the ($B_{<M>}$,b) region of Fig. 6.7 by adopting the corresponding values of η_t which allow to match the mean giant RH occurrence at $z < 0.2$. First we use the probability $P_{\Delta z}^{\Delta M}$ to form giant RHs with the cluster's mass to estimate the mass functions of giant RHs ($dN_H(z)/dMdV$):

$$\frac{dN_H(z)}{dM\,dV} = \frac{dN_{cl}(z)}{dM\,dV} \times P_{\Delta z}^{\Delta M} = n_{PS} \times P_{\Delta z}^{\Delta M}, \tag{6.13}$$

where $n_{PS} = n_{PS}(M, z)$ is the Press & Schechter (1974) mass function (Sect. 1.4.3, Eq.1.66) whose normalization depends essentially on σ_8 (present-day rms density fluctuation on a scale of $8h^{-1}$ Mpc) and Ω_o; we use $\sigma_8 = 0.9$ in a $\Omega_o = 0.3$ universe. The RHLF is thus given by:

$$\frac{dN_H(z)}{dV\,dP_{1.4}} = \frac{dN_H(z)}{dM\,dV} \Big/ \frac{dP_{1.4}}{dM}. \tag{6.14}$$

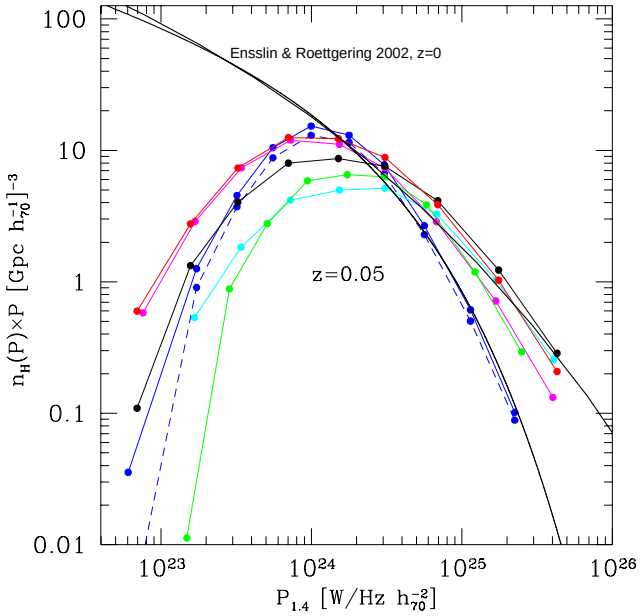

Figure 6.11: Expected RHLFs at $z \simeq 0.05$ (coloured lines with dots) obtained assuming: b=1.7, $B_{<M>} = 3.0\mu$G (blue lines: $\eta_t = 0.2$ (solid line) and $\eta_t = 0.19$ (dashed line)); b=1.7, $B_{<M>} = 2.2\mu$G and $\eta_t = 0.2$ (magenta line); b=1.5, $B_{<M>} = 1.9\mu$G and $\eta_t = 0.2$ (red line); b=0.9, $B_{<M>} = 0.18\mu$G and $\eta_t = 0.39$ (cyan line); b=0.6, $B_{<M>} = 0.2\mu$G and $\eta_t = 0.38$ (green line); b=1.0, $B_{<M>} = 0.45\mu$G and $\eta_t = 0.33$ (black line). For a comparison we report the range of Local RHLF obtained by E&R02 (black solid thick lines).

$dP_{1.4}/dM$ depends on the adopted values of ($B_{<M>}$, b) since each allowed configuration in Fig. 6.7 selects a value of the slope of $P_{1.4} - M_v$ (*e.g.,* Tab. 6.3) which is consistent (at 1 σ) with the value of the observed slope obtained with present observations ($\alpha_M = 2.9 \pm 0.4$; see Sec. 6.4). In particular from Fig. 6.5 one has that, for a given b, larger values of the magnetic field select smaller values of the slope of the $P_{1.4} - M_v$ correlation (and viceversa).

In Fig.6.11 we report the Local RHLFs (number of giant RHs per comoving Gpc^3 as a function of the radio power) as expected from our calculations. *The most interesting feature in the RHLFs is the presence of a cut-off/flattening at low radio powers. This flattening is a unique feature of particle acceleration models since it marks the effect of the decrease of the efficiency of the particles acceleration (in 1 Mpc h_{50}^{-1} cube) in the case of the less massive galaxy clusters. We stress that this result does not depend on the particular choice of the parameters.*

To highlight the result, in Fig.6.11 we also compare our RHLFs with the range

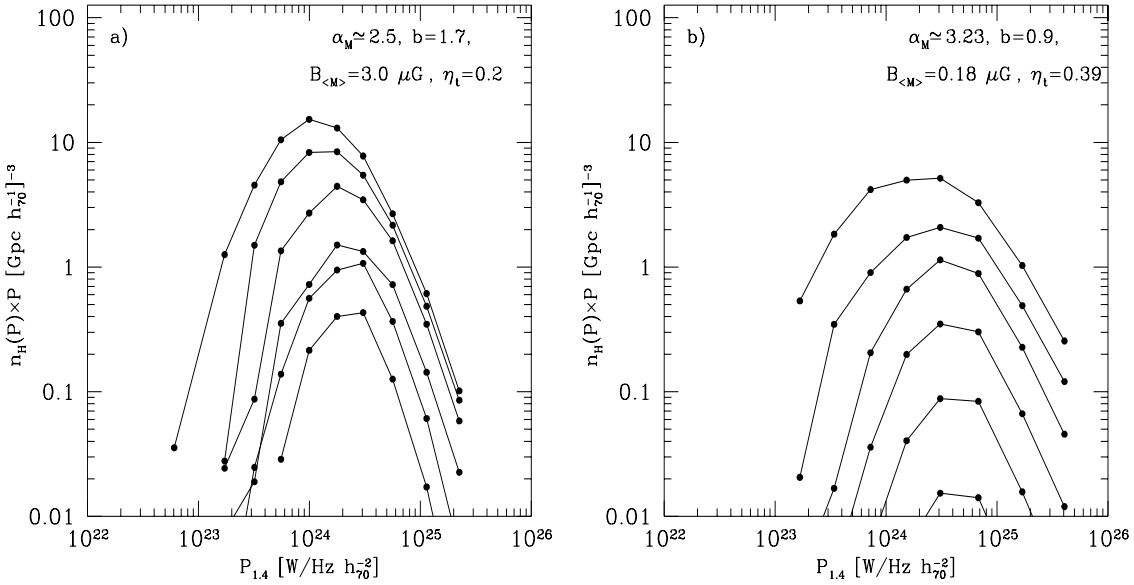

Figure 6.12: Evolution of RHLFs with redshift. The RHLFs are reported from redshifts 0-0.1 to 0.5-0.6 (curves from top to bottom). Calculations are developed for: Panel a) b=1.7, $B_{<M>} = 3.0\,\mu$G, $\eta_t = 0.2$, $\alpha_M \simeq 2.5$ and Panel b) b=0.9, $B_{<M>} = 0.18\,\mu$G, $\eta_t = 0.39$, $\alpha_M \simeq 3.23$.

of Local $(RHLFs)_{E\&R}$ (black solid lines) reported by Enßlin & Röttgering (2002). These $(RHLFs)_{E\&R}$ are obtained by combining the X-ray luminosity function of clusters with the radio-X-ray correlation for giant RHs and assuming that a costant fraction, $f_{rh} = 1/3$, of galaxy clusters have giant RHs independently from the cluster mass (see Enßlin & Röttgering 2002).

The most important difference between the two expectations is indeed that a low-radio power cut-off does not show up in the $(RHLFs)_{E\&R}$ in which indeed the bulk of giant RHs is expected at very low radio powers. The agreement between the two Local RHLFs at higher synchrotron powers is essentially because the derived occurrence of giant RHs in massive objects (Sect. 6.6) is in line with the fraction, $f_{rh} = 1/3$, adopted by Enßlin & Röttgering (2002) *in fitting the observed occurrence of RHs.*

In Fig. 6.12 we report the RHLFs expected by our calculations in different redshift bins. The calculations are performed by using two relevant sets of parameters (a super–linear and a sub–linear case as given in the caption of Fig. 6.12) allowed from the observed correlations. With increasing redshift the RHLFs decrease due to the evolution of the clusters mass function with z and to the evolution of the

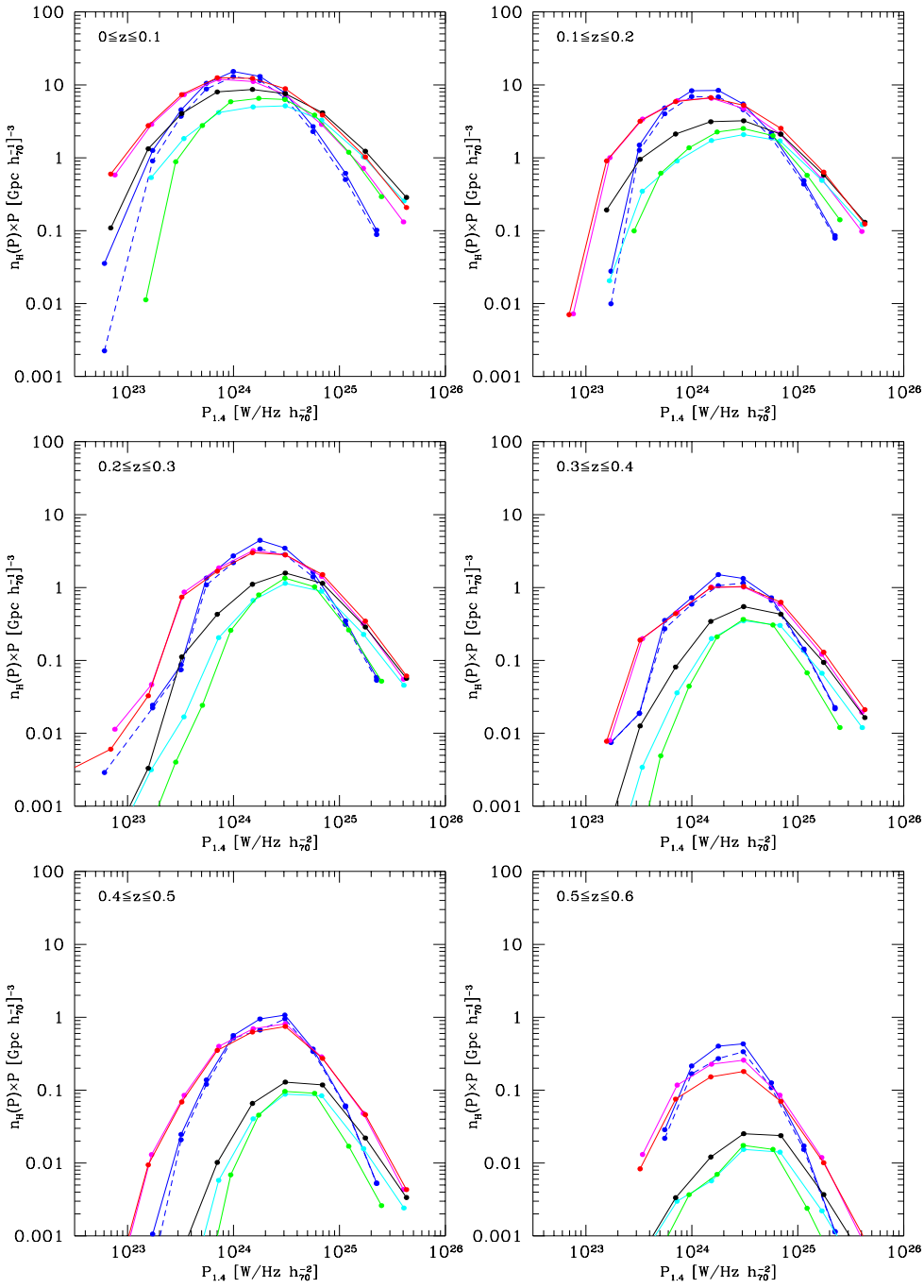

Figure 6.13: Expected RHLFs in 6 redshift bins (as reported in the panels). Calculations are performed by using the following values of the parameters : b=1.7, $B_{<M>} = 3.0\mu$G (blue lines: $\eta_t = 0.2$ (solid lines) and $\eta_t = 0.19$ (dashed lines)); b=1.7, $B_{<M>} = 2.2\mu$G and $\eta_t = 0.2$ (magenta lines); b=1.5, $B_{<M>} = 1.9\mu$G and $\eta_t = 0.2$ (red lines); b=0.9, $B_{<M>} = 0.18\mu$G and $\eta_t = 0.39$ (cyan lines); b=0.6, $B_{<M>} = 0.2\mu$G and $\eta_t = 0.38$ (yellow lines); b=1.0, $B_{<M>} = 0.45\mu$G and $\eta_t = 0.33$ (black lines).

probability to form giant RHs with z.

Fig. 6.12, allows to readily appreciate the different behavior of the RHLFs in the case of a super-linear scaling of B with M, $b = 1.7$, (Fig. 6.12, Panel a)) and of a sub-linear scaling, $b = 0.9$ (Fig. 6.12, Panel b)): the evolution with redshift in the Panel b) (sub–linear case) is faster than that in the Panel a) (super–linear case). This difference is driven by the probability to form giant RHs as a function of redshift in the two cases: in the super–linear case the probability to form giant RHs does not decrease rapidly with z, while a rapid decrease of such a probability is obtained in the sub–linear case (see also Figs. 6.9, 6.10).

In Fig. 6.13 we report the RHLFs obtained by our calculations by adopting the selected set of configurations given in Tab. 6.3 (colour code is the same of Fig. 6.7). The combination of these configurations define a bundle of expected RHLFs which determines the range of the possible RHLFs.

All the calculations are performed for the corresponding range of values of η_t which allow to be consistent with the observed probability to form radio halos at $z \lesssim 0.2$. One finds that with increasing redshift the bundle of the RHLFs broadens along the $n_H(P) \times P$ axis. This is again due to the different evolutions of the probability to form giant RHs with z of the super–linear and sub–linear cases.

6.8 Number Counts of Giant Radio Halos

In this Section we derive the expected number counts of giant radio halos (RHNCs). This will allow us to perform a first comparison between the model expectations and the counts of giant RHs which can be derived from present observations, but also to derive expectations for future observations. As for the case of the RHLFs, in calculating the RHNCs we adopt the configurations of parameters which allow to reproduce the observed mean probabilities of giant RHs at $z < 0.2$. However, we point out that the fact that our expectations are consistent with the observed mean probability to form giant RHs at $z \lesssim 0.2$ does not imply that they should also be consistent with the observed flux distribution of giant RHs in the same redshift interval.

Given the RHLFs $(dN_H(z)/dP_{1.4}dV)$ the number of giant RHs with $f > f_{1.4}$ is given by:

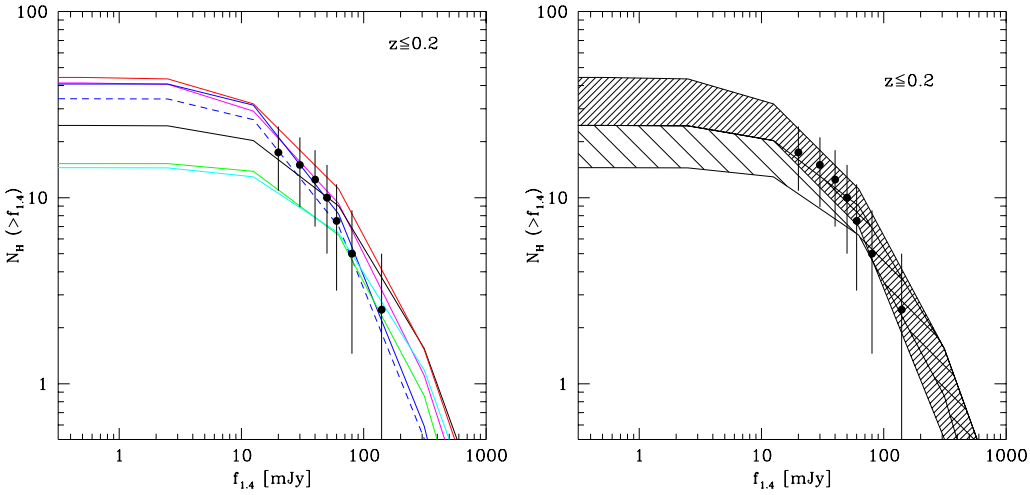

Figure 6.14: Number of expected giant RHs above a given radio flux at 1.4 Ghz from a full sky coverage up to $z \leq 0.2$. The black points are the data taken from Giovannini et al.(1999) and corrected for the incompleteness of their sky-coverage ($\sim 2\,\pi$ sr). **a)** The colour code is that of Fig.6.11; **b)** calculations are reported for the superlinear scaling ($b > 1$, upper region) and for the sublinear scaling ($b < 1$, lower region).

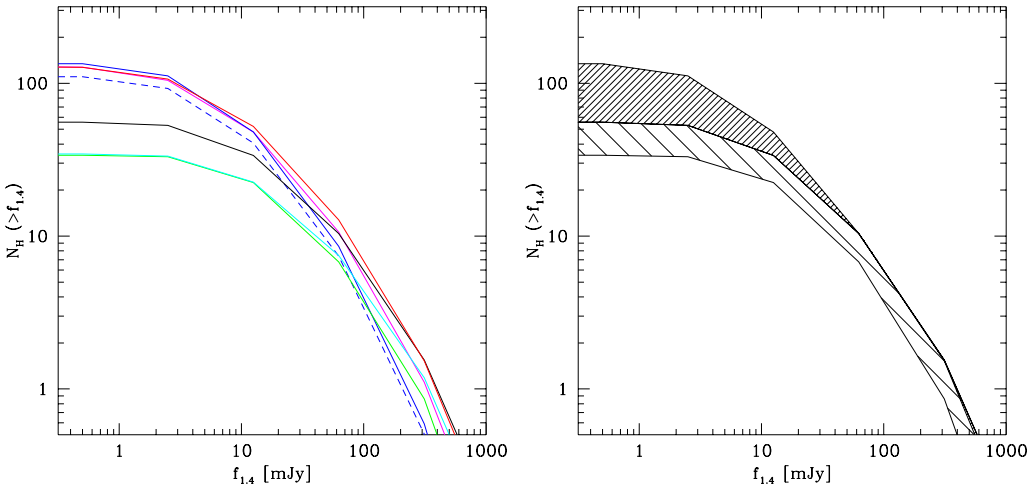

Figure 6.15: Number of expected giant RHs from the whole universe above a given radio flux at 1.4 GHz. **a)** The colour code is the same of Fig.6.11; **b)** calculations are reported for the superlinear scaling ($b > 1$, upper region) and for the sublinear scaling ($b < 1$, lower region).

$$N_H(> f_{1.4}) = \int_{z=0}^{z} dz' (\frac{dV}{dz'}) \int_{P_{1.4}(f^*_{1.4},z')} \frac{dN_H(P_{1.4},z')}{dP_{1.4}\, dV} dP_{1.4} \qquad (6.15)$$

where dV/dz is the comoving volume element in the ΛCDM cosmology (*e.g.,* Carroll et al. 1992); the radio flux and the radio power are related by $P_{1.4} = 4\pi\, d_L^2\, f_{1.4}$ with d_L the luminosity distance (where we neglect the K-correction since the slope of the spectrum of radio halos is close to unity).

As a first step, we use Eq. 6.15 to calculate the number of expected giant RHs above a given radio flux at 1.4 Ghz from a full sky coverage up to $z \lesssim 0.2$ and compare the results with number counts derived by making use of the present day observations (Fig. 6.14, the colour code is that of Fig.6.11). Calculations in Fig. 6.14 are obtained by using the full bundle of RHLFs obtained in the previous Section (Fig. 6.13). The black points are obtained by making use of the radio data from the analysis of the radio survey NVSS by Giovannini et al.(1999); normalization of counts is scaled to correct for the incompleteness due to the sky-coverage in Giovannini et al. ($\sim 2\,\pi$ sr). The NVSS has a 1σ level at 1.4 GHz equal to 0.45 mJy/beam (beam=45×45 arcsec, Condon et al. 1998). By adopting a typical size of giant RH of the order of 1 Mpc, the surface brightness of the objects which populate the peak of the RHLFs ($\sim 10^{24}$ W/Hz) at z$\sim$0.15 is expected to fall below the 2σ limit of the NVSS. These giant RHs have a flux of about 20 mJy, thus below this flux the NVSS becomes poorly efficient in catching the bulk of giant RHs in the redshift bin z=0–0.2 and a fair comparison with observations is not possible. *For larger fluxes we find that the expected number counts are in excellent agreement with the counts obtained from the observations.* We note that assuming a superlinear scaling of B with cluster mass, up to 30-40 giant RHs at $z < 0.2$ are expected to be discovered with future deeper radio surveys. On the other hand, the number of these giant RHs in the case of a sublinear scaling should only be a factor of ~ 2 larger than that of presently known halos (Fig. 6.14b).

As a second step, we calculate (Fig.6.15) the whole sky number of giant RHs expected up $z = 0.7$ (the probability to form giant RHs at $z > 0.7$ is negligible). We note that the number counts of giant RHs increases down to a radio flux of $f_{1.4} \sim 2 - 3$ mJy and then flattens due to the strong (negative) evolution of the RHLFs (Fig. 6.13). We note that the expected total number of giant RHs above 1 mJy at 1.4 GHz is of the order of ~ 100 depending on the scaling of the magnetic

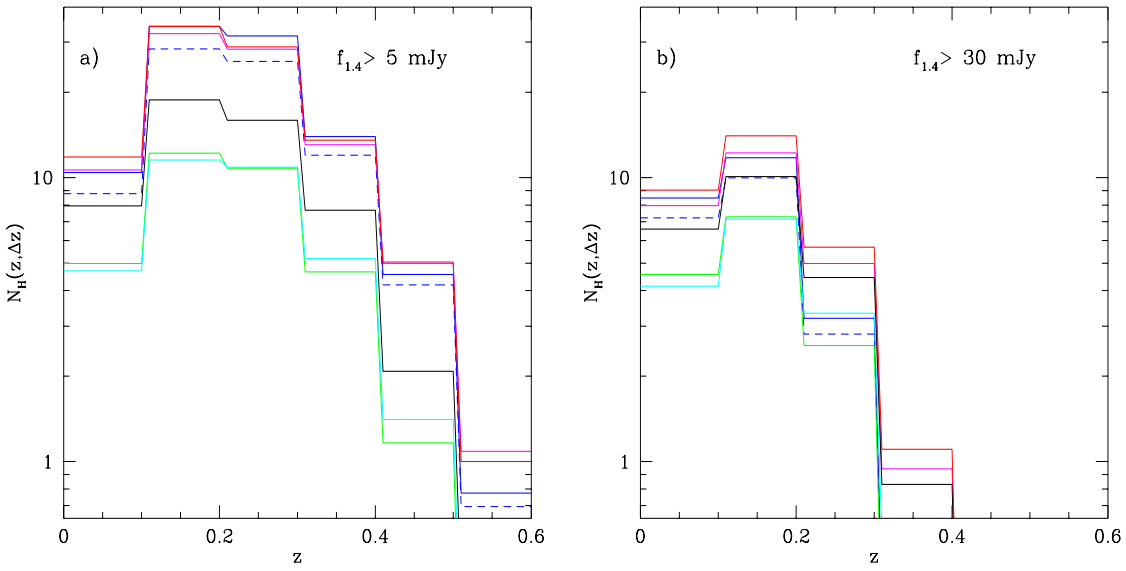

Figure 6.16: Expected total number of giant RHs above a given radio flux in different redshift bins: panel a) above 5 mJy; panel b) above 30 mJy. In both panels the colour code is the same of Fig.6.11.

field with cluster mass (Fig. 6.16b).

Finally we calculate the expected number counts of giant RHs above a given radio flux in different redshift bins. This allows us to catch the redshift at which the bulk of giant RHs is expected. In Fig. 6.16 we report the RHNCs integrated above 5 mJy (Panel a)) and above 30 mJy (Panel b)). *We note that the bulk of giant RHs at 1.4 GHz is expected in the redshift interval* $0.1 - 0.3$ *and this does not strongly depend on the flux limit.* We note that the *"relatively high value"* of such redshift range is also due to the presence of the low radio power cut-off in the RHLFs which suppresses the expected number of low power giant RHs. On the other hand, at radio fluxes > 30 mJy the contribution from higher redshift decreases since the requested radio luminosities at these redshift correspond to masses of the parent clusters which are above the high–mass cut-off of the cluster mass function.

6.9 Towards low radio frequencies: model expectations at 150 MHz

Due to their steep radio-spectra, giant RHs are ideal targets for upcoming low-frequency radio telescopes, such as LOFAR and LWA. Having in hands apowerful

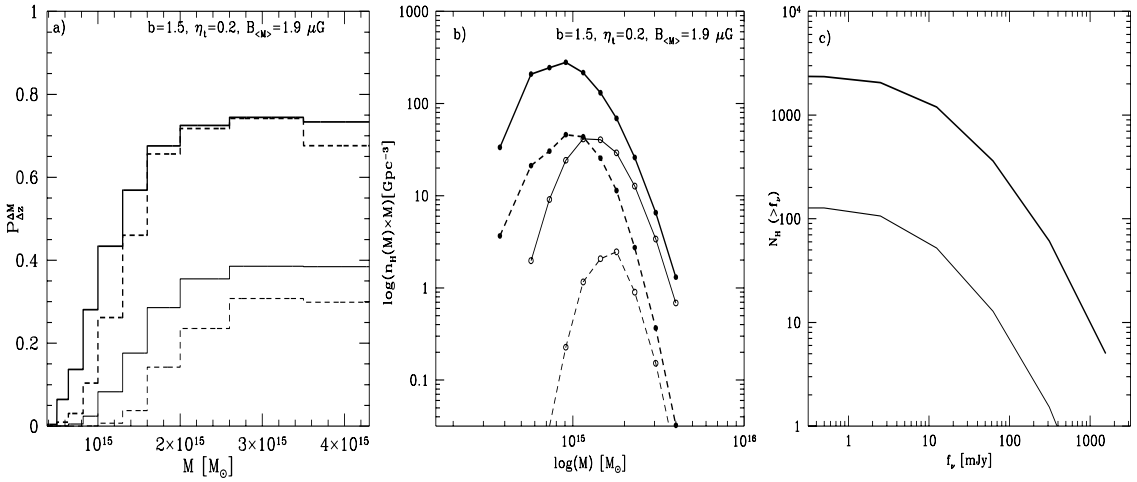

Figure 6.17: **a)** The occurrences of giant RHs as a function of the cluster mass in the redshift bins 0-0.1 (solid lines) and 0.4-0.5 (dashed lines) are reported for 150 MHz (thick lines) and for 1.4 GHz (thin lines). **b)** Mass functions of giant RHs in the redshift bins 0-0.1 (solid lines) and 0.4-0.5 (dashed lines) are reported for 150 MHz (thick lines) and for 1.4 GHz (thin lines). **c)** Comparison between the expected RHNCs above a given radio flux at 1.4 Ghz (thin lines) and at 150 MHz (thick lines) from a full sky coverage up to $z \leq 0.6$.
All the calculations have been performed assuming: b=1.5, $B_{<M>} = 1.9\mu$G and $\eta_t = 0.2$.

(and presently unique) tool to calculate statistical expectations of RHs, in this section we present calculations of the statistics of giant RHs at 150 MHz derived from the electron reacceleration model.

For simplicity, we present these results only for one set of the parameters in the plane $(B_{<M>}, b)$ (Fig.6.7): a super-linear case (b=1.5, $B_{<M>} = 1.9\mu$G) (see Sect. 6.5.3).

First, we calculate the probability to have giant RHs at ~ 150 MHz as a function of the cluster's mass following the procedure outlined in Sect. 6.6 and requiring a break frequency $\nu_b \gtrsim 20$ MHz to account for the new observation frequency. In Fig.6.17a we report the probability to have giant RHs as a function of virial mass in two redshift bins at 1.4 GHz (thin lines) and at 150 MHz (thick lines). As expected, the probability at 150 MHz is substantially larger than that calculated at 1.4 GHz, particularly for higher redshifts and for low massive clusters. *The increase of the occurrence of RHs towards lower observing frequencies is a unique expectation of the re-acceleration model.*

One of the main findings of our work is the presence of a cut-off in the RHLFs

at low radio powers (see Sec.5), which reflects the drop of the probability to form giant RHs as the cluster's mass decreases. In Fig.6.17b we plot the mass functions of radio halos (RHMFs) at 1.4 GHz and at 150 MHz in two redshift bins (see caption of Fig.6.17). We note that the number density of giant RHs is increased by only a factor ~ 2 for $M > 2 \cdot 10^{15}\, M_{\odot}$, but by more than one order of magnitude for $M \leq 10^{15}\, M_{\odot}$. *The most interesting feature is again the presence of a low mass cut-off in the RHMFs at 150 MHz, which however is shifted by a factor* ~ 2 *towards smaller masses with respect to the case at 1.4 GHz. This is related to the fact that a smaller energy density in the form of turbulence is sufficient to boost giant RHs at lower frequencies, and this allows the formation of giant RHs also in slightly smaller clusters, which indeed are expected to be less turbulent* (Chapt.5).

Finally, in order to obtain estimates for the RHLFs and RHNCs at 150 MHz, we tentatively assume the same $P_R - M$ scaling found at 1.4 GHz, scaled at 150 MHz with an average spectral index $\alpha_{\nu} \sim 1.2$, and follow the approach outlined in Secs. 6.7 and 6.8. In Fig.6.17c we report the expected integral number counts of radio halos from a full sky coverage above a given radio flux at 1.4 GHz (thin lines) and at 150 MHz (thick lines) up to a redshift $z \sim 0.6$. *The expected number of giant RHs at 150 MHz are a factor of* ~ 10 *larger than the number expected at 1.4 GHz, with the bulk of giant RHs at fluxes* $\geq$ *few mJy.*

The increase of the number of RH toward lower frequencies is driving by the increase of the probability to have RH emitting at lower frequencies (Fig. 6.17a) and is again a unique signature of the particle re-acceleration scenario. In the near future LOFAR will be able to detect diffuse emission on Mpc scale at 150 MHz down to these fluxes and this would be sufficient to catch the bulk of these giant RHs and to test the re-acceleration scenario.

6.10 Summary and Discussion

The observed correlations between radio and X-ray properties of galaxy clusters provide useful tools in constraining the physical parameters that are relevant to the reacceleration models for the onset of giant radio halos (RHs). The presented analisis is based on the calculations presented in Chapt.5, in which we have assumed that a seed population of relativistic electrons reaccelerated by magnetosonic (MS) waves is released in the ICM by relatively recent merger events. To this end we have

collected from the literature a sample of 17 giant RH clusters for all of which, but one (A2254), both radio and X-ray homogeneous data are available, as summarized in Tab.1 & 2. Based on the relationships derived in the previous Chapt.5, we have been able to constrain the (likely) dependence of the average magnetic field intensity (B) on the cluster mass, under the assumption that B can be parameterized as $B = B_{<M>}(M/ < M >)^b$ (with $B_{<M>}$ the average field intensity of a cluster of mean mass $< M >= 1.6 \times 10^{15}\, M_{\odot}$ and b positive). *This is an important achievement because both the emitted synchrotron spectrum and losses depend critically on the field intensity.* Following the approach outlined in Chapt.5, the merger events are obtained in the statistical scenario provided by the extended Press & Schechter formalism that describes the hierarchical formation of galaxy clusters. The main results of our study can be summarized as follows:

- *Observed correlations*

  In Sect. 6.4 we derive the correlations between the radio power at 1.4 GHz ($P_{1.4}$) and the X-ray luminosity (0.1-2.4 keV), ICM temperature and cluster mass. Most important for the purpose of the present investigation is the $P_{1.4} - M_v$ correlation which has been derived by combining the $L_X - M_v$ correlation obtained for a large statistical sample of galaxy clusters (the HIFLUGCS sample plus our sample) with the $P_{1.4} - L_X$ correlation derived for our sample of giant RHs. This procedure allows us to avoid the well known uncertainties and limits which are introduced in measuring the masses of small samples of galaxy clusters, especially in the case of merging systems. We find a value of the slope $\alpha_M = 2.9 \pm 0.4$ ($P_{1.4} \propto M_v^{\alpha_M}$). A steep correlation of the synchrotron luminosity with the ICM temperature is also found, although with a large statistical error in the determination of the slope : $\alpha_T = 6.4 \pm 1.6$ ($P_{1.4} \propto T^{\alpha_T}$).

- *Constraining the magnetic field dependence on the cluster mass*

  A correlation between the radio power and the cluster virial mass is naturally expected in the framework of electron acceleration models. This relationships, discussed in Sec. 6.5 (Eq.6.8), can reproduce the observed correlation for viable values of the physical parameters. For instance, in the case $B << B_{cmb}$, it is

$P(\nu_o) \propto {M_v}^{a(2-\Gamma+b)+b}$ and the exponent agrees with the observed one ($\alpha_M \sim 3$) by adopting a typical slope of the radio spectrum $a = 1 - 1.2$ and a sub–linear scaling $b \sim 0.6 - 0.8$.

A systematic comparison of the expected correlations between the radio power and the cluster mass with the observed one (Sects.6.5.1 and 6.5.3) allows the definition of a permitted region of the parameters' space ($B_{<M>}$,b), where a lower bound $B_{<M>} = 0.2\,\mu$G is obtained in order not to overproduce via the IC scattering of the CMB photons the hard X-ray fluxes observed in the direction of a few giant RHs (Sect. 6.5.3 and Fig. 6.7). It is found a lower bound at $b \sim 0.5 - 0.6$ and that a relatively narrow range of $B_{<M>}$ values is allowed for a fixed b. The boundaries of the allowed region, aside from the lower bound of $B_{<M>}$, are essentially sensitive to the limits from the $P_{1.4} - M_v$ correlation.

A super–linear scaling of B with mass, as expected by MHD simulations (Dolag et al. 2004) falls within the allowed region.

The values of the average magnetic field intensity in the superlinear case are close (slightly smaller) to those obtained from the Faraday rotation measurements (*e.g.,* Govoni & Feretti 2004), which, however, generally sample regions which are even more internally placed than those spanned by giant RHs.

Future observations will allow to better constrain the radio-X ray correlations and thus to better define the region of the model parameters.

- *Probability to form giant RHs*

In Sect. 6.6 we report on extensive calculations aimed at constraining η_t, the fraction of the available energy in MS waves, which is required to match the observed mean occurrence of giant RHs at redshifts $z \leq 0.2$ (Fig. 6.8). By adopting a representative sampling of the allowed ($B_{<M>}$,b) parameter space (Fig.6.7) we find $0.15 \leq \eta_t \leq 0.44$: the larger values are obtained for $B_{<M>}$ approaching the lower bound of the allowed region, because of the larger acceleration efficiency necessary to boost electrons at higher energies to obtain a fixed fraction of clusters with giant RHs.

With the constrained value of η_t for each set of ($B_{<M>}$,b) parameters we can calculate the probability of occurrence of giant RHs from smaller to larger redshifts for which observational data are not available. *This probability depends on the merging history of clusters and on the relative importance of the synchrotron and IC losses, and shows a somewhat complicated behavior with cluster mass and redshift. The maximum value of this probability at a given redshift is found for a cluster mass M_* (Eq.6.12) which mark the transition between the Compton and the synchrotron dominated phases.*

In the case of sublinear scaling of the magnetic field with cluster mass (b$\sim$0.6–0.9) the allowed values of the strength of the magnetic field are relatively small (Fig. 6.7), the value of M_* is large and the IC losses are always dominant for the mass range of clusters with known giant RHs. As a consequence the probability to have giant RHs increases with cluster mass and decreases with redshift (Fig 6.10). On the other hand superlinear scalings (b$\sim$1.2–1.7) imply allowed values of $B_{<M>}$ relatively large (Fig. 6.7), and even larger values of the magnetic field for the most massive objects. In this case the value M_* falls within the range of masses spanned by giant RH clusters: the predicted fraction of clusters with giant RHs increases with mass, then reaches a maximum value at about $M_v \sim M_*$, and finally falls down for larger masses (Fig 6.9). At variance with the case of sublinear scaling, in this case the fraction of the most massive objects with giant RHs is expected to slightly increase with redshift, at least up to z=0.2–0.4 (Fig 6.9) where the bulk of turbulence is injected in a ΛCDM model (Chapt.5).

- *Luminosity functions (RHLFs)*

In Sect. 6.7 we report the results of extensive calculations following a fair sampling of the ($B_{<M>}$,b) allowed region as summarized in Tab. 6.3; this essentially allows a full coverage of all possible RHLFs given the present correlations at 1σ. We find that, although the large uncertainties in the ($B_{<M>}$,b) region, *the predicted local RHLFs are confined to a rather narrow bundle, the most characteristic common feature being the presence of a flattening/cut-off at radio powers* below about 10^{24} W/Hz at 1.4 GHz

(Fig.6.11). The fraction of giant RHs with 1.4 GHz luminosity below $\sim 5 \times 10^{22}$W Hz^{-1} h$_{70}^{-2}$, a factor of $\sim$ 5 smaller than the luminosity of the less powerful giant RH (A2256, z=0.0581) known so far, is negligible. *This characteristic shape of the RHLFs, obtained in our work for the first time, represents a unique prediction of particle acceleration models, and does not depend on the adopted physical details for the particle acceleration mechanism.* This is due to the decrease of the efficiency of particle acceleration in the case of less massive clusters which is related to three major reasons (see Chapt.5):

i) smaller clusters are less turbulent than larger ones since the turbulent energy is expected to scale with the thermal one (see Chapt.5);

ii) turbulence is typically injected in large Mpc regions in more massive clusters and thus these are favoured for the formation of giant RHs (Chapt.5);

iii) since in the present work we found $B \propto M^b$ with $b \gtrsim 0.5$, higher energy electrons should be accelerated in smaller clusters to emit synchrotron radiation at a given frequency.

Deep radio survey with future radio telescopes (LOFAR, LWA, SKA) are required to test the presence of this cut-off/flattening in the luminosity function of the giant RHs.

The predicted evolution of the RHLFs with redshift is illustrated in Fig. 6.13: the comoving number density of giant RHs decreases with redshift due to the evolutions of the cluster mass function and of the probability to form giant RHs. The decrease with redshift of the RHLFs calculated by adopting sublinear scaling of the magnetic field with cluster mass is faster than that in the superlinear scaling causing a spread in the RHLFs bundle with z.

- *Number counts (RHNCs) at 1.4 GHz*

In Sect. 6.8 we have derived the integral number counts of giant RHs at 1.4 GHz. We find that the number counts predicted for the same set of RHLFs discussed in Sect. 6.7 generally agree with those derived from the NVSS at

the limit of this survey and within $z = 0.2$ (Fig.6.14). *The flattening of the counts below* $\sim 50 - 60$ *mJy is both due to the combination of the low power cut-offs of the RHLFs with the redshift limit, and to the RHLFs evolution with redshift.* On the other hand, past extrapolations of the data which assume a fixed fraction of giant RHs with cluster mass predict an increasing number of sources at lower fluxes (*e.g.,* Enßlin & Röttgering 2002).

Giant RHs around the peak of our LFs ($P_{1.4GHz} \sim 10^{24}$W/Hz) and at z$\sim$0.15 would be detectable at fluxes below about 20 mJy, which however is below the sensitivity limit of the NVSS for this type of objects. We estimate that the number of giant RHs below this flux could be up to 30-40 (whole sky, $z \leq 0.2$) if superlinear scalings of the mass with B hold.

The predicted number of giant RHs (Fig.6.15) (whole Universe) could be up to $\gtrsim 100$ if a superlinear scaling of the mass with B holds, while a sublinear scaling would give a number 2-3 times smaller. A substantial number of these objects would be found also down to a flux of a few mJy at 1.4 GHz in the case of a superlinear scaling, while in the case of sublinear scalings the number of giant RHs below about 10 mJy would be negligible.

We also find that the bulk of giant RHs is expected at $z \sim$0.1–0.3 (Fig.6.16). It should be mainly composed by those RHs populating the peak of the RHLFs, *i.e.,* objects similar (or slightly more powerful) to the giant RH in the Coma cluster.

- *Toward expectations at low radio frequencies: 150 MHz*

In Sect. 6.9 we have extended our estimates to the case of low frequency observations which will be made with upcoming instruments, such as LOFAR and LWA. *Lower energetic electrons contribute to these frequencies and thus - in the framework of the particle re-acceleration scenario - the efficiency of producing giant RHs in galaxy clusters is expected to be higher than that of giant RHs emitting at 1.4 GHz.*

By presenting the analysis for a representative set of parameters, we have shown that *the probability to have giant RHs emitting at 150 MHz is significantly*

larger than that of those emitting at 1.4 GHz, particularly in the mass range $\sim 5 \cdot 10^{14} - 1.5 \cdot 10^{15}\, M_{\odot}$. Consequently, the low mass cut-off in the RHMFs is shifted down by a factor of ~ 2. *This is naturally expected and is due to the fact that slightly less turbulent systems are able to generate giant RHs at lower frequencies.*

We have also estimated that the number counts of giant RHs at low frequencies might outnumber those at 1.4 GHz by at least one order of magnitude. We estimate that LOFAR is likely to discover $\gtrsim 10^3$ (all sky) giant RHs down to a flux of few mJy at 150 MHz.

Chapter 7

Revised statistics of giant radio halos (work in progress)

The calculations carried out in the previous Chapters (Chapt. 5 and Chapt. 6) provide a "unique" predictive power which combined with deep radio observations of complete samples of galaxy clusters can be used to constrain the models for the formation of giant radio halos (RHs) and the physical properties of the ICM.

In particular we have estimated the energy of turbulence injected in galaxy clusters through cluster mergers, and derived the expected occurrence of giant RHs as a function of the mass and dynamical status of the clusters in the framework of the merger–induced particle re–acceleration scenario (Chapt. 5). The most relevant result of those calculations is that the occurrence of giant RHs increases with the cluster mass, which is in agreement with observation at z$\leq$ 0.2 (*e.g.,* Giovannini et al. 1999). Most importantly we have also derived the evolution with redshift of the formation rate of RHs in galaxy clusters with different masses for different scaling laws between the rms magnetic field strength and the virial mass of the parent clusters ($B \propto M_v^b$).

In Sect. 6.8 we have also shown that the bulk of giant RH is expected to be in the redshift range $z \sim 0.1 \div 0.3$ (see also Fig. 7.1) and this comes from two competing effects: the general decrease of the number density of RHs as a function of redshift (or the negative evolution of the RHLFs) and the increase of the volume of the Universe with increasing redshift.

Unfortunately these expectations cannot be tested with present radio surveys as the cross correlation of X-ray cluster samples with both the NVSS at 1.4 GHz (Giovannini et al. 1999) and the WENSS at 327 MHz (Kempner & Sarazin 2001),

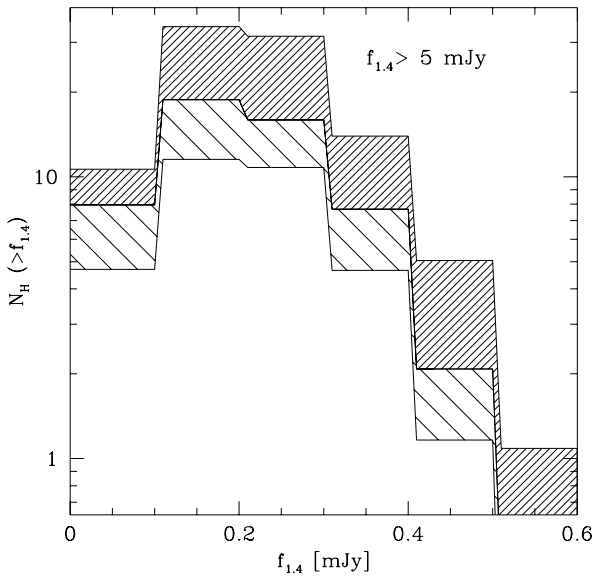

Figure 7.1: Expected total number of giant RHs above 5 mJy in different redshift bins. The calculations are reported for the superlinear scaling ($b > 1$, upper region) and for the sublinear scaling ($b < 1$, lower region); see Chapt.6 for a discussion.

which used clusters samples which were complete up to $z < 0.2$.

Starting from the results of the present PhD project and with the main aim to derive the fraction of massive galaxy clusters hosting a RH at relatively higher redshift ($0.2 \leq z \leq 0.4$) we carried out relatively deep observations of 50 massive (X-ray luminous) galaxy clusters at 610 MHz with the Giant Metrewave Radio Telescope (GMRT, Pune, India). We will refer to this project as the GMRT Radio Halos Survey.

The combination of this project with previous efforts from the NVSS will allow us to have a large complete sample of X-ray selected clusters in the redshift range $0 < z < 0.4$ and thus to perform a "statistical" analysis of these clusters, deriving the occurrence of RHs as a function of mass and redshift taking into account the observational biases and selection effects. We stress that this study is extremely important for understanding the origin of the RHs in galaxy clusters.

In general the main steps of this work can be summarized as follow:

- measure for the *first time* the occurrence of RHs in the redshift range $0.2 \leq z \leq 0.35$;
- constrain the dependence of their occurrence with cluster mass;

- combine the results with that at $z < 0.2$ (Giovannini et al. 1999) and test the theoretical expectation of the re-acceleration model

All the quantities are reported for a ΛCDM cosmology ($H_o = 70$ Km s^{-1} Mpc^{-1}, $\Omega_{o,m} = 0.3$, $\Omega_\Lambda = 0.7$, $\sigma_8 = 0.9$).

7.1 Selection of the sample in the redshift bin: $0.2 \div 0.4$

In order to obtain a statistically significant sample of clusters suitable for our aims, we based our selection on the ROSAT–ESO Flux Limited X–ray (REFLEX) galaxy cluster catalog (Böhringer et al. 2004) and on the extended ROSAT Brightest Cluster Sample (eBCS) catalog (Ebeling et al. 1998, 2000). These two catalogs have almost the same flux limit in the $0.1 - 2.4$ keV band ($\gtrsim 3 \cdot 10^{-12}$erg s^{-1} cm^{-2}) and thus we can selected an homogeneous flux limited sample. Form these catalogs we selected all clusters satisfying the following criteria:

1) $L_X(0.1\text{–}2.4 \text{ keV}) > 5 \times 10^{44}$ erg s^{-1};

2) $0.2 \leq z \leq 0.4$;

7.1.1 The Reflex sub-sample

The Reflex survey covers the southern sky up to declination $\delta = +2.5°$, avoiding the Milky Way and the regions of the Magellanic clouds, for a total area of 13924 deg^2 (4.24 sr). The sample is complete for X-ray fluxes larger than $\sim 3 \cdot 10^{-12}$erg s^{-1} cm^{-2} up to $z \sim 0.3$; above this redshift only very luminous objects (with X-ray luminosities of several 10^{45} erg/s) are observed (Böhringer et al. 2001). In order to have a good u-v coverage with the GMRT we selected in this sample only clusters with $\delta \geq -30°$.

In Fig. 7.2 we report the distribution of the REFLEX clusters in the plane $L_X - z$ and highlight with red circles the clusters which meet all the above criteria. We obtain a total sample of 27 clusters. The source list is reported in Tab. 7.1, where we give (1) the REFLEX name, (2) alternative name from other catalogs, (3) and (4) J2000 coordinates, (5) redshift, (6) the X–ray luminosity in the 0.1–2.4 keV band in unit of 10^{44} erg/s.

Among these 27 clusters, there are three clusters with known RHs, *i.e.,* A 2744, A 1300 and A 2163. From the remaining 24 clusters in Tab. 7.1 we selected all clusters with no radio information available in the literature and we also excluded all

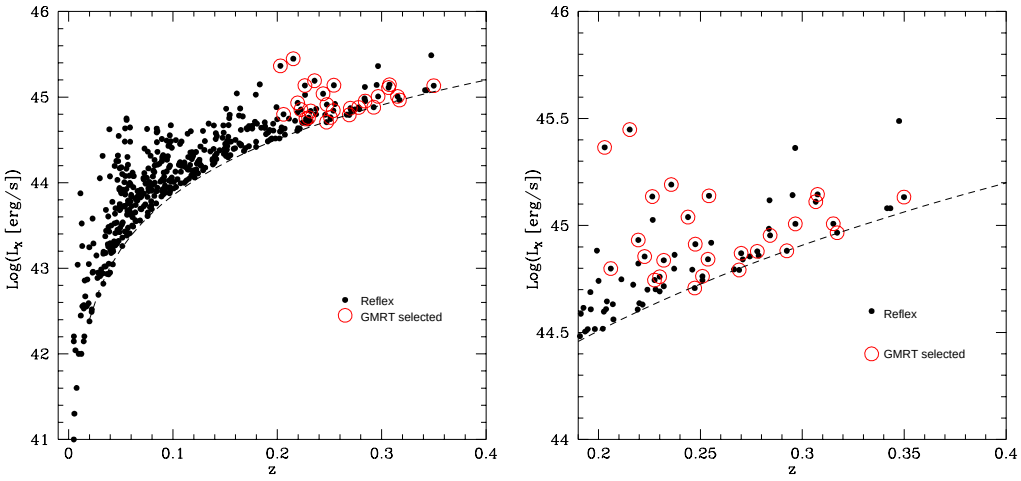

Figure 7.2: X-ray luminosity (in $0.1 - 2.4$ keV band) versus z for the REFLEX clusters (black filled circles). Open red circles select the clusters belonging to our sample.

clusters belonging to the GMRT Cluster Key Project (P.I. Kulkarni), and remained with 18 clusters (marked with the symbol $\surd$ in Tab. 7.1) which were all observed with the GMRT (in several observational run from January 2005 to August 2005).

7.1.2 The extended BCS sub-sample

The *ROSAT* Brightest Cluster Sample (BCS; Ebeling et al. 1998) is a 90 per cent flux-complete sample of the 201 clusters of galaxies in the northen hemisphere selected from the *ROSAT* All-Sky Survey (RASS). All these clusters have fluxes higher than 4.4×10^{-12} erg cm^{-2} s^{-1} in the 0.1-2.4 keV band. This sample is combined with a low-flux extension of the BCS (Ebeling et al. 2000) which consist of 99 clusters of galaxies with fluxes higher than 2.8×10^{-12} erg cm^{-2} s^{-1} in the 0.1-2.4 keV band. The combination of these two samples forms the homogeneously selected extended BCS (eBCS) which is statistically complete within a redshift $z \sim 0.3$ (Ebeling et al. 1998, 2000).

From the eBCS catalog we select all clusters which meet the above criteria and with $15° < \delta < 60°$, and obtain a total sample of 23 clusters. In Fig. 7.3 we report the distribution of the eBCS clusters in the plane $L_X - z$ and highlight with red circles the clusters which meet our selection criteria. The source list is reported in Tab. 7.2, where we give (1) the cluster's name, (2) and (3) J2000 coordinates, (4) redshift, (5) the X–ray luminosity in the 0.1–2.4 keV band in unit of 10^{44} erg/s. Among these 23

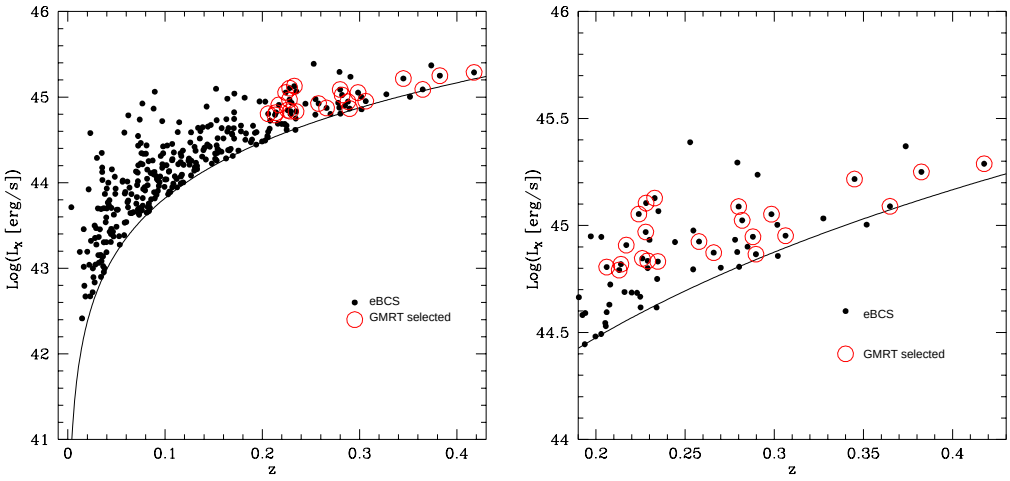

Figure 7.3: X-ray luminosity (in $0.1 - 2.4$ keV band) versus z for the REFLEX clusters (black filled circles). Open red circles select the clusters belonging to our sample.

objects 4 have already known diffuse radio emission (A 773, A 1758, A 2219, A 2390) and 3 other clusters have been already observed with the VLA (at 1.4 GHz) and the data are available in the VLA archive. Thus we ended up with a subset of 16 galaxy clusters which we observed with the GMRT (in August-September 2005).

7.1.3 Preliminary published results: the REFLEX sub-sample

The preliminary observational results of this work have been published in Venturi et al. (2007) and concern the observation at 610 MHz of 11 clusters from the REFLEX sub-sample. The sensitivity (1σ) in the obtained GMRT radio maps is in the range 35–100 μJy beam^{-1} for all clusters. We found three new RHs (see Fig. 7.4), in particular, giant RHs were found in A 209 and RXCJ 2003.5–2323, and one halo (of smaller size) was found in RXCJ 1314.4–2515. Furthermore, a radio relic was found in A 521, and two relics were found in RXCJ 1314.5–2515.

The remaining six clusters observed do not host extended emission of any kind at the level of 50-100 μJy/beam. This is an important and basic point of our investigation, since it is expected that the bulk of clusters of galaxies do not host an extended RH, therefore the deep upper limits on "radio-quiet" clusters are important at least as the detections.

In Fig. 7.5 we report the location of the giant RHs in A 209 and RXCJ 2003.5–2323 on the $L_{\rm X} - P_{1.4}$ correlation, where all the previously known clusters with

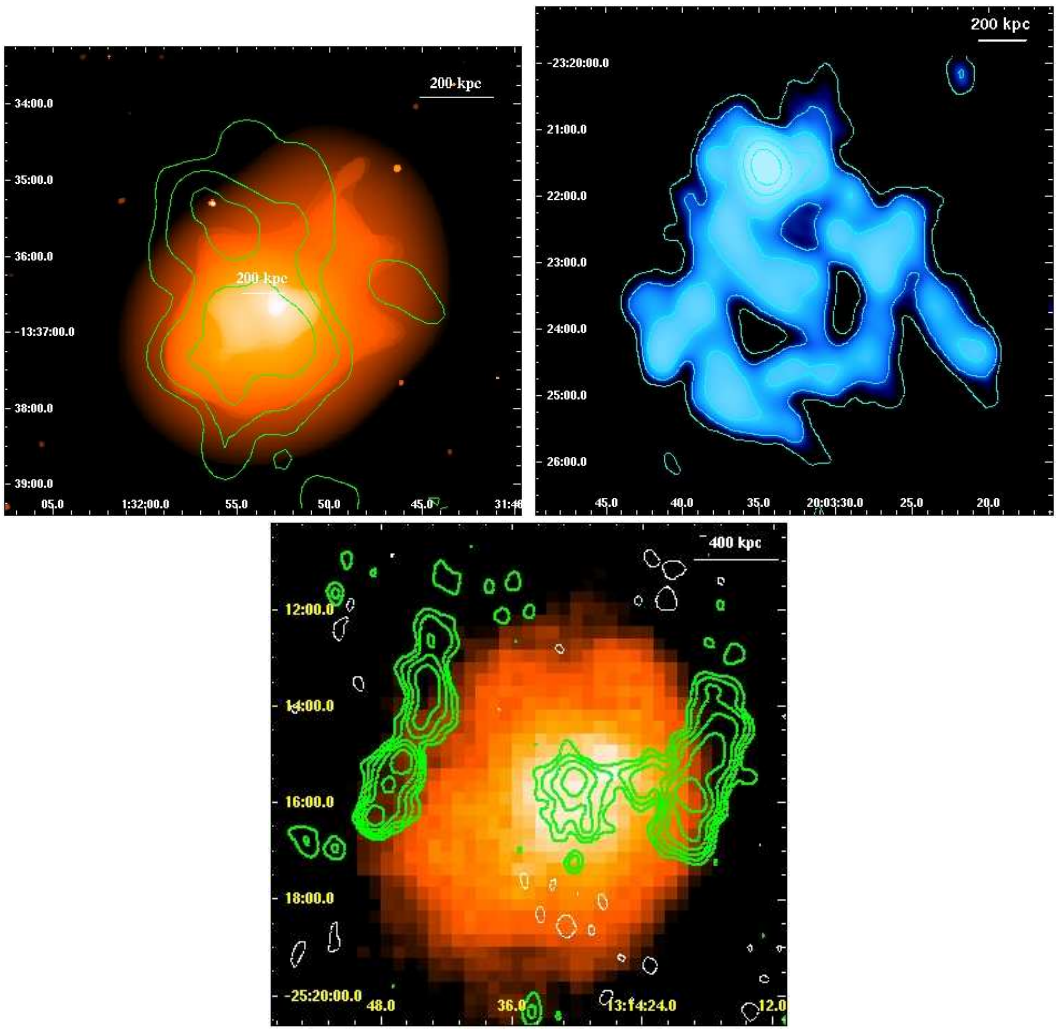

Figure 7.4: **a)** Radio conturns of A 209 RH after subtraction of the discrete radio sources on the X-ray archive Chandra image (colour) in the 0.3-9 keV band; the radio map has a resolution of 32" × 30" and an rms of 0.15 mJy/beam; the RH has LLS= $810\,h_{70}^{-1}$ kpc. **b)** Radio conturns and colour image of the RH in RXCJ2003-2323 after subtraction of the discrete radio sources. The radio map has a resolution of 32" × 23" and an rms of 100 μJy/beam; the RH has LLS= $1.4\,h_{70}^{-1}$ Mpc. **c)** Radio conturns of RXCJ1314-2515 superposed on the X-ray archive ASCA image (colour), the radio map has a resolution of 25" × 32" and an rms of 0.18 mJy/beam; the RH has LLS= $460\,h_{70}^{-1}$ kpc.

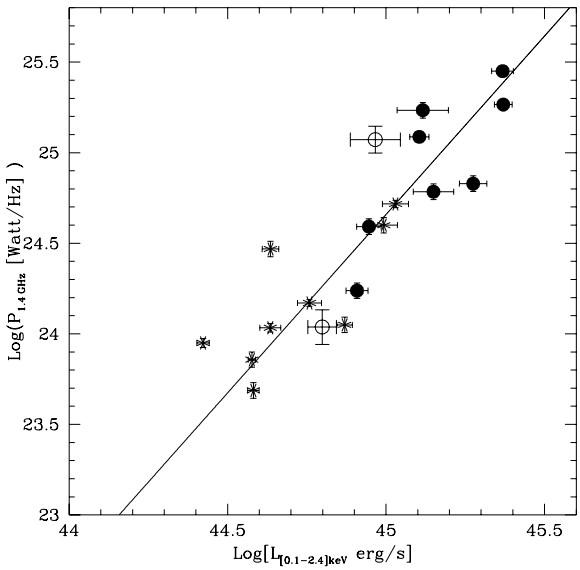

Figure 7.5: X-ray luminosity–radio power correlation for cluster with RHs. Stars represent the literature clusters at z<0.2 and filled circles the literature clusters at z> 0.2. Open circles show the location of A 209 (lower left) and RXCJ 2003.5–2323 (upper right).

giant RHs are also reported (see Chapt.6). The radio power at 1.4 GHz for these two clusters was obtained scaling the measured flux density at 610 MHz with a spectral index $\alpha_{610\ \mathrm{MHz}}^{1.4\ \mathrm{GHz}} = 1.2 \pm 0.2$ (the uncertainty assumed here dominates over the 610 MHz flux density error). Clusters at z<0.2 and those at z>0.2 are shown with different symbols. The location of A 209 and RXCJ2003.5–2323 on the plot is in good agreement with the distribution of all giant radio halos known in the literature.

An important piece of information would be the knowledge of the merging stage of the clusters in the sample, since cluster mergers are a major ingredient in the re–acceleration model. The literature information on the clusters presented here is not homogeneous, and it is not possible to make conclusive statements on the connection between merging/non–merging signatures and the presence/absence of RHs. A 209 is known to be undergoing merging events, but no information is available for RXCJ 2003.5–2323, except for an elongated X–ray emission imaged by ROSAT (Venturi et al. 2007). The three RH clusters known from the literature and belonging to our sample are all reported to be dynamically active (see for instance Finoguenov et al. 2005; Zhang et al. 2006). Signature of cluster merger is present

in the optical and X–ray bands for A 521 (Giacintucci et al. 2006, and references therein) and RXCJ 1314.4–2515, which host extended radio emission in the form of RHs and relics. Elongated or more complex X–ray isophotes are visible in S 780, A 141, A 2631 and in RXCJ 0437.1+0043, which lack cluster scale radio emission. The remaining two clusters without extended emission are considered "relaxed" on the basis of the X–ray emission (Venturi et al. 2007).

To summarize, the optical and X–ray information for the REFLEX sub-sample of clusters presented in Venturi et al. (2007) is in line with the findings that clusters with RHs are characterized by signatures of merging processes. On the other hand, clusters without extended radio emission ("radio quiet") may or may not show dynamical activity at some level.

7.2 Towards a revision of the occurrence of RHs within $z < 0.4$: preliminary results

The importance of the statistical properties of RHs resides in the fact that these can be used to discriminate among the possible models for the origin of RHs. Therefore an unbiased and exhaustive investigation of the present statistics of RHs is crucial in order to achieve a firm conclusion on the origin of RHs.

With this goal in mind we planned to revise the occurrence of RHs in the redshift range 0-0.4, combining the low redshift ($z < 0.2$) statistical study of XBACs clusters with the NVSS (Giovannini et al. 1999) with our recent results from the radio follow up of REFLEX and eBCS clusters, the GMRT RH survey, at relatively higher redshift ($0.2 < z < 0.4$).

The XBACs clusters (Ebeling et al. 1996) are extracted from an all-sky, X-ray flux limited sample of 242 clusters from the catalog of Abell (1989) (ACO) detected in the RASS with an X-ray flux above $5 \cdot 10^{12}\,\mathrm{erg\,cm^{-2}\,s^{-1}}$ in the 0.1-2.4 keV band and within $z < 0.2$ (which is the nominal completeness limit of the ACO clusters).

The NVSS is a radio survey performed at 1.4 GHz with the Very Large Array (VLA) in the D configuration, has an angular resolution of 45" (HPBW), a noise level of 0.45 mJy/beam (1 σ) and cover all the sky north of $\delta = -40°$. Because of the lack of short baseline the NVSS is insensitive to structure larger then $15'$, thus, since RHs have a typical total extension of about 1 Mpc, Giovannini et al. (1999) have limited their search to clusters with $z > 0.044$ (in a LCDM cosmology

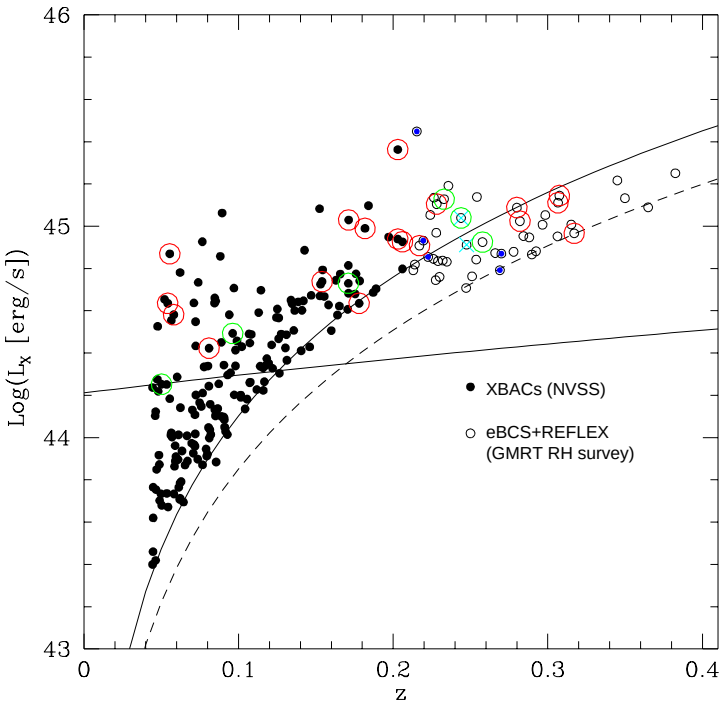

Figure 7.6: X-ray luminosity (in $0.1 - 2.4$ keV band) versus z for the XBACs clusters inspected with the NVSS (black filled circles) and for the REFLEX and eBCS clusters inspected with the GMRT (black open circles). Are also marked the 5 clusters belonging to the GMRT cluster key project (blue filled circles), the giant RH (open red circles), the small and/or mini halos (open green circles) and the relics we found in the REFLEX+eBCS sub-samples (cyan crosses). The black straight line gives the lower limit on cluster X-ray luminosity for a detection of a RH with size of $\sim 1\,h_{50}^{-1}$ Mpc in the NVSS, assuming a 1σ brightness limit and the radio power – X-ray luminosity correlations.

these means that the maximum detectable size at $z \sim 0.044$ is about 780 kpc). We select all clusters with $0.044 \leq z \leq 0.2$ and with $\delta > -40$ from the XBACs and end up with a XBACs sub-sample of 182 clusters which have been all inspected in the NVSS (once one excludes A 1773 and A 388 which fall in the few remaining gaps of the NVSS) by Giovannini et al. (1999).

In Fig. 7.6 we report the total sample of 230 clusters which have been observed in the radio (NVSS or GMRT). From the REFLEX sub-sample we exclude A 2163 (z=0.203) and A 209 (z=0.206) and from the eBCS sub-sample A 963 (0.206), which were already included in the XBACs sub-sample. On the other hand in the REFLEX sub-sample there are 5 clusters which are part of the GMRT cluster Key Project (P.I. Kulkarni) and for which no public radio information are available at present (they are marked with blue filled circles in Fig. 7.6). The total cluster sample is made of 210 clusters between $0.044 \leq z \leq 0.4$. In Fig. 7.6 we also mark with open red circles the clusters hosting a giant RH and with open green circles those hosting smaller or mini RHs: there is a tendency of RH to be hosted in high X-ray luminosity clusters, and this is line with previous claims (Giovannini et al. 1999).

This point, however, needs further investigation because, in order to derive the occurrence of RHs in galaxy clusters from the presented samples, one has to carefully check how the radio observations affect the completeness of the samples themselves. The observations carried out by our group at the GMRT are deep enough ($1\sigma \sim 35-100$ μJy beam^{-1}, depending on the specific objects) to guarantee that the non-detections of extended diffuse emissions are significant (Venturi et al., in prep; Brunetti et al. in prep.). On the other hand the NVSS survey is affected by surface brightness-limit ($1\sigma = 0.45$ mJy/beam) and this may affect the statistic of RH in the less X-ray luminous clusters.

As an example we report in Fig. 7.6 the lower limit on cluster X-ray luminosity for a detection of a RH with size of $\sim 1\,h_{50}^{-1}$ Mpc in the NVSS, assuming 1σ NVSS brightness limit and that the radio power – X-ray luminosity correlations observed for high X-ray luminous clusters, $L_X \gtrsim 2 \cdot 10^{44}\,h_{70}^{-2}$ erg/s (Chapt. 6, Fig.6.1), is valid also for lower X-ray luminosities.

This issue needs to be carefully explored and represent the final goal of this project. By taking into account the brightness limit of the NVSS radio survey and the the X-ray flux limits of the X-ray cluster samples, we will perform a detailed

and unbiased statistical analysis of the occurrence of RHs as a function of X-ray luminosity (mass) and redshift, and to compare these results with our expectations carried out in the framework of the re-acceleration scenario. This will be discussed in an upcoming paper (Cassano et al. in prep.).

Table 7.1: Cluster sample from the REFLEX catalog.

	REFLEX Name	Alt. name	RA_{J2000}	DEC_{J2000}	z	L_X
✓	RXCJ 0003.1−0605	A 2697	00 03 11.8	−06 05 10	0.2320	6.876
⋆	RXCJ 0014.3−3023	A 2744	00 14 18.8	−30 23 00	0.3066	12.916
✓	RXCJ 0043.4−2037	A 2813	00 43 24.4	−20 37 17	0.2924	7.615
✓	RXCJ 0105.5−2439	A 141	01 05 34.8	−24 39 17	0.2300	5.762
✓	RXCJ 0118.1−2658	A 2895	01 18 11.1	−26 58 23	0.2275	5.559
✓	RXCJ 0131.8−1336	A 209	01 31 53.0	−13 36 34	0.2060	6.289
✓	RXCJ 0307.0−2840	A 3088	03 07 04.1	−28 40 14	0.2537	6.953
	RXCJ 0437.1+0043	–	04 37 10.1	+00 43 38	0.2842	8.989
✓	RXCJ 0454.1−1014	A 521	04 54 09.1	−10 14 19	0.2475	8.178
	RXCJ 0510.7−0801	–	05 10 44.7	−08 01 06	0.2195	8.551
✓	RXCJ 1023.8−2715	A 3444	10 23 50.8	−27 15 31	0.2542	13.760
✓	RXCJ 1115.8+0129	–	11 15 54.0	+01 29 44	0.3499	13.579
⋆	RXCJ 1131.9−1955	A 1300	11 31 56.3	−19 55 37	0.3075	13.968
	RXCJ 1212.3−1816	–	12 12 18.9	−18 16 43	0.2690	6.197
✓	RXCJ 1314.4−2515	–	13 14 28.0	−25 15 41	0.2439	10.943
✓	RXCJ 1459.4−1811	S 780	14 59 29.3	−18 11 13	0.2357	15.531
	RXCJ 1504.1−0248	–	15 04 07.7	−02 48 18	0.2153	28.073
✓	RXCJ 1512.2−2254	–	15 12 12.6	−22 54 59	0.3152	10.186
	RXCJ 1514.9−1523	–	15 14 58.0	−15 23 10	0.2226	7.160
⋆	RXCJ 1615.7−0608	A 2163	16 15 46.9	−06 08 45	0.2030	23.170
✓	RXCJ 2003.5−2323	–	20 03 30.4	−23 23 05	0.3171	9.248
	RXCJ 2211.7−0350	–	22 11 43.4	−03 50 07	0.2700	7.418
✓	RXCJ 2248.5−1606	A 2485	22 48 32.9	−16 06 23	0.2472	5.100
✓	RXCJ 2308.3−0211	A 2537	23 08 23.2	−02 11 31	0.2966	10.174
✓	RXCJ 2337.6+0016	A 2631	23 37 40.6	+00 16 36	0.2779	7.571
✓	RXCJ 2341.2−0901	A 2645	23 41 16.8	−09 01 39	0.2510	5.789
✓	RXCJ 2351.6−2605	A 2667	23 51 40.7	−26 05 01	0.2264	13.651

Symbols are as follows: ✓ marks the clusters observed by us with the GMRT as part of our radio halo survey; ⋆ marks the clusters with radio halo known from the literature (A 2744 Govoni et al. 2001; A 1300 Reid et al. 1999; A 2163 Herbig & Birkinshaw 1994 and Feretti et al. 2001). All the remaining clusters are part of the GMRT cluster Key Project (P.I. Kulkarni).

Table 7.2: Cluster sample from the eBCS catalog.

Name	RA_{J2000}	DEC_{J2000}	z	L_X
$^{\surd}$RXJ0027.6+2616	00 27 49.8	+26 16 26	0.3649	12.29
$^{\surd}$A611	08 00 58.1	+36 04 41	0.2880	8.855
$^{\surd}$A697	08 42 53.3	+36 20 12	0.2820	10.57
$^{\surd}$Z2089	09 00 45.9	+20 55 13	0.2347	6.79
*A773	09 17 59.4	+51 42 23	0.2170	8.097
$^{\surd}$A781	09 20 23.2	+30 26 15	0.2984	11.29
$^{\surd}$Z2701	09 52 55.3	+51 52 52	0.2140	6.59
$^{\surd}$Z2661	09 49 57.0	+17 08 58	0.3825	17.79
$^{\surd}$A963	10 17 09.6	+39 01 00	0.2060	6.39
$^{\surd}$A1423	11 57 22.5	+33 39 18	0.2130	6.19
$^{\surd}$Z5699	13 06 00.4	+26 30 58	0.3063	8.96
$^{\surd}$A1682	13 06 49.7	+46 32 59	0.2260	7.017
$^{\surd}$Z5768	13 11 31.5	+22 00 05	0.2660	7.465
*A1758a	13 32 32.1	+50 30 37	0.2800	12.26
A1763	13 35 17.2	+40 59 58	0.2279	9.32
$^{\surd}$Z7160	14 57 15.2	+22 20 30	0.2578	8.411
$^{\surd}$Z7215	15 01 23.2	+42 21 06	0.2897	7.34
$^{\surd}$RXJ1532.9+3021	15 32 54.2	+30 21 11	0.3450	16.485
A2111	15 39 38.3	+34 24 21	0.2290	6.83
*A2219	16 40 21.1	+46 41 16	0.2281	12.73
A2261	17 22 28.3	+32 09 13	0.2240	11.31
*A2390	21 53 34.6	+17 40 11	0.2329	13.43
$^{\surd}$RXJ2228.6+2037	22 28 34.4	+20 36 47	0.4177	19.44

Symbols are as follows: $^{\surd}$ marks the clusters observed by us with the GMRT as part of our radio halo survey; * marks the clusters with a RH known from the literature (A 773 Govoni et al. 2001; A 1758 Giovannini et al. 2006; A 2219 Bacchi et al. 2003); * marks the clusters with "mini-halos" known from the literature (A 2390 Bacchi et al. 2003).

Chapter 8

New scaling relations in cluster RHs and the re-acceleration model

In the previous Chapters (Chapt. 5 and Chapt. 6) we have reported calculations carried out *for the first time* in the framework of the *re-acceleration* scenario, in which we have modelled the connection between RHs and cosmological cluster mergers, and investigated the observed correlations between the synchrotron radio power and the X-ray properties of the hosting clusters. Observed correlations relate the radio power at 1.4 GHz ($P_{1.4}$) with the X-ray luminosity (L_X), temperature (T) and cluster mass (Liang 1999; Colafrancesco 1999; Feretti 2000,2003; Govoni et al. 2001a; Enßlin and Röttgering 2002; see also Chapt. 6); also a trend between the largest linear size of RH and the X-ray luminosities of the hosting clusters is found (Feretti 2000). In particular, in Chapt. 6 we found a correlation between $P_{1.4}$ and the virial mass M_v of the hosting clusters, $P_{1.4} \propto M_v^{2.9\pm0.4}$, and discussed this correlation in the particle re-acceleration scenario. However, this correlation relates quantities which pertain to very different spatial regions: the observed radio emission comes from a radial size $R_H \sim 3-6$ time smaller than the virial radius R_v.

The formalism and procedures developed in the previous Chapts. 5 and 6 does not allow us to give a spatially resolved modeling of the particle acceleration process in galaxy clusters and for this reason the size of RH in Chapts.5 and 6 is taken $\approx 1\,\mathrm{Mpc\,h_{50}^{-1}}$. In principle in order to study at the same time the morphology and the statistical properties of RHs extensive numerical simulations (with ~ 100 clusters with $M > 10^{15}\,M_\odot$) are necessary and this is well above present ongoing projects. On the other hand, by making use of simple time-independent recipes based on the statistical modelling given in Chapts.5 and 6 one may discuss expected properties

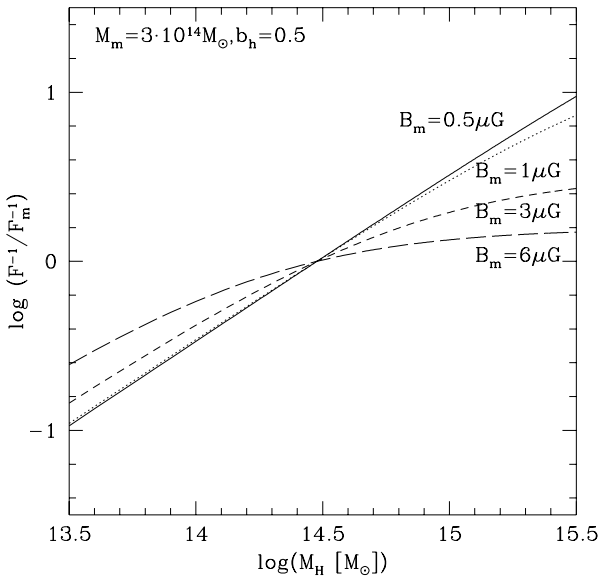

Figure 8.1: Function $\mathcal{F}^{-1}$, normalized to the $\mathcal{F}^{-1}$ value for a mean $M_H = M_m = 3 \cdot 10^{14}\, M_\odot$, as a function of M_H, for $b_H = 0.5$ and assuming different values of the magnetic field B_H corresponding to the mean mass $B_m = 0.5$, 1, 3, 6 μG, from top to bottom.

of RHs which are not restricted to virial quantities (M_v and R_v).

In this Chapter we will discuss expected scaling relations for RHs in the framework of the re-acceleration scenario in its simplest form. Then we present new observed correlations between the radio properties of RHs and dynamical quantities related to the radio emitting region and compare them with the expectations.

A ΛCDM ($H_o = 70$ Km s^{-1} Mpc^{-1}, $\Omega_m = 0.3$, $\Omega_\Lambda = 0.7$) cosmology is adopted.

The results presented in this Chapter are reported in a submitted paper (Cassano, Brunetti, Setti, Govoni, Dolag; submitted to MNRAS).

8.1 Expected scalings in the re-acceleration scenario

In this Section we derive scaling expectations for giant and powerful RH in the context of the re–acceleration scenario in its simplest form.

The most important ingredient is the energy of the turbulence injected in the ICM which is expected to be induced by the infalling sub-halos (*e.g.,* Roettiger et al. 1997; Ricker & Sarazin 2001; Tormen et al. 2004). We have derived in Chapt. 5 an estimate of the energy of merging-injected turbulence by assuming

that a fraction of the PdV work done by the infalling sub-halos is injected into compressible turbulence. We have shown also that the turbulent energy is expected to roughly scale with the thermal energy of the ICM, a result in line with recent analysis of numerical simulations (Vazza et al. 2006).

Following Chapts. 5, 6 we assume that once injected this turbulence is damped by Transit-Time-Damping (TTD) resonance with thermal and relativistic particles (at a rate Γ_{th} and Γ_{rel}, respectively). Since the damping time is shorter than the other relevant time scales (dynamical and re-acceleration) the energy density of the turbulence reaches a stationary condition given by $\dot{\varepsilon}_t/(\Gamma_{th}+\Gamma_{rel})$, where $\dot{\varepsilon}_t$ is the turbulence injection rate (see Chapt. 5 for details). When re–acceleration starts, the bulk of the energy density of compressible modes which is damped by the relativistic electrons goes into the re–energization of these electrons. On the other hand, after a few re–acceleration times, in a time–scale of the order of the typical age of RHs, particle re–acceleration is balanced by radiative losses, a quasi stationary situation is reached, and it can be assumed that the energy flux of the turbulent modes is essentially re–radiated via synchrotron and inverse Compton mechanisms:

$$(\frac{\dot{\varepsilon}_t\,\Gamma_{rel}}{\Gamma_{th}+\Gamma_{rel}}) \propto (\dot{\varepsilon}_{syn}+\dot{\varepsilon}_{ic}) \qquad \Rightarrow \dot{\varepsilon}_{syn} \propto \frac{\dot{\varepsilon}_t \times (\Gamma_{rel}/\Gamma_{th})}{(1+\frac{\dot{\varepsilon}_{ic}}{\dot{\varepsilon}_{syn}})} \tag{8.1}$$

where $\dot{\varepsilon}_{syn}$ and $\dot{\varepsilon}_{ic}$ are the synchrotron and IC emissivities (and $\Gamma_{th} >> \Gamma_{rel}$, see Chapt. 5; Brunetti & Lazarian 2007).
The ratio $\dot{\varepsilon}_{ic}/\dot{\varepsilon}_{syn}$ simply depends on $(B_{cmb}/B_H)^2$, where $B_{cmb} = 3.2\,(1+z)^2\,\mu$G is the equivalent magnetic field strength of the CMB (z, the redshift) and B_H the mean magnetic field strength in the radio halo volume, which can be parameterized as $B_H \propto M_H^{b_H}$ with M_H the total cluster mass within R_H (the average radius of the radio emitting region).

Based on the results of Chapt. 5, the injection rate of the turbulence in the RH volume can be estimated as $\dot{\varepsilon}_t \propto \overline{\rho}_H\, v_i^2/\tau_{cros}$, where $\overline{\rho}_H$ is the mean density of the ICM in the RH volume, v_i is the cluster-cluster impact velocity, $v_i^2 \propto M_v/R_v$, and τ_{cros} is the cluster-cluster crossing time (roughly constant). In the case R_H is larger than the cluster core radius one simply has $v_i^2 \propto \sigma_H^2 \approx GM_H/R_H$, where σ_H is the velocity dispersion inside R_H, and we shall assume $\dot{\varepsilon}_t \propto \overline{\rho}_H\,\sigma_H^2$. The term Γ_{rel}/Γ_{th} scales with $\epsilon_{rel}/\epsilon_{th} \times\sqrt{T}$ (Brunetti 2006, Brunetti & Lazarian 2007), where T is the temperature of the cluster gas, and $\epsilon_{rel}/\epsilon_{th}$ is the ratio between the

energy densities in relativistic particles and in the thermal plasma. Although this ratio might reasonably vary from cluster to cluster, we shall assume that it does not appreciably change in any *systematic* way with cluster mass (or temperature), at least if one restricts to the relatively narrow range in cluster mass spanned by clusters with giant RHs (see also the results from numerical simulations in Jubelgas et al. 2006). Then from Eq.8.1 the total emitted radio power is:

$$P_R = \int \dot{\varepsilon}_{syn}\, dV_H \propto \frac{M_H\, \sigma_H^3}{\mathcal{F}(z, M_H, b_H)} \tag{8.2}$$

where we have taken$\sqrt{T} \propto \sigma_H$ and defined $\mathcal{F}(z, M_H, b_H) = [1 + (3.2\,(1+z)^2/B_H)^2]$. The expression $\mathcal{F}$ (Fig.8.1) is costant in the asymptotic limit $B_H^2 >> B_{cmb}^2$ or in the simple case in which the rms magnetic field in the RH region is independent of the cluster mass. For $B_H^2 << B_{cmb}^2$ one has that $\mathcal{F}^{-1} \propto M_H^{2b_H}$, thus in the general case the expected scaling is steeper (slightly for B_H of the order of a few μG) than that obtained by assuming a constant $\mathcal{F}$.

It is important to stress here that the expression in Eq.8.2 is a general theoretical trend which implies simple scaling relations. Indeed, by taking $\sigma_H \approx \sqrt{GM_H/R_H}$ and under the very reasonable assumption that the mass scales with R_H as $M_H \propto R_H^\alpha$ (see also Sect. 8.2.2), Eq.8.2 (with $\mathcal{F} \sim$ cost) entails the correlations:

$$P_R \propto M_H^{\frac{5\alpha-3}{2\alpha}} \tag{8.3}$$

$$P_R \propto R_H^{\frac{5\alpha-3}{2}} \tag{8.4}$$

$$P_R \propto \sigma_H^{\frac{5\alpha-3}{\alpha-1}} \tag{8.5}$$

the effect of a non constant $\mathcal{F}$ is a steepening (although not substantial for $\sim \mu$G fields) of these scalings.

8.2 Observed scaling relations in clusters with radio halos

Motivated by the theoretical expectations outlined in the previous Section, we have searched for the predicted scaling relations in the available data set for giant RHs.

We consider a sample of 15 clusters with known giant RH ($R_H \gtrsim 300$ kpc) already analyzed in Chapt. 6, with the exclusion of CL0016+16, due to the lack of

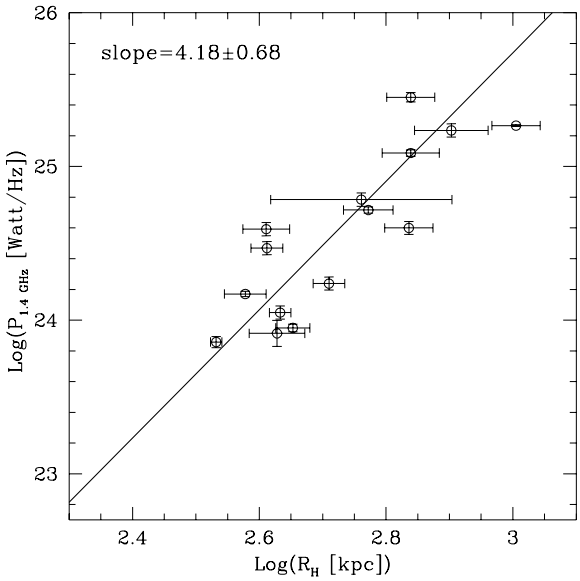

Figure 8.2: $P_{1.4}$ versus R_H. The fit has been performed using a power-law form in the log-log space and the best fit slope is reported in the panel.

good radio images to measure R_H, and of A754, due to very complex radio structure. References for 14 giant RHs are given in Chapt. 6, while for A2256 we use the more recent radio data from Clarke & Enßlin (2006). In Tab.8.1 we report the relevant observed and derived quantities for our sample.

8.2.1 Radio power versus sizes of radio halos

The first point that we want to investigate is the existence of a $P_R - R_H$ correlation (Eq.8.4) by making use of directly measurable quantities, such as the power and the radius at 1.4 GHz. In the present literature it is customary to use the Largest Linear Size (LLS), obtained from the Largest Angular Size (LAS) measured on the radio images as the largest extension of the 2σ or 3σ contour level, as a measure of the radio emitting region (*e.g.,* Giovannini & Feretti 2000; Kempner & Sarazin 2001). Since a fraction of RHs in our sample is characterized by a non–spherical morphology, meaning a non-circular projection on the plane of the sky, an adequate measure of a RH's size can be obtained by modelling the emitting volume with a spherical region of radius $R_H = \sqrt{R_{min} \times R_{max}}$, R_{min} and R_{max} being the minimum and maximum radius measured on the 3σ radio isophotes. In this way we have derived the R_H values for all 15 RHs, as reported in Tab.8.1, by making use of the

Table 8.1: In Col.(1): Cluster name. Col.(2): cluster redshift. Col.(3): logarithm of the radio power at 1.4 GHz, $P_{1.4}$, in unit of Watt/Hz. Col.(4): logarithm of the size of the RH, R_H, in unit of kpc h_{70}^{-1}. Col.(5): logarithm of the total cluster mass inside R_H, M_H, in unit of solar masses. The references for the cluster redshift and radio power are reported in CBS06, while for A2256 we use the more recent radio data from Clarke & Enßlin (2006).

cluster's name	z	Log($P_{1.4}$) [Watt/Hz]	Log(R_H) [kpc h_{70}^{-1}]	Log(M_H) [$M_\odot\, h_{70}^{-1}$]	Log(σ_H^2) [$km^2\, s^{-2}$]
1E50657-558	0.2994	25.45 ± 0.03	2.84 ± 0.04	14.83 ± 0.07	6.63 ± 0.08
A2163	0.2030	25.27 ± 0.01	3.01 ± 0.04	15.02 ± 0.05	6.65 ± 0.07
A2744	0.3080	25.23 ± 0.04	2.90 ± 0.06	14.76 ± 0.10	6.49 ± 0.11
A2219	0.2280	25.09 ± 0.02	2.84 ± 0.05	14.66 ± 0.08	6.46 ± 0.09
A1914	0.1712	24.72 ± 0.02	2.77 ± 0.04	14.68 ± 0.05	6.54 ± 0.06
A665	0.1816	24.60 ± 0.04	2.84 ± 0.04	14.57 ± 0.09	6.37 ± 0.10
A520	0.2010	24.59 ± 0.04	2.61 ± 0.04	14.21 ± 0.10	6.24 ± 0.11
A2254	0.1780	24.47 ± 0.04	2.61 ± 0.03	$--$	$--$
A2256	0.0581	23.91 ± 0.08	2.63 ± 0.04	14.17 ± 0.09	6.18 ± 0.11
A773	0.2170	24.24 ± 0.04	2.71 ± 0.03	14.43 ± 0.05	6.36 ± 0.06
A545	0.1530	24.17 ± 0.02	2.58 ± 0.03	14.08 ± 0.30	6.13 ± 0.30
A2319	0.0559	24.05 ± 0.04	2.63 ± 0.02	14.30 ± 0.03	6.30 ± 0.03
A1300	0.3071	24.78 ± 0.04	2.76 ± 0.14	14.54 ± 0.17	6.42 ± 0.22
Coma (A1656)	0.0231	23.86 ± 0.04	2.53 ± 0.01	14.12 ± 0.03	6.22 ± 0.03
A2255	0.0808	23.95 ± 0.02	2.65 ± 0.03	14.16 ± 0.07	6.14 ± 0.07

most recent radio maps available in literature. In Fig.8.2 we report $P_{1.4}$ versus R_H for our sample. We find a clear trend with R_H increasing with $P_{1.4}$, *i.e.,* the more extended RHs are also the most powerful. The best-fit of this correlation is given by:

$$\log\left[\frac{P_{1.4\,GHz}}{5\cdot 10^{24}\,h_{70}^{-2}\,\frac{Watt}{Hz}}\right] = (4.18\pm 0.68)\log\left[\frac{R_H}{500\,h_{70}^{-1}\,kpc}\right] - (0.26\pm 0.07) \qquad (8.6)$$

A Spearmann test yields a correlation coefficient of ~ 0.84 and a $s = 0.00011$ significance, indicative of a relatively strong correlation.

Uncertainties in the measure of the size of RH

The dispersion of the $P_{1.4} - R_H$ correlation is relatively large, a factor of ~ 2 in R_H, and this may be due to the errors associated with the measure of R_H. Indeed, RHs are low brightness diffuse radio sources which fade away gradually, until they are lost below the noise level of a given observation. Thus, the measure of a physical size is not obvious and, in any case, it needs to be explored with great care. However, what is important here is not so much the precise measure of R_H for each RH, but rather the avoidance of selection effects which might force a correlation.

In principle the sensitivity in the different maps may play a role because the most powerful RHs are also the most bright ones (Feretti 2005), and thus they might appear more extended then the less powerful RHs in the radio maps. To check if this effect is present, in Fig.8.3 we plot the ratios between the average surface brightness of each RH in our sample and the rms of each map used to get R_H. It is clear that there is some scattering in the distribution which would yield a corresponding dispersion in the accuracy of R_H, however, and most importantly, the ratios are randomly scattered, and there is no trend with R_H, *i.e.,* fainter RHs are usually imaged with a higher sensitivity and thus the $P_{1.4} - R_H$ correlation cannot be forced by the maps used to derive R_H.

An additional effort in assessing the reliability of R_H (and of the $P_{1.4} - R_H$ correlation) would be to measure the radial brightness profile of regular RHs which are not severely affected by powerful and extended radio sources. In our sample it is feasible to obtain accurate radial profiles from available data for the following RHs: A2163, A2255, A2744, A545 and A2319. We take the data at 1.4 GHz (Feretti et al. 2001, Govoni et al. 2005, Govoni et al. 2001a, Bacchi et al. 2003, Feretti et al. 1997,

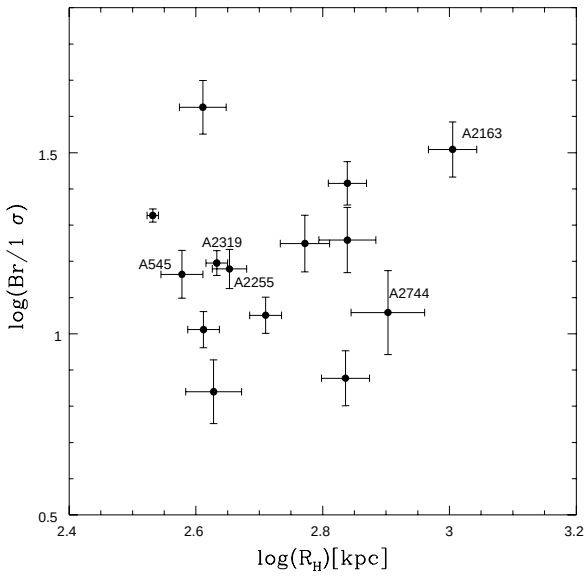

Figure 8.3: Ratios between the average surface brightness of each RH and the corresponding 1σ noise level from the radio maps. The five most regular RHs are earmarked.

respectively), and use the software package SYNAGE++ (Murgia 2001) to extract the radial brightness profiles, after subtraction of the embedded radio sources.

In Fig.8.4 we report the integrated brightness profiles of these RHs. It is seen that the profiles flatten with distance from the respective clusters centres, indicating that basically all the extended radio emission is caught and that it is possible to extract an accurate physical size. In Fig.8.5 we report for these 5 RHs the comparison between R_H, estimated directly from 3σ radio isophotes (see the above definition), and R_{85} and R_{75}, *i.e.,* the radii respectively containing the 85% and 75% of the flux of the RHs. We apply the same procedure also to the case of the Coma cluster at 330 MHz for which a brightness profile and radio map were already presented in the literature (Govoni et al 2001b). For Coma at 330 MHz we find $R_H \sim 520\, h_{70}^{-1}\, kpc$ and $R_{85} \sim 610\, h_{70}^{-1}\, kpc$, which set Coma in a configuration similar to that of the other clusters in Fig.8.5.

The linear, almost one-to-one correlation between R_H and R_{85} and the relatively small dispersion, consistent with the uncertainties in the profiles due to source subtraction, prove that our definition of R_H is a simple but representative estimate of the physical size of RHs.

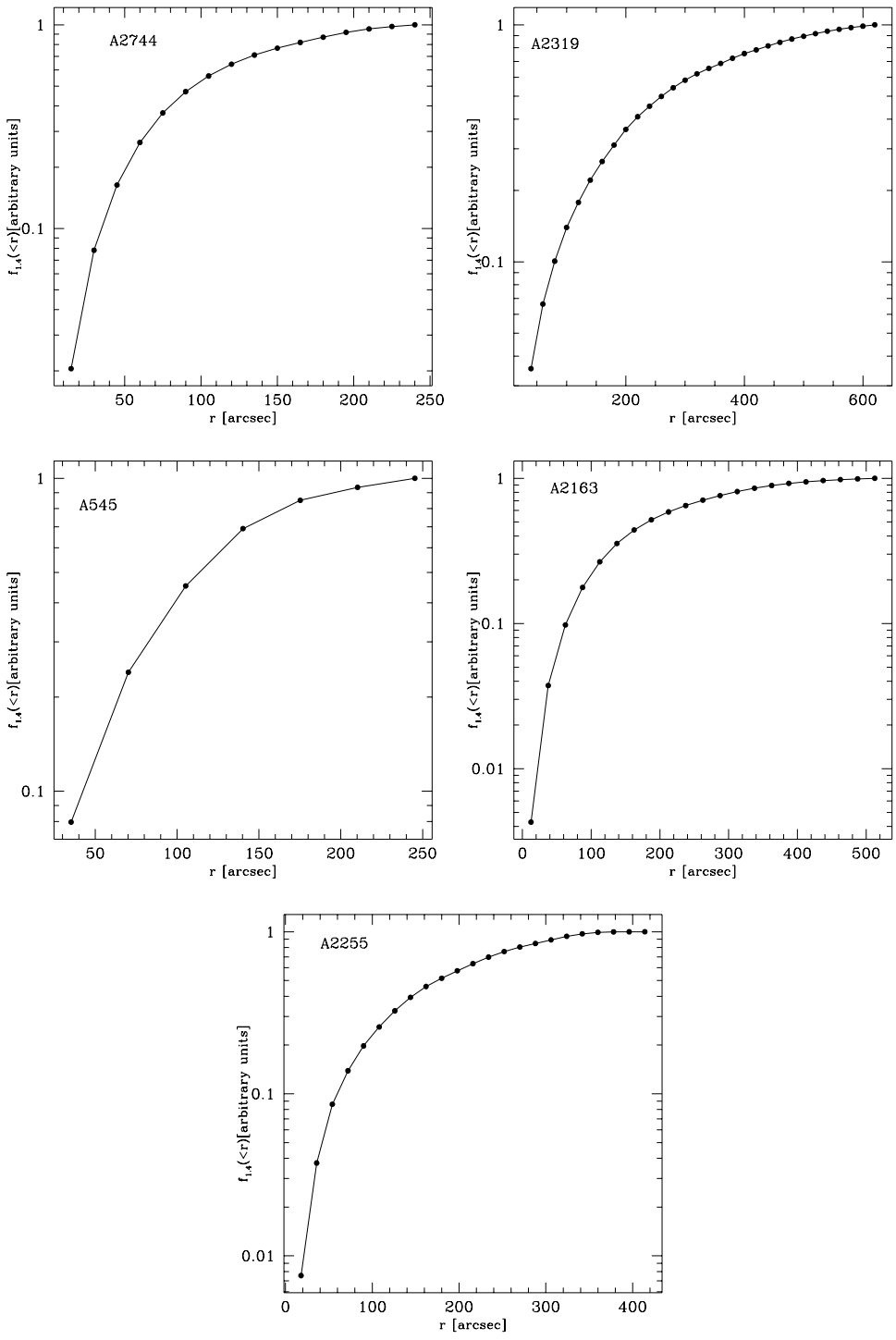

Figure 8.4: Integrated radial brightness profiles of the cluster RHs in A2744, A2319, A545, A2163 and A2255 (from the top left to the bottom right corner). The errors in the profiles, including the uncertainties in the sources subtraction and the statistical errors, are between $5 - 10\%$ depending on the cluster.

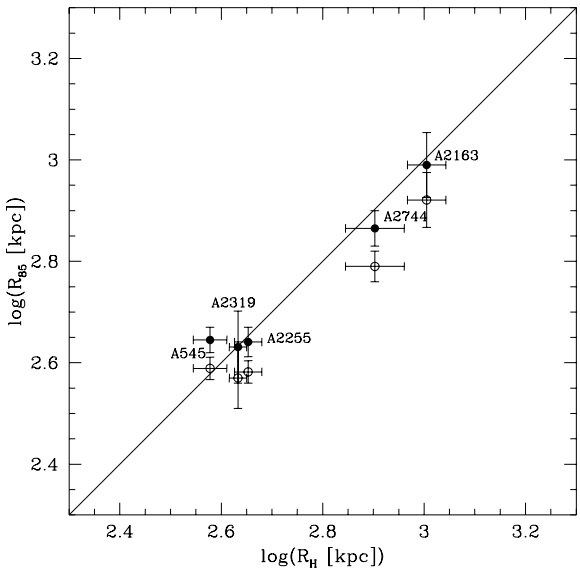

Figure 8.5: Radius enclosing the 85% (filled circles) and the 75% (open circle) of the total radio flux at 1.4 GHz obtained by the profiles (Fig.8.4) versus R_H estimated directly from the radio maps at 1.4 GHz.

We note that the sensitivities of the radio maps, the physical sizes R_{85} and powers $P_{1.4}$ of the 5 regular halos are representatives of the values encompassed by the full RH sample. Moreover, for these 5 RHs alone we find $P_{1.4} \propto R_{85}^{4.25\pm0.63}$, fully consistent with the $P_{1.4} - R_H$ correlation obtained for the total sample.

Possible biases in the selection of the sample

One has to check whether this correlation may not be forced by observational biases due to the selection of the RH population itself. Indeed the great majority of these RHs have been discovered by follow-ups of candidates, mostly identified from the NVSS (GTF99), which has a brightness limits of 1σ=0.45 mJy/beam (beam=45×45 arcsec, Condon et al. 1998), and this may introduce biases in the selected sample.

The upper bound of the correlation is likely to be solid: objects as powerful as those at the upper end of the correlation ($\log P_{1.4} \geq 25$) but with small R_H (similar to that of RHs in the lower end of the correlation) should appear in the NVSS up to the largest redshifts of the sample, since, even at $z \sim 0.3$, they should be $\geq$10 times brighter than the low power RH in the correlation and extended ($\sim 2.5'$). As a matter of fact A545 (z=0.15) and A520 (z=0.2), which are among the smaller RHs

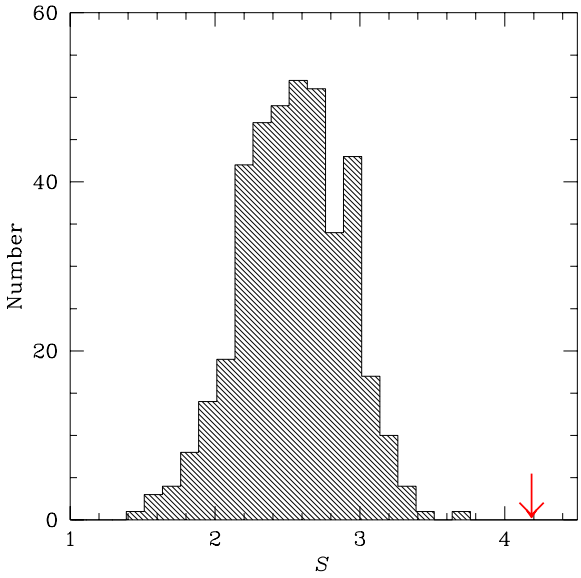

Figure 8.6: Distribution of the slopes, S, of the $P_{1.4} - R_H$ correlation obtained with our Monte Carlo procedure (with 400 trails). The arrow indicate the value of the observed best-fit slope $\simeq 4.18$.

in our sample, are already detected in the NVSS up to a redshift 0.2 and there is no reason why objects with similar extension, but $\sim 8 - 10$ times brighter should not have been detected at $z \leq 0.3$.

The lower bound of the correlation deserves much care since the brightness limit of the NVSS may play some role. It is clear that present surveys may significantly affect the selection of the faint end of the RH population. However, Feretti (2005) and Clarke (2005), have already concluded that the typical brightness of the powerful and giant RHs are well above the detection limit.

In any case, a brightness limit should drive a $P_{1.4} \propto R_H^2$ correlation, much flatter then the observed one. In order to provide a further compelling argument against observational biases, we have run Monte Carlo simulations. To this end we have randomly extracted brightness values of hypothetical RHs within a factor of ~ 5 interval (consistently with the range spanned in our sample) above a given minimum brightness and each time randomly assigned R_H and z among the observed values. In Fig.8.6 we report the distribution of the $P_{1.4} - R_H$ slopes obtained with our Montecarlo procedure and note that this distribution is peaked around ~ 2.5 with a dispersion of ± 0.4 (this is somewhat steeper than the expected $P_{1.4} \propto R_H^2$

due to the well known redshift effect, however small given the small redshift range of our sample). The values of the slopes from the Montecarlo procedure are far from the observed value (Fig.8.6) and a statistical test allows us to conclude that the probability that the observed $P_{1.4} - R_H$ correlation is forced by observational biases is $\lesssim 0.05\%$.

8.2.2 Radio power versus mass and velocity dispersion

In order to observationally investigate the existence of $P_{1.4} - M_H$ and $P_{1.4} - \sigma_H$ correlations the main difficulty concerns the measure of the cluster mass inside a volume of size R_H. Here the only possibility is to use the X-ray mass determination based on the assumption of hydrostatic equilibrium. Nevertheless, RH clusters are not well relaxed systems and thus the assumption of hydrostatic equilibrium and spherical symmetry may introduce sizeable errors in the mass determination. As discussed in Chapt. 1 several studies indicate that in the case of merging clusters the hydrostatic equilibrium method might lead to errors up to 40% of the true mass, which can be either overestimated or underestimated (*e.g.,* Evrard et al. 1996; Röttiger et al. 1996; Schindler 1996; Rasia et al. 2006). This would cause an unavoidable scattering in the determination of the mass in our sample, although there are indications that a better agreement between the gravitational lensing, X-ray and optically determined cluster masses is achieved on scales larger than the X-ray core radii (*e.g.,* Wu 1994; Allen 1998; Wu et al. 1998), which is the case under consideration ($R_H > r_c$).

However, what is important here is that the mass determination does not introduce systematic errors which depend on the mass itself and which may thus affect the *real* trend of the $P_{1.4} - M_H$ correlation. We thus compute the total gravitational cluster mass within the radius R_H as:

$$M_H = M_{tot}(< R_H) = \frac{3K_B T R_H^3 \beta}{\mu m_p G} \left(\frac{1}{R_H^2 + r_c^2} \right) \tag{8.7}$$

where r_c is the core radius, T the isothermal gas temperature and β the ratio between the kinetic energy of the dark matter and that of the gas (*e.g.,* Sarazin 1986). We have excluded from our analysis A2254 for which no information on the β-model is available. For the remaining 14 clusters references are given in Chapt. 6. From Eq.8.7 one has that $M_H \propto R_H$ for $R_H >> r_c$ and $M_H \propto R_H^3$ for $R_H << r_c$. In

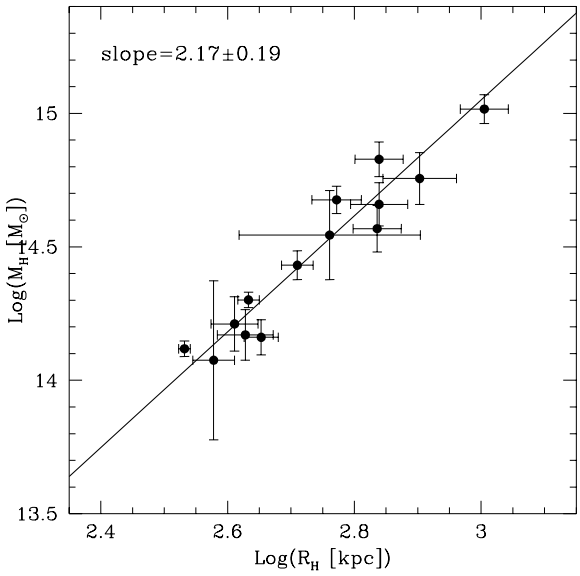

Figure 8.7: M_H versus R_H for giant RHs. The best-fit power-law and the value of the slope are also reported in the panel.

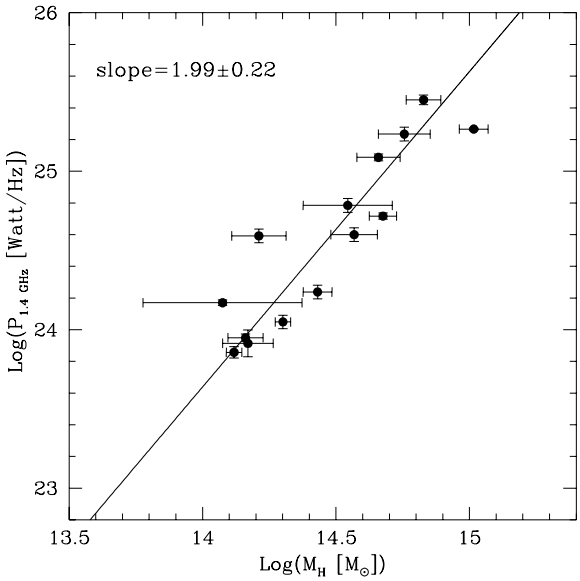

Figure 8.8: $P_{1.4}$ versus M_H for giant RHs. The best-fit power-law and its slope are also reported in the panel.

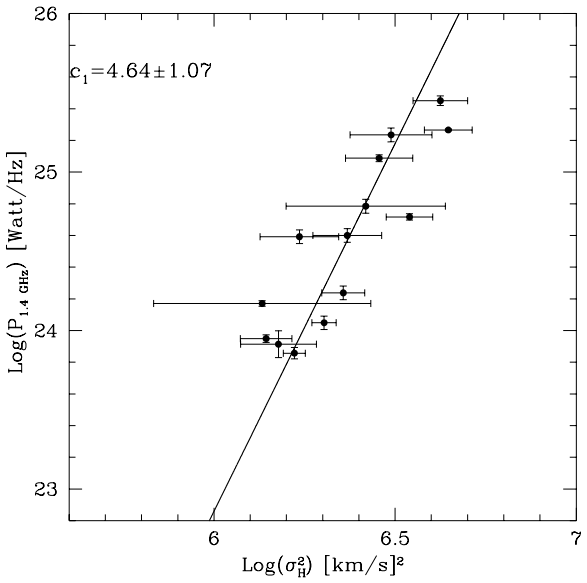

Figure 8.9: $P_{1.4}$ versus σ_H for the giant RH. The best-fit power-law and its slope are also reported in the panel.

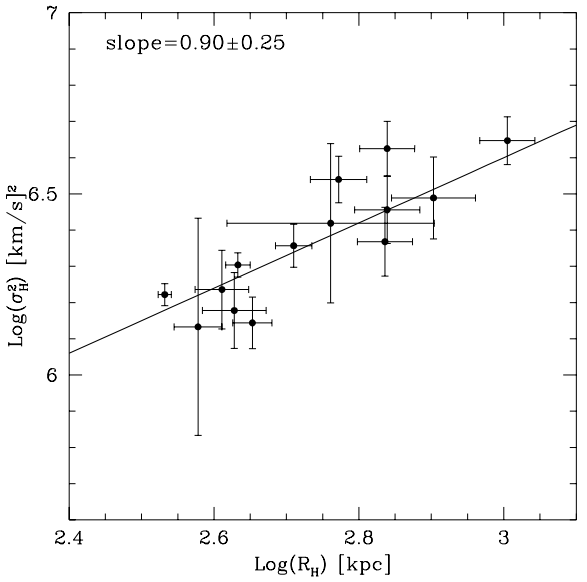

Figure 8.10: Square of the velocity dispersion inside R_H versus R_H. The best-fit power-law and its slope are also reported in the panel.

Fig.8.7 we plot R_H versus M_H for our sample: we find $M_H \propto R_H^{2.17\pm0.19}$, which falls in between the above asymptotic expectations.

The two correlations that we have found so far for giant RHs, $P_{1.4} - R_H$ (Eq. 8.6) and $M_H - R_H$, imply that $P_{1.4}$ should roughly scale as $M_H^{1.9-2}$. In Fig.8.8 we report $P_{1.4}$ versus M_H for our sample together with the best-fit: $P_{1.4} \propto M_H^{1.99\pm0.22}$, which is indeed in line with the above expectation. A Spearmann test of this correlation yields a correlation coefficient of ~ 0.91 and $s = 7.3 \cdot 10^{-6}$ significance, indicative of a very strong correlation.

As discussed at the end of Sect. 8.1, the $P_{1.4}$ vs. R_H and M_H correlations should translate in a $P_{1.4}$ vs. σ_H correlation. In Fig.8.9 we report $P_{1.4}$ versus σ_H for our sample of clusters with giant RH together with the best-fit: $P_{1.4} \propto (\sigma_H^2)^{4.64\pm1.07}$. A Spearmann test of this correlation yields a correlation coefficient of ~ 0.89 and to $s = 2 \cdot 10^{-5}$ significance, indicative of a very strong correlation.

As a by-product of all the derived scalings, it is worth noticing that also a trend between $R_H - \sigma_H$ is expected (Fig.8.10). This finding might also be tested with observations in the optical domain.

8.3 Some implications of the derived scalings

Given that the larger RHs are also the most powerful ones and are hosted in the most massive clusters, we expect that the size of a giant RH should scale with the size of the hosting cluster. We estimate for each cluster of our sample the virial radius (R_v) by combining the virial mass–X-ray correlation ($M_v - L_X$; Chapt. 6) and the virial radius-virial mass relation (e.g. Kitayama & Suto 1996). This method allows to reduce the effect of scattering due to the uncertainties in the mass measurements (and thus in the R_v) of merging galaxy clusters (see discussion in Chapt. 6). In Fig.8.11 we plot R_H versus R_v for our sample. The best fit gives $R_H \propto R_v^{2.63\pm0.50}$, i.e. *a pronounced non-linear increase of the size of the radio emitting region with the virial radius.* A Spearmann test yields a correlation coefficient of ~ 0.74 and $s = 0.0023$ significance, indicative of a relatively strong correlation, albeit less strong than the *others correlations found in this paper.*

Given that massive clusters are almost self similar (*e.g.,* Rosati et al. 2002) one might have expected that R_H scales with R_v and that the radial profiles of the radio emission are self-similar. On the contrary, our results prove that self-similarity is

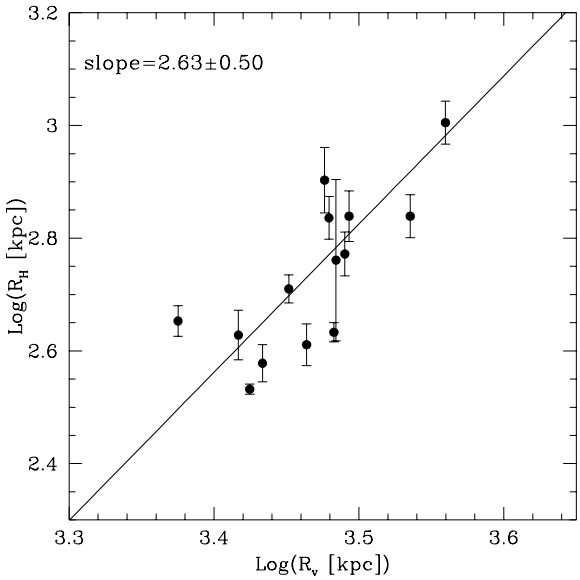

Figure 8.11: R_H versus virial radius,R_v, of hosting clusters estimated from the $Lx - M_v$ correlation (see CBS06). In the panel is also reported the best-fit correlation.

broken in the case of the non-thermal cluster components. This property of RHs was also noticed by Kempner & Sarazin (2001), which used a sample of RHs taken from Feretti (2000) and found evidence for a trend of the Largest Linear Size, LLS, with the X-ray luminosity in the 0.1-2.4 keV band, $LLS \propto L_x^{1/2}$, while a flatter scaling, $LLS \propto R_v \propto L_X^{1/6}$ is expected in the case of a self-similarity. Their results imply $R_H \propto R_v^3$; if one takes $R_H \approx LLS$, this is substantially in line with our findings. It is also worth noticing that X-ray–radio comparison studies of a few RHs indicates that the profile of the radio emission is typically broader than that of the thermal emission (*e.g.,* Govoni et al. 2001b). The two ingredients which should be responsible for the break of the self–similarity are the distributions of relativistic electrons and magnetic fields. In MHD cosmological simulations (Dolag et al. 2002, 2005) it is found that the magnetic field strength in cluster cores increases non-linearly with cluster mass (temperature). This implies that the radio emitting volume should increase with cluster mass because the magnetic field at a given distance from the cluster centre increases with increasing the mass. A detailed analysis of the magnetic field profiles of massive clusters from MHD simulations could be of help in testing if the magnetic field is the principal cause of the break of the self-similarity.

A basic constraint on the rms magnetic field (B_H) inside R_H may come

from the $P_{1.4} - M_H$ correlation. Indeed, under the assumption that the number density of relativistic electrons does not critically depend on cluster mass and that the average radio spectral index is $\sim$ 1.2 (*e.g.,* Feretti 2005), the synchrotron radio power should be $P_{1.4} \propto B_H^{2.2} R_H^3$. From the scaling $M_H \propto R_H^{2.17\pm0.19}$ one finds $P_{1.4} \propto M_H^{2.2\,b_H+(1.38\pm0.12)}$, where b_H has already (Sect. 8.1) been defined as $B_H \propto M_H^{b_H}$, which should be compared with the observed $P_{1.4} - M_H$ correlation. By taking into account the actual values of the observed correlations and the error propagation we obtain $0.12 \lesssim b_H \lesssim 0.43$, implying that B_H does not critically depend on cluster mass inside R_H and that *RHs might essentially select the regions of the cluster volume in which the magnetic field strength is above some minimum value* (say $\sim$ μG level). It is important to note that a roughly constant B_H with cluster mass does not contradict the scaling of B, averaged in a fixed volume, with cluster mass (or temperature) found in the MHD simulations (B within the cluster core radius, $r_c \sim 300\,h_{70}^{-1}\,kpc$), and also found in Chapt. 6 (B averaged within a fixed region of $\sim$ $720\,h_{70}^{-1}\,kpc$ size), because the magnetic field B_H is averaged over a volume of radius R_H that becomes substantially larger than the core radius with increasing the cluster mass (R_H/r_c goes from $\sim$ 1.1 to $\sim$ 3 with increasing cluster mass in our sample).

8.4 Particle re-acceleration model and observed scalings

Although we have been guided by the analysis of Eq.8.2 to predict the existence of scaling relationships, the observed correlations derived in Sect. 8.2 are actually independent of the form of this equation. To test Eq.8.2 against the observed quantities of our sample of RH we shall make use of the monochromatic $P_{1.4}$ instead of the unavailable bolometric P_R. This is possible because of the typical shape of RH spectra (because of the negligible K-correction; see discussion in Chapt. 6).

In Fig.8.12 we report $P_{1.4}$ versus $M_H\,\sigma_H^3$. The best fit gives $P_{1.4} \propto (M_H\,\sigma_H^3)^{1.24\pm0.19}$. The observed scaling is slightly steeper, but still in line with the linear scaling expected from Eq.8.2 for $\mathcal{F}$ constant (dashed line). As already discussed in Sec. 8.1 $\mathcal{F}$ is constant for $B_H^2 >> B_{cmb}^2$ or in the case in which the rms magnetic field in the RH region is quite independent from the cluster mass (small b_H), while formally a non–constant $\mathcal{F}$ always implies a steepening of the $P_{1.4} - M_H\,\sigma_H^3$ scaling. Namely, in the case of $\sim$ μG magnetic fields, by combining

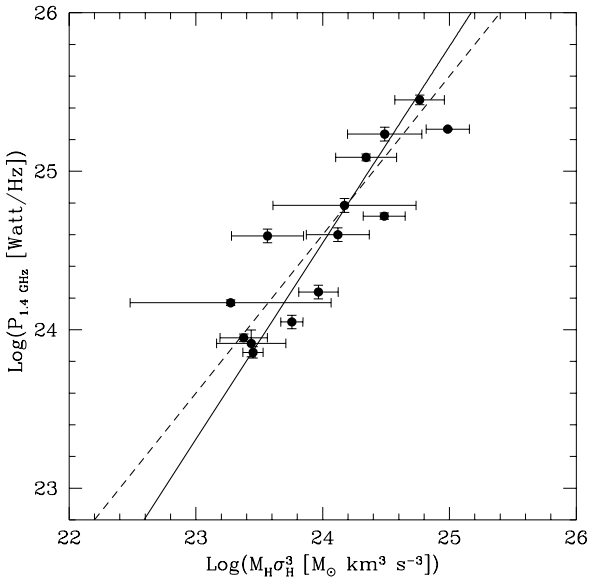

Figure 8.12: $P_{1.4}$ versus $M_H\,\sigma_H^3$. The best-fits correlations (solid line) and the predicted scaling with $\mathcal{F} \sim$ constant (dashed line) are reported.

Eq.8.2 with the observed $M_H - R_H$ correlation (Sec. 8.2.2, Fig.8.7), one has that the best-fit in Fig.8.12 is fulfilled by the model expectations for $0.05 \leq b_H \leq 0.39$, which is also consistent with the findings of Sec. 8.3.

In principle the fit can be used to set constraints on the values of the theoretical parameters entering the *normalization* of Eq.8.2, (namely $\epsilon_{CR}/\epsilon_{th}$, and the fraction of the PdV work which goes into turbulence), but we will not pursue this any further here (see however discussion in Chapt. 5, Sect. 5.6.2).

It is important to stress that not only the trend in Fig. 8.12, but also the existence of the correlations found in Sec. 8.2 could have been predicted on the basis of the re-acceleration model (Sec. 8.1, Eqs. 8.3, 8.4, 8.5) under the very reasonable assumption that $M_H \propto R_H^{\alpha}$. Indeed, if one uses the observed scaling $M_H \propto R_H^{2.17\pm0.19}$ to fix the parameter α, from Eq.8.2, and assuming the most simple case in which $\mathcal{F}$ is constant, one finds $P_{1.4} \propto R_H^{3.9}$ and $P_{1.4} \propto M_H^{1.8}$, which are actually consistent (within the dispersion) with the observed correlations (Sec. 8.2); as in the case of the trend in Fig. 8.12, an even better fulfillment of all these correlations is obtained for a slightly non-constant $\mathcal{F}$.

8.5 Summary & Conclusions

In this Chapter we have investigated new scaling relations by combining recipes for the turbulence in galaxy clusters from our Montecarlo studies (Chapt.5) with a simplified form of the particle re-acceleration model. We have found that:

• In its simplest form, as assumed here (Sect. 8.1), the re-acceleration model predicts that the *local injection of turbulence by a cluster merger, the particle re-acceleration and the radiation losses combine leading to a very simple relationship (Eq.8.2) between the total radio power P_R, the total mass M_H within the RH, the gas velocity dispersion σ_H and the average magnetic field B_H.* Under the very reasonable assumptions that M_H scales with the size R_H and that the gas is in gravitational equilibrium Eq.8.2 naturally translates into simple scaling relations: $P_R - M_H$, $P_R - R_H$ and $P_R - \sigma_H$ (Eqs. 8.3, 8.4, 8.5).

Motivated by the above theoretical considerations, we have searched for the existence of this type of correlations by analyzing a sample of 15 galaxy clusters with giant RHs. A most important point here is the measure of the size R_H, in itself a non-trivial matter, since the brightest RHs may appear more extended in the radio maps and this might force artificial correlations with radio power. A careful analysis of published 15 GHz radio maps of the RHs of our sample shows that this effect is not present (Sect. 8.2.1).

From the same data set we derive a meaningful estimate of the radius for each RH. We also show that our procedure leads to estimates fully consistent with the measurements from the brightness profiles worked out from the data for the five most regular RHs; this consistency holds over the total range spanned by R_H in our sample (Sect. 8.2.1).

• We obtain a good, *new correlation* (correlation coefficient ~ 0.84) *between the observed radio power at 1.4 GHz and the measured size of the RHs in the form* $P_{1.4} \propto R_H^{4.18\pm0.68}$(Sect. 8.2.1). In Sect. 8.2.1 we discuss in detail several selection effects which might affect this correlation and conclude that it is very unlikely that the observed correlation is driven by observational biases.

• We calculate the cluster mass and the velocity dispersion within the radius R_H for all objects in our sample and *derive relatively strong new correlations* (Sect. 8.2.2) *in the form:* $P_{1.4} \propto M_H^{1.99\pm0.22}$ *and* $P_{1.4} \propto (\sigma_H^2)^{4.64\pm1.07}$*, and, as a byproduct of these*

scalings, $\sigma_H^2 \propto R_H^{0.90\pm0.25}$.

A correlation between the size R_H and the cluster virial radius, R_v, is qualitatively expected in the framework of the particle re-acceleration model.

• In Sect. 8.3 we compare R_H vs. R_v for our sample of clusters with giant RHs, *obtaining the non-linear trend* $R_H \propto R_v^{2.63\pm0.50}$*, i.e., the fraction of the cluster volume that is radio emitting significantly increases with the cluster mass.* This *break of the self-similarity*, in line with previous suggestions (*e.g.,* Kempner & Sarazin 2001), points to the changing distributions of the magnetic fields and relativistic electrons with cluster mass and, as such, is potentially important in constraining the physical parameters entering the hierarchical formation scenario, such as the turbulence injection scale and the magnetic field strength and profile. Finally, we note that, by combining the $R_H - R_v$ and $P_{1.4} - R_H$ correlations, one easily derives $P_{1.4} \propto M_v^3$, which is consistent with previous findings ($P_{1.4} \propto M_v^{2.9\pm0.4}$, Chap. 6).

• Under the assumption that the number density of relativistic electrons does not significantly depend on the cluster mass, from the $P_{1.4} - M_H$ correlation *and the synchrotron laws* we find that the rms magnetic field intensity B inside R_H should be weakly dependent on the cluster mass ($B_H \propto M_H^{0.28\pm0.16}$).

• *These observed correlations are well understood in the framework of the particle re-acceleration model.* Indeed, we show that the theoretical expectation (Eq.8.2) is consistent with the data (see Fig.8.12). Assuming a simple constant form for $\mathcal{F}$ in Eq.8.2 and the observed $M_H - R_H$ scaling, which is necessary to fix the model parameter α (Sect. 8.1), the model expectations (Eqs. 8.3, 8.4, 8.5) naturally translates into $P_{1.4} \propto R_H^{3.9}$, $P_{1.4} \propto M_H^{1.8}$ and $P_{1.4} \propto (\sigma_H^2)^{3.4}$ correlations, all consistent (within the dispersion) with the observed correlations; an even better fulfillment of all these correlations is obtained for a slightly non-constant $\mathcal{F}$, which corresponds to $\approx \mu G$ field in the RH region.

To conclude, *the particle re-acceleration model, closely linked to the development of the turbulence in the hierarchical formation scenario, appears to provide a viable and basic physical interpretation for all the correlations obtained so far with the available*

data for giant RHs. Future deep radio surveys and upcoming data from LOFAR and LWA will be crucial to improve the statistics and to provide further constraints on the origin of RHs.

Chapter 9

Summary and Conclusions

9.1 Focus of the Thesis

It is now clear that the Intra Cluster Medium (ICM) is made not only of the thermal gas but also of magnetic fields and relativistic particles (leptons and hadrons). Relativistic electrons diffusing throughout turbulent magnetic fields emit synchrotron radiation in the form of Radio Halos (RH) and may give sufficient IC radiation to explain the hard X-ray (HXR) excess. Turbulent magnetic fields and cosmic rays in the ICM may drive still unexplored physical processes and this call for a "revision" of the physics of the ICM (*e.g.,* Schekochihin et al. 2005; Brunetti & Lazarian 2007).

Among the models which have been proposed to explain the origin of the electrons emitting RHs (and hard X-ray emission), a *re-acceleration scenario* in which MHD turbulence injected during cluster mergers re-accelerates high energy particles seem to be favoured by present observations (Brunetti 2004; Blasi 2004; Hwang 2004). The complex physics of the particle acceleration due to turbulence in galaxy clusters deserved some attention in literature (*e.g.,* Ohno et al. 2002; Fujita et al. 2003; Brunetti et al. 2004; Brunetti & Blasi 2005; Brunetti & Lazarian 2007, see also Chapt. 4) still a *theoretical investigation of the statistical properties of RH (occurrence, correlations with thermal properties and luminosity functions) in the framework of the re-acceleration model was completely lacking at the beginning of this PhD work.*

Despite the complex and still poorly explored physics of this model, RHs (as well as the relative IC emission in the hard X-rays) in this scenario should have unique and unavoidable properties which should leave an imprint in the statistical

behavior of these sources. *Crucial constraints on the origin of these RHs* can thus be provided by statistical observational studies which have shown so far that RHs are "rare" and that a connection exist between the formation of these sources and cluster mergers. This PhD work is inspired by the possibility to *open this new tool of investigation* and the main goals of the PhD have been to derive the theoretical expectations from the re-acceleration scenario for the statistical properties of the RHs in galaxy clusters, to compare them with present observations, and to obtain expectations to test with incoming facilities. In the following we summarized the *main results* obtained.

9.2 Statistical calculations

9.2.1 Main ingredients and Monte-Carlo based procedure

We developed a semi-analytical procedure to model "self-consistently" the formation and evolution of galaxy clusters ("merging history"), the injection of turbulence during mergers and the evolution of relativistic electrons in the ICM, due to both energy losses and gains. Our approach is based on the following main steps:

- A Monte-Carlo procedure based on the extended Press & Schechter theory technique has been developed to build up extensive *merger trees* of galaxy clusters with different present day virial masses. We ended up with a synthetic cluster population with present day masses $\gtrsim 2 \cdot 10^{14}\, M_{\odot}$ (we have ~ 500 clusters with masses $\gtrsim 10^{15}\, M_{\odot}$).

- Cluster turbulence was assumed to be injected during cluster mergers and dissipated in a time-scale of the order of the cluster-cluster crossing time. The energetics of the chaotic motions injected at large scales in the ICM was "calibrated" with the PdV work done by the infalling subclusters in passing through the volume of the most massive one. We assumed that a non negligible fraction, $\eta_{\mathbf{t}}$, of this large scale turbulent motions was channelled into the form of *fast magnetosonic waves* (MS waves). The evolution of the spectrum of these MS waves was calculated solving a turbulent-diffusion equation with cosmic time and by combining the effect of all mergers at that cosmic epoch.

- Relativistic electrons were assumed to be continuously injected in the ICM at some "minimum" level (by shocks, AGNs and star forming galaxies). These

electrons are necessary to have a "relic" population of relativistic particles to be re-accelerated during mergers (this is the assumption of the "standard" re-acceleration scenario). The total energy injected in the relativistic electrons during the cluster life up to $z = 0$ was simply assumed to be a fraction, $\eta_{\mathbf{e}}$, of the thermal energy of the clusters at the present epoch. The cosmological evolution of the relativistic electrons was calculated by solving a Fokker-Planck equation and accounting for the acceleration by MS waves and the particle's energy losses.

- Then the ensuing synchrotron and IC emission in the radio and hard X-ray band respectively, were calculated for the synthetic population of galaxy clusters as a function of cosmic time.

It is almost impossible to obtain a spatially resolved (morphological) description of turbulence, particle acceleration and non-thermal emission in galaxy clusters by making use of semi-analytical techniques. This in principle would be possible by making use of *ad hoc* numerical simulations, which however goes well beyond present projects. Thus *we chosen to model "average quantities" in galaxy clusters in a fixed spherical volume of radius* $\approx 0.5\,\mathrm{h}_{50}^{-1}\,\mathrm{Mpc}$*, typical of giant RHs.*

- RHs (*at 1.4 GHz*) at a given z were identified with those clusters in our synthetic cluster population having a break frequency $\nu_b \gtrsim 200 - 300$ MHz in the synchrotron spectrum computed at that cosmological time; this condition is necessary to have a slope of the synchrotron spectrum around 1.4 GHz consistent with that of the observed RHs ($\nu_b < 200$ MHz would give a synchrotron spectrum too steep and the RH should "disappear").

9.2.2 Results from Monte-Carlo calculations

The case of a magnetic field constant with cluster mass

In Chapt.5 we consider the simplest situation in which the magnetic field strength averaged in the fixed volume has a constant value of $\approx 0.5\,\mu$G which does not depend on cluster mass. We thus report a first comparison between the results from our Monte-Carlo calculations and the observations, which can be summarized in two main steps:

- First we show that the typical observed radio and hard X-ray luminosities can be successfully reproduced by our modelling in the case of typical merging clusters with virial mass $M_v \sim 10^{15}\,M_\odot$ in our synthetic cluster population provided that a fraction of the energy of the large scale turbulent motions, $\eta_t \sim 0.2 - 0.3$, is channeled into MS waves during major mergers, and that the total energy injected in cosmic ray electrons during the cluster life up to the present epoch is $\approx 10^{-3} - 10^{-4}$ times that of the thermal energy of the ICM.

- Then, we show that the fraction of galaxy clusters in our modelled population in which a RH can form at $z < 0.2$ is consistent with present observations provided that $\eta_t \approx 0.24 - 0.34$. More specifically, in this case, this fraction is found to *naturally increase with cluster mass:* 20-30 % for $M > 2 \times 10^{15}\,M_\odot$ clusters, 2-5 % for $M \sim 10^{15}\,M_\odot$ clusters, and negligible for less massive objects in agreement with present data.

An important finding from our calculations is that small clusters "hardly" form RHs emitting at 1.4 GHz and that essentially only massive clusters can host these giant RHs (the probability to form these diffuse radio sources rapidly increases for clusters with $M \geq 2 \times 10^{15} M_\odot$). This is because *the energy of the turbulence injected in galaxy clusters by merger events is found to roughly scale with the thermal energy of the clusters* and thus the energy density of the MS waves (and the efficiency of particle acceleration) is an increasing function of the mass of the clusters. In addition we found that turbulent motions are typically injected in large Mpc regions in more massive clusters and this favors the formation process of giant RHs.

The case of a magnetic field changing with cluster mass

In Chapt.6 we present a natural extensions of the analysis performed in the Chapt.5 by considering the case of a magnetic field in galaxy clusters whose strength, B, depends on cluster virial mass, M_v. To this end in our modelling *we have adopted a scaling law between the rms magnetic field strength (averaged in the synchrotron emitting volume) and the virial mass of the parent clusters,* $B \propto M_v^b$. The main results of Chapt.6 can be summarized as follow:

- *Observed correlations and magnetic field constraints*:

The assumption of a scaling between B and M_v has allowed us to model expected scalings between radio properties and virial quantities. Observationally we thus have collected a sample of 17 clusters with giant RHs (making use of available data from the literature) and derived the correlations between the monochromatic radio power at 1.4 GHz ($P_{1.4}$) and the X-ray luminosity (L_X), temperature and cluster virial mass (M_v; see Sect.6.4 for details).

A systematic comparison of the model-expected correlation, between radio power and cluster virial mass, with the observed power-mass scaling allowed us to the define a permitted region of the parameters' space ($B_{<M>}$,b); $B_{<M>}$ being the rms magnetic field associated to a cluster with mass equal to the mean mass $< M >$ of the cluster sample. Additionally, a lower bound $B_{<M>} \simeq 0.2\,\mu$G was obtained in order not to overproduce via IC scattering of the CMB photons the typical observed hard X-rays luminosities. It was found that $b \gtrsim 0.5 - 0.6$ and that a *relatively narrow range of values of $B_{<M>}$ is allowed for a fixed b.* In addition a super–linear scaling of B with mass, as expected by MHD simulations (Dolag et al. 2004), was found to fall within the allowed region.

- *Probability to form giant RHs emitting at 1.4 GHz*:

  For each set of costrained magnetic parameters ($B_{<M>}$,b) we have found the range of the values of η_t which is required to match the observed occurrence of giant RHs in the redshift bin $z \sim 0 - 0.2$. With these constrained values of η_t and for each set of ($B_{<M>}$,b) we have calculated the differential occurrence of giant RHs with redshifts and obtained expectations for the redshifts at which observational data are not available. We show in Chapt. 6 that *this probability depends on the merging history of clusters and on the relative importance of the synchrotron and IC losses.* The interplay between these two effects drives a somewhat complicated behavior of the probability to form RHs with cluster mass and redshift. *However, the important finding is that the maximum value of this probability at a given redshift was found for clusters with masses for which the synchrotron and IC losses have the same strength.*

- *Luminosity functions of RHs (RHLFs) at 1.4 GHz*

  We calculated the RHLFs by adopting a fair sampling of the ($B_{<M>}$,b) allowed

region. We found that *the main feature of the derived RHLFs* is *the presence of a flattening/cut-off at low radio powers* (below about 10^{24} W/Hz at 1.4 GHz). *This characteristic shape of the RHLFs is a unique prediction of particle re-acceleration models, and does not depend on the adopted physical details for the particle acceleration mechanism.* This is essentially due to the decrease of the efficiency of particle acceleration in the case of less massive clusters (see also Sect. 9.2.2) and also because in the case of $B \propto M^b$ (with $b \gtrsim 0.5$) higher energy electrons should be accelerated in smaller clusters to emit synchrotron radiation at a given frequency.

Deep future radio surveys will be of great importance to test the expected shape of the RHLFs.

- *Number counts (RHNCs) at 1.4 GHz*:

  We have also derived the integral number counts of giant RHs at 1.4 GHz. We found that the RHNCs predicted at relatively low ($z < 0.2$) redshift generally agree with those derived from the NVSS within the flux limit of this survey. *We have found that the model-expected RHNCs should flatten below* $\sim 50 - 60$ *mJy, because of the combination of the low power cut-offs of the RHLFs with the redshift limit, and because of the RHLFs evolution with redshift.* On the other hand, past extrapolations of the data which assume a fixed fraction of giant RHs with cluster mass lead to a monotonic increase of the number of sources at lower fluxes (*e.g.,* Enßlin & Röttgering, 2002).

  The expected number of giant RHs in the whole Universe from our modeling is $\gtrsim 100$ in the case of a superlinear scaling ($b > 1$) of the magnetic field with cluster mass, while a sublinear scaling ($b < 1$) would give a number 2-3 times smaller.

  Our calculations suggest that the bulk of these giant RHs is expected to be at $z \sim$0.1–0.3. *This expectation has triggered an observational follow up of the occurrence of RHs at* $z \gtrsim 0.2$ *and 180 hours of observations were obtained to carry out pointed observations of* $\sim$ *50 massive clusters in the redshift bin* $0.2 < z < 0.4$ *at the GMRT in India.* In Chapt.7 we briefly discuss first results from this project and present a work in progress on the "revision" of the occurrence of Radio Halos. We combined past informations from the NVSS

radio survey at $z < 0.2$ with our ongoing GMRT observations at $0.2 < z < 0.4$. The total sample is of 205 galaxy clusters at $0.05 < z < 0.4$, and a carefull analysis of the properties of this sample and a comparison with our model expectations will be shortly concluded.

- *Toward expectations at low radio frequencies: 150 MHz*:

  LOFAR and LWA will operate at still poorly explored frequencies in a few years and *this represents a unique possibility to test the expectations of the re-acceleration model.* For this reason we have extended our calculations to the case of low frequency observations. *Synchrotron emission from lower energetic electrons contributes to these frequencies and thus - in the framework of the particle re-acceleration scenario - the efficiency of producing "low-frequency" giant RHs in galaxy clusters is expected to be larger than that of giant RHs emitting at 1.4 GHz.*

  We found that *the fraction of galaxy clusters with giant RHs emitting at 150 MHz is expected to be significantly larger than that of galaxy clusters with RHs emitting at 1.4 GHz*, and this increase is particularly large for less massive clusters. Consequently, the low mass cut-off in the mass functions of RHs was found to be shifted at lower masses by a factor of ~ 2 with respect to the case at 1.4 GHz: *slightly less turbulent systems are able to generate giant RHs at 150 MHz but not able to produce the necessary re-acceleration efficiency to have electrons emitting at higher frequencies.* This boost up the number of RHs in the Universe emitting at lower frequencies and indeed *we have estimated that the number counts of giant RHs at lower frequencies may result at least one order of magnitude larger than that at 1.4 GHz.*

9.3 Time-independent calculations and size of Radio Halos

As outlined above, Monte-Carlo calculations do not allow to have a spatially resolved modeling of the particle acceleration process in galaxy clusters and for this reason the size of RH in Chapts.5-7 was taken $\approx 1\,h_{50}^{-1}\,\mathrm{Mpc}$.

In Chapt.8 we relax the hypothesis of a fixed size and assume that the mass of the cluster contained within the radio emitting region scales with the size of the RH, $M_H \propto R_H^{\alpha}$. Starting with this assumption we use a simplified time-independent

version of the re-acceleration model to investigate novel scaling relations between the radio power and properties of the ICM in the RH region. We adopted the recipes developed in Chapts.5 and 6 for estimating the turbulent energy and consider a quasi stationary situation in which the energy flux of the turbulent modes which is damped by the relativistic electrons is assumed to be re–radiated via synchrotron and IC. We have shown that *the re-acceleration model predicts simple relationships between the total radio power P_R, the size of the RH, R_H, the total cluster mass within R_H, M_H, and the gas velocity dispersion σ_H.*

Stimulated by these results we have searched for the existence of these correlations from present data. By analyzing the most recent radio maps of a sample of 15 galaxy clusters with giant RHs we were able *to obtain new observed correlations:* $P_{1.4} \propto R_H^{4.18\pm0.68}$, $P_{1.4} \propto M_H^{1.99\pm0.22}$ and $P_{1.4} \propto (\sigma_H^2)^{4.64\pm1.07}$, and *found that these observed trends can be well reconciled with our expectations once the slope α of the "geometrical" scaling between M_H and R_H is fixed from observations* ($M_H \propto R_H^{2.17\pm0.19}$) and provided that the mean magnetic field strength in the radio halo volume has only a slight variation with the cluster mass within the same volume. A byproduct correlation $\sigma_H^2 \propto R_H^{0.90\pm0.25}$ is also found, and can be tested by optical studies.

This is a relevant point as *in this Chapt. 8 we have concluded that all the observed scalings known so far for giant RHs are now understood provided that the radio emission from these RHs essentially traces the volume of turbulent/merging galaxy clusters magnetized at $\approx \mu G$ level.*

In addition, we found that *observationally the size of Radio Halos scales non-linearly with the virial radius of the host cluster*, $R_H \propto R_v^{2.63\pm0.50}$, *i.e.,* the fraction of the cluster volume that is radio emitting significantly increases with the cluster mass. This *break of the self-similarity*, in line with previous suggestions (*e.g.,* Kempner & Sarazin 2001), could be driven by the behavior of the profiles of the magnetic field and density of relativistic electrons with cluster mass and/or by the behavior of the injection and developing of the turbulence with cluster mass.

9.4 Immediate future developments

LOFAR, LWA and GLAST will shortly observe in essentially still unexplored regions of the electromagnetic spectrum, and the non-thermal emission from galaxy clusters

is among the main issues to address with these instruments. The near future for the research in this field is thus expected to be very bright also because new measures in the hard X-ray band (*Suzaku*) may also come and help in planning the science with very sensitive hard X-ray telescopes which hopefully will become available within 5-15 years (*e.g., Simbol-X*).
The immediate next steps in the project started with this PhD thesis can be briefly summarized as follows:

- *Revision of the statistics of Radio Halos:*
  The observed fraction of galaxy clusters at $z < 0.2$ with RH was found to increase with cluster mass (or X-ray luminosity). This is an important point as it appears to be in line with the expectations from the re-acceleration scenario and represents a challenge for other proposed models. However observational biases still need to be carefully addressed and the relatively poor statistics of present studies requires extensive new surveys. As explained in Chapt. 7, by combining past NVSS results and our GMRT survey *we have in hands a sample of* ~ 200 *clusters at* $0.05 < z < 0.4$ *with radio follow up and this will allow us to calculate an "unbiased" occurrence of RHs with cluster mass and redshift, and to compare the observations with the model expectations.*

- *Exploring the LOFAR sky:*
  Although in Chapt. 6 we have presented the first model expectations at low frequency, the behavior of the re-acceleration model at these frequencies is still poorly explored by this PhD work and a detailed study requires an improvement of our procedures. What is now clear from our work is that *the study of differential changes of RH statistics with observing frequency is among the most powerful tools to understand the origin of these sources.* LOFAR will survey the sky between 40 MHz and 240 MHz within 2-3 years and will probably discover thousands of new RHs. *Potentially we have in hand the first tool to calculate the statistical properties of RHs with redshift, mass and observing frequency and thus it will be crucial to work on expectations to interpret the LOFAR data.*

- *Hard X-ray tails*
  This PhD work was mainly focused on RHs for which enough data are available.

On the other hand hard X-ray tails may also be powered by IC emission from re-accelerated electrons. One of the most important step forward of this project is to explore, using procedures based on our semi-analytical recipes, the expected properties of hard X-ray tails with mass and redshift of the parent clusters, and to understand how common they are expected to be. Our expectation will also provide important indications for the planning of the science case of future HXR detectors (*e.g., Simbol-X*).

Bibliography

Abell GO. 1958. *Ap. J. Suppl.* 3:211–278.

Abell GO, Corwin HGJr, Olowin RP. 1989.*Ap. J. Suppl.* 70:1–138

Achterberg A., 1981, A&A 97, 259

Allen S.W., 1998, MNRAS296, 392

Akritas M.G.,Bershady M.A., 1996, ApJ 470, 706

Arnaud M., Evrard A.E., 1999, MNRAS 305, 631

Atoyan, A. M., Völk, H. J. 2000, ApJ, 535, 45

Bacchi, M., Feretti, L., Giovannini, G., & Govoni, F. 2003, A&A, 400, 465

Bailey, M. E. 1982, MNRAS, 201, 271

Barnes A., Scargle J.D., 1973, ApJ 184, 251

Bartelmann, M. 2003, Astronomical Society of the Pacific Conference Series, 301, 255

Bauer, F. E., Fabian, A. C., Sanders, J. S., Allen, S. W., & Johnstone, R. M. 2005, MNRAS, 359, 1481

Belsole, E., Pratt, G. W., Sauvageot, J.-L., & Bourdin, H. 2004, A&A, 415, 821

Bennett, C. L., et al. 1996, ApJ, 464, L1

Berezinsky V.S., Blasi P., Ptuskin V.S., 1997, ApJ 487, 529

Berrington R.C., Dermer C.D., 2003, ApJ 594, 709

Bertoglio J.-P.,Bataille F., Marion J.-D., 2001, Physics of Fluids 13, 290

Binney J., Tremaine S., 1987, Galactic Dynamics, Princeton University Press, Princeton

Binney, J., & Tabor, G. 1995, MNRAS, 276, 663

Biermann P.L., Enßlin T.A., Kang H., Lee H., Ryu D., 2003, in "Matter and Energy in Clusters of Galaxis", ASP Conf. Series, vol.301, p.293, eds. S. Bowyer and C.-Y. Hwang

Birk, G. T., Wiechen, H., & Otto, A. 1999, ApJ, 518, 177

Bîrzan, L., Rafferty, D. A., McNamara, B. R., Wise, M. W., & Nulsen, P. E. J. 2004, ApJ, 607, 800

Biviano, A. 2005, invited review at the XXIst IAP Colloquium "Mass Profiles and Shapes of Cosmological Structures", Paris 4-9 July 2005, Editors: G. Mamon, F. Combes, C. Deffayet, B. Fort, EDP Sciences, astro-ph/0509679

Biviano, A. 2006, ArXiv Astrophysics e-prints, arXiv:astro-ph/0607040

Blandford, R. D. 1986, AIP Conf. Proc. 144: Magnetospheric Phenomena in Astrophysics, 144, 1

Blasi, P. 1999, *Astrophys. J.* **525**, 603.

Blasi, P. 2000, ApJ, 532, L9

Blasi P., 2001, APh 15, 223

Blasi P., 2003, in 'Matter and Energy in Clusters of Galaxis', ASP Conf. Series, vol.301, p.203, eds. S. Bowyer and C.-Y. Hwang

Blasi, P. 2004, Journal of Korean Astronomical Society, 37, 483

Blasi, P., & Colafrancesco, S. 1999, Astroparticle Physics, 12, 169

Blasi, P., Gabici, S., & Brunetti, G. 2007, Review Paper to appear in the International Journal of Modern Physics:astro-ph/0701545

Böhringer, H., Voges, W., Fabian, A. C., Edge, A. C., & Neumann, D. M. 1993, MNRAS, 264, L25

Bohringer, H., Briel, U. G., Schwarz, R. A., Voges, W., Hartner, G., & Trumper, J. 1994, Nature, 368, 828

Böhringer, H., et al. 2001, A&A, 369, 826

Böhringer, H., Schuecker, P., Guzzo, L., et al., 2004, A&A, 425, 367

Bonamente, M., Lieu, R., Joy, M. K., & Nevalainen, J. H. 2002, ApJ, 576, 688

Borgani, S., et al. 2004, MNRAS, 348, 1078

Boschin, W., Girardi, M., Barrena, R., Biviano, A., Feretti, L., & Ramella, M. 2004, A&A, 416, 839

Bowyer, S., Lampton, M., & Lieu, R. 1996, Science, 274, 1338

Bowyer, S., Lieu, R., & Mittaz, J. P. 1998, IAU Symp. 188: The Hot Universe, 188, 185

Bowyer S., Berghöfer T., Korpela E., 1999, ApJ 526, 592

Bowyer, S., & Berghöfer, T. W. 1998, ApJ, 506, 502

Bowyer, S., Korpela, E. J., Lampton, M., & Jones, T. W. 2004, ApJ, 605, 168

Bond, J. R., Cole, S., Efstathiou, G., & Kaiser, N. 1991, ApJ, 379, 440

Böhringer, H., Briel, U. G., Schwarz, R. A., Voges, W., Hartner, G., & Trumper, J. 1994, Nature, 368, 828

Bower, R. G. 1991, MNRAS, 248, 332

Braginskii S.I., 1965, Rev. Plasma Phys. 1, 205

Briel, U. G., et al. 1991, A&A, 246, L10

Brüggen, M., Ruszkowski, M., Simionescu, A., Hoeft, M., & Dalla Vecchia, C. 2005, ApJ, 631, L21

Brunetti G., 2002, in "Matter and Energy in Clusters of Galaxis", ASP Conf. Series, 301, p.349, eds. S. Bowyer and C.-Y. Hwang

Brunetti, G. 2003, Astronomical Society of the Pacific Conference Series, 301, 349

Brunetti G., 2004, JKAS 37, 493

Brunetti G., 2006, Astronomische Nachrichten 327, No 5/6, 615 (proceedings of "The Origin and Evolution of Cosmic Magnetism", 29 August - 2 September 2005, Bologna, Italy)

Brunetti G., Setti G., Feretti L., Giovannini G., 2001a, MNRAS 320, 365

Brunetti, G., Setti, G., Feretti, L., & Giovannini, G. 2001b, New Astronomy, 6, 1

Brunetti, G., Blasi, P., Cassano, R., & Gabici, S. 2004, MNRAS, 350, 1174

Brunetti, G., & Blasi, P. 2005, MNRAS, 363, 1173

Brunetti, G., Lazarian, A., MNRASin press

Bruni, M., Maartens, R., & Tsagas, C. G. 2003, MNRAS, 338, 785

Bryan, G. L., & Norman, M. L. 1995, Bulletin of the American Astronomical Society, 27, 1421

Buote, D. A. 1998, MNRAS, 293, 381

Buote D.A, 2001, ApJ 553, 15

Buote, D. A., & Tsai, J. C. 1995, ApJ, 452, 522

Buote, D. A., & Tsai, J. C. 1996, ApJ, 458, 27

Burns, J. O. 1990, AJ, 99, 14

Burns, J. O., Sulkanen, M. E., Gisler, G. R., & Perley, R. A. 1992, ApJ, 388, L49

Cane, H. V., Erickson, W. C., Hanisch, R. J., & Turner, P. J. 1981, MNRAS, 196, 409

Carroll S.M., Press W.H., Turner E.L., 1992, ARA&A 30, 499

Cassano, R., & Brunetti, G. 2005, MNRAS, 357, 1313

Cassano, R., Brunetti, G., & Setti, G. 2006a, MNRAS, 369, 1577

Cassano, R., Brunetti, G., & Setti, G. 2006, Astronomische Nachrichten, 327, 557

Cavaliere, A., & Fusco-Femiano, R. 1976, A&A, 49, 137

Cen, R. Y., Ostriker, J. P., Jameson, A., & Liu, F. 1990, ApJ, 362, L41

Cen, R. 1992, ApJS, 78, 341

Clarke T.E., 2005, ASP Conference Series, Eds. by N.E. Kassim, M.R. Perez, W.Junor and P.A. Henning, Vol 345, pag. 227

Clarke, T. E. 2003, Astronomical Society of the Pacific Conference Series, 301, 185

Clarke, T. E., Kronberg, P. P., Böhringer, H. 2001, ApJ, 547, L111

Clarke T.E., Enßlin T.A., 2006, AJ 131, 2900

Colafrancesco, S. 1999, "Diffuse Thermal and Relativistic Plasma in Galaxy Clusters", 269; :astro-ph/9907329

Colafrancesco, S., & Blasi, P. 1998, Astroparticle Physics, 9, 227

Colafrancesco, S., Marchegiani, P., & Perola, G. C. 2005, A&A, 443, 1

Cole, S. 1991, ApJ, 367, 45

Cole, S., Aragon-Salamanca, A., Frenk, C. S., Navarro, J. F., & Zepf, S. E. 1994, MNRAS, 271, 781

Coles, P., & Lucchin, F. 1995. *Cosmology. The origin and evolution of cosmic structure*, Chichester: UK: Wiley

Condon, J. J., Cotton, W. D., Greisen, E. W., Yin, Q. F., Perley, R. A., Taylor, G. B., & Broderick, J. J. 1998, AJ, 115, 1693

Cordey, R. A. 1985, MNRAS, 215, 437

Carroll, S. M., Press, W. H., & Turner, E. L. 1992, ARA&A, 30, 499

Cho, J., Lazarian, A., & Vishniac, E. T. 2003, ApJ, 595, 812

Churazov, E., Forman, W., Jones, C., Böhringer, H. 2000, A&A, 356, 788

Churazov E., Forman W., Jones C., Sunyaev R., Böhringer H., 2004, MNRAS347, 29

Couchman, H. M. P., Thomas, P. A., & Pearce, F. R. 1995, ApJ, 452, 797

Crawford C.S., Hatch N.A., Fabian A.C., Sanders J.S., 2005, MNRAS363, 216

David L. P., Slyz A., Jones C., Forman W., Vrtilek S. D., Arnaud K. A.,1993, ApJ 412, 479

Davis, M., Efstathiou, G., Frenk, C. S., & White, S. D. M. 1985, ApJ, 292, 371

de Lapparent, V., Geller, M. J., & Huchra, J. P. 1986, ApJ, 302, L1

Deiss, B. M., & Just, A. 1996, A&A, 305, 407

Deiss, B. M., Reich, W., Lesch, H., & Wielebinski, R. 1997, A&A, 321, 55

Dennison B., 1980, ApJ 239

Diemand, J., Moore, B., & Stadel, J. 2004, MNRAS, 353, 624

Diemand, J., Zemp, M., Moore, B., Stadel, J., & Carollo, C. M. 2005, MNRAS, 364, 665

Dogiel, V. A. 2000, A&A, 357, 66

Dolag, K., Bartelmann, M., & Lesch, H. 1999, A&A, 348, 351

Dolag, K. & Enßlin, T. A. 2000, A&A, 362, 151

Dolag K., Schindler S., Govoni F., & Feretti L. 2001, A&A, 378, 777

Dolag K., Bartelmann M., Lesch H, 2002, A&A 387, 383

Dolag, K., Bartelmann, M., Perrotta, F., Baccigalupi, C., Moscardini, L., Meneghetti, M., & Tormen, G. 2004, A&A, 416, 853

Dolag K., Vazza F., Brunetti G., Tormen G., 2005, MNRAS, 364, 753

Dolag K., Grasso D., Springel V., Tkachev I.,2005,JCAP 1, 9

Domainko, W., Gitti, M., Schindler, S., & Kapferer, W. 2004, A&A, 425, L21

Dunn, R. J. H., & Fabian, A. C. 2006, MNRAS, 373, 959

Durret, F., Slezak, E., Lieu, R., Dos Santos, S., & Bonamente, M. 2002, A&A, 390, 397

Ebeling, H., Voges, W., Bohringer, H., Edge, A. C., Huchra, J. P., & Briel, U. G. 1996, MNRAS, 281, 799

Ebeling, H., Edge, A.C., Böhringer, H., et al.,1998, MNRAS, 301, 881

Ebeling, H., Edge, A.C., Allen, S.W., et al., 2000, MNRAS, 318, 333

Edge, A. C., Stewart, G. C., & Fabian, A. C. 1992, MNRAS, 258, 177

Efstathiou, G., & Rees, M. J. 1988, MNRAS, 230, 5P

Ensslin T.A., Biermann P.L., Kronberg P.P., Wu X.-P., 1997, ApJ 477, 560

Ensslin, T. A., & Biermann, P. L. 1998, A&A, 330, 90

Ensslin, T. A., Biermann, P. L., Klein, U., & Kohle, S. 1998, A&A, 332, 395

Enßlin, T. A., Lieu, R., & Biermann, P. L. 1999, A&A, 344, 409

Enßlin, T. A., & Gopal-Krishna 2001, A&A, 366, 26

Enßlin, T. A., & Brüggen, M. 2002, MNRAS, 331, 1011

Enßlin T.A., Röttgering H., 2002, A&A, 396, 83

Enßlin, T. A. & Vogt, C. 2003, A&A, 401, 835

Eilek, J. 1999, "Diffuse Thermal and Relativistic Plasma in Galaxy Clusters", 71

Eilek J.A., 1979, ApJ 230, 373

Eilek J.A., Henriksen R.N., 1984, ApJ277, 820

Eilek, J. A., & Hughes, P. A. 1991, Beams and Jets in Astrophysics, 428

Eke, V. R., Cole, S., & Frenk, C. S. 1996, MNRAS, 282, 263

Ettori S., Fabian A.C., 1999, MNRAS305, 834

Ettori S., Tozzi P., Borgani S., Rosati P., 2004 A&A 417, 13

Evrard A.E., Metzler C.A., Navarro J.F., 1996, ApJ469, 494

Evrard, A. E. 1988, MNRAS, 235, 911

Fabian, A. C. 1994, ARA&A, 32, 277

Fabian, A. C., Celotti, A., Blundell, K. M., Kassim, N. E., & Perley, R. A. 2002, MNRAS, 331, 369

Fabian A.C., Sanders J.S., Crawford C.S., Conselice C.J.,Gallagher J.S., Wyse R.F.G., 2003, MNRAS344, L48

Fabian, A. C., Sanders, J. S., Taylor, G. B., & Allen, S. W. 2005, MNRAS, 360, L20

Fall, S. M., & Efstathiou, G. 1980, MNRAS, 193, 189

Feretti, L. 2000, Invited review at IAU 199 'The Universe at Low Radio Frequencies' in Pune, India:astro-ph/0006379

Feretti, L. 2003, Astronomical Society of the Pacific Conference Series, 301, 143

Feretti L., 2002, in "The Universe at Low Radio Frequencies", Proceedings of IAU Symposium 199, held 30 Nov - 4 Dec 1999, Pune, India. Edited by A. Pramesh Rao, G. Swarup, and Gopal-Krishna, p.133

Feretti L., 2004, in "X-Ray and Radio Connections", eds. L.O. Sjouwerman and K.K. Dyer, published electronically by NRAO, Held 3-6 Febraury 2004 in Santa Fe, New Mexico, USA.

Feretti, L. 2005, X-Ray and Radio Connections (eds. L.O. Sjouwerman and K.K Dyer) Published electronically by NRAO, http://www.aoc.nrao.edu/events/xraydio Held 3-6 February 2004 in Santa Fe, New Mexico, USA, (E8.02) 10 pages,

Feretti, L., & Giovannini, G. 1996, IAU Symp. 175: Extragalactic Radio Sources, 175, 333

Feretti L., Giovannini G., Bohringer H., 1997, New Astronomy 2, 501

Feretti, L., Fusco-Femiano, R., Giovannini, G., & Govoni, F. 2001, A&A, 373, 106

Feretti, L., Orrù, E., Brunetti, G., Giovannini, G., Kassim, N., & Setti, G. 2004, A&A, 423, 111

Feretti, L., Schuecker, P., Böhringer, H., Govoni, F., & Giovannini, G. 2005, A&A, 444, 157

Finoguenov, A., Briel, U. G., & Henry, J. P. 2003, A&A, 410, 777

Finoguenov, A., Böhringer, H., & Zhang, Y.-Y. 2005, A&A, 442, 827

Frenk, C. S., et al. 1999, ApJ, 525, 554

Fukuda, Y., et al. 1998, Physical Review Letters, 81, 1562

Furlanetto, S. R., & Loeb, A. 2001, ApJ, 556, 619

Fusco-Femiano, R., dal Fiume, D., Feretti, L., Giovannini, G., Grandi, P., Matt, G., Molendi, S., & Santangelo, A. 1999, ApJ, 513, L21

Fusco-Femiano R., Dal Fiume D., De Grandi S., 2000, ApJ 534, L7

Fusco-Femiano, R., Dal Fiume, D., Orlandini, M., Brunetti, G., Feretti, L., & Giovannini, G. 2001, ApJ, 552, L97

Fusco-Femiano R.,Dal Fiume D., Orlandini M., De Grandi S., Molendi S., Feretti L., Grandi P., Giovannini G., 2003, in 'Matter and Energy in Clusters of Galaxis', ASP Conf. Series, eds., vol.301, p.109, S. Bowyer and C.-Y. Hwang

Fusco-Femiano R., Orlandini M., Brunetti G., Feretti L., Giovannini G., Grandi P., Setti G., 2004, ApJ 602, 73

Fusco-Femiano, R., Landi, R., & Orlandini, M. 2005, ApJ, 624, L69

Fujita, Y., & Sarazin, C. L. 2001, ApJ, 563, 660

Fujita Y., Takizawa M., Sarazin C.L., 2003, ApJ 584, 190

Gabici S., Balsi P., 2003, ApJ 583, 695

Gabici, S., & Blasi, P. 2004, Astroparticle Physics, 20, 579

Gastaldello F., Molendi S., 2004, ApJ 600, 670

Gheller, C., Pantano, O., & Moscardini, L. 1998, MNRAS, 295, 519

Giacintucci, S., et al. 2005, A&A, 440, 867

Giacintucci, S., Venturi, T., Bardelli, S., Brunetti, G., Cassano, R., & Dallacasa, D. 2006, New Astronomy, 11, 437

Gingold, R. A., & Monaghan, J. J. 1977, MNRAS, 181, 375

Giovannini, G., Feretti, L., Venturi, T., Kim, K.-T., & Kronberg, P. P. 1993, ApJ, 406, 399

Giovannini G., Tordi M., Feretti L., 1999, NewA 4, 141

Giovannini, G., & Feretti, L. 2000, New Astronomy, 5, 335

Giovannini G., Feretti L., 2002 in 'Merging Processes in Galaxy Cluster', vol.272, p.197, eds. L.Feretti, I.M.Gioia, G.Giovannini

Giovannini, G., & Feretti, L. 2004, Journal of Korean Astronomical Society, 37, 323

Giovannini, G., Feretti, L., Govoni, F., Murgia, M., & Pizzo, R. 2006, Astronomische Nachrichten, 327, 563

Gitti, M., Brunetti, G., & Setti, G. 2002, A&A, 386, 456

Govoni, F. 2006, Astronomische Nachrichten, 327, 539

Govoni, F., Feretti, L., Giovannini, G., Böhringer, H., Reiprich, T. H., & Murgia, M. 2001, A&A, 376, 803

Govoni, F., Enßlin, T. A., Feretti, L., & Giovannini, G. 2001, A&A, 369, 441

Govoni F., Feretti L., 2004, Int. J. Mod. Phys. D 13, 1549

Govoni F., Markevitch M., Vikhlinin A., VanSpeybroeck L., Feretti, L., Giovannini G., 2004, ApJ 605, 695

Govoni, F., Murgia, M., Feretti, L., Giovannini, G., Dallacasa, D., & Taylor, G. B. 2005, A&A, 430, L5

Grasso, D. & Rubinstein, H. R. 2001, Phys. Rept., 348, 163 [astro-ph/0009061]

Gruber, D., & Rephaeli, Y. 2002, ApJ, 565, 877

Hamilton, R.J., Petrosian V., 1992, ApJ 398, 350

Hanish,R.J. 1982,Astron.Astrophys.,111,97.

Hanisch, R. J., & Erickson, W. C. 1980, AJ, 85, 183

Henry, J. P., & Briel, U. G. 1995, ApJ, 443, L9

Henriksen, M., Donnelly, R. H., & Davis, D. S. 2000, ApJ, 529, 692

Herbig, T., & Birkinshaw, M. 1994, Bulletin of the American Astronomical Society, 26, 1403

Hernquist, L., & Katz, N. 1989, ApJS, 70, 419

Hicks, A. K. 2002, Bulletin of the American Astronomical Society, 34, 706

Hughes J.P., Butcher J.A., Stewart G.C., Tanaka Y., 1993, ApJ 404, 611

Hwang, C.-Y. 1997, Science, 278, 1917

Hwang C.-Y., 2004, JKAS 37, 461

Inoue, S., Aharonian, F. A., & Sugiyama, N. 2005, ApJ, 628, L9

Jaffe W.J., 1977, ApJ 212, 1

Jaffe, W. J., & Rudnick, L. 1979, ApJ, 233, 453

Jones, C., Mandel, E., Schwarz, J., Forman, W., Murray, S. S., & Harnden, F. R., Jr. 1979, ApJ, 234, L21

Jones, C., & Forman, W. 1984, ApJ, 276, 38

Jones, C., & Forman, W. 1999, ApJ, 511, 65

Kaastra, J. S. 2004, Journal of Korean Astronomical Society, 37, 375

Kaastra, J. S., Lieu, R., Tamura, T., Paerels, F. B. S., & den Herder, J. W. 2003, A&A, 397, 445

Kaastra, J. S., Lieu, R., Tamura, T., Paerels, F. B. S., & den Herder, J. W. 2004, Advances in Space Research, 34, 2504

Kauffmann, G., White, S. D. M., & Guiderdoni, B. 1993, MNRAS, 264, 201

Kauffmann, G., Colberg, J. M., Diaferio, A., & White, S. D. M. 1999, MNRAS, 303, 188

Kato S., 1968, PASJ 20, 59

Katz, N., Weinberg, D. H., & Hernquist, L. 1996, ApJS, 105, 19

Kelner, S. R., Aharonian, F. A., & Bugayov, V. V. 2006, Phys. Rev. D, 74, 034018

Kempner, J. C., & Sarazin, C. L. 2001, ApJ, 548, 639

Kempner, J. C., & David, L. P. 2004, MNRAS, 349, 385

Kim, K.-T., Kronberg, P. P., Dewdney, P. E., & Landecker, T. L. 1990, ApJ, 355, 29

Kim, K.-T., Kronberg, P. P., & Tribble, P. C. 1991, ApJ, 379, 80

King, I. 1962, AJ, 67, 471

Kitayama T., Suto Y., 1996, ApJ.469, 480

Kraichnan R.H., 1965, Phys. Fluids 8, 1385

Krall N.A., Trivelpiece A.N., *Principles of Plasma Physics* (McGraw–Hill, New York, 1973).

Kronberg P. P., Lesch, H., & Hopp, U. 1999, ApJ, 511, 56

Kulsrud, R. M.; Cen, R.; Ostriker, J. P. & Ryu, D. 1997, ApJ, 480, 481 [astro-ph/9607141]

Kuo P.-H., Hwang C.-Y.; Ip, W.-H., 2003, ApJ 594, 732

Kuo P.-H., Hwang C.-Y., Ip W.-H., 2004, ApJ 604, 108

Lacey, C., & Cole, S. 1993, MNRAS, 262, 627

Lacey, C., & Cole, S. 1994, MNRAS, 271, 676

Landau L.D., Lifshitz E.M., 1959, *Fluid Mechanics*, Pergamon Press, Oxford

Lazarian A., 2006, invited review, Astronomische Nachrichten in press (proceedings of "The Origin and Evolution of Cosmic Magnetism", 29 August - 2 September 2005, Bologna, Italy)

Lazarian, A., & Beresnyak, A. 2006, MNRAS, 373, 1195

Lemonon L., Pierre M., Hunstead R., Reid A., Mellier Y., Boehringer H., 1997, A&A 326, 34

Liang H., 1999, in "Diffuse thermal and relativistic plasma in galaxy clusters". Edited by Bohringer H., Feretti L., Schuecker P.. Garching, Germany : Max-Planck-Institut fur Extraterrestrische Physik, 1999. ("Proceedings of the Workshop...Ringberg Castle, Germany, April 19-23, 1999".), p.33

Liang H., Hunstead R.W., Birkinshaw M., Andreani P., 2000, ApJ 544, 686

Lieu, R., Mittaz, J. P. D., Bowyer, S., Lockman, F. J., Hwang, C.-Y., & Schmitt, J. H. M. M. 1996, ApJ, 458, L5

Lieu, R., Mittaz, J. P. D., Bowyer, S., Breen, J. O., Lockman, F. J., Murphy, E. M., & Hwang, C.-Y. 1996, Science, 274, 1335

Lieu, R., Ip, W.-H., Axford, W. I., & Bonamente, M. 1999, ApJ, 510, L25

Loeb, A., & Waxman, E. 2000, Nature, 405, 156

Lynden-Bell, D. 1967, MNRAS, 136, 101

Łokas, E. L., & Mamon, G. A. 2003, MNRAS, 343, 401

Lucy, L. B. 1977, AJ, 82, 1013

Marchegiani, P., Perola, G. C., & Colafrancesco, S. 2007, ArXiv Astrophysics e-prints, arXiv:astro-ph/0701592

Markevitch M., 1996, ApJ, 465, 1

Markevitch M., Forman W. R., Sarazin C. L., Vikhlinin A., 1998, ApJ503, 77

Markevitch, M., Sarazin, C. L., & Irwin, J. A. 1996b, ApJ, 472, L17

Markevitch, M., Sarazin, C. L., & Vikhlinin, A. 1999, ApJ, 521, 526

Markevitch, M., et al. 2000, ApJ, 541, 542

Markevitch, M., & Vikhlinin, A. 2001, ApJ, 563, 95

Markevitch, M., Gonzalez, A. H., David, L., Vikhlinin, A., Murray, S., Forman, W., Jones, C., & Tucker, W. 2002, ApJ, 567, L27

Markevitch, M., Govoni, F., Brunetti, G., & Jerius, D. 2005, ApJ, 627, 733 (M05)

Markevitch, M. 2006, in "The X-ray Universe 2005", September

Melrose D.B., 1968, ApSS 2, 171

Menci, N., Fiore, F., Perola, G. C., & Cavaliere, A. 2004, ApJ, 606, 58

Miniati, F. 2003, MNRAS, 342, 1009

Miniati F., 2002, MNRAS337, 199

Miniati F., Ryu D., Kang H., et al., 2000, ApJ542, 608

Miniati F., Jones T.W., Kang H., Ryu D., 2001, ApJ562, 233

Miller J.A., La Rosa T.N., Moore R.L., 1996, ApJ461, 445

Mittaz, J. P. D., Lieu, R., & Lockman, F. J. 1998, ApJ, 498, L17

Mohr, J. J., Fabricant, D. G., & Geller, M. J. 1993, ApJ, 413, 492

Mohr, J. J., Evrard, A. E., Fabricant, D. G., & Geller, M. J. 1995, ApJ, 447, 8

Moore, B., Quinn, T., Governato, F., Stadel, J., & Lake, G. 1999, MNRAS, 310, 1147

Moskalenko, I. V., & Strong, A. W. 1998, ApJ, 493, 694

Murgia M, 2001, Ph.D Thesis, Univerity of Bologna

Murgia, M., Govoni, F., Feretti, L., Giovannini, G., Dallacasa, D., Fanti, R., Taylor, G. B., & Dolag, K. 2004, A&A, 424, 429

Mushotzky R. F., Scharf C. A.,1997, ApJ 482, 13

Navarro, J. F., & White, S. D. M. 1993, MNRAS, 265, 271

Navarro, J. F., Frenk, C. S., & White, S. D. M. 1995, MNRAS, 275, 720

Navarro, J. F., Frenk, C. S., & White, S. D. M. 1997, ApJ, 490, 493

Navarro, J. F.; Hayashi, E.; Power, C.; Jenkins, A. R.; Frenk, C. S.; White, S. D. M.; Springel, V.; Stadel, J.; Quinn, T. R. 2004, MNRAS, 349, 1039

Neumann, D. M., & Arnaud, M. 1999, A&A, 348, 711

Neumann, D. M., & Arnaud, M. 2001, A&A, 373, L33

Nevalainen, J., Markevitch, M., Forman, W., 2000, ApJ 532, 694

Nevalainen, J., Lieu, R., Bonamente, M., & Lumb, D. 2003, ApJ, 584, 716

Newman, W. I., Newman, A. L., & Rephaeli, Y. 2002, ApJ, 575, 755

Norman, M. L., & Bryan, G. L. 1999, ASSL Vol. 240: Numerical Astrophysics, 19

Ohno H., Takizawa M., Shibata S., 2002, ApJ 577, 658

Ostriker, J. P., & Steinhardt, P. 2003, Science, 300, 1909

Orrù, E., et al. 2007, ArXiv Astrophysics e-prints, arXiv:astro-ph/0701776

Overduin, J. M., & Wesson, P. S. 1993, ApJ, 414, 449

Overduin, J. M., & Wesson, P. S. 1997, ApJ, 480, 470

Owen, F., Morrison, G., & Voges, W. 1999, Diffuse Thermal and Relativistic Plasma in Galaxy Clusters, 9

Owen, F. N., Eilek, J. A., & Kassim, N. E. 2000, ApJ, 543, 611

1993, Physics Today, 46, 87

Peacock JA. 1999, *Cosmology Physics*. Cambridge, UK: Cambridge Univ Press

Peterson, J. R., Kahn, S. M., Paerels, F. B. S., Kaastra, J. S., Tamura, T., Bleeker, J. A. M., Ferrigno, C., & Jernigan, J. G. 2003, ApJ, 590, 207

Peterson, J. R., & Fabian, A. C. 2006, Phys. Rep., 427, 1

Petrosian V., 2001, ApJ 557, 560

Petrosian, V. 2003, Astronomical Society of the Pacific Conference Series, 301, 337

Petrosian, V., Madejski, G., & Luli, K. 2006, ApJ, 652, 948

Pfrommer, C., & Enßlin, T. A. 2004, A&A, 413, 17

Pfrommer, C., Springel, V., Enßlin, T. A., & Jubelgas, M. 2006, MNRAS, 367, 113

Pierre M., Matsumoto H., Tsuru T., Ebeling H., Hunstead R., 1999, A&AS 136, 173

Plionis, M., & Basilakos, S. 2002, MNRAS, 329, L47

Press W.H., Schechter P., 1974, ApJ 187, 425

Randall S.W., Sarazin C.L., Ricker P.M., 2002, ApJ 577, 579

Rasia E., Ettori S., Moscardini L., Mazzotta P., Borgani S., Dolag K., Tormen G., Cheng L.M., Diaferio A, 2006, MNRAS369, 2013

Reid, A. D., Hunstead, R. W., Lemonon, L., & Pierre, M. M. 1999, MNRAS, 302, 571

Reimer, O., Pohl, M., Sreekumar, P., & Mattox, J. R. 2003, ApJ, 588, 155

Reimer, A., Reimer, O., Schlickeiser, R., & Iyudin, A. 2004, A&A, 424, 773

Reiprich T.H., Böhringer H., 2002, ApJ 567, 716

Rengelink, R. B., Tang, Y., de Bruyn, A. G., Miley, G. K., Bremer, M. N., Roettgering, H. J. A., & Bremer, M. A. R. 1997, A&AS, 124, 259

Rephaeli, Y. 1979, ApJ, 227, 364

Rephaeli Y., Gruber D., Blanco P., 1999, ApJL 511, 21

Rephaeli Y., Gruber D., 2002, ApJ 579, 587

Rephaeli Y., Gruber D., 2003, ApJ 595, 137

Ricker P.M., Sarazin C.L., 2001, ApJ 561, 621

Rosati, P., Borgani, S., & Norman, C. 2002, ARA&A, 40, 539

Rosner, R., & Tucker, W. H. 1989, ApJ, 338, 761

Röttgering, H. J. A., Wieringa, M. H., Hunstead, R. W., & Ekers, R. D. 1997, MNRAS, 290, 577

Röttiger K., Burns J.O., Loken C., 1996, ApJ473, 651

Röttiger K., Loken C., Burns J.O., 1997, ApJ 109, 307

Röttiger, K., Burns, J. O., & Stone, J. M. 1999, ApJ, 518, 603

Ryu, D., Kang, H., & Biermann, P. L. 1998, A&A, 335, 19

Ryu, D., Ostriker, J. P., Kang, H., & Cen, R. 1993, ApJ, 414, 1

Ryu D., Kang H., Hallman E., Jones T.W., 2003, ApJ 593, 599

Salvador-Sole E., Solanes J.M., Manrique A., 1998, ApJ 499, 542

Sarazin C.L., 1986, Reviews of Modern Physics 58, 1

Sarazin C.L., 1999, ApJ 520, 529

Sarazin C.L., 2002, in 'Merging Processes in Clusters of Galaxies', vol.272, p.1, edited by L. Feretti, I. M. Gioia, and G. Giovannini

Sarazin, C. L., & Lieu, R. 1998, ApJ, 494, L177

Sarazin, C. L., & Kempner, J. C. 2000, ApJ, 533, 73

Schekochihin A.A., Cowley S.C., Kulsrud R.M., Hammett G.W., Sharma P., 2005, ApJ 629, 139

Schindler S., 1996, A&A, 305, 756

Schindler S., 2002, in "Merging Processes in Galaxy Clusters." Edited by L. Feretti, I.M. Gioia, G. Giovannini. Astrophysics and Space Science Library, Vol. 272. Kluwer Academic Publishers, Dordrecht, 2002, p. 229-251

Schlickeiser R., 2002, *Cosmic Ray Astrophysics*, Springer-Verlag, Berlin Heidelberg

Schlickeiser R., Sievers A., Thiemann H., 1987, A&A 182, 21

Schlickeiser R., Miller J.A., 1998, ApJ 492, 352

Schuecker P., Böhringer H.; Reiprich T.H., Feretti L., 2001, A&A 378, 408

Schuecker P., Finoguenov A., Miniati F., Boehringer H., Briel U.G., 2004, A&A 426, 387

Smith, S. 1936, ApJ, 83, 23

Sheth R.K., Tormen G., 1999, MNRAS 308, 119

Silk, J., Djorgovski, S., Wyse, R. F. G., & Bruzual A., G. 1986, ApJ, 307, 415

Sijbring, 1993 Sijbring, L.G., 1993. PhD thesis, University of Groningen.

Somerville, R. S.; Kolatt, T. S., 1999, MNRAS, 305, 1

Springel, V. 2005, MNRAS, 364, 1105

Springel, V., Yoshida, N., & White, S. D. M. 2001, New Astronomy, 6, 79

Springel, V., et al. 2005, Nature, 435, 629

Steinmetz, M., & Muller, E. 1995, MNRAS, 276, 549

Steinmetz, M. 1996, MNRAS, 278, 1005

Sun M., Jones C., Forman W., Nulsen P.E.J., Donahue M., Voit G.M., 2006, ApJ637, L81

Sunyaev, R. A., Norman, M. L., Bryan, G. L., 2003, Astronomy Letters, vol. 29, p. 783-790

Takizawa M., Naito T., 2000, ApJ 535, 586

Taylor, G. B., Govoni, F., Allen, S. W., & Fabian, A. C. 2001, MNRAS, 326, 2

Thierbach, M., Klein, U., & Wielebinski, R. 2003, A&A, 397, 53

Tormen G., Bouchet F. R., White S. D. M., 1997, MNRAS, 286, 865

Tormen G., Moscardini L., Yoshida N., 2004, MNRAS 350, 1397

Tribble, P. C. 1989, MNRAS, 238, 1247

Tribble, P. C. 1993, MNRAS, 263, 31

Tsay M., Hwang C.-Y., Bowyer S., 2002, ApJ 566, 794

Tsuru T., Koyama K., Hughes J.P., Arimito N., Kii T., Hattori M., 1996, in "UV and X-ray Spectroscopy of Astrophysical and Laboratory Plasmas": Edited by K. Yamashita and T. Watanabe. Tokyo : Universal Academy Press, 1996. (Frontiers science series ; no. 15)., p.375

Tucker, W. H., & Rosner, R. 1983, ApJ, 267, 547

Yan H., Lazarian A., 2004, ApJ 614, 757

Yoshida N., Sheth R. K., Diaferio A., 2001, MNRAS, 328, 669

van Haarlem, M., & van de Weygaert, R. 1993, ApJ, 418, 544

Vazza, F., Tormen, G., Cassano, R., Brunetti, G., & Dolag, K. 2006, MNRAS, 369, L14

Venturi, T., Giovannini, G., & Feretti, L. 1990, AJ, 99, 1381

Venturi T., Bardelli S., Dallacasa D., Brunetti G., Giacintucci S., Hunstead R.W., Morganti R., 2003, A&A 402, 913

Venturi, T., Giacintucci, S., Brunetti, G., Cassano, R., Bardelli, S., Dallacasa, D., & Setti, G. 2007, A&A, 463, 937

Vikhlinin, A., Markevitch, M., & Murray, S. S. 2001, ApJ, 551, 160

Vogt, C., & Enßlin, T. A. 2003, A&A, 412, 373

Voigt, L. M., Schmidt, R. W., Fabian, A. C., Allen, S. W., & Johnstone, R. M. 2002, MNRAS, 335, L7

Völk H.J., Aharonian F.A., Breitschwerdt D., 1996, SSRv 75, 279

Völk, H. J., & Atoyan, A. M. 1999, Astroparticle Physics, 11, 73

Völk, H. J., & Atoyan, A. M. 2000, ApJ, 541, 88

West, M. J., Jones, C., & Forman, W. 1995, ApJ, 451, L5

White, S. D. M., & Rees, M. J. 1978, MNRAS, 183, 341

White, S. D. M., Frenk, C. S., & Davis, M. 1983, ApJ, 274, L1

White, S. D. M., & Frenk, C. S. 1991, ApJ, 379, 52

White D. A., 2000, MNRAS312, 663

Willson, M. A. G. 1970, MNRAS, 151, 1

Wu X.-P., 1994, ApJ436, L115

Wu X.-P., Chiueh T., Fang L.-Z., Xue Y.-X., 1998, MNRAS301, 861

Wu, X.-P. 2000, MNRAS, 316, 299

Zhang Y.-Y., Finoguenov A., Bhringer H., Ikebe Y., Matsushita K.,Schuecker P., 2004, A&A 413, 49

Zhang, Y.-Y., Böhringer, H., Finoguenov, A., Ikebe, Y., Matsushita, K., Schuecker, P., Guzzo, L., & Collins, C. A. 2006, A&A, 456, 55

Zwicky F. 1933,Helv. Phys. Acta, 6, 110

Zwicky F. 1937. *Ap. J.* 86:217–246

Zwicky F, Herzog E, Wild P. 1966. *Catalogue of galaxies and of clusters of galaxies.* Pasadena: California Institute of Technology